

Bergische Universität Wuppertal
Fachbereich Mathematik und Naturwissenschaften
Fachgruppe Physik

DOCTORAL THESIS

A systematic investigation of carbon, metallic
and semiconductor nanostructures for
field-emission cathode applications

Dissertation zur Erlangung des Doktorgrades
des Fachbereichs Physik der Bergischen Universität Wuppertal

Author:

Pavel SERBUN

Supervisor:

Prof. Dr. Günter MÜLLER

Date of submission: 29. November 2013

Date of examination: 04. February 2014

Wuppertal – 2014

Die Dissertation kann wie folgt zitiert werden:

urn:nbn:de:hbz:468-20140311-145531-0

[<http://nbn-resolving.de/urn/resolver.pl?urn=urn%3Anbn%3Ade%3A468-20140311-145531-0>]

Abstract

In this work, various carbon, metallic and semiconductor nanostructures were fabricated within collaborations and systematically investigated for potential field emission (FE) cathode applications.

Various carbon-based cathodes were obtained by different chemical vapour deposition methods. Single-walled carbon nanotube (CNT) networks grown on n-Si substrates at $\sim 150^\circ\text{C}$ showed well-homogeneous FE with $\sim 10^4$ emitting sites/ cm^2 at low onset field E_{on} (1nA) ~ 2.5 V/ μm . During the local measurements $\varnothing 150$ μm sites yielded stable currents up to 0.2 mA. Integral measurements of the whole cathodes revealed fairly homogeneous FE resulting in at least 10 mA/ cm^2 . Arrays of entangled CNT bundles of ~ 2 μm height, 2-3 μm patch and 100, 10 and 5 μm pitch were grown on n-Si wafers with trimetallic Mo/Al/Ni layers. Highly efficient and well-aligned FE at E_{on} (1nA) ~ 15 V/ μm was obtained from CNT arrays with a pitch of 100 μm , however, the highest current up to 0.5 mA at 400 V was achieved from a spot of 150 μm for cathodes with a pitch of 5 μm . Integral measurements of the whole cathodes showed fairly homogeneous FE at currents up to 4.4 A/ cm^2 . CNT columns of $\varnothing=250$ μm and different height ($h = 70$ or 350 μm) forming quadratic arrays with a pitch of 650 μm showed fairly aligned and efficient FE at comparatively low E_{on} (1nA) ~ 2 V/ μm . Maximum current values up to 600 μA at 15 V/ μm were achieved independently of the column height. The FE triode tests of single CNT columns yielded anode-cathode current ratio up to 97 % at a gate (anode) voltage of 247 (2500) V. Structuring of carbon nanowall (CNW) films was successfully performed with a laser for the optimization of their FE properties. Such cathodes exhibited fairly aligned and efficient FE at E_{on} (1nA) = 10-20 V/ μm . Local FE measurements of selected CNW patches revealed maximum current values up to ~ 100 μA .

Mechanically stable and randomly distributed copper nanocones (Cu-NCs) were fabricated by ion-track template method. Depending on the process parameters, Cu-NCs of ~ 28 μm length, ~ 3 μm base, with different ~ 60 -300 nm tip radius and number density were fabricated. The cathode with high number density of Cu-NCs (10^7 cm^{-2}) yielded stable currents up to 280 μA at 100 V/ μm from an emission spot of 30 μm . In contrast, the cathodes with a triangular patch array ($\varnothing 150$ μm , 320 μm pitch) of less Cu-NCs (10^5 cm^{-2}) provided fairly homogeneous and well-aligned FE of all Cu-NC patches at much reduced E_{on} (1nA) < 10 V/ μm and demonstrated an average current of 30 μA /patch at 32 V/ μm . The FE performance of the Cu-NC cathode was improved by a thin Au coating resulting in an average current of 151 μA at 50 V/ μm . Integral FE measurements on the whole Cu-NC cathode showed fairly homogeneous FE at 8 mA/ cm^2 .

Silicon technology is the most suitable for fabrication of highly-uniform arrays of bare p- and n-type Si tips. Rather homogeneous and well-aligned FE from all tips and stable currents up to ~ 0.1 (0.6) μA for p-(n-) type tips were achieved. In comparison, Au-coated n-type Si tips showed improved FE uniformity and at least 5 times higher current values (i.e. ~ 3 μA /tip), at $\sim 30\%$ higher extraction field though. P-Si tips showed a current saturation region of about 10 nA. In this region, emitters provide the highest current stability ($< 5\%$) and an optical current switching ratio of ~ 2.5 .

Potential applications of the described above materials are discussed.

Contents

Symbols and abbreviations

1. Introduction	1
2. Theoretical background of electron field emission (FE)	3
2.1. Electron emission from metals under applied electric field	3
2.2. Field enhancement factor, mutual shielding and adsorbate effects	6
2.3. Field emission from semiconductors	12
3. Potential applications of cold field emission cathodes	16
3.1. Fast-switchable and miniaturized X-ray tubes	18
3.2. THz and mm-wave amplifiers	19
3.3. Vacuum sensors	22
4. Experimental techniques for cold cathodes and surface analysis	23
4.1. Field emission scanning microscope (FESM)	23
4.2. Integral measurement system with luminescent screen (IMLS)	26
4.3. Scanning electron microscope with energy dispersive X-ray analysis	29
5. Field emission from carbon nanostructures	30
5.1. CNT networks grown at $\sim 150^\circ\text{C}$ on Si substrates	31
5.2. CVD growth of CNT bundles using Mo/Al/Ni catalysts	37
5.3. Catalytic water-assisted CVD synthesis of short CNT bundles	42
5.4. Vertically aligned CNT columns of different height and triode tests	47
5.5. Laser-structured carbon nanowalls on Si and stainless steel substrates	53
5.6. Conclusions and outlook	58
6. Metallic nanocones grown in polymer ion-track membranes	60
6.1. Fabrication of copper nanocones (Cu-NC)	61
6.2. Role of the contact interface and number densities of nanocones	64
6.3. Performance of Au-coated Cu-NCs of reduced number density	67
6.4. Current carrying capability of single bare copper nanocones	77
6.5. Integral measurement results	80
6.6. Conclusions and outlook	82
7. Silicon tip arrays fabricated by anisotropic etching technology for FE device	83
7.1. Optimal tip shape considerations and silicon emitter design	83
7.2. Fabrication	85
7.3. Field emission performance of highly uniform silicon emitters	89
7.4. Properties of single p-Si tips, optical current modulation and current scaling	93
7.5. Conclusions and outlook	97
8. Thesis summary and outlook	99
References	104
Acknowledgements	123
List of papers	124

Symbols and abbreviations

ADC	Analog-to-digital converter
AES	Auger Electron Spectroscopy
CCD	Charge-coupled device
CCM	Constant current mode
Cu-NC	Copper nanocones(s)
CNT	Carbon nanotube(s)
CNW	Carbon nanowall(s)
CVD	Chemical vapor deposition
CVM	Constant voltage mode
HFCVD	Hot-filament chemical vapor deposition
PECVD	Plasma-enhanced chemical vapor deposition
DC	Direct current
E, F	Electric field
EDX	Energy dispersive X-ray analysis
E_{\max}	Maximum electric field
E_{on}	Onset electric field (1nA)
E_c	Conduction band (lower edge)
E_f	Fermi level
E_g	Band gap (upper edge)
E_v	Valence band
FE	Field emission
FEA	Field emitter array
FESM	Field emission scanning microscope
Fig.	Figure
FN	Fowler-Nordheim
GPIO	General purpose interface bus
GbE PCI	Gigabit Ethernet Peripheral Component Interconnect
H, h	Height
I	Current
I_c, I_g, I_a	Cathode current, gate current, anode current, respectively
IMLS	Integral Measurement System with Luminescent Screen
j, J	Current density

MIM	Metal-insulator- metal
MOS	Metal-oxide semiconductor
MWNT	Multiwall CNT
N_e	Number density
NW	Nanowire
NC	Nanocone
P	Power
PC	Personal computer
PID	Proportional-integral-derivative
ppm	Parts per million
r	Radius
rf	Radio frequency
RIE	Reactive ion etching
S	Effective emitting surface
SEM	Scanning electron microscopy
SWNT	Singe walled carbon nanotube
t	Time
$^{\circ}\text{C}$, T	Temperature
Tab.	Table
TEM	Transmission electron microscope
THz	Terahertz
TMP	Turbo molecular pump
UHV	Ultra high vacuum
U	Voltage
V_0	Potential
α	Field correction factor
\emptyset	Diameter
ϕ	Work function
ϕ_{eff}	Effective work function
β	Field enhancement factor
χ	Surface barrier height
Δz , d	Anode-cathode gap
2D, 3D, 4D	Two, Three, Four dimensional

1. Introduction

Vacuum micro- and nanoelectronics attract much attention because of their several advantages compared with solid-state electronics [Dams11, Dams12, Boos11]. They offer a unique opportunity to build novel devices which are either not available or difficult to realize with semiconductor electronics and offer such advantages as high speed and low energy dissipation because of the ballistic electron transport in vacuum as well as performance unaffected by harsh environments.

Potential applications include high-power millimetre-wave and terahertz sources [Boos08, Boos11, Qiu09, Kart04, Miln06a, Nati99], compact and fast-switching X-ray sources [Fili12, Jeon13a, Jeon13b], integrated sensor systems [Dams12, Serb13, Lee92], flat light sources [Obra13] and many others [Zhu01, Eich08, Brod94, Bust92, Sait10, Ren13]. For instance, the average power attained by solid-state devices at 30 GHz is about 1-10 W [Miln04, Miln06], whereas vacuum tubes are capable of providing hundreds of kilowatts of power at 35 GHz and at THz regime frequencies they provide power of about 1 mW instead of 1 μ W for solid-state electronic devices [Koop12, Whal00, Boos08, Boos11, Qiu09, Whal09]. To obtain higher power levels in a THz regime, high current density of ~ 50 -100 A/cm² is required [Boos11]. Development of high-power terahertz sources is a very challenging task and has many benefits such as higher-data-rate communication networks (internet, wireless, etc.). Moreover, the development of new security systems, new methods of biomedical diagnostics and many other applications are possible at THz frequencies [Kemp06, DARPA, DMRC].

The electron source is the main and most critical component of such vacuum micro- and nanoelectronic devices. Cold field emission (FE) cathodes offer significant advantages compared with thermionic and photoelectric sources in this respect [Nati99, Dams12, Eich08, Zhu01, Sait10]. The greatest advantages of cold cathodes are: low power consumption because thermal power is not required to produce the emission of electrons, therefore, FE-based cathodes provide an opportunity to build compact and battery-powered electron sources or devices; fast response time and emission can be turned on with low gate voltages (< 100 V); high efficiency; a narrow energy spread of the FE-emitted electrons (0.2-0.3 eV). Nevertheless, to compete with other methods, e.g., thermionic cathodes, current densities in the range of ~ 1 -2 A/cm² are required [Miln06a]. The development and investigation of different types of materials is needed, in order to achieve the required current values.

Carbon-based, metallic and semiconducting nanostructures have mainly been discussed in the recent literature as base material for field emission cold cathodes [Eich08, Zhu01,

Sait10]. Carbon nanotubes (CNTs), since their discovery by Iijima in 1991[Iiji91], have been the most actively investigated material [Bona01a]. Because of their unique properties, a single CNT just a few nanometres in diameter can carry high FE current of $\sim 2\text{-}8 \mu\text{A}$ [Dean00, Bona03], which is about 1000 times higher than for copper [Sait10]. Moreover, CNTs are more chemically stable than metals, i. e. CNTs are more robust and would have a longer lifetime in non-ultra high vacuum operation [Fili13], which is an additional advantage over metal field emitters. CNTs have some drawbacks, however, as high temperatures above 500°C are used for their synthesis [Ren13], and hence the use of flexible polymer substrates is not possible; the uniformity and reproducibility of carbon nanotubes are still quite limited because the synthesis of CNTs with uniform chirality is a difficult task; CNT emitters suffer from poor contact to the substrate, which result in lifetime issues, high contact resistance and a limitation of the FE current; furthermore, varying alignment and positioning of single nanotubes [Navi10, Navi10a] often limit the FE homogeneity and cause low transmission efficiency of the triode structures.

Metallic nanostructures could be good alternatives to CNTs in terms of higher controllability, reproducibility and better contact with the substrate. Promising FE results have been reported for unstructured cathodes with randomly distributed copper [Maur06], gold-coated nickel [Dang07] and gold nanowires (NWs) [Dang08]. Patch arrays of multiple Au-NWs obtained by a shadow mask during heavy-ion irradiation of the template [Toim12, Kari07] yielded high efficiency, good alignment and FE homogeneity at a suitable onset field [Navi09, Navi10]. The FE current limit of such patches, however, varied strongly because of random destruction of individual NWs caused by their insufficient substrate contact regarding both poly-crystalline [Dang08, Kari07, Navi09, Navi10d, Navi10c] and single-crystalline Au-NWs [Navi10c].

Advanced Si-based semiconductor technology is the most suitable for fabricating uniform and sharp nanostructures in exactly the right position. Furthermore, the electric properties of silicon emitters can be controlled by doping over a wide range, which is not possible for metals [Sze07]. B-doped Si-tip arrays are most attractive because the field emission current can be extremely stable ($< 1\text{-}5\%$) [Serb13, Teep05, Schr74,] and, in addition, the FE current can be switched by illumination with light [Serb13, Teep05, Sch74, Born12].

The goal of this thesis is a systematic investigation of various types of nanostructures as cold FE cathodes. For this purpose, different carbon-based, metallic and semiconducting nanostructures were fabricated by chemical-vapour deposition, ion-track template [Toim12, Serb12a] and anisotropic etching techniques, respectively [Dams12, Serb13]. The FE properties of these nanostructures were investigated. The possible application is also discussed.

2. Theoretical background of electron emission

The escape of electrons from the surface of a condensed phase (e.g. metal) into another (classically a vacuum) is defined as electron emission [Lath95, Gome93, Zhu01]. There are several methods of obtaining electron emission from the surface of metal [Gome93, Furs05, Eich08, Zhu01]. The first way is to heat the metal up to high temperatures (above 1000°C); this method is known as thermionic emission [Dush23]. In this case, heat energy is transformed into kinetic energy and electrons get additional energy. If the obtained energy exceeds the work function of that metal, the electrons overcome the potential barrier on metal-vacuum interface and leave the metal. The second method which does not require metal heating is known as cold or field electron emission. Field emission takes place when applied electric field is high enough to reduce the potential barrier on metal-vacuum interface. In this case electron can pass through this barrier due to quantum-mechanical tunnelling. Two other methods are associated with the bombardment of the metal surface with photons or beam of electrons and, respectively, these two methods are called photoelectron and secondary electron emission [Eich08]. It is also possible to combine these types of electron emission, for example, Schottky emission process in which the high electric field and temperature are applied to the metal. The comparison of these methods shows that FE has several advantages, resulting in its preferable use in vacuum electronics, such as low power consumption, fast response time, high brightness, compactness, high efficiency and the beam and the energy spread of the FE-emitted electrons are narrower.

This chapter contains the basic theoretical material and background of electron emission under applied electric field. It will be described how the electrostatic field depends on the presence of nanostructures, their geometry, position on the metal surface and how the presence of adsorbates influence the stability of electron tunnelling.

2.1. Electron emission from metals under applied electric field

The field emission was first observed by R. Wood in 1897 [Wood97], while the first approximate explanation of the FE phenomenon was developed by W. H. Schottky [Scho23]. Later however, the FE theory was considered in a different way by R. H. Fowler and L. W. Nordheim, in order to improve the theoretical explanation and its correlation with the experimental results [Fowl28]. The phenomenon of field emission is based on the effect of quantum-mechanical tunnelling [Schi68] of electrons via a thin potential barrier at an ideal clean and flat metal surface. For field emission to occur, the applied electric field E must be of about $\sim 10^7$ V/cm or 1 V/nm. In fig. 2.1 a schematic illustration of the FE is presented.

Under applied external electric field E , the vacuum level bends by the amount $(-eEz)$ outside the metal, and when combined with the image charge effect [Nord28, Scho23, Eng85, Forb12a, Fan42] the potential energy barrier is reduced by $\Delta\phi$. The potential barrier is described by a function, which takes into account the image effect

$$V(z) = -\frac{e^2}{16\pi\epsilon_0 z} - eEz, (z > 0), \quad (2.1)$$

where $-e^2/16\pi\epsilon_0 z$ is the potential energy from the image charge effect, $-eEz$ is the potential energy outside the metal, e is the electron charge, z is the coordinate perpendicular to the surface of metal and ϵ_0 is the dielectric constant of the vacuum.

At a high field value, the width of the barrier becomes small enough that the electrons from the metal have a non-zero probability to pass through the barrier to vacuum.

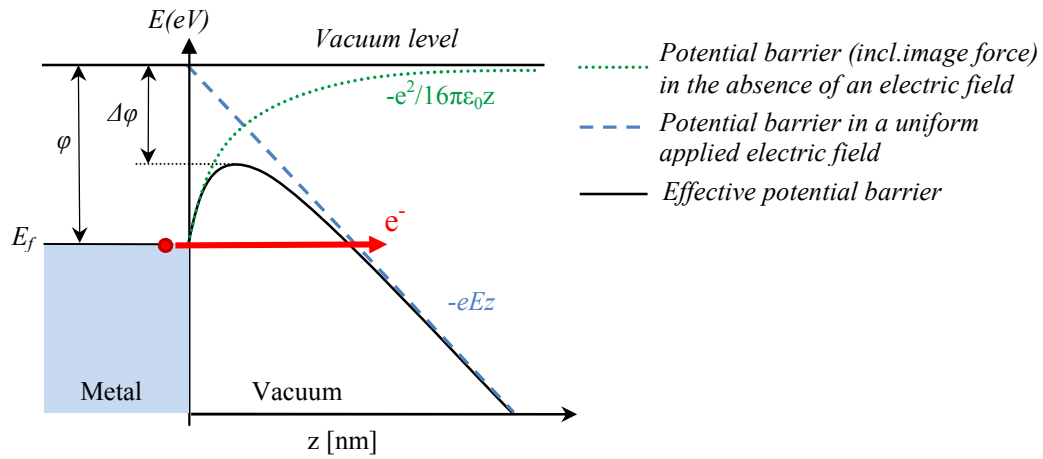


Fig. 2.1. Schematic illustration of the electron tunnelling from Fermi level E_f through the potential barrier ($V(z)$) on metal-vacuum interface. $\Delta\phi$ is the reduction of the work function potential barrier height ϕ (Schottky lowering effect) due to image charge effects under applied electric field [Scho23, Eng85, Forb12a, Nord28, Oost66, Eng85, Nati99]. z - is the distance of electron from the metal surface.

According to the Fowler-Nordheim (FN) theory, the field emission current density through the barrier is expressed by

$$j = q \cdot \int N(E)D(E)dE \quad (2.2)$$

where q is the electron charge; $N(E)$ is the total number of electrons striking unit area of surface in unit time and having energy E ; $D(E)$ is the probability of electrons, which is depends on the barrier's width and height.

The simplified FN equation for an ideal flat and clean metal surface with constant electric field outside it is given as follows

$$j(E) = \frac{AE^2}{\phi t^2(y)} \times \exp\left(-\frac{B\phi^{3/2}}{E} \nu(y)\right) \quad (2.3)$$

with $j(E)$ in A/cm^2 ; E in V/cm ; ϕ is the work function in eV and Fowler-Nordheim constants $A = 1.5414 \times 10^{-6} \text{ A eV V}^{-2}$ and $B = 6.8308 \times 10^7 \text{ eV}^{-3/2} \text{ V nm}^{-1}$; y is the Nordheim parameter, which is given by $y = \Delta\phi/\phi$, where $\Delta\phi$ is the Schottky barrier lowering $\Delta\phi = \sqrt{e^3 E / (4\pi\epsilon_0)} = 3.79 \cdot 10^{-2} \sqrt{E}$ (in eV) [Scho23, Forb12a] and ϕ is the work function of the metal. $t(y)$ and $v(y)$ are Nordheim functions that include the image charge effects. These parameters are tabulated and can be found in [Bur53] or in the ref. [Forb06].

When the image charge effect is not taken into account, the equation (2.3) is given by

$$j(E) = \frac{AE^2}{\phi} \times \exp\left(-\frac{B\phi^{3/2}}{E}\right) \quad (2.4)$$

The electric field E between ideally clean and flat metallic electrodes is homogeneously distributed and can be calculated as $E = V/d$, where V is the applied voltage and d is the gap between the electrodes. In that case, to pull the electrons out of the metals (depends on the work function) a high electric field of about $2\text{-}4 \times 10^7 \text{ V}/\text{cm}$ is required [Fowl28]. However, it has been found experimentally that the field emission appears at much lower fields of about $3\text{-}6 \times 10^4 \text{ V}/\text{cm}$ [Nied86, Dang07, Navi10]. An explanation for this effect was made by W. Schottky in 1923. He suggested the possible existence of a pointed microtip (or surface roughness) on the metal surface that can enhance the external electric field by factor β , so that $E_{\text{max}} = \beta \cdot E$ [Scho23]. The apex of the microtip corresponds to an effective emitting area S and therefore $I(E) = S \cdot J(E)$.

In the presence of a pointed tip on the metal surface, the applied electric field is distributed non-uniformly as shown in Fig. 2.2. Numerical simulation of the electric field shows that the largest field of $\sim 4 \text{ V}/\mu\text{m}$ is at the tip of the emitter, while on the flat part of the cathode the field is $\sim 1 \text{ V}/\mu\text{m}$. Hence, the original FN equation (2.4), which is correct for flat and clean emitter surface with constant electric field outside it, can not be used.

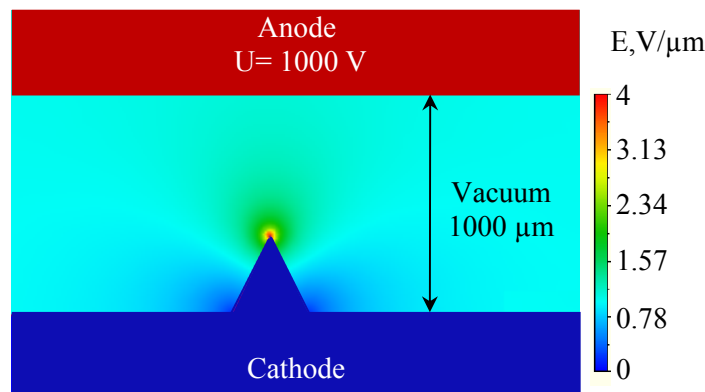


Fig. 2.2. Results of a numerical simulation of electric field distribution between two planar electrodes (1 mm spacing) in the presence of a tip on the cathode surface shows the nonuniformity of the E ; field enhancement at the apex of the tip achieves $4 \text{ V}/\mu\text{m}$ compared to $1 \text{ V}/\mu\text{m}$ on the flat part of the cathode [Navi10].

Thus, Fowler-Nordheim equation (2.4) has to be modified as follows

$$I(E) = \frac{A \cdot S(\beta \cdot E)^2}{\varphi} \times \exp\left(-\frac{B\varphi^{3/2}}{\beta \cdot E}\right) \quad (2.5)$$

where β is the so-called geometrical field-enhancement factor, which reflects the ability of the emitters to enhance the local electric field, S is an effective emitting area in cm^2 through which the emission current flows. The β and S parameters can be found from the current-voltage (field) curve plotted in the Fowler-Nordheim coordinates $\ln(I/E^2)$ versus $1/E$ as follows

$$\beta = -\frac{B\varphi^{3/2}}{K}, \quad S = \frac{\varphi \cdot \exp(C)}{A\beta^2} \quad (2.6)$$

where K is the slope of the FN plot, and C is the crossing of the y-axis (or its liner fit).

As can be seen from the equation 2.5 the field emission current depends strongly on the applied electric field and on the field enhancement factor β and on the work function value φ . Therefore, a slight change in the values of these parameters leads to significant changes of FE current. This standard Fowler-Nordheim-like equation is widely used to interpret of field emission from a single emitter or from large-area field emitters, for example, from Spindt arrays [Spin76]. Nevertheless, R. Forbes reported that the equation (2.5) may lead to erroneous conclusions on FE performance from large area arrays when experimental results are not clearly reported [Forb12a, Forb13]. As follows from equation 2.6, the variation in the slope of the FN plot (hence, the different value of the field enhancement), shows the change of the work function since the vacuum gap remains constant [You09].

2.2. Field enhancement factor, mutual shielding and adsorbate effects

Many different geometrical models of field emitters have been suggested to estimate the value of the field enhancement factor β . Utsumi et. al. concluded that the cylindrical tip with hemispherical end provided the highest β value [Utsu91, Giva95, Edgc01] and can be calculated as follows

$$\beta = \frac{h}{r} + 2 \quad (2.7)$$

where h is a tip height and r is a tip radius of curvature.

C. Edgcombe and U. Valdre combined computational and experimental investigations of the field enhancement factor as a function of aspect ratio h/r for a cylindrical tip of radius $r = 10$ nm between planar electrodes at a fixed gap of $100 \mu\text{m}$ and the anode voltage of 1000 V [Edgc01, Bari11, Forb03]. The calculated β values were slightly lower than expected and did not follow to the equation 2.6 (if h/r is more than 10). The reason of such a result can

be explained by the different values of the gap and will be discussed below. A line in fig. 2.3 represents the following approximations

$$\beta = 1.125 \cdot \left(\frac{h}{r} + 2\right)^{0.91} \quad (2.7)$$

While, the experimental results showed that the field enhancement factor in the range of h/r between 100 and 500 at the anode-cathode gap of $100 \mu\text{m}$, can be approximated by

$$\beta = 0.72 \cdot \frac{h}{r} \quad (2.8)$$

The achieved results are in good agreement with those suggested by others [Bari11, Groe99].

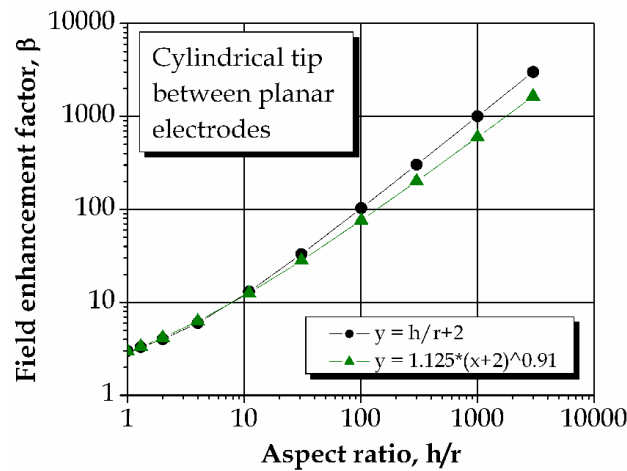


Fig. 2.3. The field enhancement factor β as a function of aspect ratio h/r for a cylindrical tip of radius 10 nm for a fixed gap of $100 \mu\text{m}$ [Edgc01].

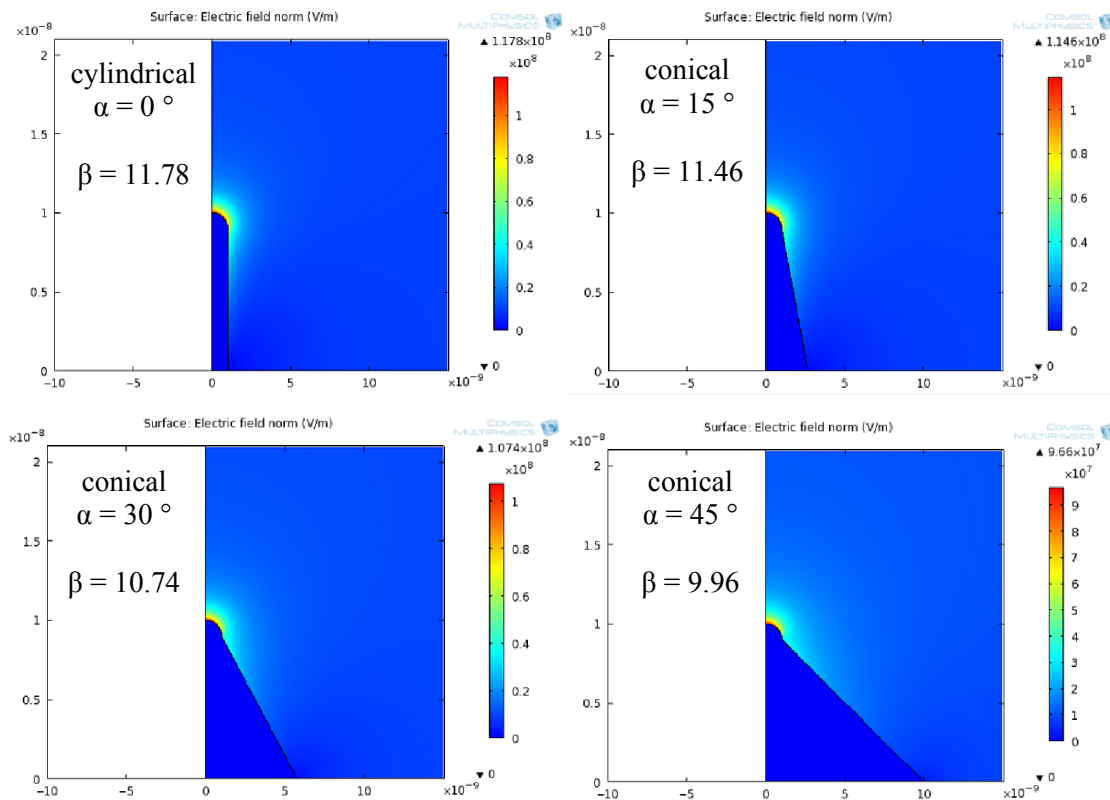


Fig. 2.4. Simulation of the electric field for various half-angled field emitter shapes, $h = 10 \text{ nm}$, $r = 1 \text{ nm}$, $V = 1 \text{ V}$ at a vacuum gap $d = 100 \text{ nm}$ [Bari11].

In fig. 2.4 the simulation of the electric fields at the apexes of various cylindrical and conical emitters at a fixed tip radius, emitter height and vacuum gap is presented. The result shows the expected highest field enhancement of 11.78 from the cylindrical-shaped emitter and the resulting beta value corresponds to the equation 2.7. While the conical structures show a decrease in beta value from 11.46 to 9.96. It means the field enhancement factor depends on the base radius of the cones and decreases when their base area becomes larger.

E. Givargizov et. al. reported that the field enhancement factor might be significantly higher than mentioned above when a small particle is sitting on the end of the tip (Fig. 2.5a) [Giva95]. In this case, the field enhancement factor is determined as the product of two β values (Fig. 2.5b, c) and, therefore, the FE current appears at much lower electric field.

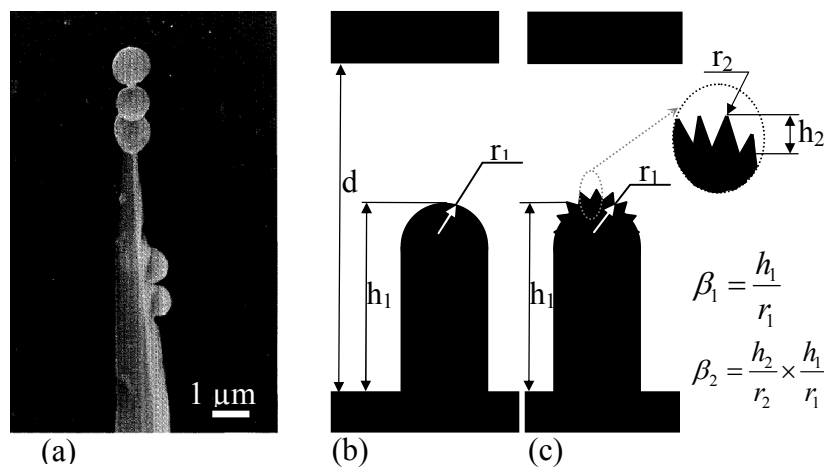


Fig. 2.5. SEM image of single-particle coated Si tip (a). Schematic diagram of an emitter without (b) and with (c) particles on the end of the tip. [Giva95].

Furthermore, Zhong et. al. and other researchers reported that the field enhancement factor also depends on the vacuum gap [Zhon02, Dang08, Xue06]. When the vacuum gap is increased from 0.7 to 5.2 mm, the field enhancement factor extracted from the slop of the FN plot increases from 3700 to 15000 (Fig. 2.6). The result also shows that $1/\beta$ is linear to $1/d$.

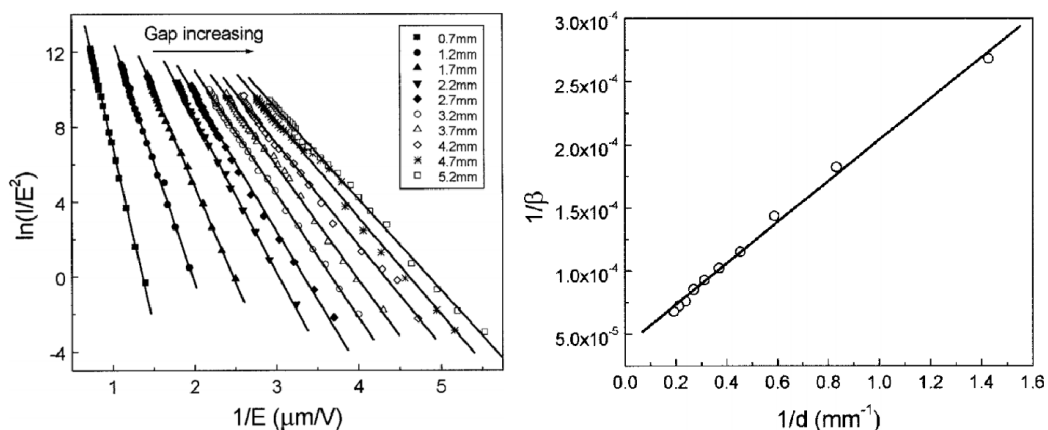


Fig. 2.6. FN-plots of FE from CNTs on an iron tip with different vacuum gaps and relationship of the field enhancement factor β and vacuum gap d . The results show a linear dependence of the β vs. d [Zhon02].

Above, the dependence of the field enhancement factor on the tip shape, height and radius of curvature and inter-electrode distance was presented; however, there is another important parameter influencing the FE properties is the spacing between emitters. It has been shown that closely-spaced emitters reduce the field enhancement factor due to insufficient electric field penetration between parallel standing tubes of $1\ \mu\text{m}$ height as shown in fig.2.7 [Bona01b, Nils00, Miln04, Teo02]. The strongest emission was for the distance of $4\ \mu\text{m}$, while moderate and the lowest enhancement was at $1\ \mu\text{m}$ and $0.5\ \mu\text{m}$, respectively. Hence, to minimize field-shielding effects and to optimize FE current density, the distance between vertically aligned emitters have to be by twice larger than their height [Miln04, Nils00, Hira08].

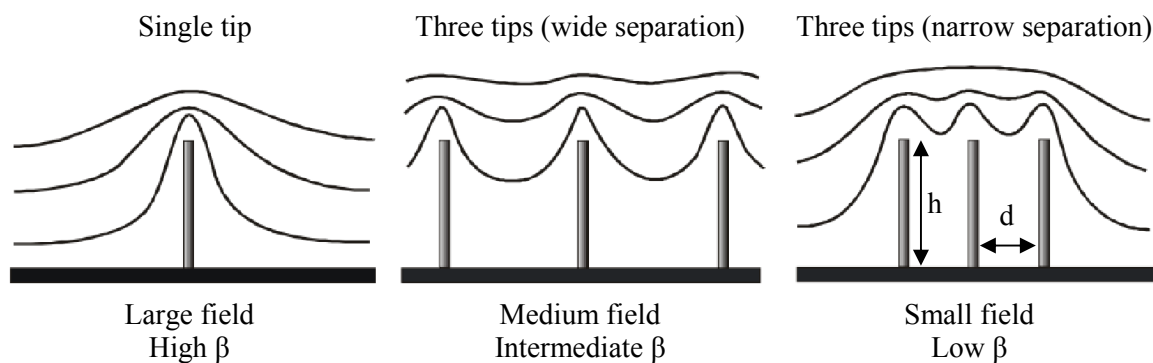


Fig. 2.7. Simulation of the equipotential lines of the electrostatic field for field emitters of $1\ \mu\text{m}$ height and $2\ \text{nm}$ radius, for distances between them of 4 , 1 and $0.5\ \mu\text{m}$ [Nils00].

Actually, the FE from a single emitter have been extensively studied experimentally and theoretically, while electron emission from a large area cathode is much more complicated due to non-uniformities of emitters and shielding of densely packed emitters. In order to analyze the nonuniformity in the FE arrays, F. Dall'Agnol and D. den Engelsen used COMSOL Multiphysics® simulation software. Fig. 2.8 shows the simulation results of a 3×3 emitter array for four different situations:

- in the first case only the heights of the emitters in a square structured array are varied. As can be seen, the maximum electric field is concentrated on the top of highest emitters, while the shorter tubes are shielded. Hence, the FE current will be provided by the highest CNTs.

- in the second case, emitters have the same pitch and the same height, but different diameter. It means that the screening effect is nearly the same for all tubes, but the field enhancement factor is different for all emitters. Hence, the maximum electric field at the apex of the thinner tube and the FE current comes from individual sharper emitters.

- in case where only the position of the emitters is varied, some tubes are more shielded than the others, however, the electric field at the tips look more uniform than in the first and second cases. In this situation the total FE current depends less on location than on the diameter and the height of the emitters.
- finally, all three parameters were taken into account. The result is nearly similar to the first case where the current is determined by the highest emitters, while the others are shielded.

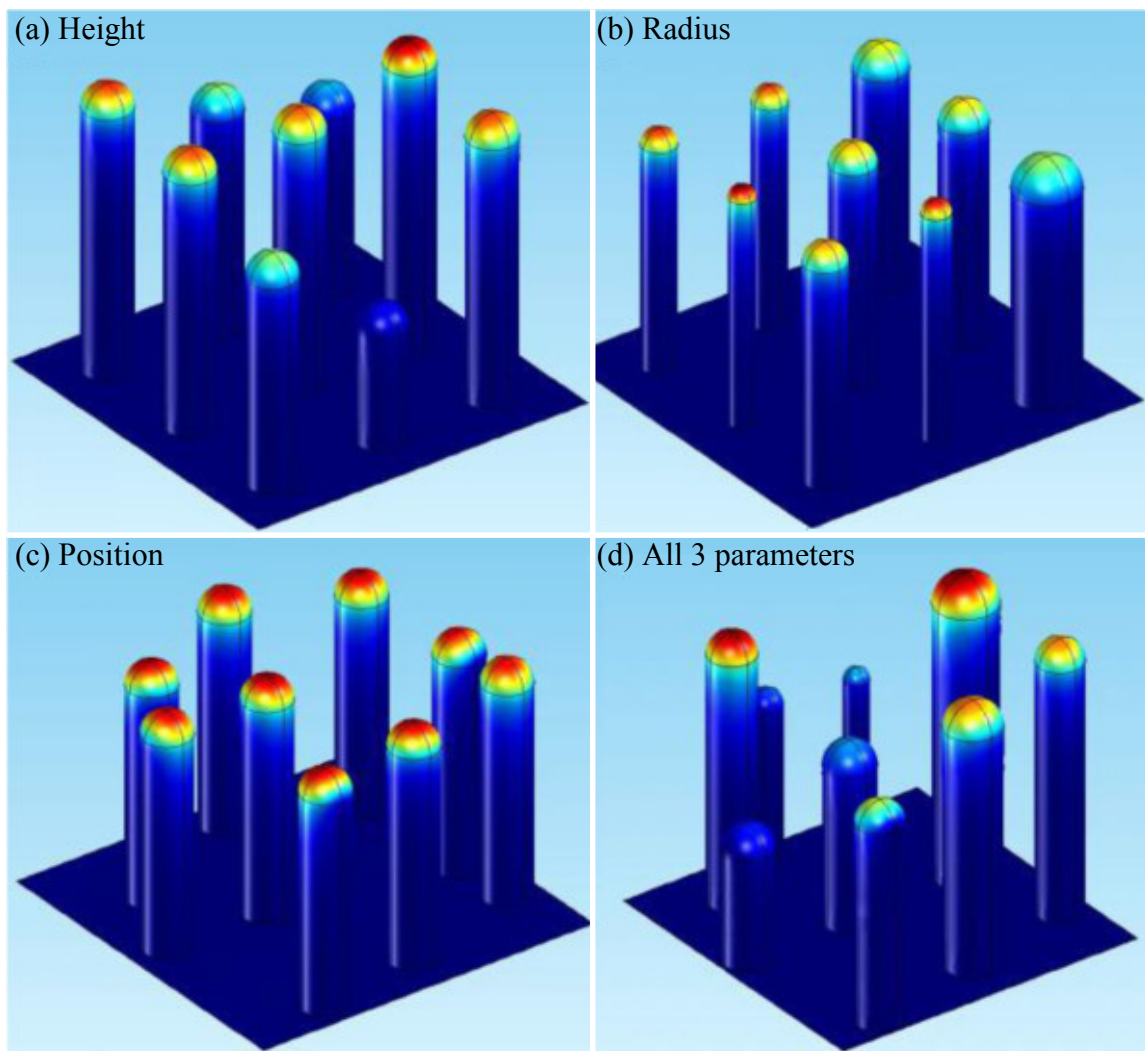


Fig.2.8. Simulation of a 3×3 tip array with different geometry and position of emitters: in (a-c) only one parameter, correspondingly, the height, radius and location is varied, while in (d) all three parameters are taken into account. The red color shows the highest field [Dall13].

These results can be taken into account in estimating of the efficiency and stability of the field emitters in the array. However, simulation of larger arrays and taking into account all the possible effects (variation of the tip geometry, the number density of emitters, shielding, heating and adsorbate effects, coating with other metals and etc.) is difficult to realise due to

insufficient computer memory and long simulation times. Thus, to build structured cold cathodes with optimal FE properties, experimental investigations are needed.

Actually, interpretation of experimental results is based on the FN theory, which describes the field electron emission from perfectly clean and flat surfaces (see chapter 2.1). However, practically, field emission even at ultra high vacuum (10^{-9} mbar) is very sensitive to slight changes of the potential barrier due to the presence of gas atoms (adatoms) or molecules such as H_2 , N_2 , O_2 , H_2O that can be adsorbed onto the cathode surfaces (i.e. W, Ni and CNTs). It was reported that the presence of the gas molecules change the FE properties for a fixed electric field, i.e. the adsorption and desorption of the atoms produce instabilities, switching between electronic states, deviation from linearity of the FN plots and resulting in unrealistic values of the field amplification factor [Burc80, Ehrl61, Alfe67, Zeit88, Zeit91, Dong03].

At first, such changes were associated only with the changing of the work function through the adsorbates [Ehrl61, Good56]. Nevertheless Duke and Alferieff reported that adsorption changes the field electron emission via the effective work-function to be used in the FN equation (2.2) is not correct, because the adsorbed atom changes the shape of the electrostatic potential seen by tunnelling electron and thus its tunnelling probability [Duke67, Gadz95]. The influence of gases on the emission currents from metallic emitters in ultra high vacuum can be found elsewhere [Luon95].

Adatoms can be easily desorbed by heating of cathode surface. Dong and Gupta reported that the baking of the vacuum chamber and cathode under 150°C does not effectively clean the cathode surface and that the gas adsorption in the low current regimes and desorption under high currents results in different FN results (Fig. 2.9) [Dong03].

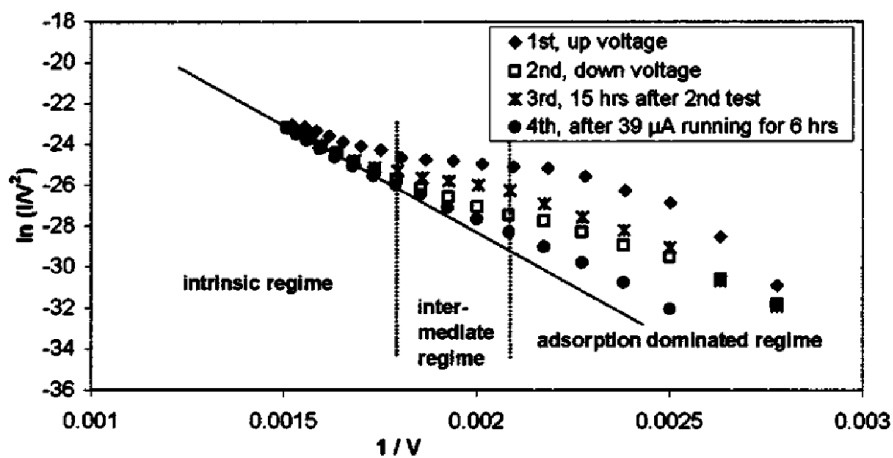


Fig. 2.9. FN plots of multiwalled CNTs tested four times in 10^{-9} mbar vacuum after baking the chamber at 150°C . The anode-cathode gap is $100\ \mu\text{m}$. After several up and down voltage cycles the CNT surface was cleaned due to Joule heating at the high emission current resulting in a straight FN line [Dong03].

Changes in the FN-slope are mainly due to variation of the adsorption state in the low current region, while in the intermediate range, gas removal occurs due to the Joule heating. In the high FE current range electrons emit from the clean surface resulting in intrinsic emission and repeatable data. The third intrinsic regime may not occur if the surface contains many chemical and physical defects. A slight deviation between the third and second cycle is associated with a time gap (about 15 hours) between the measurements. This means that during this time the reoccupation of the emission sites by gases occurred. The fourth cycle, which was performed after the cleaning of the CNT surface by the FE current for 6 h, yielded a minimum deviation from the intrinsic line.

2.2. Field emission from semiconductors

The initial theory of FE from semiconductors was developed by Margulis in 1947 and a few years later in 1955 supplemented by R. Stratton in the same way as employed by Fowler and Nordheim for metal [Marg47, Stra55, Zhu01, Modi84]. The total energy distribution of field emitted electrons from semiconductor was studied by Modinos in detail [Modi74, Modi84, Furs05, Huan97, Gome93, Sze07].

Similar to metals, FE from semiconductors can also be described as having a free electron gas [Stra55]. Nevertheless, electron emission comes from both the conduction band E_c and the valence band E_v [Stra55, Furs05, Huan97], which are separated by a band gap E_g as shown in Fig. 2.10.

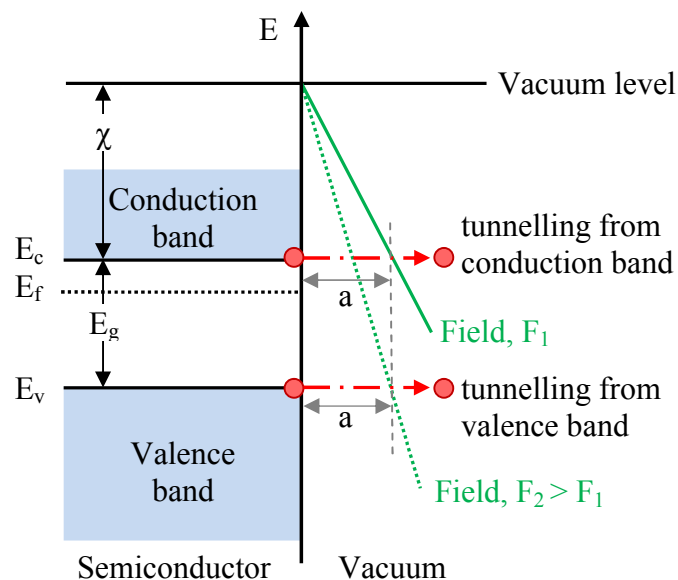


Fig.2.10. The simplest model of field emission from *n*-type semiconductor (the same model is true for *p*-type). For tunnelling of electrons from top of the valence band at the same barrier width as for the conduction band, a higher applied electric field F is required. Please note that any image force, penetration effects and surface states are neglected [Stra55, Bari11].

The surface barrier height (the energy required to remove an electron) in the conduction band is denoted by χ , while for the valence band, the surface barrier height is $\chi + E_g$. The corresponding FE current from both the conduction and the valence bands may also be defined by Eq. 2.4 by replacing of the work function ϕ by χ and $\chi + E_g$, respectively. Field emission from the valence band is often ignored because the top of this band is about 5 eV below the vacuum level [Huan97]. Hence, if the surface states [Huan97] are also ignored, the electron emission comes from the conduction band and depends on both the tunnelling probability through the barrier and on the electron supply to the emitting surface [Liu06]. Nevertheless, proof of valence band electron emission from high receptivity n-type silicon field emitters was first reported by Ding et. al. in 1999 [Ding99].

In contrast to metals, semiconductors have a much lower density of electrons that result in a deeper penetration of an applied electric field into the semiconductor than in metal. Theory indicates that in the metal the depth penetration is about 0.03 nm and, therefore, may be neglected [Stra55, Schr74]. However, in case of semiconductors the depth of field penetration is about 1 nm or less and depends on several parameters such as the cathode temperature, the doping level and the band gap [Tson79, Schr74].

The field penetration into the semiconductor causes the bending of both conduction and valence bands at the emitter surface as shown in Fig. 2.11 [Stra55, Furs05, Gome93, Schr74, Huan97]. The field penetration is also results in the reduction of the field enhancement factor β [Schr74, Chia06], i.e. when the field penetrates into the emitter and its surface is no longer equipotential.

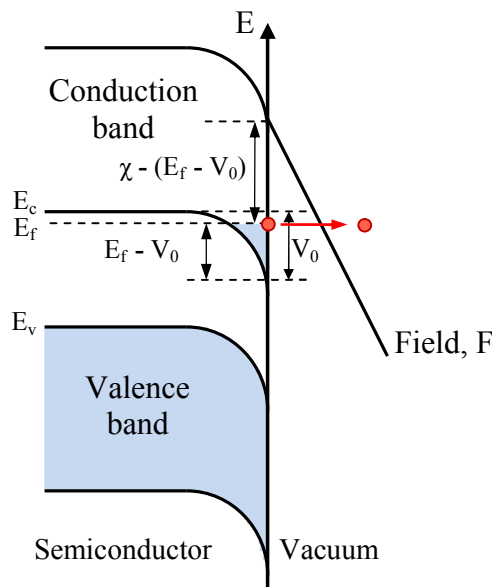


Fig. 2.11. Field emission from the conduction band of an highly doped n-type semiconductor under applied electric field. The conduction bands have bent below the Fermi level [Stra55].

When an electric field F is applied to the surface, the conduction band is bent by energy V_0 below the Fermi level, so that electrons collect in the dip. Obviously, the highest filled level of the collection coincides with the Fermi energy level. In this case, the height of the barrier is getting smaller by an amount $\Delta\varphi = E_f - V_0$ and the effective barrier height is given by: $\varphi_{eff} = \chi - (E_f - V_0)$.

Experimental data on p-type (or high resistivity n-type) and n-type semiconductor for gated and ungated emitters showed different FE properties [Liu06b, Chia09, Schr74, Teep05, Born12, Kane97, Serb13]. For p-type semiconductors the external field penetrates more deeply into the emitter forming a depleted space-charge layer of finite thickness. Some authors used the saturation of reverse current in a p-n junction to explain the formation of depletion layer [Kane97, Arth65, Sze77]. This region is free from carriers and the FE becomes limited by the supply of electrons resulting in a saturation region in the logarithm-scaled plot of the emission current versus the inverse voltage (field). In contrast, n-type semiconductor yields a linear FN behaviour, indicating that the FE is limited only by the transparency of the surface barrier [Furs05].

The FE results from p-type semiconductors were presented and discussed in detail by others [Arth65, Bask71, Yats70, Huan97, Liu06, Schr74, Borz66, Bask71, Born12]. General features of field emission are summarized in Fig. 2.12. Three different regions in the current voltage curve can be observed: (I) metal-like field emission, (II) current saturation, (III) avalanche breakdown or emission from both valence and conduction bands:

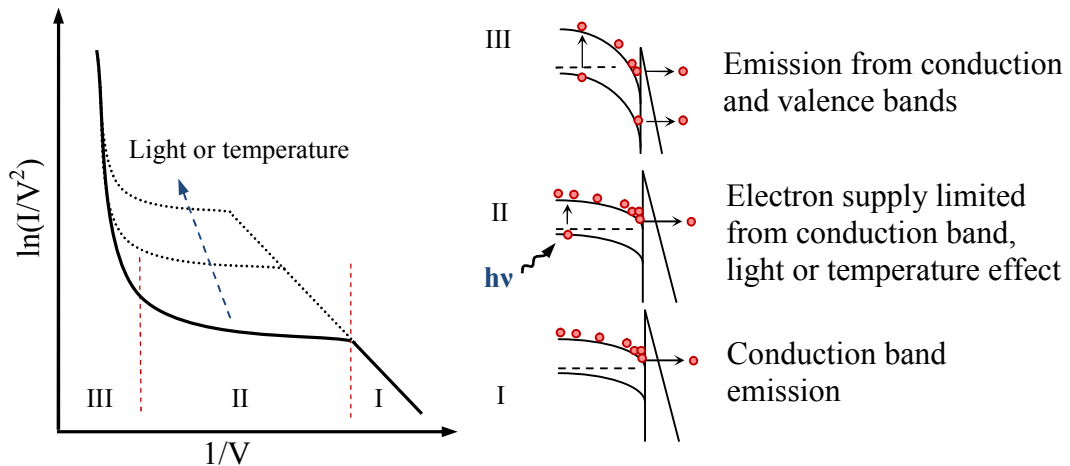


Fig. 2.12. Current-voltage behaviour of a p-type semiconductor field emitter in FN coordinates. The energy band diagrams correspond to regions I, II and III [Schr74, Ding99].

I. At low applied voltage, the concentration of electrons in the conduction band is sufficient, and the electron emission follows the FN theory for metal and, therefore, the plot in this regime displays a linear characteristic.

II. As the applied voltage increases, the supply of emission from the conduction band is limited due to field penetration that creates a depletion region. As a result, the emission current is limited and the slope of the FN-behaviour remains constant. The end and the height of the plateau are dependent on the size of the depletion region and different for different doping level (resistivity of semiconductors) [Teep05]. The FE current can be increased by an external source, i.e. by photo- or thermal-excitation [Schr74, Liu06, Serb13, Born12, Ding99, Teep05].

III. At higher voltage the FE current increases rapidly [Ding99, Schr74, Serb13]. In practice, this region often leads to destruction of the emitter and, hence, emission from this region is often not considered. Some authors attributed the phenomenon of rapid current rise to electron generation through impact ionization [Liu06, Schr74, Huan97b, Bask71], while the others argue that this is due to field electron emission from the valence band [Ding99, Borz66, Bask71]. In addition, they suggested that the electron emission comes from a two-stage process: electron come from the valence band to the conduction band and then to the vacuum. Ding et al. also suggested that a further increase of the applied voltage might lead to the saturation of valence emission and the second change in the slope of the FN plot can occur [Ding99].

P-type semiconductors are very interesting because they may provide a very economic and technically better solution for many applications where the presence (absence) of light or temperature is sensed.

3. Potential applications of cold field emission cathodes

Despite the fact that the vacuum electronic devices can operate at a higher frequency than the best solid-state materials (Fig. 3.1), such as silicon Si, gallium arsenide GaAs and indium phosphide InP, vacuum electronics will not replace widely used silicon technology, but will fill many niches where it is difficult or impossible to use solid-state electronics [Boos08, Fish88]. For example, solid-state devices are very sensitive to ambient fluctuations of temperature and ionizing radiation, which can disrupt a semiconductor's crystal structure. Therefore, vacuum technology might be very attractive for the commercial or military communication systems and NASA, which need to operate at frequencies approaching 1 THz and/or in harsh environment [Brod89, Sze07, Bari11].

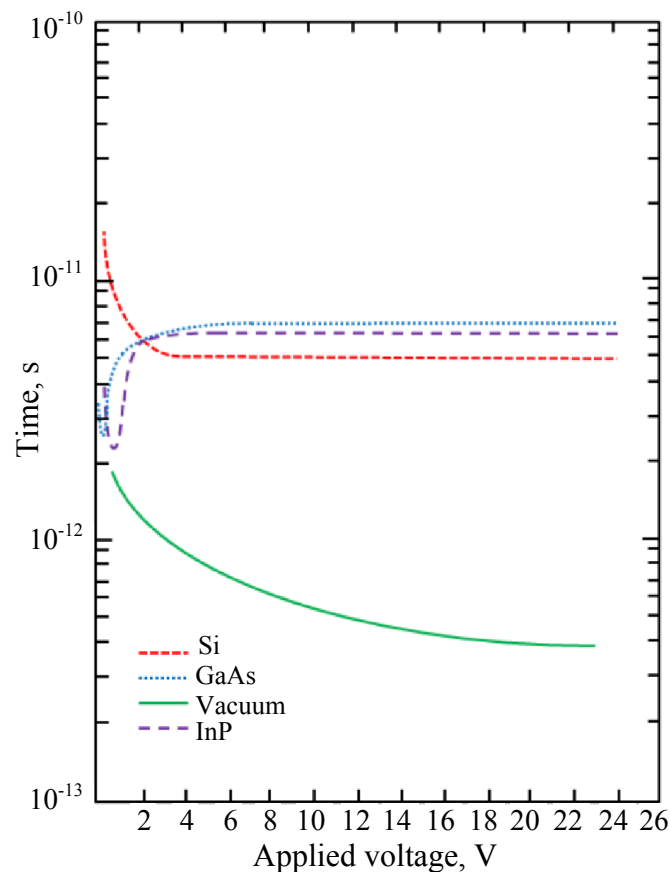


Fig. 3.1. The transit time of electrons across a gap of $d = 500$ nm as a function of an applied voltage in vacuum and solid-state materials [Brod89].

Vertical vacuum diodes (two electrodes) and triodes (three electrodes) configurations are presented in fig. 3.2. In these configurations, electrons are extracted from the cathode and collected at the anode. The triodes have an additional control electrode, which allows fast (in the nano- or microsecond time range) and accurate control the emission current.

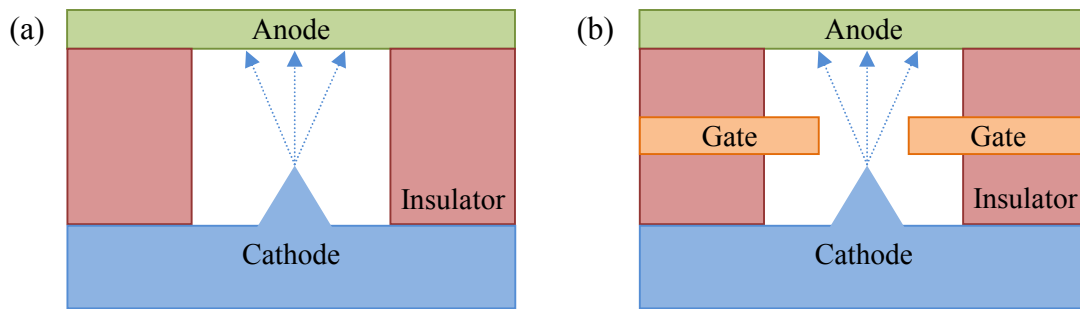


Fig. 3.2. The vacuum diode (a) and (b) triode configurations [Bari11].

Thermionic emission is the most widely used method of obtaining electron emission from the surface. However, due to the high temperature of the cathode ($>1000^{\circ}\text{C}$), the miniaturization of thermionic-based devices is quite a challenge [Sait10]. In contrast, FE sources have several advantages such as [Miln04, Brod89, Nati99]

1. The distance between the electrodes can be very small because heating is not required and therefore short electron transit times and miniaturization of vacuum devices possible.
2. Low power consumption. That is an important parameter for compact devices.
3. Quick response time to the variation of an applied electric field and a non-linear current-field relationship mean that a very high current density can be obtained in a short time from extremely small cathodes, e.g. 1000 electrons in 10^{-13} seconds from an area of 10^{-8} cm^2 corresponds to a current density of 1.6×10^5 A/cm^2 .
4. A high brightness electron beam and the narrow energy spread of electrons [Jong03].
5. Direct modulation of electron beams at RF frequencies [Whal00, Miln06a, Nati99].
6. Manufacturing of FE emitters can be combined with Si technology [Han12, Serb13].
7. Easy to program electronically.

Therefore, the FE cathodes have potential for use in a wide variety of applications, such as compact vacuum amplifiers, such as travelling wave tubes [Boos11, Zhu01, Ren13, Bark05, Eich08, Boos08, Pier50, Whal00, Whal09, Kemp06, Ives04] and compact free electron lasers [Brau98, Patt10], miniature and battery-powered X-ray tubes [Fili13, Qian12, Zhan05, Sait10, Eich08], vacuum sensors [Bust92, Schr11, Eich08, Wen07], high brightness sources of light [Eich08, Zhang05, Obra13, Sait10], efficient field emission displays [Spin88, Brod94, Bust92, Song02, Cran12, Eich08, Sait10, Furs05], mass spectrometers [Han11], e-beam lithography [Teep05, Mura00, Miln06], electron gun in microscopes and others [Zhu01, Eich08, Brod94, Bust92, Sait10, Ren13].

The main goal of this chapter is to give a brief overview of potential application areas of cold cathodes. The selected fields that have high potential are presented below.

3.1. Fast-switchable and miniaturized X-ray source

Since the discovery of X-ray radiation in 1895 by W. Röntgen [Rönt96], it has been used in a wide variety of applications such as diagnostic medical imaging and therapy [Fili13], security and industrial inspection [Sait10]. The generation of x-rays is based on the principle of striking a metal target with high accelerated electrons. In 1913, W. Coolidge introduced a hot tungsten-filament cathode for the X-ray tube, which is suitable for use in nonultrahigh vacuum [Cool13, Day96, Eich08]. Since then, the design of the thermionic emission X-ray tube was changed, but the basic principle is still in use.

In medicine portable and miniature X-ray tubes (tube diameters less than 10 mm) which can produce high resolution images in a short exposure time to avoid motion blur and/or to kill the cancer without damaging surrounding healthy tissues are required, i. e. such X-ray tubes have to be applicable for therapy and radiography [Send04, Fili13]. Traditional thermionic-based X-ray technology, however, has some limitations for developing of miniature tubes [Liu06c]: (a) short life-time: thermionic cathodes become thinner and thinner during a period of time due to tend to react with residual water molecules and an oxide and the sublimation of the oxides [Sugi01, Yue02]; (b) a high cathode operating temperature limits the miniaturization of advanced X-ray imaging systems [Fili13] and their programmability [Xin, Jeon13a, Jeon13b]; (c) slow response time and low temporal and spatial resolutions for imaging of rapidly moving objects (e.g. lung and heart) [Bade04, Liu06c, Qian12, Xin]. These limitations are possible to overcome by the generation of X-ray tubes by means of field emission [Dyke56]. Several types of miniature vacuum-sealed FE-based X-ray tubes have been recently developed and one example is shown in fig. 3.3 [Fili13, Jeon13a, Jeon13b, Heo12, Send04].

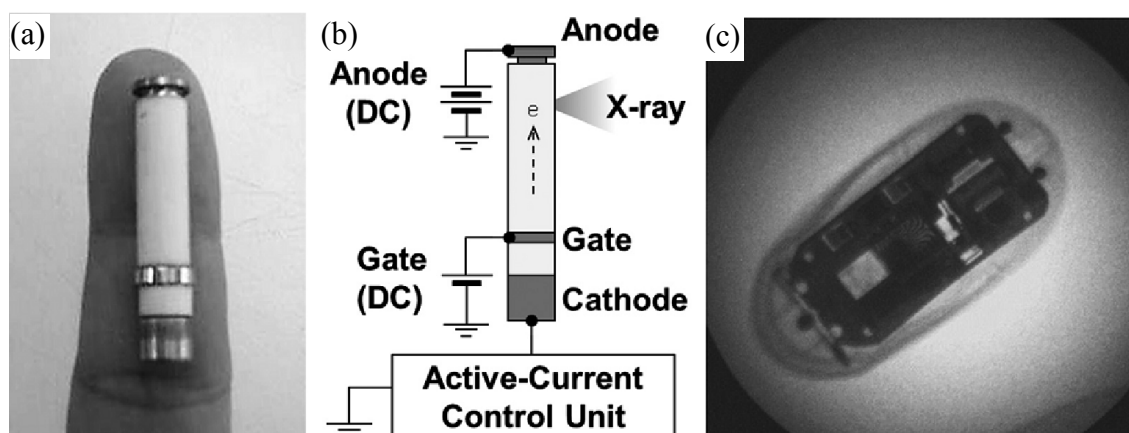


Fig. 3.3. (a) Optical image of the vacuum-sealed digital miniature X-ray tube. The diameter and the length of the X-ray tube are 6 mm and 32 mm, respectively; (b) schematic diagram of x-ray tube; (c) X-ray image of a computer mouse taken at the anode voltage of 25 kV and the cathode current of 80 μ A [Jeon13a].

FE-based X-ray tubes are also attractive for the development of multi-beam X-ray devices for imaging of objects from various viewing angles without any mechanical motion. That can significantly increase the scanning speed and the range of viewing angle and resolution of the current computed tomography scanners [Kale05, Qian12, Zhan05, Zhan06, Sait10]. At present, many researchers around the world are now actively developing this technology. For example, a 5-beam FE X-ray source was reported by Zhang et. al. in 2005 (fig. 3.4) [Zhan05]. Since then, a linear 25-beam and 31-beam FE X-ray sources [Qian09, Qian12] as well as the curved X-ray source with 100 individual FE-based tubes [Xin, Sait10] have been demonstrated for digital breast tomosynthesis [Alak13]. In the future, due to the fast response time, FE-based X-ray tubes might provide real-time 4D (3D+time) image processing.

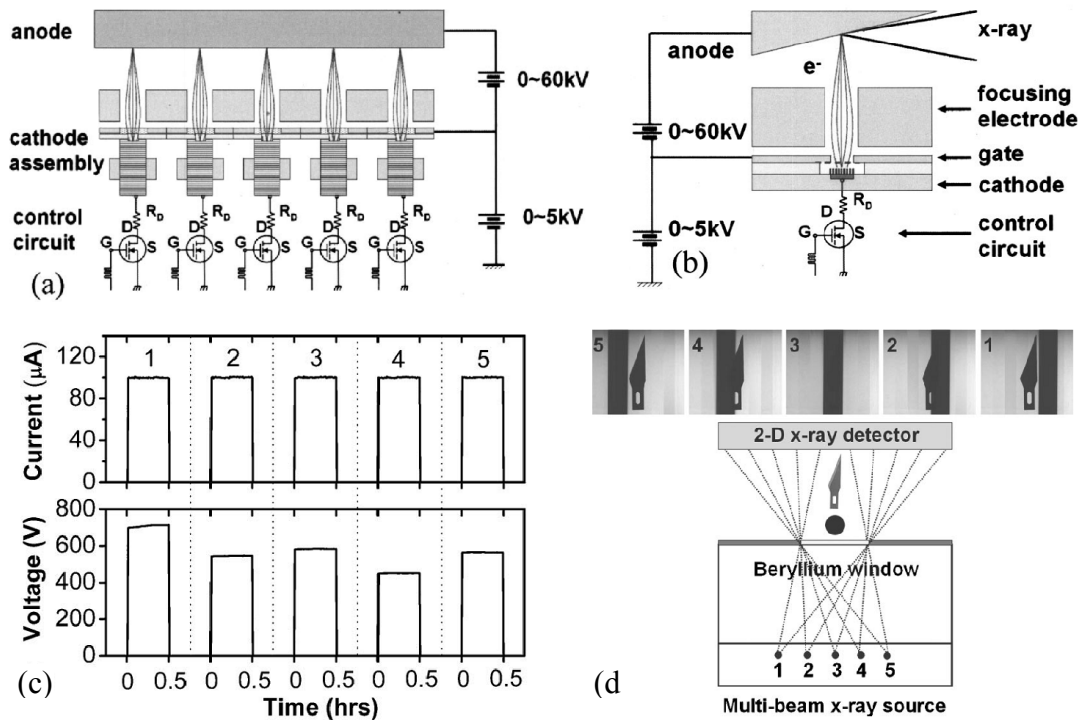


Fig. 3.4. (a, b) Schematic illustrations of a multi-beam X-ray source with 5 individual FE-based X-ray units (each pixel of about 1.5 mm in diameter, the distance between them is about 1.27 cm). The anode voltage is 40 kV, while the dc gate voltage of each X-ray tube is controlled independently by a transistor circuit. (c) Stability of the cathode current (100 μA) over a 30 min. (d) Five projection images of a blade from various viewing angles taken at anode voltage of 40 kV, 25 μA cathode current and 5 s exposure time. The resulting focal spot (the size of the anode that emits x-rays) is between 200-300 μm [Zhan05].

3.2. Millimeter-wave and THz amplifiers

The millimeter-wave and terahertz (THz) region (frequencies from 0.1 to 10 THz or wavelengths from 3 mm to 30 μm), which falls between the microwave and the infrared spectrum (Fig. 3.5), is very attractive for scientific, industrial and military applications

[Will06, Boos08, Fede10, Drag04, Drag11], because radiation at these frequencies is non-ionizing (as compared to x-ray) and can penetrate through a lot of materials, reflect back as well as provides wide bandwidth and channels for the next-generation of communications systems.

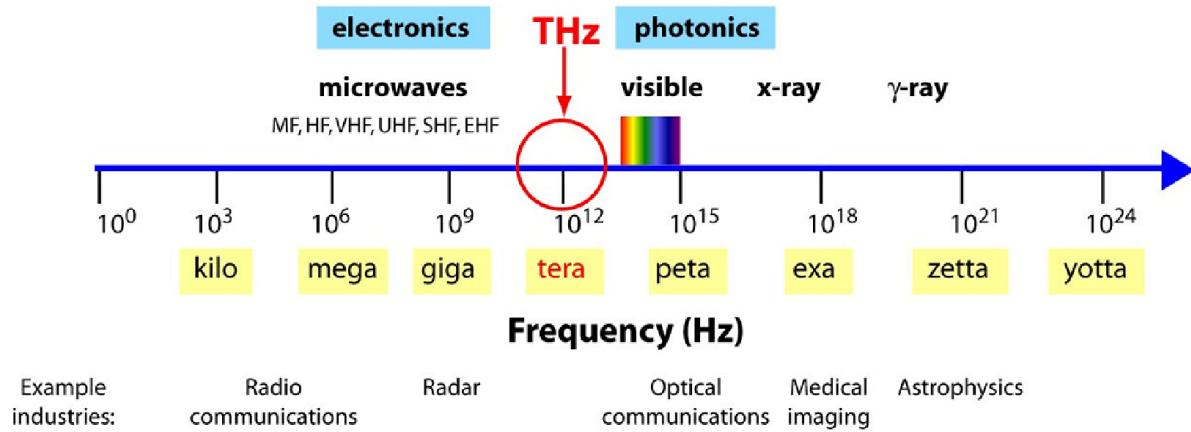


Fig. 3.5. Schematic of the electromagnetic spectrum showing the THz gap [Will06].

However, this region is almost undeveloped due to the difficulties associated with the lack of sufficient power. So far, various approaches have been proposed to solve this problem, but the maximum output power is still limited [Boos08, Boos11]. For instance, semiconductor devices such as diodes or transistors have a frequency limit below several hundred GHz, which is limited by the transient time, parasitic RC time constants and the smallest unit size that can be fabricated by lithography. The power range of these devices decreases with increasing of the frequency and scales as $P \sim f^{-2}$ [Boos08]. The average power attained by solid-state devices at 30 GHz is about 1 W and close to 1 THz is only a few μW [Miln04, Boos08]. In contrast, photonic or quantum electronic devices (such as quantum cascade lasers) are not limited by the transient time or RC time constant, but can not operate at frequency less than 10 THz [Will07, Hu09, Boos08]. In addition, a solid-state electronic source has low threshold for voltage breakdown (e.g. 40 V for GaAs and ~ 100 V for GaN [Azam10]) and it is not able to remove heat generated by the electron current in the active area (where the kinetic energy from the electrons is converted into electromagnetic field energy) at high microwave electric field strengths. In contrast to solid-state devices, vacuum tubes are capable of providing hundreds of kilowatts of power at 35 GHz and at THz regime frequencies the output power is at least 1 mW [Koop12, Whal00, Boos08, Boos11, Qiu09, Whal09]. To obtain higher power levels at THz regime, the high current density $\sim 50\text{-}100$ A/cm^2 is required [Boos11]. Therefore, a possible approach, to increase the output power in the region from 0.1 to 10 THz, could be the use of vacuum amplifiers, e.g. a traveling wave tube (TWT) which is shown in fig. 3.6 and 3.7 [Ives04, Qiu09, Boos08, Pier50].

The most important part of this device is the electron gun that has to provide a high current in order to amplify an electromagnetic THz signal. Field emission-based electron guns, due to several reasons mentioned above, provide an opportunity to build relatively simple and compact high current electron gun for TWT. The simulation results also show that the FE-based cathode is a good candidate for the generation of millimeter and terahertz waves [Lin05, Lin07, Lin08]. Moreover, a cold cathode TWT developed at L-3 Communications Electron Devices in San Carlos (California, USA) yielded 100 W (the cathode current was 120 mA) output power at 5 GHz that demonstrates the practical feasibility of such TWTs for communication, data link and radar applications [Qiu09, Whal09].

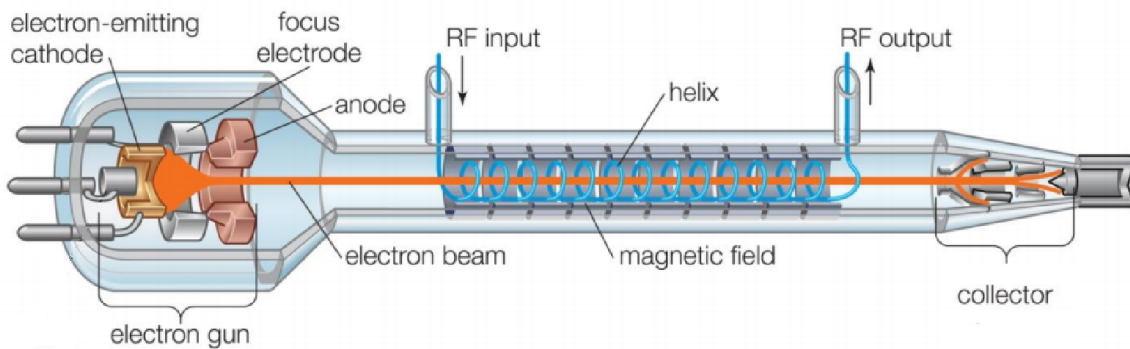


Fig. 3.6. Schematic of the traveling-wave tube. The electron gun generates the electron beam, which travels in helical coil, where the electrons are velocity modulated by an input signal to form the bunches. Then, the energy from the electron bunches is extracted from the helix output. A collector, which is located at the other end of the tube, stops the electron beam [adapted from Brit, Miln06, Miln04, Pier50].

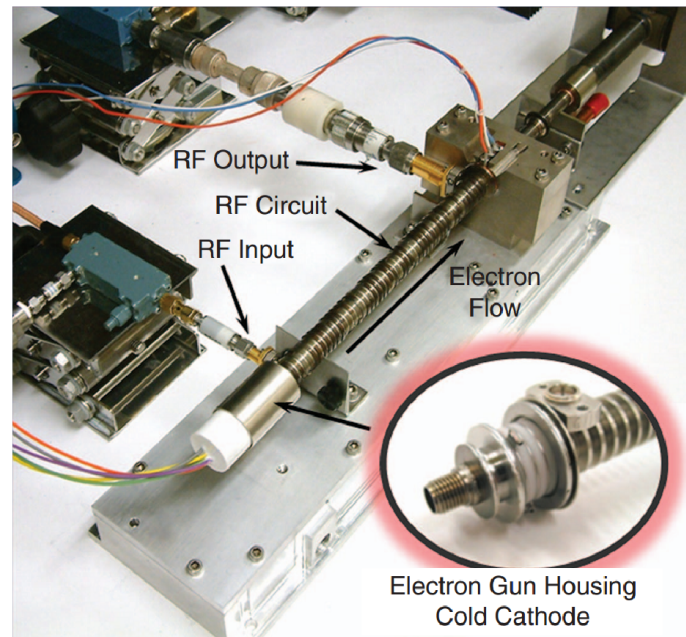
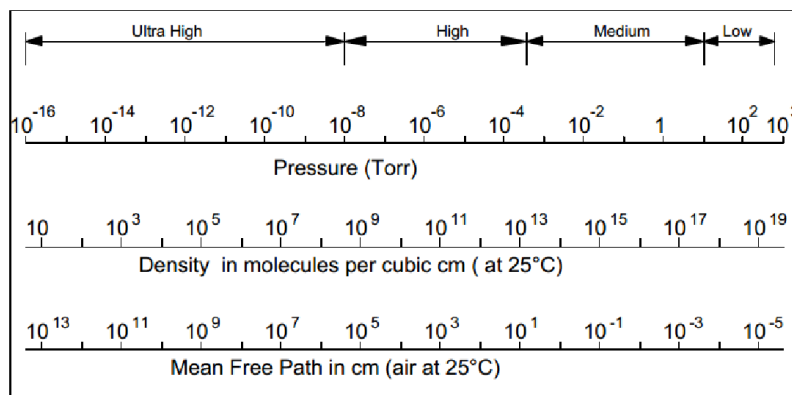


Fig. 3.7. Photograph of a cold cathode-based travelling-wave tube generating 100 W of RF output power at 5 GHz. The cathode current is 121 mA [Qiu09, Whal09].

3.3. Vacuum sensors

Vacuum is defined as an area that is filled with air or any other gases at pressure less than atmospheric pressure [Eich08, Laff98, Made84, Ohan98, Roth76, Redh68]. Depending on the types of vacuum pumps and their combinations [Eich08], different levels of vacuum can be obtained in the laboratory or industrial environments (Tab. 3.1). The instruments used for measuring the pressure are called vacuum sensors [Frad10]. There is no single sensor which could measure the full range of vacuum pressure. Therefore, different vacuum sensors such as Pirani sensor, friction sensor, capacitance sensor and ionization vacuum sensor are used [Wen07, Frad10].

Table. 3.1. Vacuum ranges [Dyla06]. Note: 1 Torr is equal to 1.33 mbar or 133 Pa.



Ionization vacuum sensors are able to measure the pressure between 10^{-2} and 10^{-10} Torr [Laff98]. A possibility of using FE cathodes as electron source in ionic sensors was investigated in detail by Alexandrov et. al. [Alex07], by Kendal [Kend97, Kend99] and by Peacock et. al. [Peac91]. Lee et. al. proposed another idea of FE-based pressure sensor and presented a detailed theoretical analysis [Lee91, Lee92]. The pressure sensor based on diode structure, which consists of a FE cathode and a thin diaphragm as a pressure sensitive element and an anode (fig. 3.8). The FE emission current is determined as a function of the pressure. Similar work has been done by Wen et. al. [Wen07]. In his work, at a fixed anode voltage, when the pressure changed from 37 kPa to 7.7 kPa, and, as a result of that, the FE current increased from 80.3 μ A to 96.3 μ A.

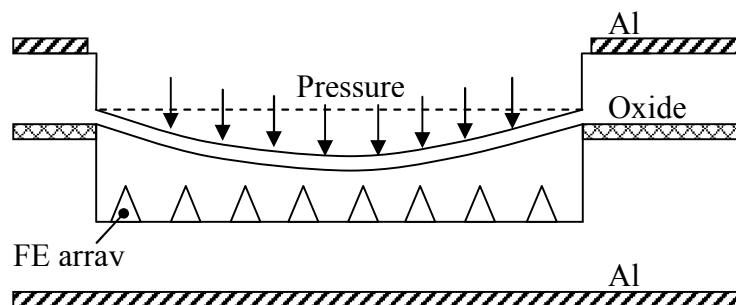


Fig. 3.8. Schematic of a FE-array-based diode pressure sensor with a thin pressure-sensitive silicon diaphragm. [Lee91, Lee92]

4. Experimental techniques for cold cathodes and surface analysis

This chapter introduces and provides a brief description of the instruments and methods being used for study field emission and cathode surface properties. The design and operating features of field emission scanning microscope (FESM), integral measurement system with luminescent screen (IMLS), and scanning electron microscope (SEM) will be described. Despite the fact that all the methods were developed earlier [Mahn95, Pupe96, Habe98, Lyse05, Lyse06], some optimization of measurement procedures was needed for this research.

4.1 Field emission scanning microscope (FESM)

The FESM is a unique microscope being used for the localization of field emitters on cold cathodes of up to $25 \times 25 \text{ mm}^2$ and measuring the FE properties of single emitters or a group of them (Fig. 4.1). The samples are installed by means of a linear transport system through a preparation chamber with a base pressure of 10^{-7} mbar onto the rotatable dock holder or scanning stage. The cathode is located in the UHV chamber with a base pressure of 10^{-9} mbar in the focus of the Ion gun, Auger Electron Spectroscopy (AES) and Scanning Electron Microscope (SEM) on the XYZ piezo translator stack, which can be tilted with respect to the anode.

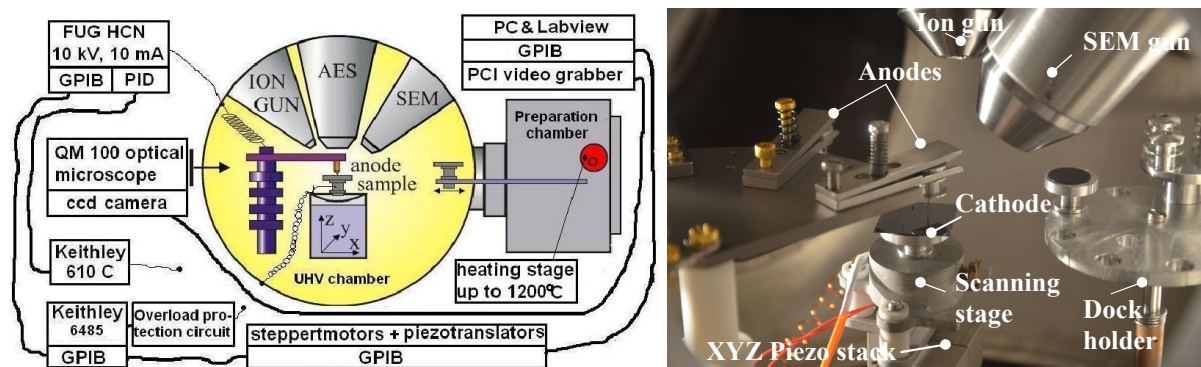


Fig. 4.1. Schematic illustration of the field emission scanning microscope (FESM) (left) and inner view into the UHV chamber of the FESM (right). The cathode is located in the focus of the Ion gun, AES and SEM (top) on the XYZ piezo translator stack (bottom) which can be tilted with respect to the anode.

The power supply FUG HCN 100 M-10000 with a PID controller provides a highly-stabilized DC voltage up to 10 kV (10 mA current) with manual or GPIB control. The FE current from 20 fA up to 20 mA can be measured with a picoammeter Keithley 6485 (at speeds up to 1000 reading per second) or from 10 fA to 0.3 A with an analog electrometer Keithley 610C. The gap between the cathode and the anode is controlled by an optical long-distance microscope (Quesstar QM-100) or calculated by an $U(z)$ -plot [Navi10, Lyse06].

The resolution of the FE scans depends not only on the step of stepper motors (minimum step width is ca. 63.5 nm) and the anode-cathode distance, but also on the size of the anode. For the preparation of the anodes, an additional equipment, consisting of a voltage power supply and a wire holder, is needed (Fig. 4.2). The tip holder is mechanically held onto the setup and can be easily vertically moved by means of a screw. Applying the DC voltage between the two electrodes, anodes of different sizes in the freshly prepared solution of NaOH can be fabricated as shown in fig. 4.2.

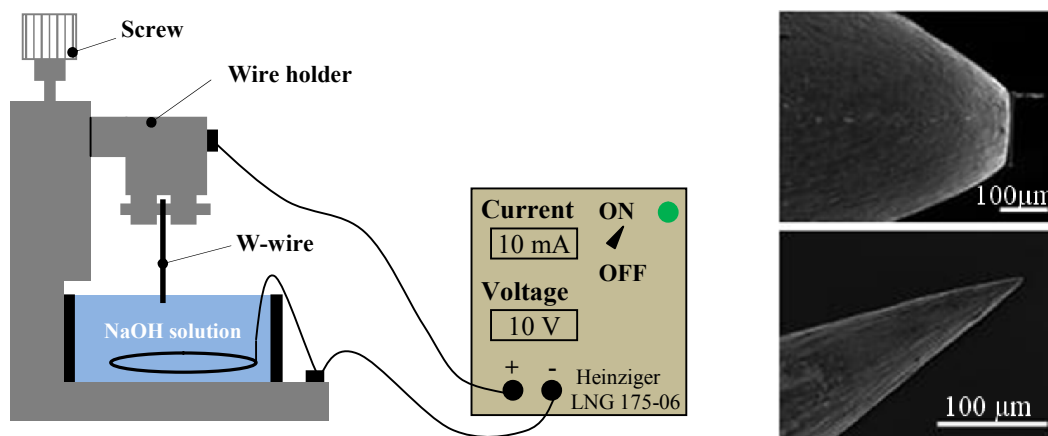


Fig. 4.2. Layout of the electrochemical etching setup (left) and SEM images of the prepared tungsten anodes of different size and shape: truncated cone and tip-like (right).

It should be noted that the electric field is almost homogeneous distributed for the truncated cone (flat) anode (see fig. 4.2right) [Song13], while the geometry of the tip-like anode and the electrode spacing has to be taken into account on the calculation of the electric field as can be seen from fig. 4.3. The electric field should be corrected with factor α , resulting in decreased electric field [Habe98].

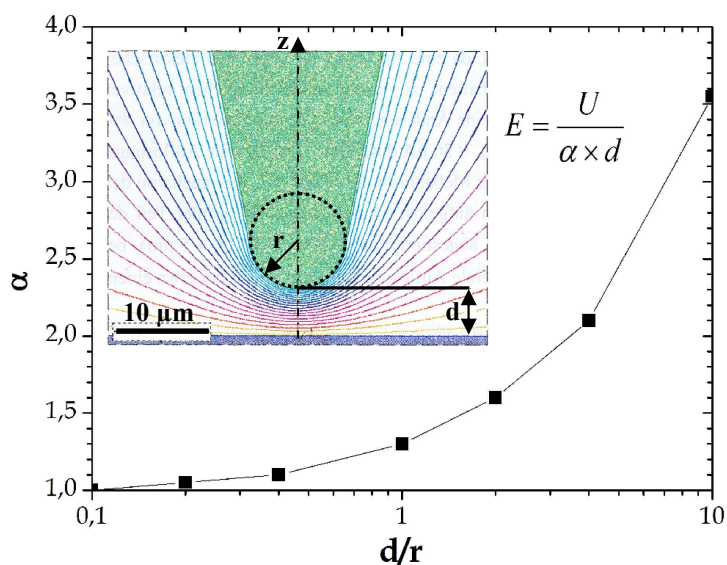


Fig. 4.3. Variation of the factor α vs. ratio of the gap d to the tip radius r . Inset shows the electric field distribution for a tip curvature of $5 \mu\text{m}$ [Habe98].

Why the FESM investigations of cold cathodes are so important? The FE properties of a cold cathode with a single emitter can be easily characterized in terms of its maximum current value, stability and field enhancement factor and for that it does not need special equipment. However, investigation of large cathodes (e.g. 1 cm^2) with large number of emitters is more complex and more careful analysis is required. The reason for that is the variation of the geometry of the individual emitters (different field enhancement factor due to fabrication difficulties) and effect of the mutual shielding of closely spaced emitters. Presence of a few very strong emitters results in variation of the FE properties from one position to another within the cathode. Therefore, careful investigation of the surface of the cathodes and the detection of strong and weak emitters, which plays an important role in terms of current stability and lifetime of the whole cathode, is highly critical.

The FESM can operate in two measurement modes: at the constant voltage mode (CVM) and at the constant current mode (CCM). In both cases the data (the FE current or the applied voltage) is measured as a function of tip position. The CVM is analogous to the FE monitored on a phosphorous screen, but with higher resolution and lower current ($< 1 \times 10^{-7} \text{ A/cm}^2$). However, the use of this method can destroy the emitters with a strong amplification factor and damage the picoammeter. In order to avoid emitter degradation, current saturation effects and to prevent instrument destruction, the PID-regulated V- scans are typically carried out at a fixed FE current [Nils01, Grön03, Lyse05]. Fig. 4.4. shows a medium resolution voltage map $U(x,y)$ for 1 nA and the corresponding current map $I(x,y)$ at 900 V. From the voltage map the potential number density of emitters of about 16×10^4 emitters/ cm^2 could be detected. However, the current map shows the actual number of about 4×10^4 emitters/ cm^2 at a given voltage value, that is more interesting from the point of view of applications. Therefore, analysis of the cathodes in both the CCM and CVM is necessary for a better understanding of the FE properties and further improvement and optimization of nanostructures.

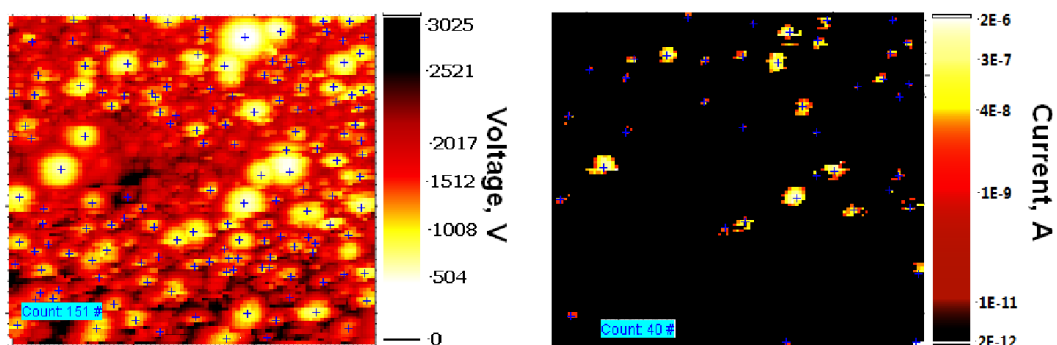


Fig. 4.4. Medium resolution voltage map (left, scanned area $\sim 300 \times 300 \mu\text{m}^2$, $\Phi_a = 10 \mu\text{m}$, $\Delta z < 20 \mu\text{m}$) and corresponding current map (right) at a fixed FE current of 1 nA and 900 V, respectively. Potential emitter number density at low current is $\sim 16 \times 10^4$ emitters/ cm^2 ; the actual number at 900 V is about 4×10^4 emitters/ cm^2 .

4.2 Integral measurement system with luminescent screen (IMLS)

Another important measurement technique is used for the investigation of the field emission properties from a whole cathode at 10^{-7} mbar (Fig. 4.5). The integral measurement system with the luminescent screen provides the information about the distribution of emission site over the cathode. Nevertheless, the resolution is limited by the grain size of the phosphors (usually, the grain size varies from $1\ \mu\text{m}$ to $8\ \mu\text{m}$). The FE current from the cathode can be measured in dc or pulsed modes in a triode or diode configurations. In order to decrease the power load on the sensitive luminescent screen and to prevent its destruction (evaporation of the luminescent layer material is controlled by a quadrupole mass spectrometer QMG 112) at high applied voltages, pulsed mode is more preferable than dc [Lyse05]. Low-voltage ZnS based-phosphors have a minimum threshold for screen response of about $10^{-7}\ \text{A}/\text{cm}^2$ at 500 eV, while the maximum input beam power density to the screen ($0.3\text{-}35\ \text{Watt}/\text{cm}^2$) depends on the mode of operation [Prox, Kimb, Fitz98]. The maximum FE current from the cathode can be achieved by using a metallic anode.

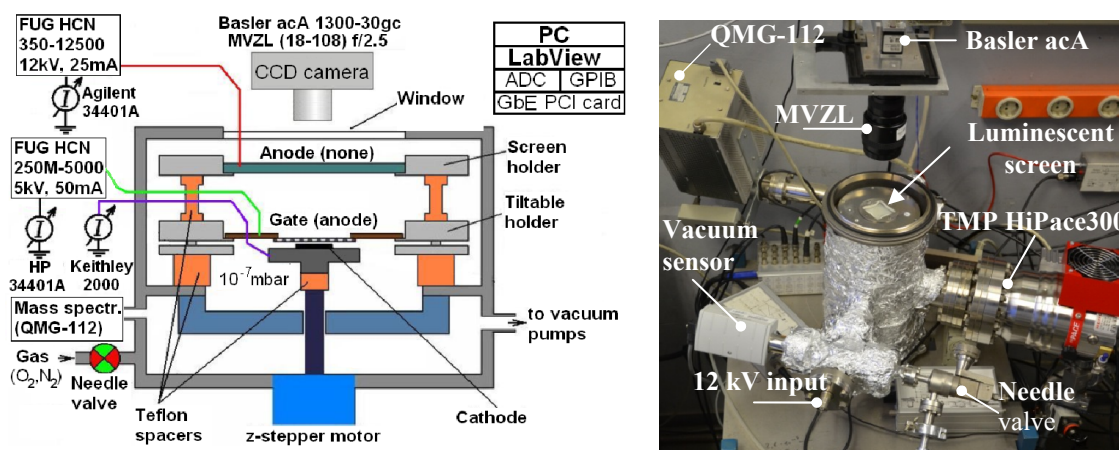


Fig. 4.5. A schematic view of the integral measurement system (IMLS) in triode (diode) configuration in DC mode and photo of the IMLS with installed luminescent screen.

The triode measurements of a structured cathode or a single emitter can be performed at a fixed anode-gate distance (at a fixed cathode-gate distance), while the cathode-gate (anode-gate) distance can be changed by using a stepping motor from 0.1 to 20 mm (Fig. 4.6).

The circuit diagram of the IMLS is given in Fig. 4.7. Low voltage pulses (0.4-10 Vdc), that are generated by a pulse generator (Hewlett-Packard 8013A) and controlled by an oscilloscope, can be amplified by the high-voltage source (FUG HCN-250M 5000, 50 mA) up to 5000 Vdc within 2 ms. Due to the different rise-time required for a different value of the output voltage, a minimum pulse width for the correct measurements is 1-3 ms (table 4.1). The two-resistor voltage divider (1:500, 50 k Ω and 25 M Ω) is used to reduce a high voltage. A single ballast resistor (10 Ω or 100 k Ω or 2M Ω) can be plugged into the circuit to limit the

FE current and to protect the cathode against electrical discharges, while the other resistors (from 1 M Ω to 200 Ω) are needed for the FE current read-out. The gate voltage and the cathode current signals pass through impedance transformer and digitized by a Keithley KPCI-3102 12-bit analog-digital converter (ADC). The anode voltage can be increased manually up to 12.5 kV using a high voltage generator (FUG HCN 350-12500, 25 mA). The gate and the anode current are measured by HP 31401 A and Agilent 34301 A using the Keithley KPCI-488LPA GPIB/IEEE-488 interface. A ccd camera (Basler acA-1300-30gm/gc, 1296 \times 966 pixel, 3.75 \times 3.75 μ m pixel size) and attached the high-magnification manual focus zoom lens (OPTEM MVZL 18-108 mm, f/2.5) provide high resolution and a rapid readout of the luminescent screen images via a Intel Pro 100 GT GbE PCI card and LabVIEW 2010.

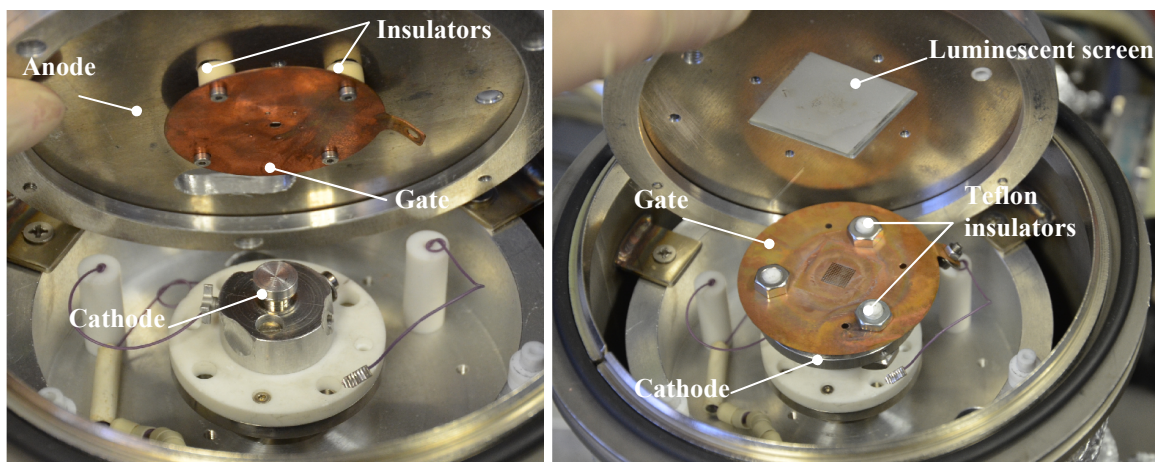


Fig. 4.6. Images of the IMLS system in a triode configuration at a fixed anode-gate distance (left) and at a fixed cathode-gate distance (right).

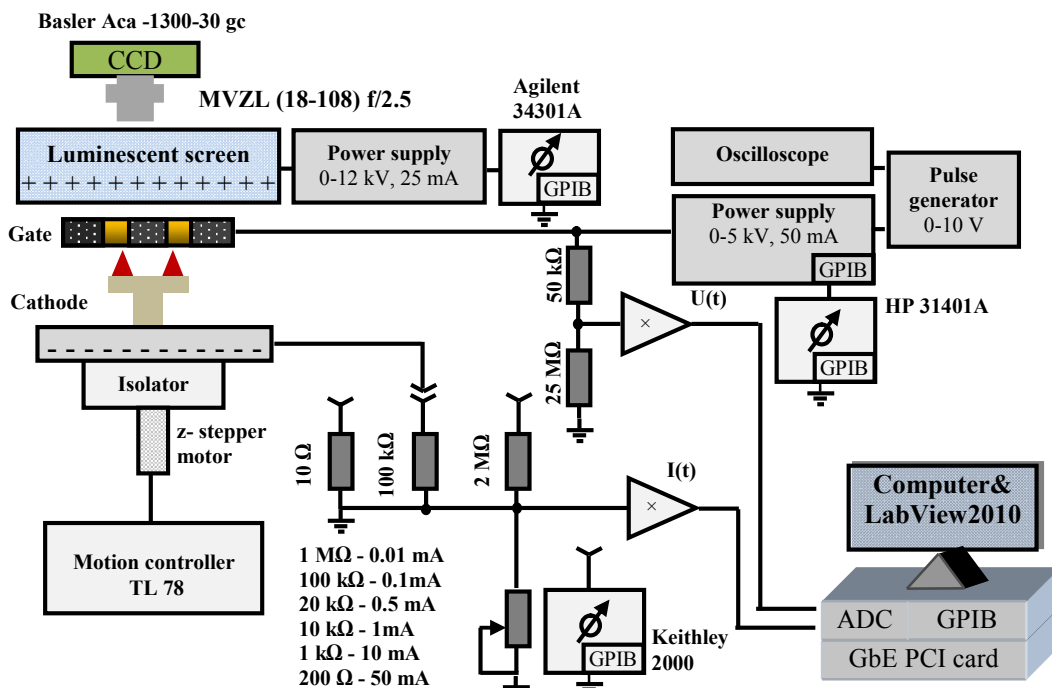
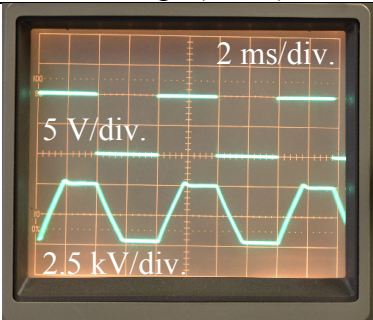


Fig. 4.7. A circuit diagram of the IMLS in the triode configuration.

Table 4.1. The high voltage output of the FUG HCN-250M 5000 in pulsed mode.

Output voltage, kV	Rise/fall times, ms	Recommended minimum pulse width, ms	O-scope image of the square-wave input voltage (upper) and a peak high output voltage (lower):
0-0.5	0.4	1-2	
0.5-1.0	0.4-0.6		
1.5-2.0	0.9-1.2		
2.5-3.0	1.3-1.5	2-3	
3.5-4.0	1.6-1.9	3-5	
4.5-5.0	2.0-2.2		

The maximum bandwidth of the FE measurements in pulsed mode is limited by the capacitance of the IMLS and coaxial cables [Spin86, Wu09]. For typical coaxial cables RG 58C/U the capacitance is about 100 pF per meter cable length that is much greater in comparison with the capacitance of the IMLS system (Fig. 4.8left). During the rise (fall) time of the anode voltage, charging (discharging) of the system occurs (Fig. 4.8right), and due to the minimum rise-time of the high voltage output signal is about 0.4 ms, short current pulses (faster than 1 ms) are detected incorrectly. Therefore, in order to minimize the capacitance value and unwanted signal, the length of the cables has to be as short as possible.

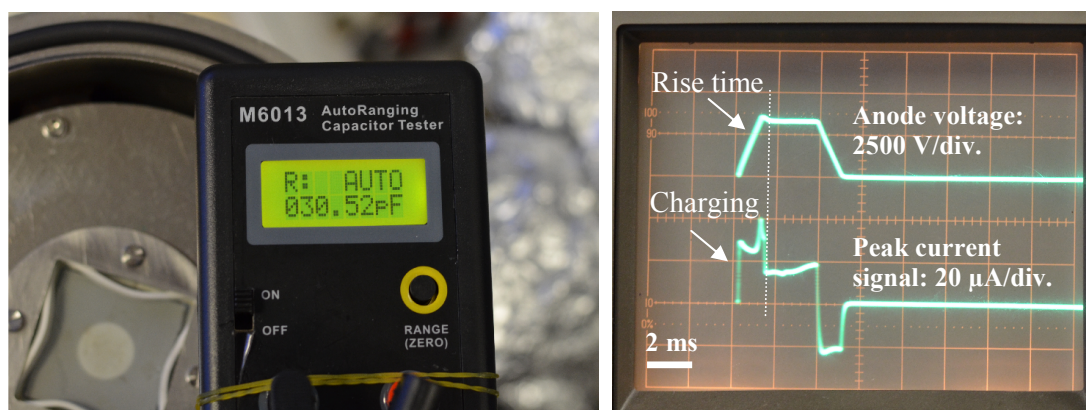


Fig. 4.8. Left: partial capacitance of the IMLS system (coaxial cables are not connected to the vacuum chamber) between the air-separated ($\Delta z = 200 \mu\text{m}$) luminescent screen and the alumina holder ($\varnothing=15 \text{ mm}$) is about 30 pF. Right: oscilloscope screen displays the anode voltage waveform (upper curve) and the corresponding FE current (bottom) versus time.

In addition, the FE current stability and lifetime of emitters can be characterized at high and poor vacuum conditions. For this, different high-purity gases (99.5% or greater) such as nitrogen, oxygen or hydrogen can be used. At the same time, by means of a Balzers QMG-112 mass spectrometer, evaporation of the luminescent layer at a high FE current can be controlled. Finally, the distance between the sample holder and the luminescent screen is measured with the Mitutoyo depth micrometer (Series 129-110, 0.01 mm resolution).

3.3. Scanning electron microscope with EDX

The resolution of a traditional optical microscope is limited by the wavelength of the incident light. The most powerful optical microscope can provide observation of particles with 100-200 nm size. In order to observe smaller particles, a scanning electron microscope was developed in the early 1930's. Scanning electron microscope (SEM) allows taking images of the surface of a sample with resolution less than 1 nm (mainly limited by the width of the electron beam and the interaction of electrons with specimen atoms) by scanning it (like electrons in CRT tube) with a narrow beam of electrons. The basic principle is that the electrons are produced in an electron gun and accelerated with a high voltage to high speeds, pass through a system of focusing lenses and bombard the surface of the sample to produce feedback signals (Fig. 4.9). Depending on the type of signal, different information about the sample can be obtained. For example, to observe the morphology of the sample, secondary electrons can be collected by a secondary electron detector and the resulting signal is analyzed with the software and displayed on a screen.

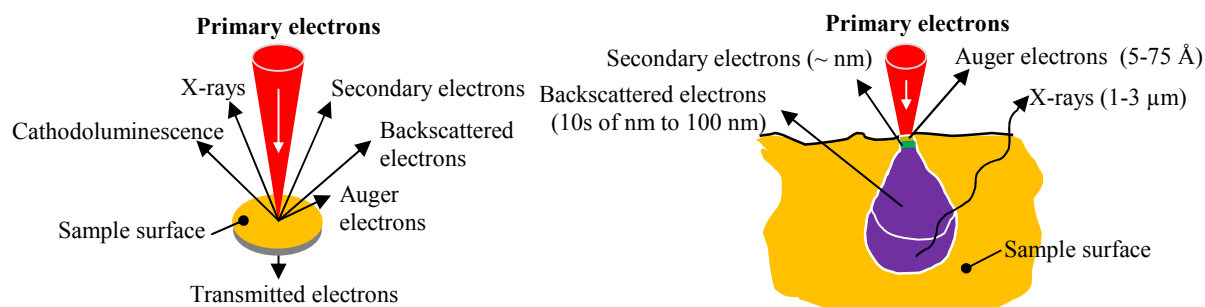


Fig. 4.9. Various signals are created during a collision of electrons with the surface (left); schematics of the electron penetration depth (right) [Reim98].

In addition, it is possible to get the elemental analysis or chemical characterization of the samples. Thereto, an energy-dispersive X-ray (EDX) detector (attached to the SEM) is used. After irradiation with primary electrons, atoms of the sample are excited and generate x-rays (Fig. 4.9). Since each chemical element has a specific set of X-ray energies (due to quantization of energy levels), nearly all elements can be detected. Light elements like H, He, Li cannot be analyzed because of no x-rays or extremely low X-ray energy [Reim98].

These methods are non-destructive that gives the possibility to analyze the sample several times. However, there are some specimen requirements for testing. The samples must be clean, dry and, what is very important, electrically conductive and grounded to avoid electrostatic charge and image artefacts. In this work, SEM analysis of nanostructures before and after the measurements was performed using a Phillips XL30S with EDX or Jeol 6500 scanning electron microscope with a resolution of 2 nm or 3 nm, respectively.

5. Field emission from carbon nanostructures

Carbon nanotube (CNT), discovered by Iijima in 1991 [Iiji91], is a relatively new material that is intensively investigated by many researchers around the world and which has opened new opportunities for the development of new nanoelectronic devices [Sait10, Zhu01]. Due to high aspect ratio, which results in high FE currents at low electric fields, CNTs are considered as the most favourable material for electron field emission. Moreover, this material has unique electrical and physical properties [Ren13], e.g. CNTs are chemically inert for formation of undesired bondings; depending on their chirality and diameter, CNTs can be semiconducting or metallic; due to strong covalent bonding, CNTs possess extremely high mechanical strength and resistant to bending that make them very steadfast to the destruction under high FE currents and stable under ion bombardment at moderate vacuum conditions [Ha13]; they have higher thermal (up to $5800 \text{ W}\times\text{m}^{-1}\times\text{K}^{-1}$) and electrical conductivity than other conductive materials such as copper [Sait10]. In addition, CNTs can also carry a very high current density (up to 10^9 A/cm^2) before the electromigration [Miln06].

Nevertheless, carbon nanotubes have some disadvantages that need to be processed in order to fully exploit their potential in application as a material for FE cathodes. CNT emitters suffer from poor contact to the substrate, which result in lifetime issues, high contact resistance and a limitation of the FE current [Nils01, Purc02]. Furthermore, varying alignment and positioning of single carbon nanotubes often limit the FE homogeneity [Navi10, Navi10a] and cause low transmission efficiency of the triode structures. Other difficulties are associated with the reproducibility and uniformity of the CNT emitters, which is still quite poor and limited because the synthesis of CNTs with uniform diameter and chirality remains a difficult task.

In this chapter, different approaches of improvement of the contact interface of CNTs as well as the field emission homogeneity, alignment and efficiency of the CNT cathodes for diode and triode applications will be presented. Moreover, based on electron trajectory calculations using COMSOL Multiphysics® software, a highly efficient triode structure was found. Finally, in order to optimize the densely grown carbon-based nanowall samples, laser-structuring of the these films into arrays of square patches of different size was performed and their FE properties were investigated. For these approaches, however, the synthesis of different carbon-based samples was performed by various chemical vapor deposition methods in research cooperation with the Belarusian State University of Informatics and Radioelectronics (Minsk, Belarus), Technische Universität Darmstadt (Darmstadt, Germany), Ajou University (Suwon, South Korea) and with the University of Duisburg-Essen and CeNIDE (Essen, Germany).

5.1. CNT networks grown at ~ 150°C on Si substrates

The FE homogeneity of most CNT cathodes is still limited by their rather fast and uncontrolled growth which usually leads to a strongly varying field enhancement and current carrying capability of the individual emitters. In addition, the maximum achievable current density of structured CNT cathodes is usually limited by their contact interface and the current supply through the substrate which can be much improved by a layer of surrounding CNTs [Navi10a]. It is well known that high quality CNT cathodes are usually fabricated by chemical vapour deposition (CVD) techniques at temperatures above 500°C which exclude their applicability to cheap low temperature substrate materials like polymer foils.

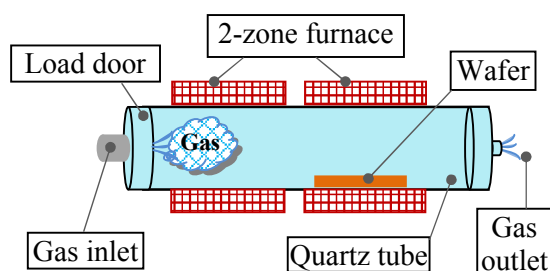
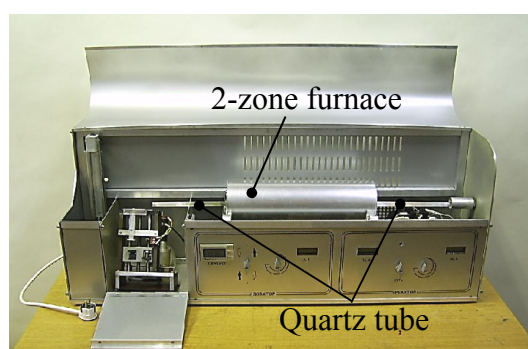
Thin films of CNT networks due to their high conductivity, transparency and flexibility are considered as a promising material not only for the field emission but also for the fabrication of flexible electronic devices such as transparent transistors [Aika12, Sun11, Artu05], supercapacitors [Kaem13], solar cells [Rowe06], organic light-emitting diodes [Zhan06], field emission symbol displays or lamps [Sait10, Spin76, Rash00, Smit98] and others [Hu10, Yell11]. For such devices, at least two transparent and flexible conductive electrodes are required. The first electrode (anode) can be fabricated by using a phosphor, polymer substrate and indium-tin-oxide. However, for the fabrication of the second one (cathode) on a flexible polymeric substrate using CNTs as the electron source is rather complicated due to high temperature of the CVD process.

Therefore, CNTs are usually produced in post-synthesis process by spin-coating, spray-coating, wet-coating, microwave-welding, filtration, printing method or by separation of CNTs from the initial substrate and subsequent transfer onto another substrate using acids [Jeon11, Lyth07, Tsai09, Wang07, Hu10, Yell11].

The direct growth of CNTs onto flexible polymer substrates (Kapton® foil) using plasma enhanced chemical vapour deposition (PECVD) at 200°C was reported by Hofmann et. al. [Hofm03a, Hofm03b]. However, transmission electron microscopy (TEM) analysis of produced CNTs showed more defects than CNTs grown at 600°C (or higher temperatures) and hence the FE measurements showed rather high onset electric fields. Therefore, new approaches are needed.

This sub-chapter of the thesis reports on a new recently developed low-temperature CVD process based on a reactor with two temperature zones which can be independently controlled. Depending on the various process parameters, self-structured CNT networks with some outgrowth of vertically-oriented single-wall CNTs were achieved. The FE properties of these cathodes were systematically measured.

CNT networks were fabricated in the group of B. Shulitski and Prof. Dr. V. Labunov in the Laboratory of Integrated Micro- and Nano-systems at Belarusian State University of Informatics and Radioelectronics (Minsk, Belarus). The CVD growth procedure is reported in detail elsewhere [Labu12]. Briefly, the CNT networks were grown directly on n-type Si substrates (6×6 mm size, 0.01 Ω·cm) using a new CVD process based on a reactor with two temperature zones (Fig. 5.1). Supported by a strong Ar carrier gas flow (100 cm³/min), the catalytic pyrolysis of mixed hydrocarbons (solution of ferrocene (Fe(C₅H₅)₂) in p-xylene (C₈H₁₀) and ethanol (C₂H₅OH)) was performed in the hot zone at 700-1100°C, while the growth of CNT onto Si wafers was carried out in another zone of the reactor at 100-150°C.



Dimensions	1.1 × 0.25 × 0.5 m
Types of hydrocarbons	fluid
Types of catalysts	volatile, localized
Diameter of the tube, Ø	1 cm
Working pressure	1÷10 ⁵
Temperature regimes	100-1000 °C
Catalyst concentration	0.1÷10 %
Rate of mixture injection	0.001÷10 cm ³ ·min ⁻¹
Rate of gas-carrier	10÷1000 cm ³ ·min ⁻¹
Power consumption	1 kW

Fig. 5.1. CVD equipment and the associated schematic drawing (more detailed disclosed in the Eurasian Patent № 015412 from 30.08.2011) and specification [Labu12].

Depending on the temperature of both zones, the injection rate of the hydrocarbon mixture, and the carrier gas flow, self-structured networks of highly entangled CNTs were obtained after 10 minutes of deposition time. As shown in Fig. 5.2a-d, the CNTs agglomerate into well-separated hills of entangled CNT bundles. The clearly visible round particles are metal-catalyst and a low-crystalline carbon. High-resolution SEM images have also revealed sparse outgrowth of vertically-oriented CNTs (typical length ~1 μm) which should result in high field enhancement and low onset fields. In addition, their anchoring in the few μm thick CNT network might improve the current carrying capability of the emitters. Moreover, TEM images reveal the presence of the single-wall nanotubes in bundles (Fig. 5.2e,f).

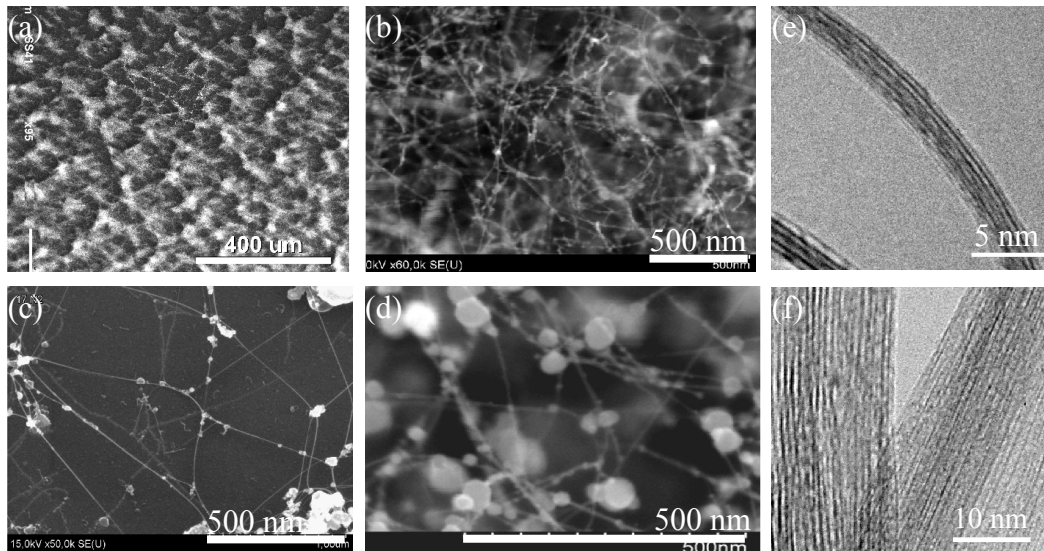


Fig. 5.2. SEM (a-d) and TEM (e,f) images of the sparsely distributed and horizontally oriented single-walled CNT networks. The diameter of CNTs is about 0.8-1 nm [Labu12].

The Raman spectrum collected by using a laser with $\lambda = 532$ nm (Fig. 5.3). Peak at 1580 cm^{-1} (G-line) corresponds to the twice degenerated deformation oscillations of the hexamerous ring in E_{2g} electronic configuration of D_{6h}^4 crystal symmetry. This peak testifies to the presence of carbon in the form of ordered hexagonal lattice. Second peak at 1320 cm^{-1} (D-line) corresponds to the vibration state of the ruinous hexagonal lattice near the crystals boundary and witnesses the presence of the not fully ordered transition forms of carbon (milled graphite, soot, another carbonized substances). The ratio of the intensities $I_G/I_D = 5,6$ characterizes high quality the structure of synthesized CNT networks. The peaks in the RBM region (at frequencies of 223 cm^{-1} and 263 cm^{-1}) testifies to the presence of single-walled CNTs in the networks with diameters of 0.87-1 nm in the bundles. The CNTs diameter was calculated by means of the following expression: $\nu = 6.5 + 223.75/d$, where ν , cm^{-1} is the frequency of the radial modes oscillations of the CNTs hexagonal lattice. The pick in the range of 1500 cm^{-1} (G-line) testifies to the considerable presence of single-walled CNTs with a metallic conduction

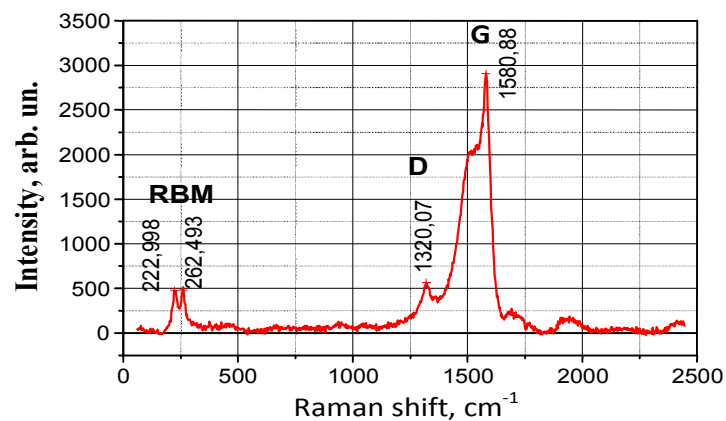


Fig. 5.3. Raman spectrum at 532 nm excitation of single-walled CNTs [Labu12].

In order to optimize the fabrication parameters of the CNT networks and to evaluate their suitability for FE devices, a row of cathodes with varying thickness has been produced on n-type Si substrates. Their systematic investigation started with the field emission scanning microscope at $\sim 10^{-7}$ Pa using tungsten anodes of diameter $\varnothing_a = 150 \mu\text{m}$ at fixed gap Δz of 50-100 μm , which was estimated by means of $U(z)$ -plot [Lyse05]. The FE homogeneity and current stability off the whole cathode were tested in pulsed diode configuration (tilt-corrected $\Delta z \approx 550 \mu\text{m}$) of the integral measurement system with luminescent screen at a vacuum of $\sim 10^{-5}$ Pa [Lyse05].

The best FESM results have been obtained for the thinnest CNT network cathodes. PID-regulated voltage scans $U(x,y)$ at a constant current of 1 nA revealed well-distributed FE with number of emitters $N_e \sim 10^4 \text{ cm}^{-2}$ at an electric onset field $E_{\text{on}}(1 \text{ nA}) \approx 2.5 \text{ V}/\mu\text{m}$ as shown in Fig. 5. 4. The position of the strongest emitters corresponds well to the gas flow conditions, i.e. nearly homogeneous FE along and a Gaussian-like FE profile (full width $\sim 3 \text{ mm}$) across the gas flow. Therefore, a homogeneous FE on large substrates could be achieved by their “scanning” or with a larger reactor. In comparison, the cathodes with a higher density of CNT hills showed similar results but at higher $E_{\text{on}}(1 \text{ nA}) = 3\text{-}6 \text{ V}/\mu\text{m}$.

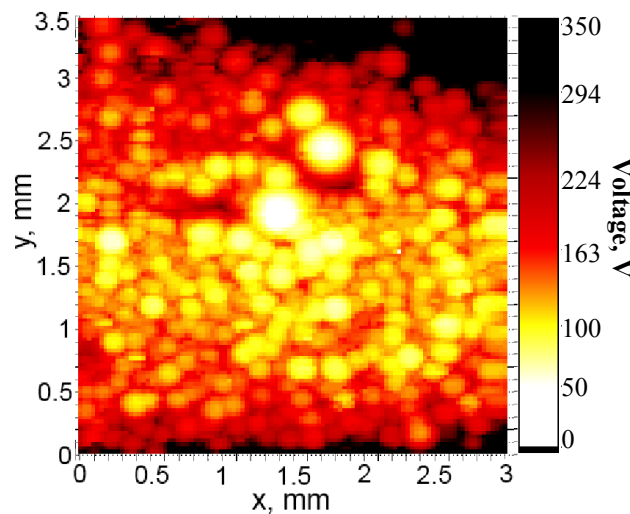


Fig. 5. 4. Regulated voltage map ($\varnothing_a = 150 \mu\text{m}$, $\Delta z = 50 \mu\text{m}$ for 1 nA, $3 \times 3.5 \text{ mm}^2$ area) of the same CNT network cathode as shown in Fig. 5. 2.

The current carrying capability of the self-structured CNT networks was locally measured with the same anode size. After some initial current processing, a stable and reproducible current curve with a constant FN plot was achieved up to 100 μA for all cathodes. The best result yielded nearly stable current (fluctuations $< 5\%$) up to 220 μA ($j = 1.25 \text{ A}/\text{cm}^2$ at $8.5 \text{ V}/\mu\text{m}$) as shown in fig. 5.5. The corresponding FN plot shows a linear FN-like behavior up to 160 μA , which corresponds to a current density of $0.9 \text{ A}/\text{cm}^2$, while at higher FE current ($> 0.9 \text{ A}/\text{cm}^2$) the plot starts to deviate from the FN theory. Similar changes

in the FN plot were observed on individual single- and multi-wall nanotubes [Bona98, Dean00]. Bonard et. al. reported that the deviations from the FN behaviour point to the presence of a non-metallic density of states at the tip of the nanotubes [Bona98]. While others argued that the deviation associated with adsorbate [Dean00, Dong03, Murr13], space-charge effects [Barb53, Chen09, Jens10], high contact resistance [Chen12, Lugi96] or can be attributed to degradation of the high aspect-ratio CNTs [Bona98] or due to interaction between emitters at high field [Coll97, Nam07] or due to non-Shottky-Nordheim barrier [Buld03] and non-uniformity of emission sites [Obra03, Eda08].

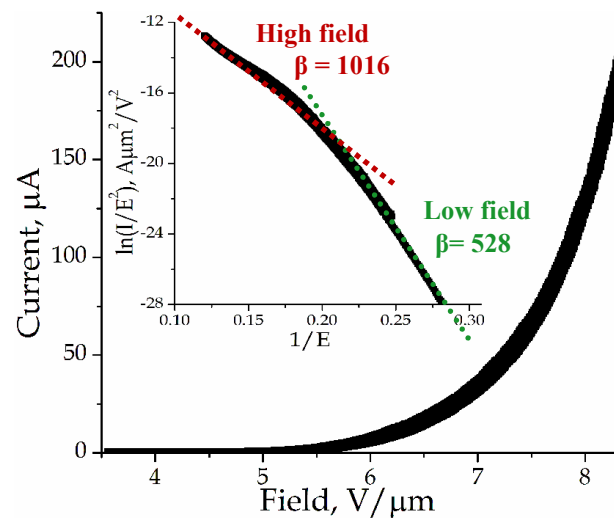


Fig. 5.5. Typical I - V and FN (inset) curves locally measured with $\varnothing_a = 150 \mu\text{m}$ at $\Delta z \approx 72 \mu\text{m}$ on the same CNT network cathode as in Fig. 5.4.

The field enhancement factor derived from the non-saturated region of the FN-plot assuming a work function value of about 4.9 eV for CNTs [Chen03] is 528 that is in good agreement with the aspect ratio of CNTs as shown in Fig. 5. 2. Increase in field enhancement factor at high field mainly attributed to the effects mentioned above.

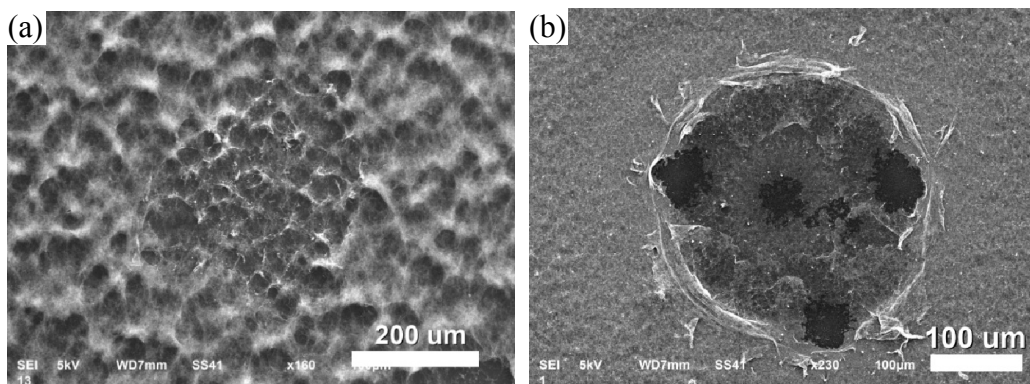


Fig. 5.6. SEM images of the self-structured CNT networks with sparsely (a) and densely (b) distributed hills processed up to $I \sim 0.4$ and 0.5 mA ($\varnothing_a = 150 \mu\text{m}$).

SEM images of the processed spots revealed only slight morphology changes for stable current but more severe ones in case of strong current jumps. Typical examples are given in Fig. 5.6 where some field alignment of the emitters can be seen for the thin CNT network but complete disruption and folding for the thick CNT network.

IMLS measurements of the cathode with a thin CNT network yielded fairly homogeneous emission (Fig. 5.7) and revealed an achievable current density of at least 10 mA/cm^2 at $8.5 \text{ V}/\mu\text{m}$ limited by the high power load on the luminescent screen which led to active layer evaporation and electrical discharges. For the full exploitation of optimized CNT network cathodes metallic anodes will be therefore required. The observed hysteresis in the current field curve is attributed to the degradation of the strong single emitters.

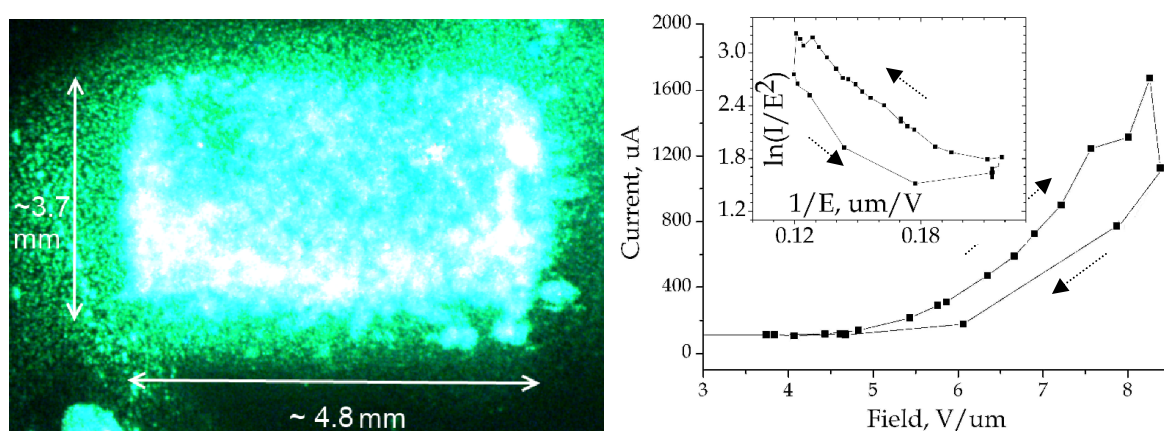


Fig. 5.7. Luminescent screen image of FE distribution from a self-structured thin CNT network cathode (similar as in Fig. 5.1.2) and the corresponding I - V curve (peak current $\sim 2 \text{ mA}$ (or 10 mA/cm^2) at $5.3 \text{ V}/\mu\text{m}$, pulse length 5 ms , duty cycle $1:4$, $\Delta z \approx 550 \mu\text{m}$).

In conclusion, a new low temperature (below 150°C) method of direct formation of horizontally aligned CNT networks on Si substrates by thermal CVD using volatile catalyst was developed. Deposition on large area surfaces might be possible by having a larger reactor. The results of the local and integral measurements show rather promising FE properties. Samples with sparsely distributed hills of entangled CNTs showed lower onset and operation field as well as more stable FE current compared to the more dense ones. Integral and long-term stability tests with metallic anodes should fully exploit the applicability of these cathodes.

This work was supported by the FP 7-INCO EU project Nr. 295043 BELERA.

5.2. CVD growth of CNT bundles using Mo/Al/Ni catalysts

Structured FE arrays with CNT columns grown on patterned Si/SiO₂ by atmospheric pressure CVD provide local (integral) current density values up to 25 A/cm² (40 mA/cm²) above 2000 V [Navi10a]. It has also been shown that the field enhancement factor β is not determined by the column height, but by the CNT outgrowth [Serb11, Navi12]. However, shorter CNT columns grown on Si/SiO₂ suffered from poor contact to the Si substrate. A well-known alternative for the fabrication of high current FE cathodes with groups of vertically aligned CNT [Teo02, Teo03a, Teo03b, Mele05] or bundles of entangled CNT [Mano05, Mano08, Navi12] of less height (< 5 μm) is based on their preferential growth on metallic catalyst patches. Such cathodes are often limited by FE current saturation due to high contact resistance to the Si substrate [Nils01].

In this study, a novel approach to improve the contact interface by using trimetallic layer on the Si substrate is described. A thick uniform Mo layer is chosen to provide a current to the CNT, while the combination of a thin Al film and Ni catalyst lead to a suitable diameter and number of CNTs per bundle [Miln04]. Moreover, a systematic decrease of their height combined with an increase of the emitter number density might lead to high current density at moderate operating voltage.

Highly-doped n-type Si substrates (3.2×1.2 mm² size, 0.01 $\Omega\cdot\text{cm}$) were first magnetron sputtered with a 300 nm thick Mo which serves as a diffusion barrier layer and have to provide good electrical contact to the CNT. The thickness of the Al underlayer and the active Ni catalyst layer are critical to nanotube growth and their good electrical contact to the substrate [Delz02, Delz01, Mele05]. A laser pattern generator was used for the maskless lift-off photolithography of a bimetallic catalyst layer (10 nm Al and 1 nm Ni) in areas of 1×0.25 mm² size. Catalyst patches of 1×2 μm^2 size and 5, 10 or 100 μm pitch were created to achieve structured cathodes with quadratic arrays of entangled CNT bundles. CNT bundles of 2-3 μm width and up to 2 μm height were obtained by atmospheric pressure CVD based on the pyrolysis of decane or ethanol at 680-700°C for 3-5 minutes. SEM images of CNT bundles are given in Fig. 5.8.

Low and high resolution SEM images of these arrays revealed the presence of hundreds entangled individual CNTs per bundle with free ends of typically 20-40 nm in diameter. Therefore, CNT bundles with well-separated multiple emitters can lead to highly efficient field emission (i.e., high current density at low applied voltages) due to less screening effects [Bona01, Nils00].

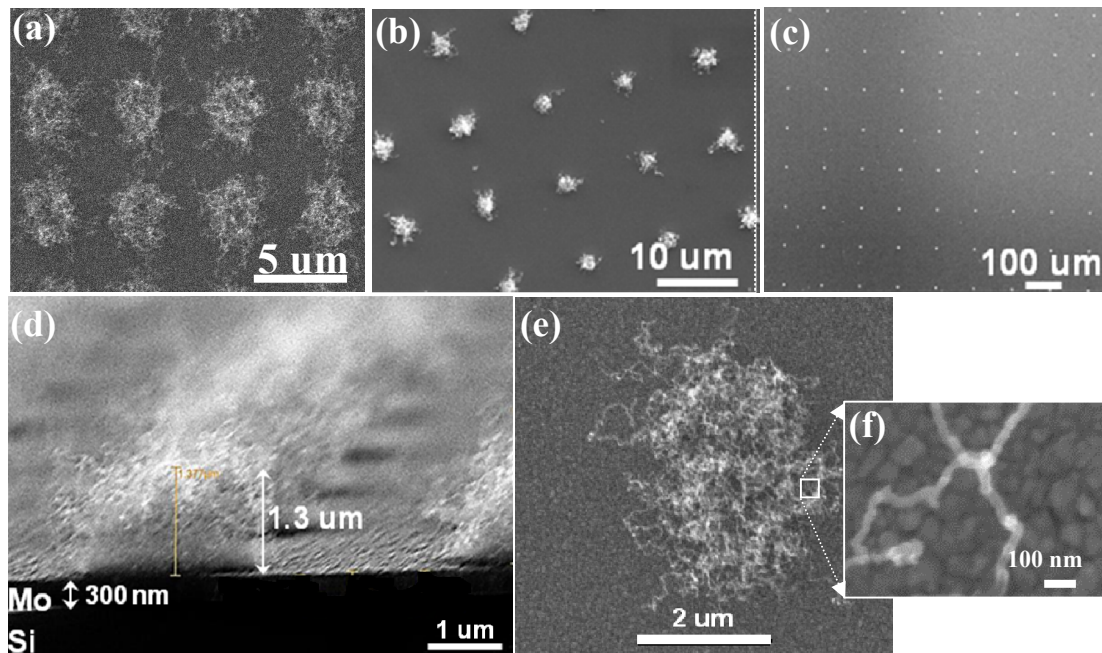


Fig. 5.8. SEM of CNT-bundle arrays with a pitch of 5 μm (a), 10 μm (b) and 100 μm (c) grown on Mo/Al/Ni catalyst; cross-section view (d) and top view of a single bundle (e) and a single CNT (f).

The FE homogeneity of the structured CNT bundle cathodes was investigated with the field emission scanning microscope at 10^{-7} Pa by means of PID-regulated voltage scans for constant current using W tip anodes of suitable diameter \varnothing_a . Arrays with large pitch showed high efficiency and clearly visible alignment of strong emitters at an onset field of about 15 V/ μm (Fig. 5.9 left) [Serb13a]. For a small pitch randomly but well-distributed emitters ($N_e > 2500/\text{mm}^2$) could be resolved at similar field levels (Fig. 5.9right). Nevertheless, the homogeneity of the CNT bundle arrays is limited by the variation of the diameter and length of the CNTs.

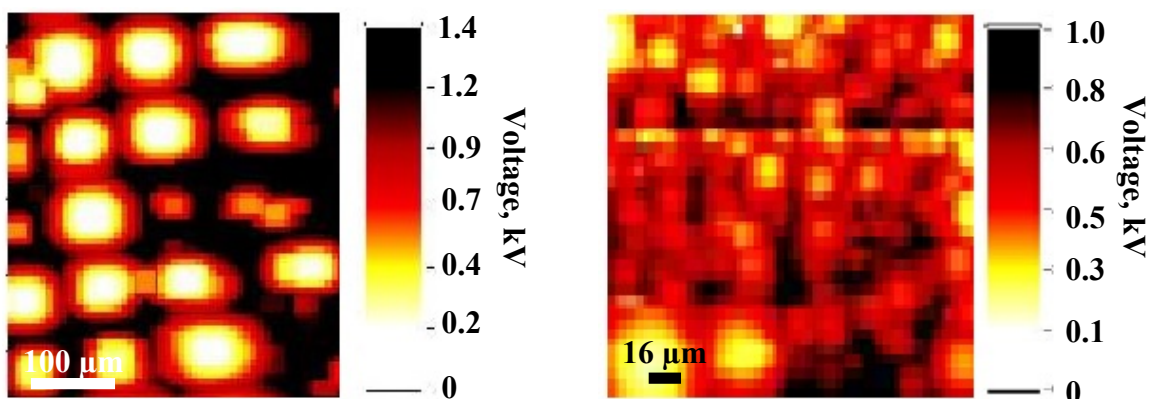


Fig. 5.9. Regulated voltage maps (at a constant current of 1 nA, $\varnothing_a = 5 \mu\text{m}$) of structured CNT bundle cathodes with a pitch of 100 μm (left) and 5 μm (right). The actual gap Δz of $\sim 15 \pm 5 \mu\text{m}$ was estimated by means of a long-distance microscope.

In order to investigate the current carrying capability of various CNT cathodes, local measurements were performed with a tungsten anode of truncated-cone shape of 150 μm in

top diameter after field calculation by means of the $U(z)$ -plot [Lyse05]. After the first voltage rise, cathodes with small and medium number density of CNT bundles yielded nearly stable current up to $\sim 50 \mu\text{A}$ (at 2450 V @ $18 \mu\text{m}$ gap) and $\sim 250 \mu\text{A}$ (at 2040 V @ $34 \mu\text{m}$ gap), respectively. Observed hysteresis for these cathodes might be associated with adsorbate effects [Chen11] and/or due to partial destruction/evaporation of taller CNTs at high FE current densities [Liu01]. For comparison, the cathode with smaller pitch (higher number density of CNT bundles) showed stable and reproducible current up to $\sim 500 \mu\text{A}$ at a lower supply voltage of $\sim 410 \text{ V}$ @ $35 \mu\text{m}$ gap (Fig. 5.10).

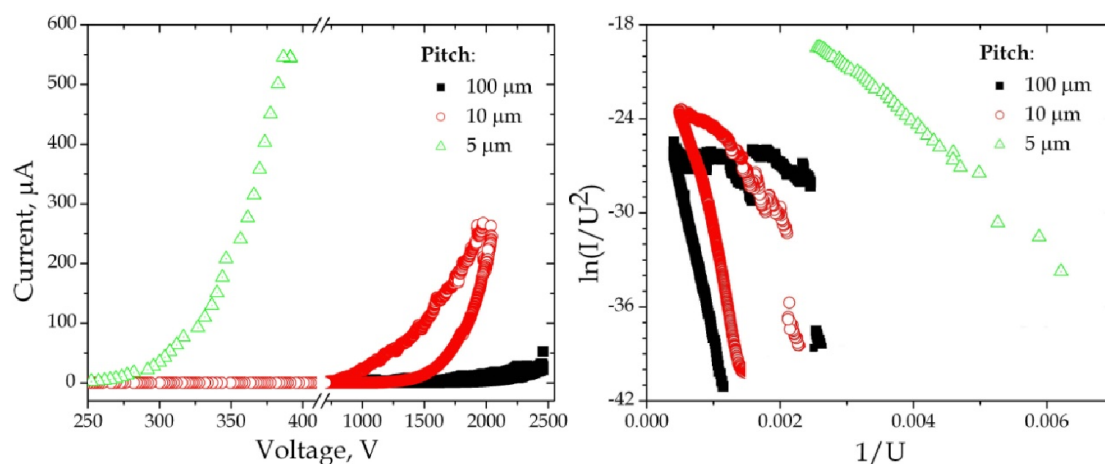


Fig. 5.10. Current-voltage curves (right) and corresponding Fowler-Nordheim plots (left) of the locally measured ($\varnothing_a = 150 \mu\text{m}$) CNT bundle cathodes for different pitch values.

The field enhancement factors extracted from the FN plots at low currents (assuming work function of 4.9 eV for CNT [Grön01]) are 76, 104 and 91 for the cathodes with $100 \mu\text{m}$, $10 \mu\text{m}$ and $5 \mu\text{m}$ pitch, respectively. These values are in rather good agreement with the diameter (20-40 nm) and the length (up to $2 \mu\text{m}$) of CNTs (Fig. 5.8).

For several cathode spots, a slow mean current increase or a small current drop were observed at constant voltage. Such processing effects can be explained by destruction of individual dominant carbon nanotube emitters in the bundles [Bona03] (Fig.5.11left) and field-alignment of individual CNTs [Wei01] or by desorption of the adsorbates by FE current (Fig.5.11right) [Dean00, Purc02].

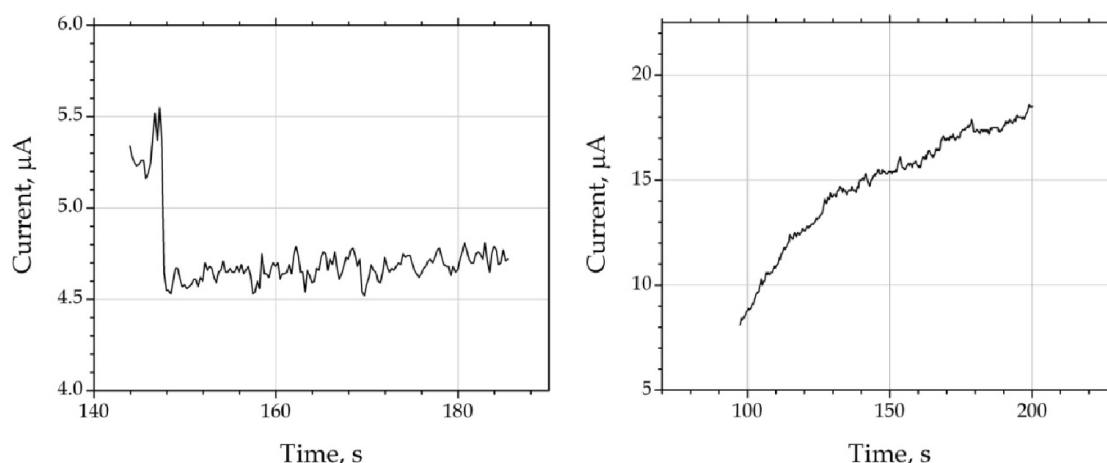


Fig. 5.11. Stability of a CNT bundle array ($p = 5 \mu\text{m}$, $\varnothing_a = 150 \mu\text{m}$) at moderate current.

High current processing, however, often leads to strong degradation of the cathode. SEM analysis of measured spots revealed disruption of whole CNT bundles (Fig.5.12a). Melted a 300 nm thick Mo and Al/Ni catalyst layers (Fig. 5.12b) give a hint of high current (300 nA) that flow through a CNT and not sufficient electric contact between the CNTs and the substrate [Nils01]. A high contact resistance might limit the FE current and can lead to overheating of the substrate or even melt it. As can also be seen, some CNTs are detached from the substrate that might be due to a combination of resistive heating at the CNT-Mo/Al/Ni interface and a strong electric field, which might peel the CNTs off the substrate [Ha13]. In addition, disruption of CNT bundles is inhomogeneous, perhaps, due to the unflatness of the used anode. Thus, the electric field under the anode was inhomogeneous and not all the bundles were involved in the FE. Hence, the effective emission area is much smaller than the $\varnothing_a = 150 \mu\text{m}$ and the real potential of such CNTs might be very high.

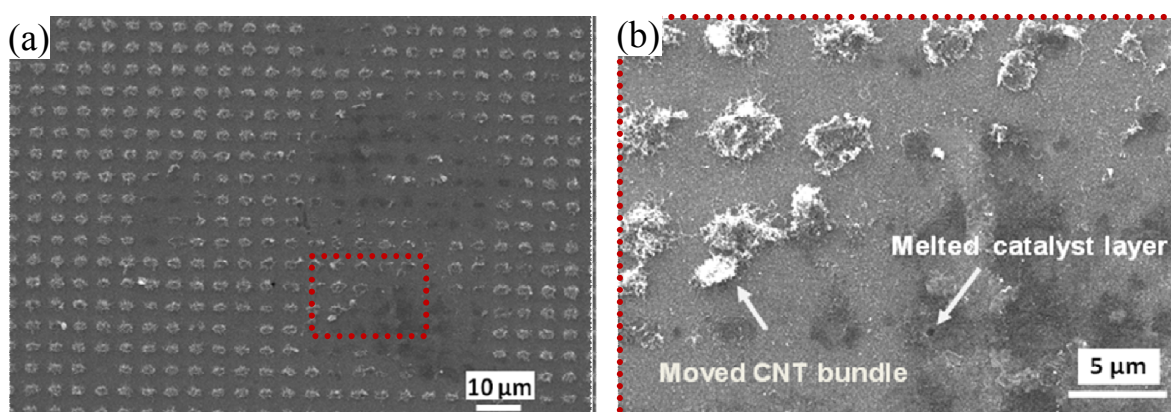


Fig. 5.12. Low- (a) and high-resolution (b) SEM images of CNT bundle cathode with $5 \mu\text{m}$ pitch after processing at $I_{max} = 500 \mu\text{A}$ ($j \sim 3 \text{ A/cm}^2$), $\varnothing_a = 150 \mu\text{m}$.

The FE performance of a selected CNT bundle cathode with $p = 5 \mu\text{m}$ was tested in diode configuration of the integral measurement system with luminescent screen at 10^{-5} Pa [Lyse05]. Measurements in pulsed mode (duty cycle 1:10) showed stable and reproducible FN up to $250 \mu\text{A}$ ($j = 100 \text{ mA/cm}^2$) at $13.5 \text{ V}/\mu\text{m}$ (Fig. 5.13a). Beside the strong

homogeneous FE in the CNT bundle array area, a slight emission also occurred at the sample edges due to parasitic CNT growth. At such values of power load (~ 0.7 W) the sensitive luminescent screen damages over several seconds. Using a solid Cu anode, maximum peak current values $I = 11$ mA (corresponding to $j = 4.4$ A/cm²) from the CNT bundle cathode were achieved at 23 V/ μ m but limited by strong fluctuations. Saturation of the field emission current at high field region (Fig. 5.13b) might be explained by space-charge effects [Barb53, Bona98, Chen09, Dean00, Jens10] or by the presence of high resistance at the nanotube-substrate contact [Bona03, Lugi96]. In the last case, the voltage drop across a resistance would lead to decrease of the applied voltage (field) and therefore to a smoothing of FN-curve. It is not a trivial task to take into account this effect and it is constantly being discussed at the International Vacuum Nanoelectronics Conferences [Forb12a, Forb12b, Forb13a, Forb13].

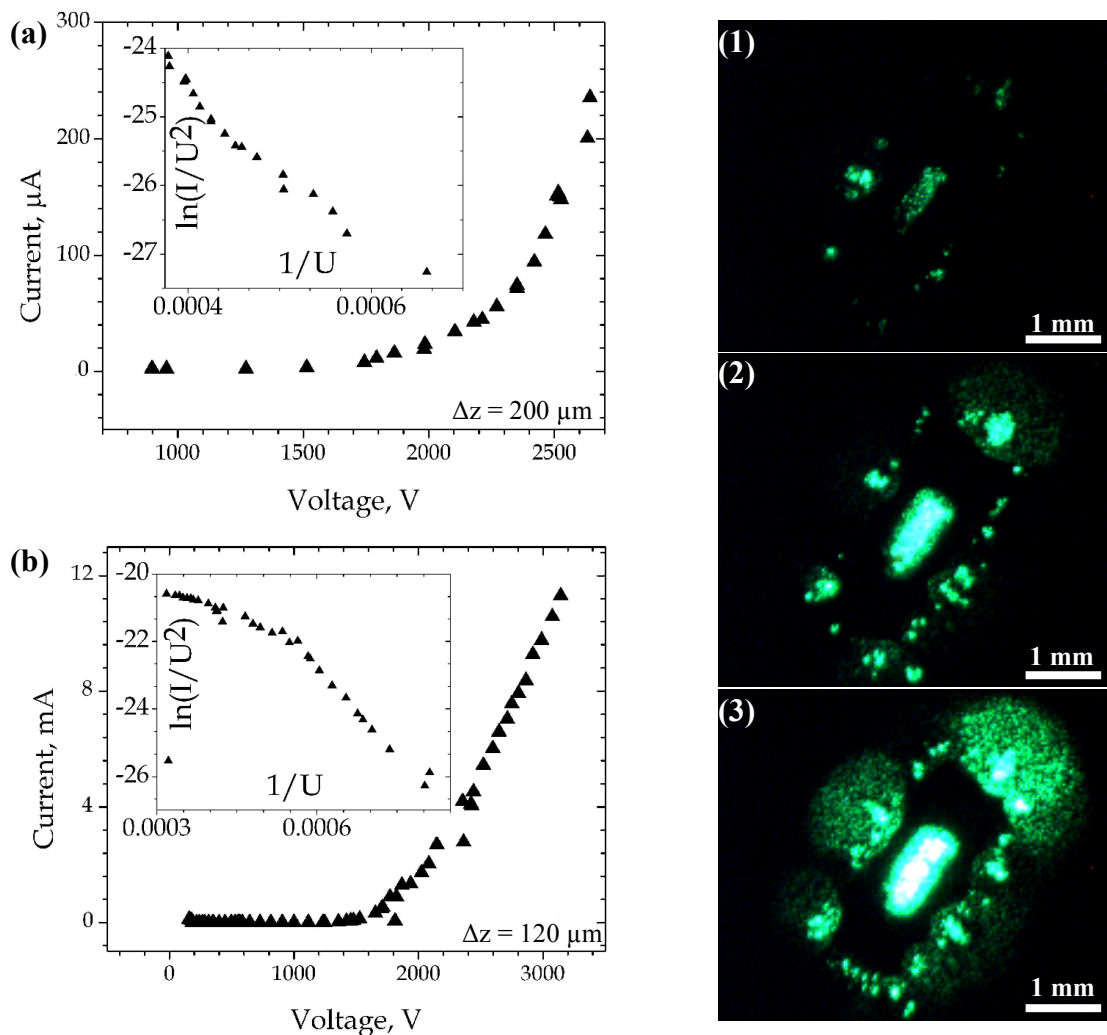


Fig. 5.13. I - V curves and corresponding FN-plots (instes) of CNT cathode with $p = 5 \mu\text{m}$ measured in pulsed mode (2:20 ms) with luminescent screen (a) and metallic anode (b). Screen images (left, inset) taken at (a) $I = 20 \mu\text{A}$, (b) $I = 100 \mu\text{A}$, and (c) $I = 250 \mu\text{A}$.

Overall, the present study demonstrates that CNT bundle arrays of reduced height and small pitch grown on trimetallic Mo/Al-Ni catalyst films are well-suited to achieve high current densities (4.4 A/cm^2) at rather low voltages/fields. The FE performance of the CNT bundle array cathodes is suitable for high current application, e.g. a focused spot X-ray source. Nevertheless, the FE homogeneity of the structures cathodes should be improved, e.g. by vertical aligned growth of CNT. Moreover, the contact and adhesion of the CNT bundles should be optimized to avoid their disruption.

This work was supported by the FP 7-INCO EU Project Nr. 295043 BELERA.

5.3. Catalytic water-assisted CVD synthesis of CNT bundles

Previous pure and TiO_2 -coated CNT block arrays [Navi10, Josh11] showed the ability to reach high currents per single blocks, but the height of the blocks (150-300 μm) led to a limited FE homogeneity and alignment of the emitters due to significant outgrowth of single CNTs or bundles from the block surface. The blocks suffered from a limited mechanical stiffness and occasional bending too. The field enhancement factor β was determined rather by the outgrown CNTs than by the block geometry. Moreover, the often observed hysteresis at fields above 20 $\text{V}/\mu\text{m}$ was mostly caused by an effective gap change due to reversible alignment of the outgrown CNTs [Wei01]. Most CNT blocks provided irreversible current instability (at 10-200 μA) due to stepwise destruction of loose CNT and complete block destruction at 200-800 μA .

Therefore, regular arrays of much shorter CNT columns were considered in order to improve the homogeneity and alignment as well as stability of such structured FE cathodes. The origin of a local heating observed as glowing spots [Navi10] on CNTs as FE current limiting factor is under further investigation and discussion here too.

The water-assisted CVD method of the CNT synthesis was introduced at Technical University of Darmstadt (TUD) [Tud] by the group of Prof. J. Schneider including J. Engstler and R. K. Joshi.

The successive fabrication steps of the structured CNT cathodes are shown in Figure 5.14. P-doped silicon (100) wafers with a thin dielectric SiO_2 layer (600 nm) and a resistivity ρ of 10-20 $\Omega \text{ cm}$ were used for the CNT bundles. The substrates were coated by means of electron beam evaporation first with a thin aluminum buffer layer (10-12 nm) and then with a very thin patterned iron film (0.6-1.5 nm). Patterning of the iron film was achieved by fixation of a perforated metal or nylon foil on the aluminum layer as shadow mask. Thereafter, the samples were heated within a \varnothing 2.5 cm quartz tube oven up to 800°C under a flow of argon and hydrogen (Fig.5.15). At this temperature, according to the Rayleigh

instability theory [Rayl78, Kari06], the bimetallic films are supposed to crack and form small Fe-Al nanoparticles which served as catalyst for the following CNT growth [Josh11]. Aluminum film promoted the small particle formation [Delz02, Eres04]. In addition, depending on the thickness of aluminum, carbon nanotubes with different morphologies can be obtained [Delz01, Delz02, Mele05]. The CNTs were synthesized from a flow of ethylene and some water vapor which was picked up by argon through a water bubbler and acted as a catalyst activator. The resulting growth rate of the CNTs was typically 1-5 μm per minute. Columns with a diameter of about 20 μm consisting of entangled CNTs of 5 μm height were obtained in an asymmetric triangular array with 256 and 270 μm pitch as shown in Fig. 5.16. In contrast to other fabrication techniques [Navi10], relatively efficient selectivity of the CNT growth was achieved.

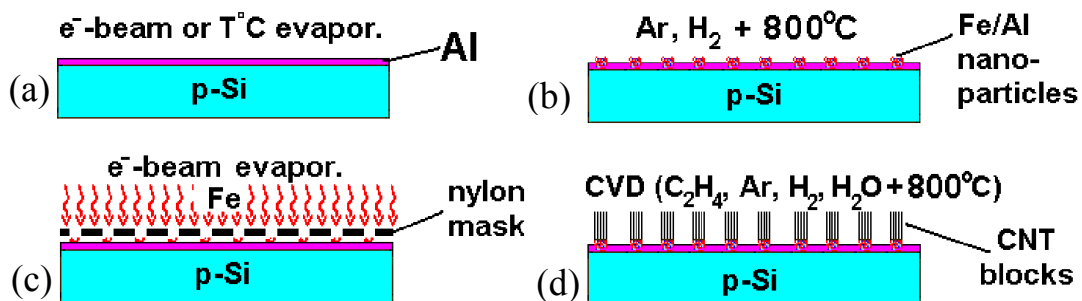


Fig. 5.14. Schematic of the structured cathode fabrication: (a) deposition of 10-12 nm thick Al buffer layer by electron beam evaporation on Si substrate, (b) deposition of 0.8-1.2 nm thick Fe patches through a shadow mask by electron beam evaporation, (c) annealing of the metal films in a quartz tube under inert gas flow with formation of bimetallic Fe/Al nanoparticles serving as a catalyst for the CNT growth and (d) synthesis of CNTs.

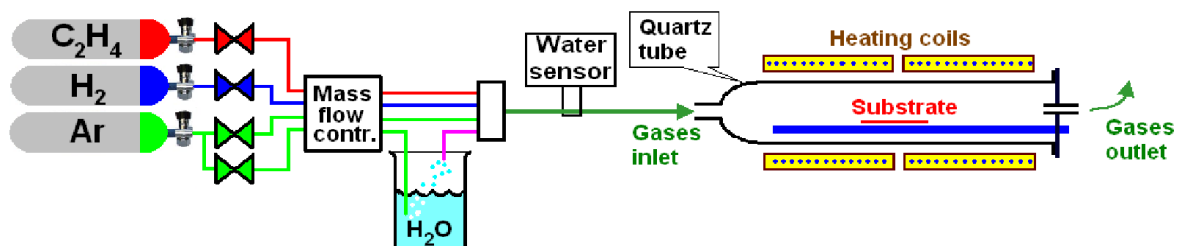


Fig. 5.15. Schematic sketch of the water assisted CVD setup at TUD.

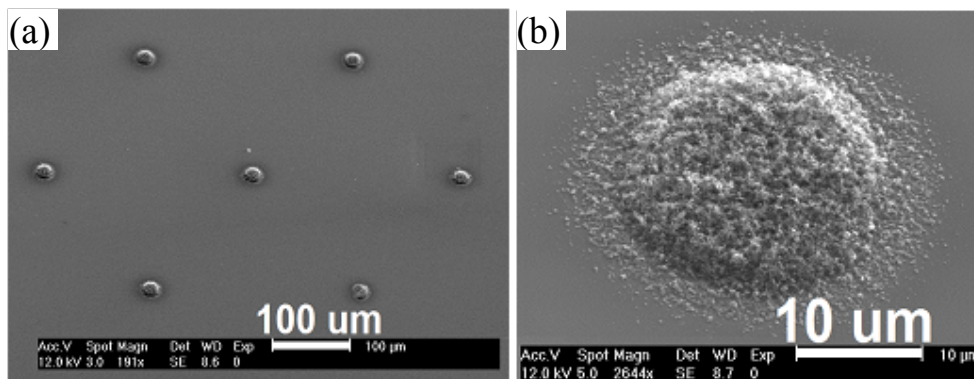


Fig. 5.16. SEM images of the arrays (a) and of a single column of entangled CNTs (b) ($\varnothing = 20 \mu\text{m}$, $p = 256/270 \mu\text{m}$, $h = 5 \mu\text{m}$).

The FE properties of these structured CNT cathodes were systematically investigated with the field emission scanning microscope at 10^{-7} Pa. The tilt of each cathode was corrected with respect to the truncated cone anode of diameter \varnothing_a to achieve a constant gap Δz within $\pm 1 \mu\text{m}$ for the selected scan area. The emitter distribution was non-destructively imaged by means of a PID-regulated voltage supply (10 kV, FUG HCN 100M, 25 mA) controlled by the FE current (Keithley 610C) as described elsewhere [Lyse05]. Some emitting microstructures were arbitrarily chosen for local measurements to get their current-voltage characteristics and correlated SEM studies. The macroscopic electric field E was calculated as ratio of the applied voltage U to the effective distance d between the anode and the relevant emitter. For each microstructure, d was determined by the linear extrapolation of PID-regulated $U(z)$ curve (for a fixed FE current of 1 nA) to 0 V, which corresponds to a contact between the anode and the emitter. The effective field enhancement factor β of the FE sites was derived from the measured I-V data using the modified Fowler-Nordheim equation (see chapter 2.1) and assuming a work function of 4.9 eV for CNTs [Grön01]. It should be mentioned that the obtained values of the applied field (voltage) are more relevant for the actual measurement geometry than for real triode devices, where the real shape of the gate and the gap has to be taken into account [Zhir01]. As suggested partially by the two-region FE model of Zhong et al. [Zhon02], β and the required field (voltage) are influenced by the d value as well.

The FE voltage map of the structured CNT cathodes demonstrates well-aligned and fairly homogeneous FE and about 100% efficiency was reproducibly achieved at onset field E_{on} (1 nA) $\approx 45 \text{ V}/\mu\text{m}$ (Figure 5.17) [Navi11, Navi12]. Correlated SEM-FESM investigations indicate that the individual microstructure of the bundles (see Fig. 5.16) and the presence of some CNTs near the patches are responsible for the remaining slight FE inhomogeneity.

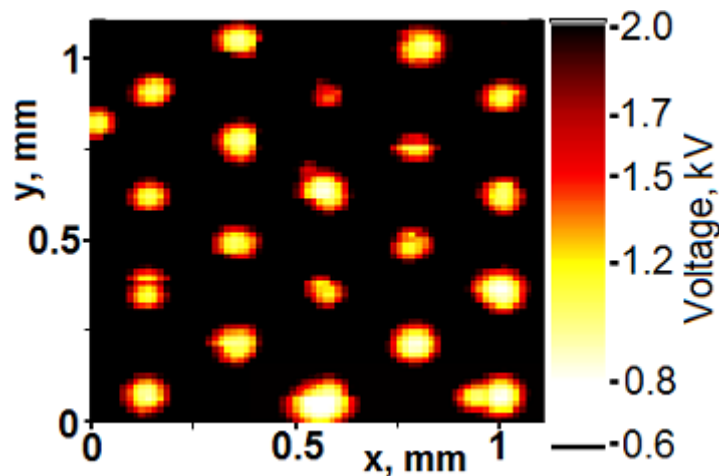


Fig. 5.17. Voltage map (at constant current of 1 nA, $\varnothing_a = 30 \mu\text{m}$, $\Delta z = 20 \mu\text{m}$) of structured CNT column array.

Local FE measurements of single bundles revealed unusual current-voltage (I-V) dependence with four sections (Fig. 5.18). The first section starts at the initial E_{on} (1 nA) of about 11 V/ μm and follows the FN-law up to a current level around 0.1 μA . Then a current saturation occurred at 1-2 μA in the field range 20-60 V/ μm (Sect.2). In both sections the FE current was rather reproducible and stable ($\pm 10\%$). In contrast, an irreversible FE current increase of typically a factor 10 was usually observed at a constant field in Section 3. Such strong activation effects were often following soon after or combined with a visible light emission from hot spots at the top of the bundles (Fig.5.3.5 inset). In Section 4 stable FN-like I-V curves resulted in onset fields of about 30 V/ μm and average β of 220, which are still determined by the sparsely outgrown CNTs. Maximum currents of about 40 μA at 65 V/ μm were achieved finally, limited by irreversible strong current drops and severe destructions of the CNT bundles as confirmed by correlated SEM images.

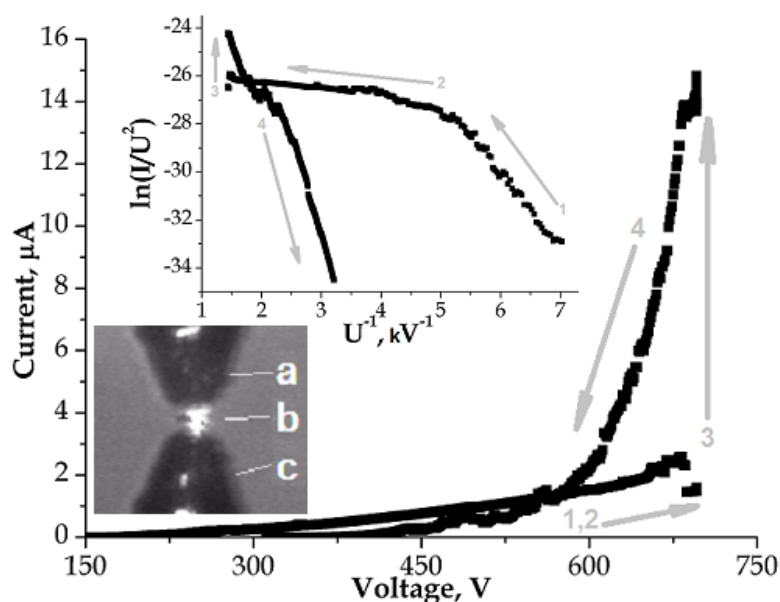


Fig. 5.18. Typical I-V and corresponding FN-plot (inset) measured with $\varnothing_a = 30 \mu\text{m}$ at $\Delta z = 14 \mu\text{m}$. Inset: hot spot (b) between the anode (a) and its mirror image on cathode (c).

The observed current saturation cannot be explained by a limited supply of electrons from the p-type Si substrate because this would not be changed after the emitter activation. Therefore, the silicon oxide layer SiO_2 of the contact interface between the CNTs and the substrate is considered to be responsible for the phenomena. Moreover, the presence of water vapor at the elevated CVD process temperature [Josh11] may enhance the oxidation of Si as well as of the bimetallic catalyst, especially if a nanoparticulate structure of the annealed Al/Fe catalyst is taken into account. Therefore, the catalyst can hardly protect the underlying Si from oxidation.

In order to understand the possible role of the oxide layer at the contact interface to the CNTs for the observed FE behavior, it is helpful to consider the energy band diagrams

resulting for such structure. These depend on the applied field and are very similar to the ones used for metal-insulator-metal (MIM) emitters [Lath95] or metal-oxide semiconductor (MOS) transistors [Ning78]. At low fields (Fig.5.19a), band bending and voltage drop V across the thin contact interface cause electron tunneling into the conduction band of the oxide where the limited electron supply leads to the observed current saturation. At high voltages (Fig.5.19b) the enhanced field penetration creates hot electron emission and avalanche multiplication in the Si conduction band which then leads to the electric breakdown of the oxide (typically 1-1.6 V/nm for SiO₂ thin films) [Ning78]. Thermalization of the hot electrons leads most probably to enhanced energy dissipation in the poorly cooled CNT and to the observed glowing spots. Hot-electron-induced electroluminescence [Toya96] cannot be excluded yet. As a result of the breakdown, conducting channels are formed in the contact interface, which cause geometric field enhancement and usual FN-like behavior of well-connected CNTs. The observed final current limits are governed, therefore, more by the intrinsic limits of the emitting CNTs [Dean01].

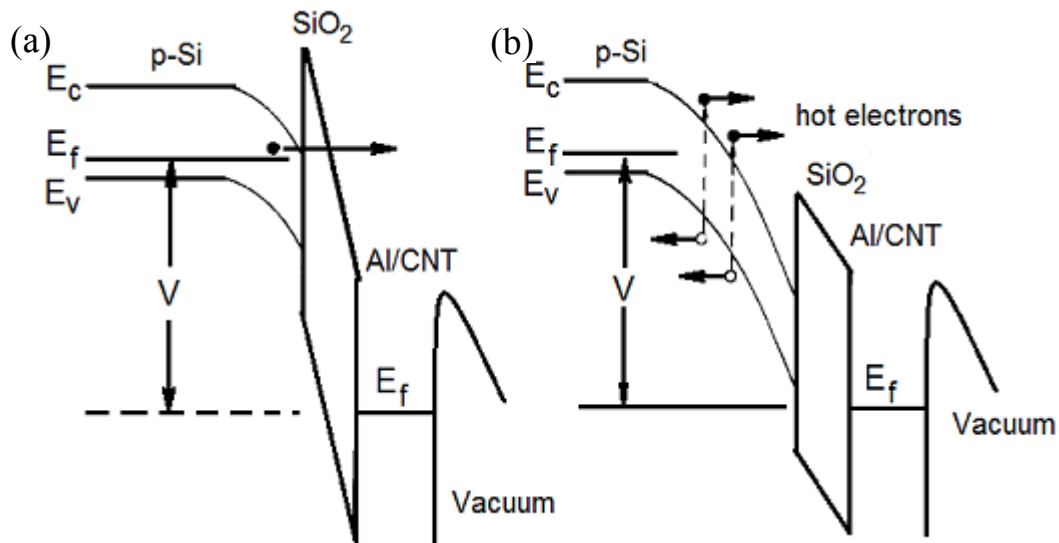


Fig.5.19. Energy band diagrams for electron FE through the Si/SiO₂/Me/CNT interface: (a) at low field band bending in Si and voltage drop over SiO₂ lead to current saturation due to limited electron transport in the oxide; (b) at much higher voltage field penetration into Si cause hot electrons and avalanche multiplication which burn conducting channels into the oxide.

In conclusion, these results prove that the contact interface plays an important role for the FE homogeneity of structured CNT columns on Si substrates. Moreover, it might be possible to stabilize or control the FE current by tuning the properties of the interface or using the oxide as a ballast resistor. The systematic FE investigations of structured CNT cathodes have determined the main direction for the optimization of the cold cathode design for device applications. The arrays of short CNT columns demonstrated high efficiency and

alignment than previous long CNT block arrays. High current densities in the range of A/cm^2 could be expected from uniform CNT arrays in case of sufficient FE homogeneity as well as from optimized arrays of the short CNT bundles (e.g. smaller pitch). Slight increase of the height of the CNT or decrease of their diameter, however, might reduce the onset and operation fields. Current saturation and glowing spots just before electric breakdown have been observed. Band structure considerations indicate that the contact interface and hot electrons play an important role for these phenomena. It might be possible, however, to stabilize or control the FE current by tuning the properties of the interface or using the oxide as a ballast resistor.

5.4. Vertically aligned CNT columns of different height and triode tests

Structured cathodes with columns of entangled CNTs grown on patterned Si/SiO₂ substrates have shown to provide low $E_{on}(1 \text{ nA})$ as well as high FE current [Navi10, Navi10a]. The emitter distribution and alignment of such cathodes, however, suffer from the dispersion of the positions of actually emitting CNTs which are often located at the edge of columns or even between them due to the limited growth selectivity.

Here another approach to obtain structured cathodes with CNT columns grown on highly-doped Si substrates with iron catalyst patches by hot-filament chemical-vapor-deposition (HFCVD) is presented. Quadratic arrays of columns of diameter $\varnothing = 250 \text{ }\mu\text{m}$, height $h = 70$ or $350 \text{ }\mu\text{m}$ and $650 \text{ }\mu\text{m}$ pitch were systematically investigated for their FE performance. Moreover, single columns of $\varnothing 1.5 \text{ mm}$ and $h = 250 \text{ }\mu\text{m}$ were tested in triode configuration.

The HFCVD growth procedure is reported in detail elsewhere [Hong09a, Hong09b]. Briefly, the fabrication steps of the structured vertically-aligned carbon nanotube (VA-CNT) column cathodes by HFCVD method are shown in Figure 5.20. Highly-doped n-Si (100) wafers ($12 \times 12 \text{ mm}^2$ size) were coated with a 10 nm aluminum buffer and 1.5 nm iron catalyst layers, which were deposited in succession by magnetron sputtering. Patch structuring was realized by means of photolithography. Prior to HFCVD growth of CNTs, the silicon substrates with a catalyst layer were heat-treated at $500\text{-}700^\circ\text{C}$ for 10-15 min in order to form high-density catalyst particles. Such treatment provided necessary conditions for the CNTs growth. Synthesis of CNTs was performed from methane and hydrogen gas mixture in a HFCVD reactor at the filament and substrate temperatures of 700°C and 2000°C , respectively.

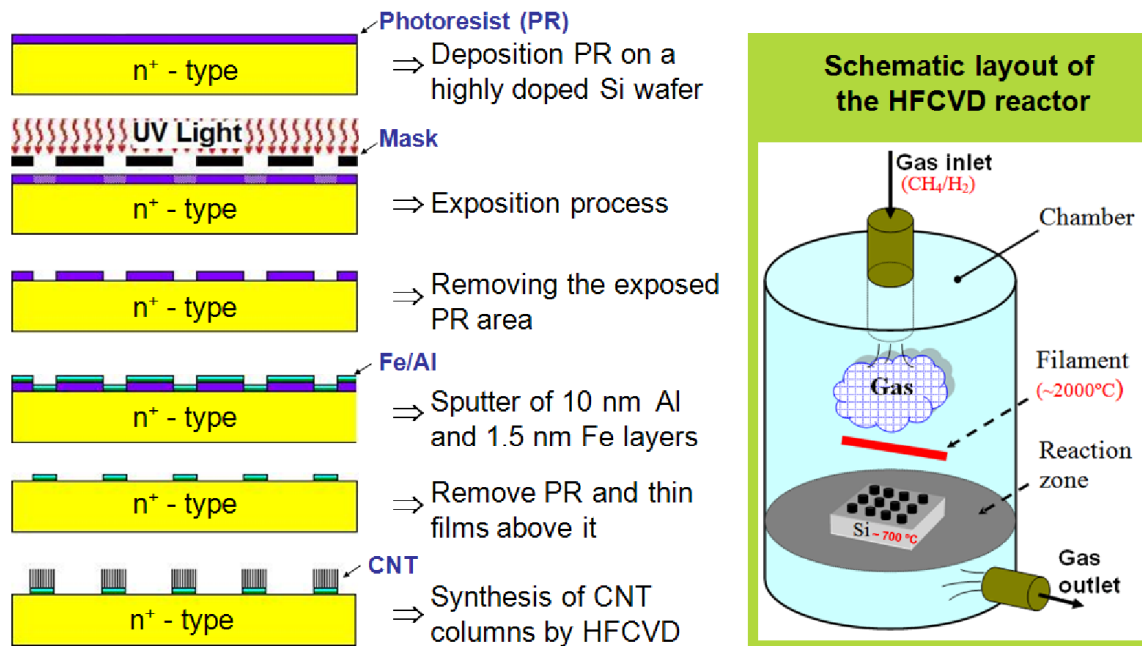


Fig. 5.20. Schematic of the cathode fabrication steps and a HFCVD reactor (not to scale).

Large quadratic arrays of vertically aligned CNT columns of diameter $\varnothing = 250 \mu\text{m}$, height $h = 70$ or $350 \mu\text{m}$ and $650 \mu\text{m}$ pitch, and single columns of $\varnothing 1.5 \text{ mm}$ and $h = 250 \mu\text{m}$ were obtained as shown in fig. 5.21. However, such closely packed arrangement of CNTs in the column is not optimal for the field electron emission (see chapter 2.2) as the closely packed CNTs shield the applied electric field [Nils00, Bona01, Grön00]. Thus, the FE current will be provided by single CNTs located at the edges and/or at the top of the CNT columns.

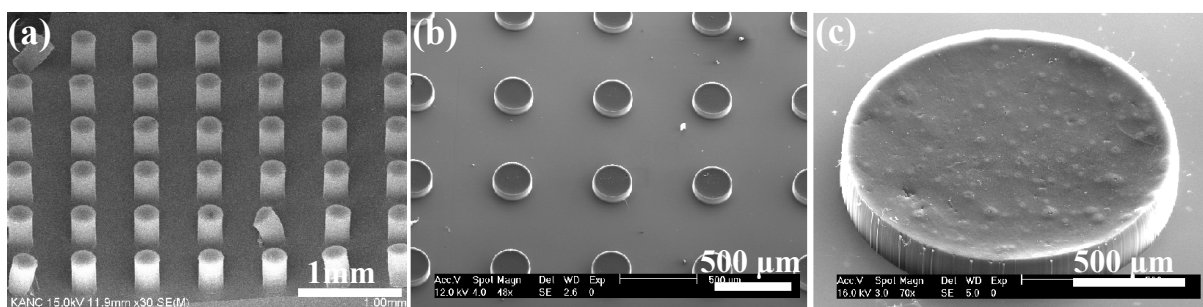


Fig. 5.21. SEM images of vertically aligned CNT-column arrays grown by HFCVD on patterned catalyst: columns of diameter $\varnothing = 250 \mu\text{m}$ and different height $h = 350 \mu\text{m}$ (a) and $70 \mu\text{m}$ (b) in quadratic arrays of $650 \mu\text{m}$ pitch, and single column of $\varnothing = 1.5 \text{ mm}$ and $h = 250 \mu\text{m}$ (c).

The FE properties of such cathodes were measured with a field emission scanning microscope at a vacuum of 10^{-9} mbar using tungsten anodes of truncated cone shape of adjustable diameter \varnothing_a [Lyse05]. Fairly aligned FE was obtained from nearly all short columns at $E_{\text{on}}(1\text{nA}) \approx 2\text{-}6 \text{ V}/\mu\text{m}$ as shown in Fig. 5.22a. Comparable maps at about the same $E_{\text{on}}(1\text{nA})$ values resulted for the 5 times higher columns (Fig.5.22b).

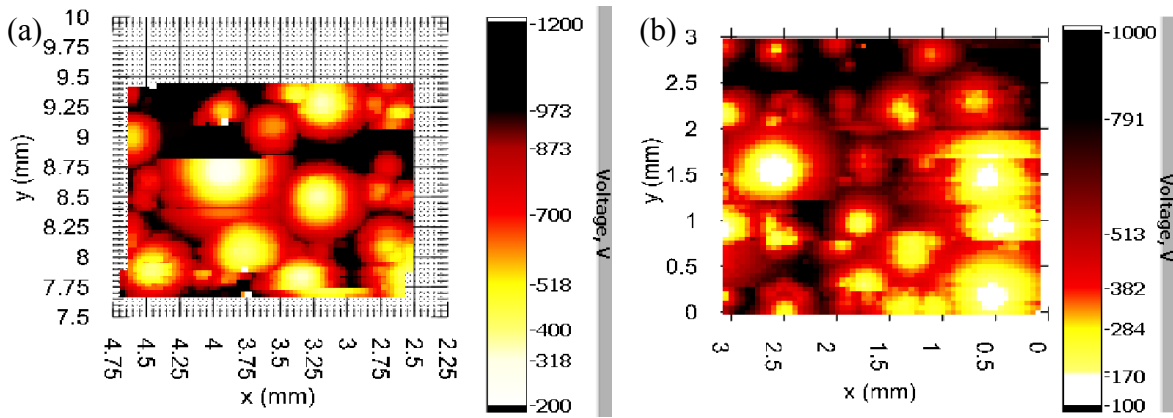


Fig. 5.22. Voltage maps (at $I=1nA$, $\varnothing_a = 100 \mu m$, $\Delta z = 50 \mu m$) of CNT arrays with $70 \mu m$ (a) and $350 \mu m$ (b) height.

By means of an in-situ optical imaging system, the alignment of individual CNTs under an applied electric field was observed (Fig.5.23). The influence of the applied electric field on CNT protruding from a surface was investigated in detail by Wei et. al. [Wei01]. As mentioned above (see chapter 2.2), in that case, the maximum electric field is concentrated on the top of the longest CNT emitters and hence the FE current is only provided by these CNTs. Moreover, during the scanning at a fixed FE current, the protruding CNTs from the column surface dragged by the anode due to the ponderomotor forces that lead to a limited FE homogeneity and alignment of the CNT columns. Moreover, if the length of the protruding CNTs is high enough to touch the anode, a short circuit will happen, that sometimes caused the partial or complete destruction of the CNT columns.

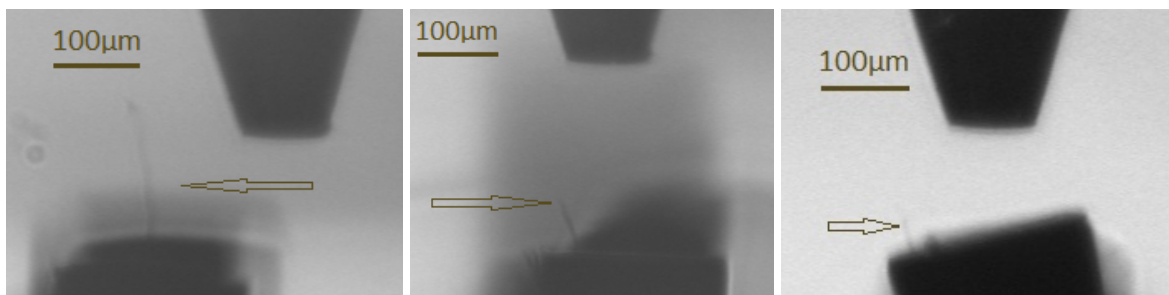


Fig.5.23. Optical images of the CNT-columns during the voltage scans ($I=1nA$, $\varnothing_a = 100 \mu m$). Alignment of CNTs under electric field was observed.

In order to investigate the current carrying capability of the CNT columns, local current-voltage (I-V) measurements were performed with anodes of adjusted size. The local field was always calibrated by means of $U(z)$ plots [Lyse05]. In Fig. 5.24 typical results for columns of different height are compared. Obviously, both I-V curves and Fowler-Nordheim plots nearly coincide in the high field region, thus revealing similar effective field enhancement β . Assuming a work function of 4.9 eV, the resulting β values extracted from

FN plots are 1112 (831) for the CNT-columns of 70 (350) μm height (Fig.5.24.a). Moreover, the rather high I_{max} values of about 600 μA at 15 $\text{V}/\mu\text{m}$ did not depend on the column height (Fig. 5.24b). The excellent results for I_{max} suggest the existence of multiple CNT emitters per column, i.e. about 30-60 if the measured current limit of 10-20 μA for multiwall CNT is assumed. Nevertheless the mutual shielding effect will enforce a tradeoff between low operation fields and high current limits of optimized CNT columns.

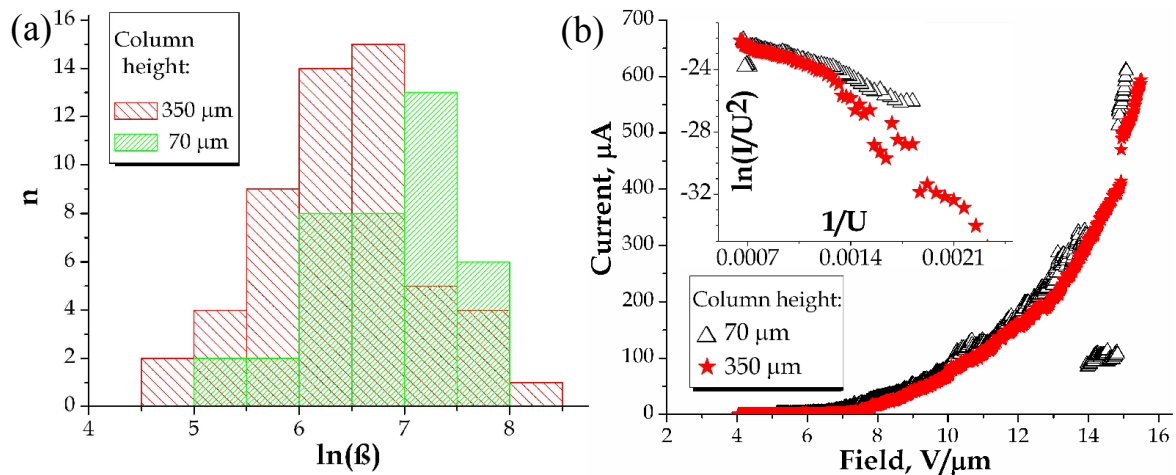


Fig. 5.24. Histograms of average field enhancement factor $\beta = 1112$ (831) for CNT columns with $h = 350$ (70) μm for a work function of 4.9 eV (a). Typical current-field curves and corresponding FN plots (inset) of two CNT columns of different height (b).

At high electric fields stepwise current jumps occurred which often accompanied by visible light spots at the top of the processed columns. The glow could be even seen through the color filters (red, yellow, green and violet) indicating thermal emission due to Joule heating along the CNTs above at least 1000°C [Purc02, Vinc02, Raga09, Dean01]. Comparable glow effects were also observed elsewhere [Navi12]. The heating limited the maximum current value and might cause the destruction of the CNT-column. [Dean01]. Typical results are shown in figure 5.25. The microscopic inspection revealed a partial destruction of the corresponding columns at about 205 μA . It can be seen that partial destruction led to splitting of the column at the edge and pollution of the substrate by CNT bundles. Debris of destructed CNT-column were found in some hundreds of μm away indicating μ -plasma discharge.

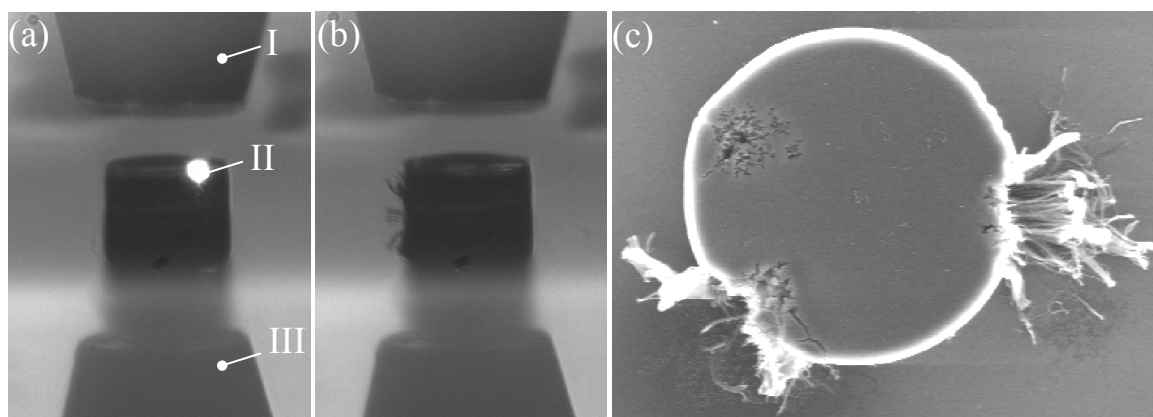


Fig. 5.25. Local measurements have shown a reproducible thermal glow effect (a), which precedes the partial destruction of the CNT-column (b, c). II – hot spot at the edge of the CNT column ($\varnothing = 250 \mu\text{m}$) at current of $205 \mu\text{A}$; I, III – an anode and its mirror image.

As a next step towards application of CNT columns in vacuum electronic devices, is the investigation of the single CNT column cathodes in an integral measurement system with the luminescent screen anode at a vacuum of 10^{-7} mbar [Lyse05]. A triode configuration with low gate and high anode voltages is mostly preferred for fast control of electron currents. Moreover, the proximity of the gate to the CNTs enhances the current extraction efficiency and protects the cathode from secondary effects. Therefore, in order to design suitable triode configuration, COMSOL Multiphysics® software was used to calculate the electron trajectories. The simulation results showed that the highest transmission efficiency (anode/cathode current ratio) can be achieved by using a planar gate with round cone-shaped hole at a certain cathode-gate and gate-anode distances [Rutk12, Serb11]. Based on the simulation results, a triode construction (planar copper gate with a conical hole of 2.5/3.5 mm in diameter, thickness $500 \mu\text{m}$) for a single CNT column (see fig. 5.21c) at a fixed anode-gate distance of 6.5 mm was realized [Rutk12, Serb11].

The cathode-gate distance was in situ varied by a stepping motor from 500-800 μm at anode voltage of 2500 V. In Fig. 5.26 the typical results for a single column are shown. As it can be seen, the transmission efficiency increased strongly up to 80 % at 500 μm . Further gate approach, however, often resulted in the destruction of CNT column, probably, due to strong field enhancement at the column edge. In addition, there was a sufficient rise of the gate current that limited the efficiency of the configuration in question. However, the measurements of similar single CNT column at the same cathode-gate gap and anode voltage showed the transmission efficiency of ~97%. Such differences can be explained by the fact that the fabricated procedures are hardly reproducible. By decreasing of the anode voltage from 2.5 kV to 1 kV the transmission efficiency dropped to 40% (Fig.5.27).

In all cases, the emission homogeneity was observed on the luminescent screen. The image, shown in Fig. 5.27 provides nearly uniform emission over the cathode with slightly enhanced edge current. The achievable current levels ($< 40 \mu\text{A}$) in dc mode were limited by the power load (100 mW) on the luminescent screen.

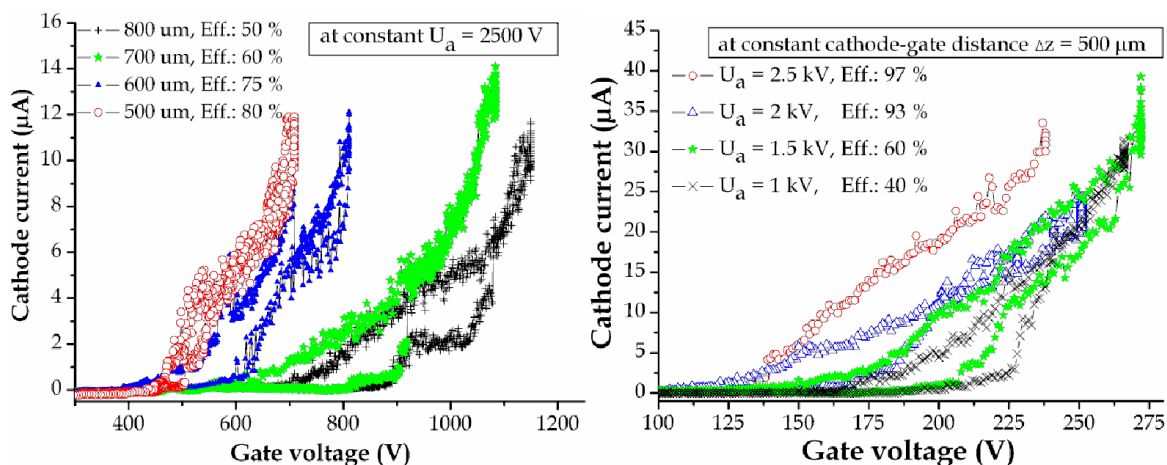


Fig. 5.26. Cathode current vs. gate voltage at a constant anode voltage (U_a) of a single CNT column at four different cathode-gate distances (left). The mean efficiency values were determined from the measured anode current. Cathode current vs. gate voltage for a fixed gap $500 \mu\text{m}$ at different anode voltages U_a (right). The anode-gate distance is 6.5 mm .

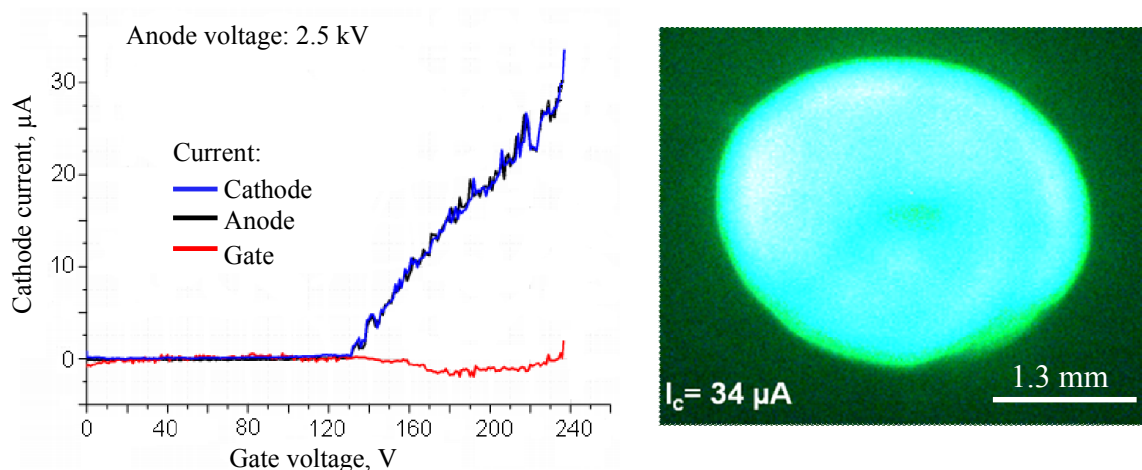


Fig. 5.27. Cathode-current vs. gate voltage (left) and corresponding emission image (right) at $\Delta z = 500 \mu\text{m}$ shows good emission uniformity over the cathode with slightly enhanced edge current. The achievable cathode current value ($I_c = 34 \mu\text{A}$) was limited by the power load on the luminescent screen.

In conclusion, both the FESM and IMLS results of CNT columns on Si substrates presented here prove their suitability especially for high current FE applications. For the column arrays, however, matched gates have to be developed which might result in up-scaled current densities above 1 A/cm^2 .

5.5. Laser-structured CNWs on Si and stainless steel substrates

For the last 20 years many carbon-based nanostructures were considered as one of the best cathode materials for vacuum nanoelectronic devices [Sait10]. Besides the various types of carbon nanotubes, nanographite crystallites or carbon nanowalls (CNWs) have shown to possess comparably low onset fields and homogeneous emitter distribution with large number densities [Obra03, Band13]. For instance, the high emission site density in the range of 10^7 - 10^8 cm⁻² at 5 V/ μ m was achieved by Obraztsov et al. [Obra00]. Microscopic field emission investigations suggested that a high electric field enhancement occurs at the conducting graphene layers between diamond crystallites [Kara01]. Despite their random growth, these vertically-oriented two-dimensional carbon nanostructures with high aspect ratio and sufficient electric conductivity might be useful for FE devices in diode configuration (e.g. for an energy-efficient cathodoluminescent light sources [Obra13]). For such devices, cold cathodes with high number of emission sites are required.

Here an approach on how to reduce the shielding of densely grown CNWs by laser-structuring is reported. The FE properties of such laser-modified cathodes were investigated.

CNW-based samples were fabricated and laser-structured in the group of Prof. Dr. V. Buck at the faculty of Physics and Chemistry at the university of Duisburg-Essen and CeNIDE, Germany.

Carbon nanowall films were grown on silicon and stainless steel substrates using inductively/capacitively coupled plasma-enhanced chemical vapor deposition (ICP/CCP-PECVD) (Fig. 5.27). Aluminum acetylacetonate ($\text{Al}(\text{acac})_3$) was used as metalorganic precursor in the presence of argon without additional catalyst. The plasma was generated in a gaseous electronics conference radio-frequency reference cell reactor evacuated by a turbomolecular pump using a modified ICP antenna allowing high plasma densities even at low particle energies [Kade04]. The precursor was sublimated in a fluidized bed evaporator held at a constant temperature of 150°C and then transported to the reaction chamber using Ar as the carrier gas. The pressure was kept constant at 10^{-2} mbar. The following CVD process parameters were varied: Ar flow rate 28-55 sccm, plasma power 500 or 800 W and the substrate temperature from 200°C up to 665°C using a special substrate heater.

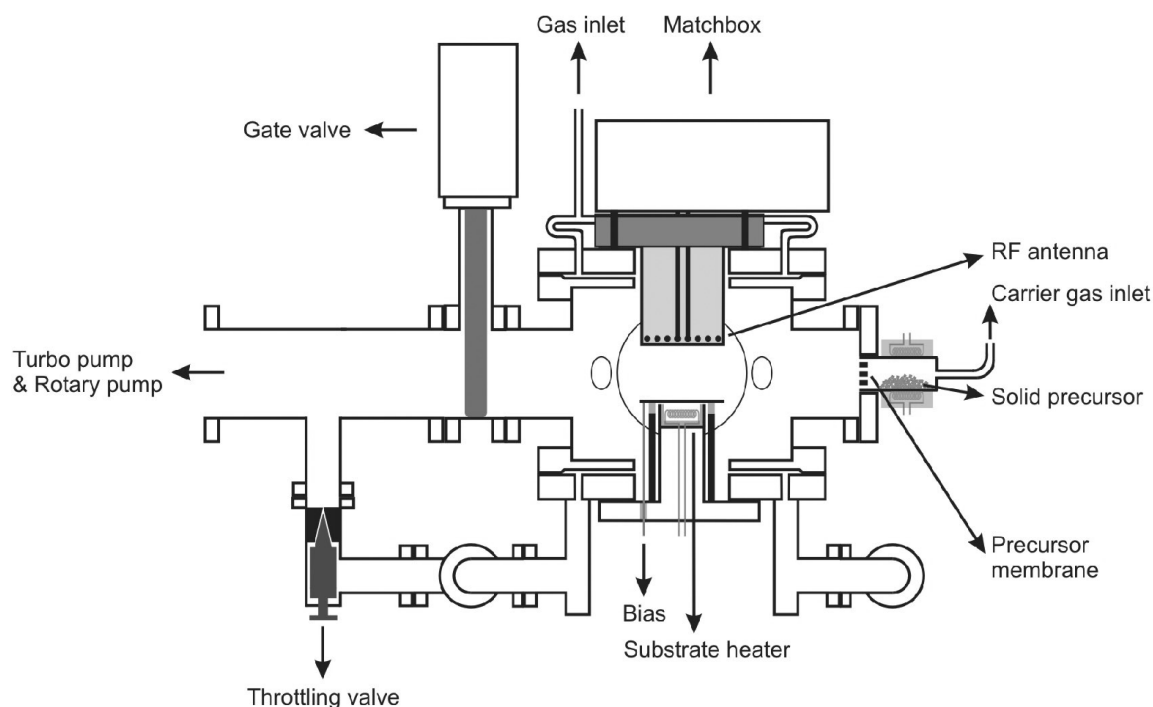


Fig. 5.27. Schematic diagram of the ICP/CCP-PECVD apparatus [Jain11, Neub11].

CNWs with a thickness of a few nm and adjustable number densities between 35 and $300 \mu\text{m}^{-2}$ were obtained on Si and stainless steel substrates, respectively (Fig. 5.28). Al is embedded in the carbon matrix in form of Al_4C_3 crystals of about 30 nm size. The percentage of Al can be adjusted from nearly zero to about 10 at. %. The correlation of deposition parameters like Ar gas flow and substrate temperature with growth features and structure of the CNWs were systematically studied. Detailed results based on SEM, TEM, SIMS, XPS, NRA-technique and Raman spectroscopy are reported elsewhere [Jain11, Jain12, Neub11].

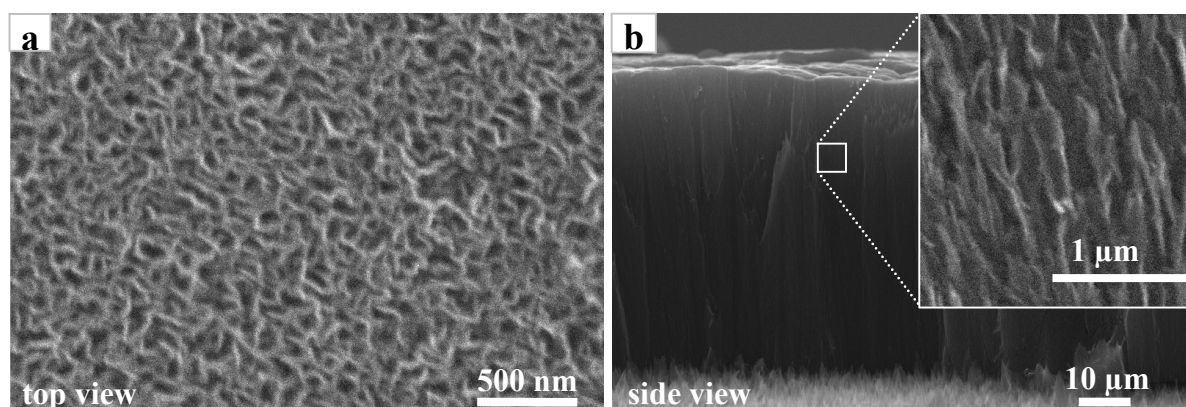


Fig. 5.28. (a) top-view and (b) side-view SEM images of CNW film on stainless steel substrate fabricated by ICP/CCP-PECVD. The inset image is taken at higher magnification.

Afterwards, the CNW-coated Si and stainless steel samples were patterned with a diode-pumped solid-state laser (EdgeWave) using a galvano scanner (SCANLAB) and a theta objective (LINOS) for writing and focusing. The laser was operated at a wavelength of

532 nm, a pulse length of 10 ns and a pulse frequency of 50 kHz. During patterning the focused laser spot with a $1/e^2$ diameter of about 30 μm was moved across the sample surface at a writing speed of 30 cm/s. The average laser power was set to 1.15 W (Si) and 2.08 W (stainless steel), respectively. Quadratic grid patterns with a pitch of $\sim 35\text{--}40\ \mu\text{m}$ were fabricated over an area of $5\times 5\ \text{mm}^2$ (Fig. 5.29). Resulting CNW-patches with a nominal size of $\sim 20\times 20\ \mu\text{m}^2$ show some variation of the effective shape. As can be seen from the HRSEM micrograph, the morphology of the CNWs was also changed (see also Fig. 5.28). Spherical CNW clusters of arbitrary shape and different sizes (larger on steel substrate, probably, due to the higher laser power) can be observed. The height of CNW patches after the laser structuring, however, was considerably reduced from 60 μm to $\sim 20\ \mu\text{m}$ (to a few μm) on Si (steel) substrates, indicating that the laser power was so high, that initiated the evaporation or burning of carbon material and heating of the substrates up to their melting points (Fig. 5.30).

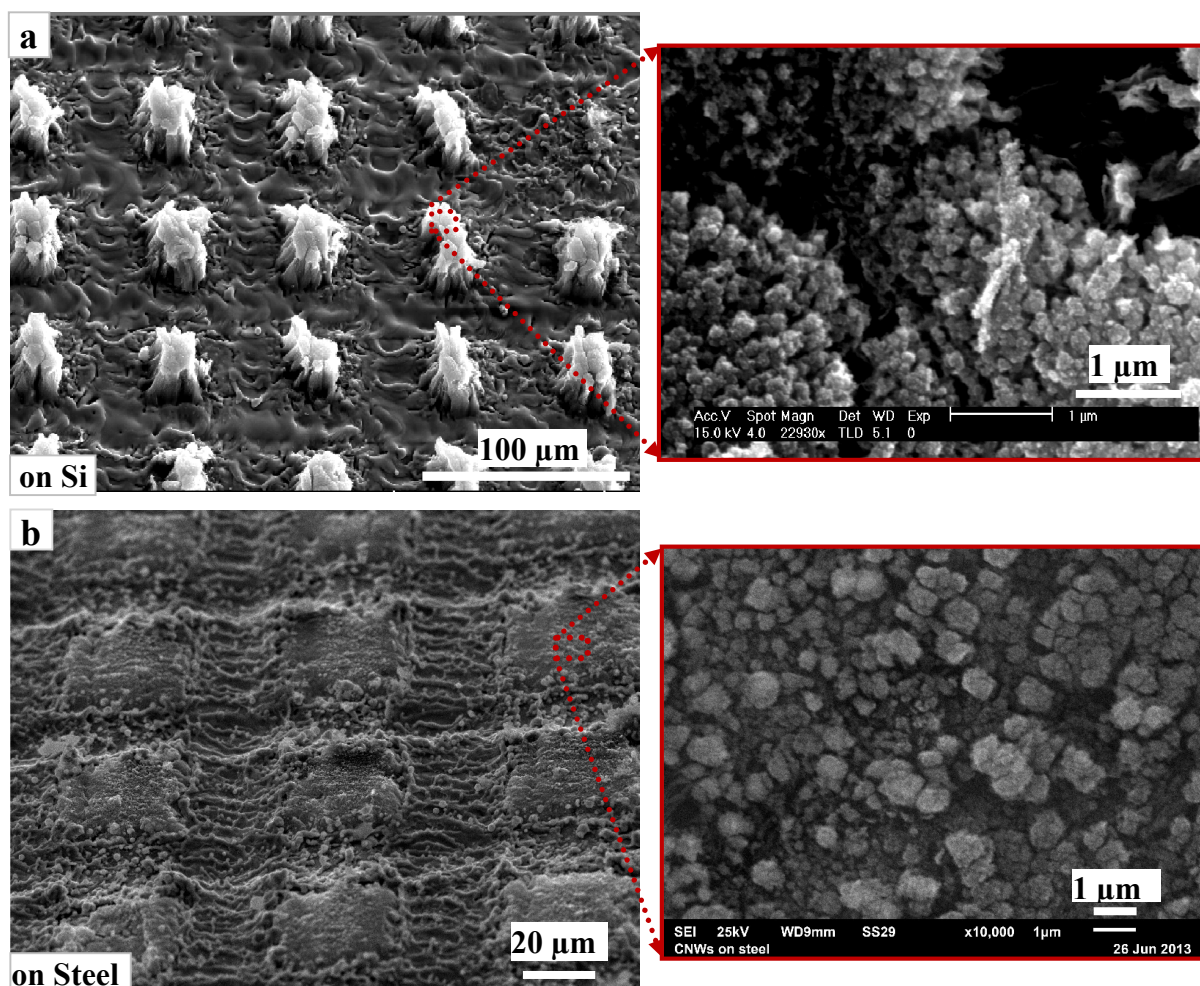


Fig. 5.29. SEM images (30° tilt angle) of CNWs on Si (a) and on stainless steel (b) after the laser-structuring; laser power was set to 1.15 W (Si) and 2.08 W.

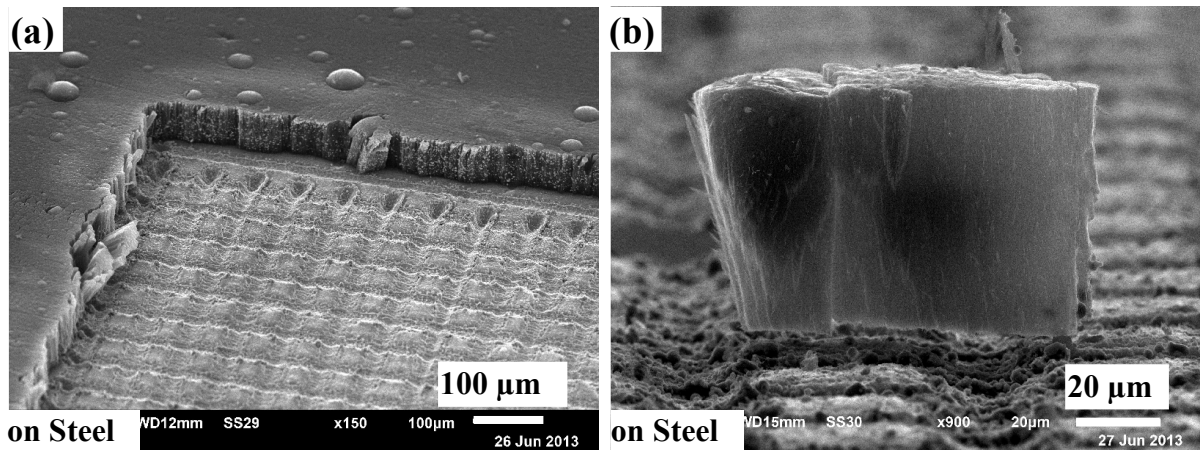


Fig. 5.30 SEM images show that the height of CNW film on stainless steel substrate was considerably reduced after the laser-structuring. Laser power was set to 2.08 W.

The FE properties of the laser-structured CNW cathodes were measured with the FESM at a vacuum of 10^{-9} mbar using a tungsten anode of truncated cone shape with adjusted diameter ($\varnothing_a = 30 \mu\text{m}$) [Lyse05]. As shown in Fig. 5.31, fairly-aligned FE was obtained from nearly all CNW patches at $E_{\text{on}} (1\text{nA}) = 10\text{-}20 \text{ V}/\mu\text{m}$ on both substrates. The homogeneity of the FE, however, appears rather limited due to the varying shape of the individual CNW patches (Fig. 5.29). One interesting value is the emitter number density N_e . The number of emitting sites N_e of about 9×10^3 emitters/ cm^2 and 20×10^3 emitters/ cm^2 at $10\text{-}20 \text{ V}/\mu\text{m}$ has been obtained for CNWs on Si and steel, respectively. However, the resolution of the FESM is limited by the anode size and Δz value.

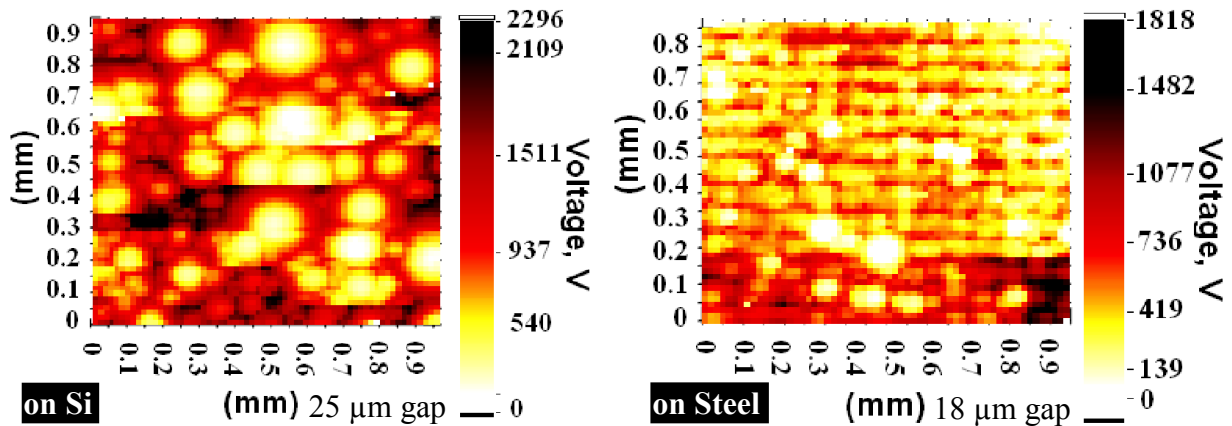


Fig. 5.31. V-maps (for 1 nA FE current, $\varnothing_{\text{anode}} = 30 \mu\text{m}$, $\Delta z = 25$ (18) μm on Si (steel)) show that nearly all CNW-patches of both cathodes emit fairly aligned at a field of $10\text{-}20 \text{ V}/\mu\text{m}$, however, the homogeneity is limited due to the varying shape of the CNW-patches.

In order to investigate the FE mechanism and achievable current limit of the CNWs, local current-voltage measurements were performed on selected patches with the same anode. The local field was always calibrated by means of $U(z)$ plots [Lyse05]. Typical current-field curve of single CNW patches shows usual Fowler-Nordheim-like behavior with stable FE current up to $60 \mu\text{A}$ at $43 \text{ V}/\mu\text{m}$ and $57 \mu\text{A}$ at $89 \mu\text{m}$ for Si and stainless steel substrates,

respectively (Fig. 5.32). The processing effects are correlated with partial destruction of the CNW patch.

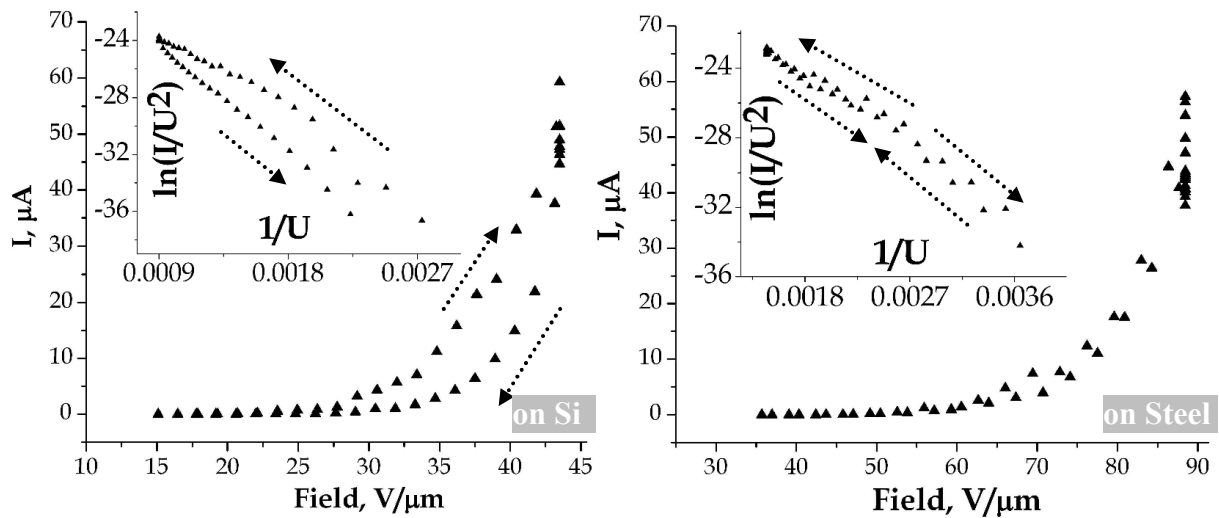


Fig. 5.32. Typical current-field curves of single CNW patches and corresponding FN-behavior for Si (left) and steel (right) substrates. $\varnothing_a = 30 \mu\text{m}$, $\Delta z = 25$ (18) μm on Si (steel).

Hyperbolic correlations between E_{on} (1nA) and the field enhancement factor β (assuming the work function of the CNTs to be 4.9 eV) are found for both types of cathodes (Fig. 5.33). The measured E_{on} (1nA) values for CNWs on stainless steel were on average somewhat higher and less correlated to the β values. Average β value of about 164 (180) was achieved for the CNWs cathode on Si (stainless steel) substrate.

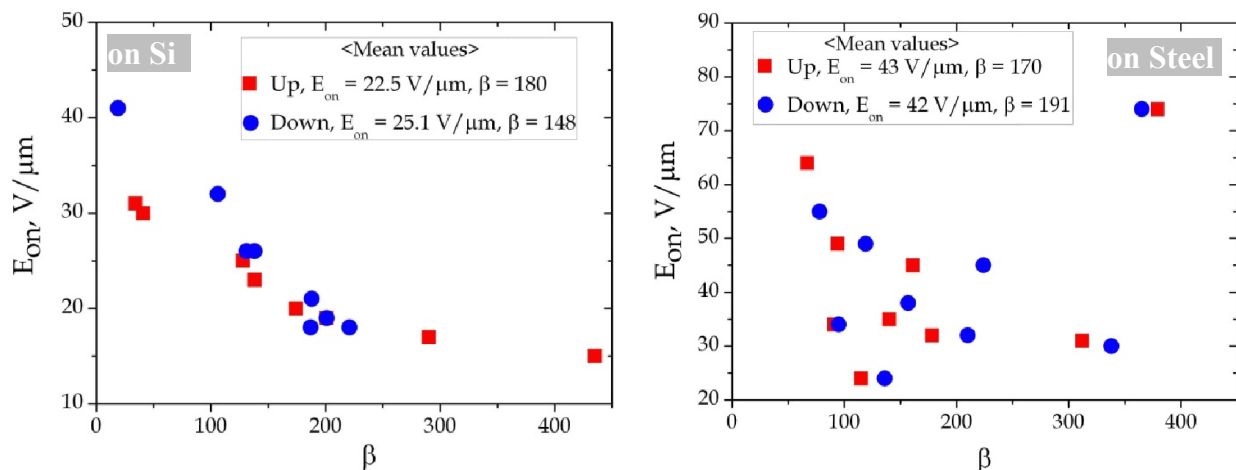


Fig. 5.33. Electric onset field (for 1nA) vs. field enhancement factor obtained from up and down cycle measurements of CNW patches on Si (left) and stainless steel (right).

A large dispersion was also found for the maximum current values I_{max} (~ 1 -100 μA) of the CNW patches on both substrate materials (Fig. 5.34). SEM analysis after the current processing showed strong modification of CNW patches on both substrates by the FE current (Fig. 5.34).

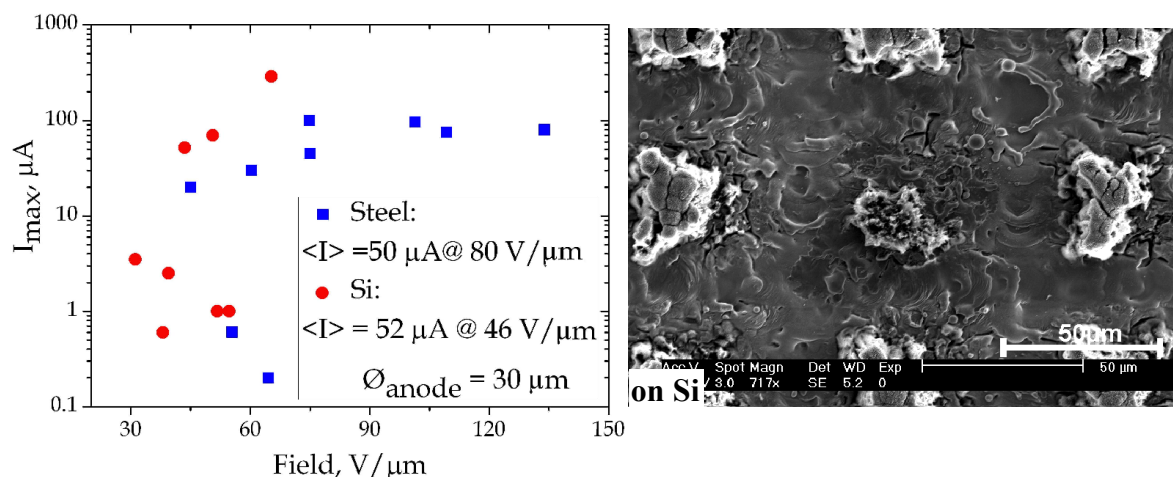


Fig. 5.34. Maximum achieved current I_{max} versus corresponding operation field for single CNW-patches on both types of substrates (left). SEM image of the single CNW-patch on Si after the current processing, which provided a current of about 50-70 μA .

In conclusion, the laser-structuring of extremely dense CNW-based cathodes have been successfully performed on both Si and stainless steel substrates. The FE results of first samples were encouraging, but further optimization of the laser power and the writing speed is required to exploit their full potential for device applications. FE measurements of different types of the laser-structured CNW cathodes are ongoing and the results will be presented in the near future.

5.6. Conclusions and outlook

For the first time, high-purity single-walled CNT networks were grown on Si substrates by chemical vapour deposition under rather low temperature. FESM and IMLS investigations revealed well-distributed FE with high number of emission sites and high FE current at low applied voltages.

The contact interface between CNT bundles and the substrate has been significantly improved by using trimetallic Mo/Al/Ni catalyst layer. In addition, the optimization of the pitch size of CNT bundles led to the rise of current densities up to $4.4 \text{ A}/\text{cm}^2$ at rather low voltages/fields. However, the FE homogeneity and current stability remain to be improved.

FE properties of CNT columns of different heights were studied. The experiments revealed that the field enhancement factor depends not only on the height of the CNT columns, but also on the CNTs outgrowth. It was shown that the protruding CNTs from the column surface limit the FE homogeneity and alignment of the CNT columns.

Guided by the simulation results we have designed the most suitable triode configuration which provided high transmission efficiency. The advantages of the developed configuration can be used for different devices of vacuum electronics.

The emission properties of CNW cathodes fabricated by ICP/CCP-PECVD were studied by FESM. It was shown that the laser-treatment can sufficiently improve the FE characteristics of this material.

To sum, application-oriented study of various carbon-based cathodes were performed. It was shown that such materials can produce high current densities at low fields and most of them demonstrate well-aligned FE characteristics with uniform distribution of emission sites. Possible applications were proposed.

6. Metallic emitters grown in polymer ion-track membranes

Noble metal nanowires (NWs) with high aspect ratio, good mechanical stability and conductivity fabricated by electrochemical deposition into etched ion-track membranes [Kohl97, Toim12, Vila04] are considered as interesting field emitters with controllable size and shape [Liu06]. Promising FE results were already reported on unstructured cathodes with randomly distributed copper [Maur06], gold-coated nickel [Dang07] and gold NWs [Dang08]. Patch arrays of multiple Au-NWs obtained by using a shadow mask during heavy-ion irradiation of the template [Kari07] yielded high efficiency, good alignment and FE homogeneity at a suitable onset field [Navi09, Navi10]. The FE current limit of such patches, however, varied strongly due to random destruction of individual NWs caused by their insufficient substrate contact both for poly-crystalline [Dang08, Kari07, Navi09, Navi10d, Navi10c] and single-crystalline Au-NWs [Navi10c]. In order to improve the contact and achieve higher and more stable FE currents, the emitter shape from cylindrical to conical geometry was modified by changing the ion-track etching process from two-side to one-side etching of the ion-irradiated polymer foil. Thus, arrays of conical structures with a significantly enlarged base contact but still nanometer-sized tips are obtained [Alber11, Dobr01, Duan08]. Copper was chosen for deposition because of its fairly good conductivity and mechanical properties [Toim01]. Gold or silver, for instance, might be better, but the electrodeposition process of these metals is more complicated.

In this chapter the synthesis procedure and FE properties of unstructured and patch-structured cathodes with randomly distributed and vertically aligned bare and gold-coated copper nanocones (Cu-NCs) will be described. Based on the results of scanning electron microscope (SEM) and field emission scanning microscope (FESM) [Lyse05] investigations, the improved mechanical stability and FE properties of the bare and the gold-coated nanocones as compared to those of cylindrical nanowires will be shown and the further optimization potential will be discussed.

The irradiation of polycarbonate foils with heavy ions was made in the group of Prof. Dr. Christina Trautmann at the GSI Helmholtz Centre for Heavy Ion Research (GSI) located in Darmstadt, Germany, while the electrochemical deposition process was performed at GSI by Dr. I. Alber and partially at the Bergische University of Wuppertal by F. Jordan [Jord12b].

6.1. Fabrication of copper nanocones

At first, by means of the linear accelerator (UNILAC) at GSI, Darmstadt, stacks of several 30 μm thick polycarbonate (PC) membranes (Makrofoil KG) were irradiated with heavy ^{136}Xe or ^{238}U ions at energy about 11.4 MeV/nucleon and ion fluence $10^6 - 10^7 \text{ cm}^{-2}$ (Fig.6.1a). Patch-structuring is usually obtained during irradiation through a shadow mask (Invar, 150 μm thick with a triangular array of round holes of 150 μm diameter and 320 μm pitch). The produced ion tracks are randomly distributed but highly parallel oriented and represent nanometer-sized damage cylinders throughout the entire PC foil which are preferentially dissolved in a suitable chemical etchant [Toim12, Afra13].

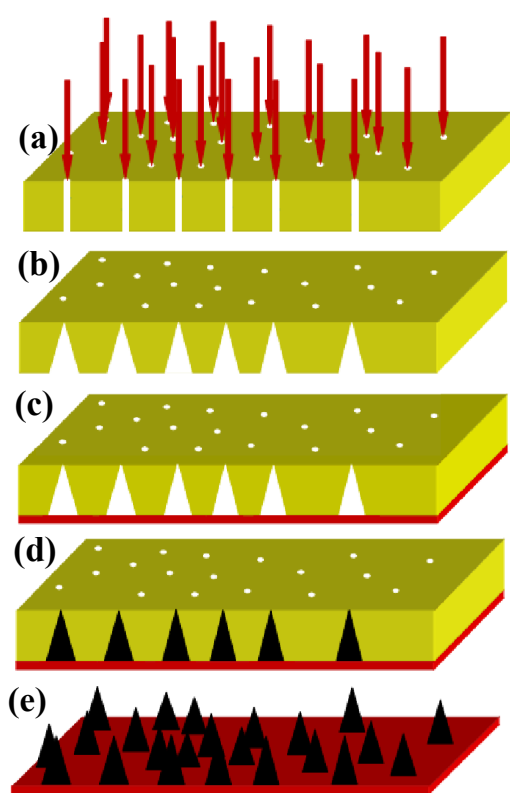


Fig. 6.1. Fabrication steps of Cu-NC cathode:

(a) – irradiation of polycarbonate membrane of 30 μm thick with heavy ions;

(b) – chemical etching of PC membrane in a solution of 9 M sodium hydroxide and methanol in 40:60 volume ratio;

(c) – magnetron sputtering of a 50 nm gold film acting as a cathode during further electrochemical reinforcing with a 20 μm Cu layer;

(d) - electrochemical deposition of Cu into the pore of PC using an electrolyte containing copper sulphate (0.95M CuSO_4) and sulphuric acid (0.5M H_2SO_4);

(e) – dissolution of PC membrane in dichloromethane solution resulting in free-standing Cu-NCs.

Conical pore shape requires asymmetric etching conditions, i.e., etching of the ion-template from one side only. Accordingly, the irradiated PC foils were inserted in an electrolytic cell with two compartments. One side was filled with an etchant solution consisting of 9M sodium hydroxide (NaOH) and methanol in 60:40 or 40:60 volume ratios. The high methanol concentration increases the etching rate of undamaged bulk PC, thus leading to structures with enlarged apex angle [Duan08]. The other compartment was filled with distilled water that slows down the etching at the instant of pore breakthrough and thus also further pore growth.

The etching process was performed at 30°C and was monitored by inserting Au electrodes in each of the two compartments, applying a voltage of 1V and measuring the

electrical current across the membrane [Apel01a]. A rapid current rise occurs when the first pore becomes opened and finally $I(t)$ curves show a kink and slope changes when all pores are opened [Albe11]. The shape of the resulting $I(t)$ curves reproducibly depends on the stack position (Fig. 6.2left) [Jord12a,b]. Due to the increasing energy loss of the ions [Fink04], less damaged material has to be removed for the first than the third foil. At the occurrence of the first hole, the conductivity of the etchant and thus the current is much higher for the first foil, and often a peak results when all pores are opened due to the later increase of resistance. In contrast, the current for the third foil is always much lower because the etchant has dissolved more PC ($\sim 2 \mu\text{m}/15 \text{ min}$).

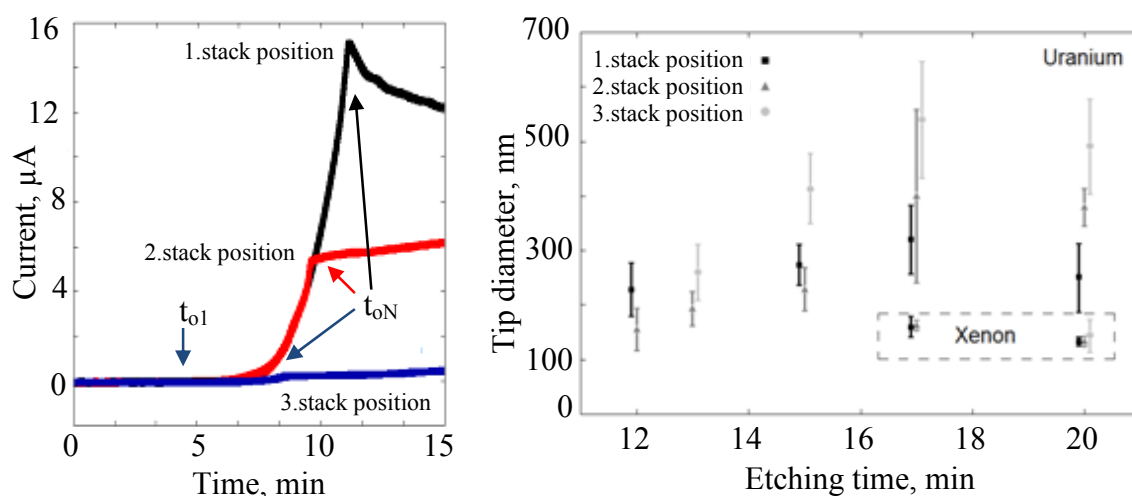


Fig.6.2. Left: typical current vs. time curves during the conical pore etching of irradiated PC foils. Same time of first pore opening t_{o1} , but last pore t_{oN} depends on stack position due to the increasing energy loss for deeper penetration of PC. Slope change and different I level due to etchant consumption and ion diffusion. Right: average Cu-NC tip diameter as function of the etching time for different stack positions. The dashed rectangle marks the data for ^{136}Xe ion tracks.

The size of the conical pores in the membranes and hence of the Cu-NCs mainly depends on the etching time but also on the stack position and ion type as shown in Fig. 6.2right [Jord12a, Jord12b, Serb12a, Serb12b]. A systematic increase of the mean tip diameter with etching time is obvious up to 17 min, and the aging of the etchant is considered to be responsible for the rather low values for the 20 min etching which was performed one day later. Due to the different total energy loss, the complete pore opening required a longer etching time for ^{136}Xe ($\sim 20 \text{ min}$) than for ^{238}U ion tracks ($\sim 15 \text{ min}$). It is most remarkable that the sharpest Cu-NCs were grown in the ^{136}Xe ion tracks.

As next step, 20-50 nm Au film was deposited on the PC membrane side with large pore openings by means of a magnetron sputter coater (SC 7620). Accordingly, some gold atoms are deposited onto the side wall of the pores forming ring-like base structures ($2.4 \mu\text{m}$

diameter) for the latter nanocones growth. The Au layer serves as an electrode for the following electrochemical deposition of copper which was performed at room temperature for ~ 30 min and a potential difference of -0.5 V to the copper anode. This results in a back-layer of ~ 20 μm thickness covering all pores completely. The cones were then electrochemically grown in a two-electrode arrangement through the small pore openings at 50°C using an electrolyte containing copper sulphate and sulphuric acid (Fig. 6.1d).

Two different deposition voltages were tested for unstructured membranes that were etched with the 60% methanol content solution. Fast growth at -90 mV started preferentially at the ring-like base structures and led to a rough cone surface, significant scattering of the tip radius (> 120 nm) (Fig. 6.3a) and a tube-like Cu-NC contact region to the back-layer (Fig. 6.3b). In contrast, slow growth at -40 mV resulted in less surface roughness (Fig. 6.3c) and reduced scattering of the tip radius (> 190 nm). No broken cones were observed revealing excellent mechanical stability and improved substrate contact. For comparison, sharper Cu-NCs grown in membranes etched with 40% methanol content solution were less mechanically stable and sometimes broken despite a better solid contact interface completely filled with Cu (Fig. 6.3d).

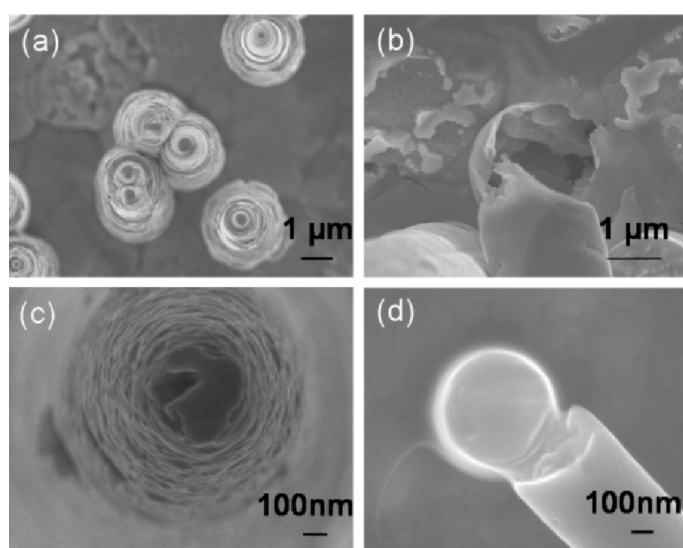


Fig. 6.3. SEM images (top view) of the Cu-NCs grown at 50°C . The deposition voltage of -90 mV leads to (a) rough cone surfaces, scattering of the tip radius and (b) a tube-like contact region; while -40 mV results in (c) cones with smoother surfaces, more uniform tip and (d) a completely filled base.

After dissolution of the PC template in dichloromethane (CH_2Cl_2) for 8 hours free-standing, randomly distributed and vertically aligned Cu-NC of ~ 28 μm height were obtained as shown in Fig. 6.4. For the unstructured samples, their number density corresponds to the applied fluence (Fig. 6.4a, average distance ~ 3 μm). For the structured samples, however, the number density is smaller than the applied fluence (10^6 ions/ cm^2) since inhomogeneous filling of the channels resulted in some incompletely grown Cu-NCs (Fig. 6.4b). Finally, all Cu-NC samples of $\sim 5 \times 5$ mm^2 were glued on flat aluminum holders of about 8 mm in diameter by

means of silver glue. The main parameters of the fabricated cathodes are summarized in Table 6.1.

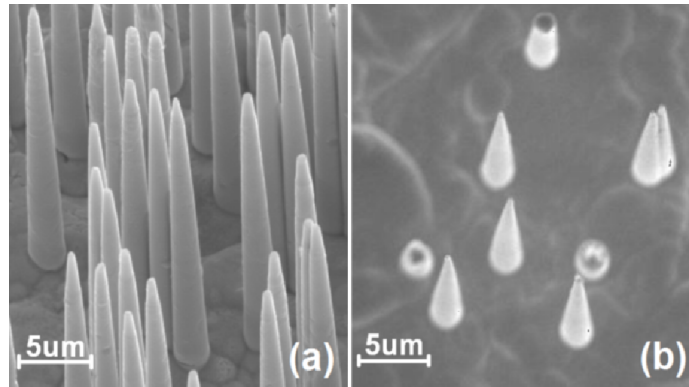


Fig. 6.4. SEM images at different viewing angle of freestanding and randomly distributed Cu-NCs with different number density and tip radius: (a) 10^7 cm^{-2} , $>190 \text{ nm}$ (cathode A), (b) $< 10^6 \text{ cm}^{-2}$, $>95 \text{ nm}$ (cathode C).

Table. 6.1. Parameters of the fabricated cathodes.

#	Etching (min)	Voltage (mV)	Number density	Tip radius (nm)	Aspect ratio
A	15	40	10^7 cm^{-2} unstructured	> 190	< 147
B	15	90		> 120	< 233
C	13	40	$< 10^6 \text{ cm}^{-2}$ structured	> 95	< 295
D	15	40		> 220	< 127

6.2. Role of the contact interface and number densities of nanocones

The FE properties of the Cu-NC cathodes (see the table 6.1) were measured with the FESM under ultrahigh vacuum conditions ($\sim 10^{-9}$ mbar) using a freshly prepared tungsten anode of a truncated cone shape of diameter $\varnothing_a = 30 \text{ }\mu\text{m}$. After the tilt correction of the cathode, the gap Δz between anode and Cu-NCs during the voltage scan was controlled with a long-distance microscope (Questar QM 100, $1 \text{ }\mu\text{m}$ resolution) and the actual electric field for the voltage maps was calculated as ratio of the applied voltage U to Δz . While the actual electric field E during the local measurement was estimated by means of $U(z)$ plot [Lyse05].

In order to investigate the emitter distribution and homogeneity, regulated voltage maps $U(x,y)$ at a constant FE current ($I = 1 \text{ nA}$) were measured over selected flat parts of the cathodes of 1 mm^2 size. In figure 6.5a, the fairly distributed FE of the best unstructured cathode A with ~ 100 emitting spots at onset field $E_{\text{on}}(1\text{nA}) = 25\text{-}80 \text{ V}/\mu\text{m}$ is shown. The varying strength of these emitters is mainly caused by the random position and arbitrary mutual shielding of the rather closely packed Cu-NCs, what is resulting in a low emitter number density N_e of about 10^4 cm^{-2} . In contrast, the best structured cathode C exhibit well-aligned FE from nearly all patches, i.e. 90% efficiency at much lower $E_{\text{on}}(1\text{nA}) = 8\text{-}20 \text{ V}/\mu\text{m}$

(Fig. 6.5b). Moreover, up to 10 emitters (five on average) per patch are obvious which improve the homogeneity and average N_e to $3 \times 10^4 \text{ cm}^{-2}$ what is close to the resolution limit of the chosen anode. These results support assumption that the optimum number density of Cu nanocones for low operation fields is lower than for the metallic cylindrical nanowires (i.e., the best FE result in term of efficiency and alignment was achieved from Au-NW cathode with number densities of 10^7 NW/cm^2 at $E_{\text{on}} (1\text{nA}) > 30\text{V}/\mu\text{m}$ [Navi09]).

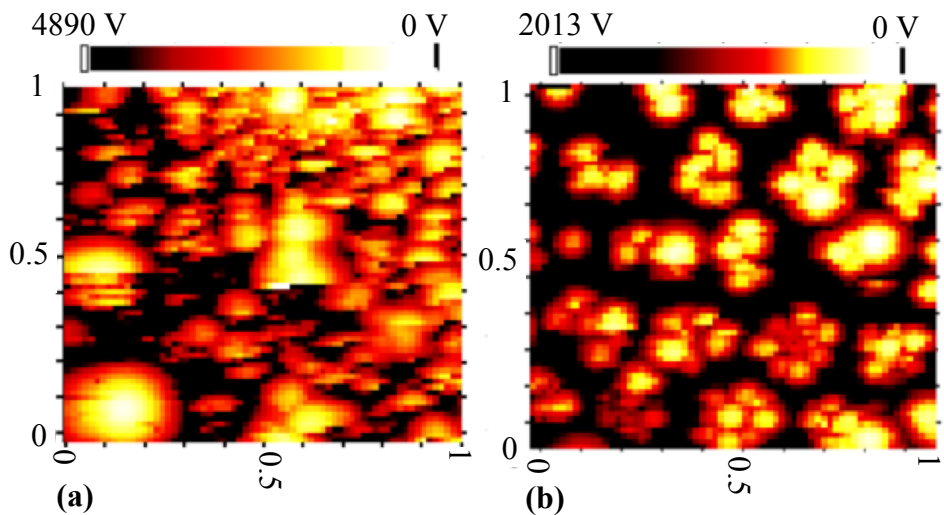


Fig. 6.5. Typical regulated voltage maps $V(x, y)$ for 1 nA FE current of: (a) cathode A ($\varnothing_a = 30 \mu\text{m}$, $\Delta z = 40 \mu\text{m}$) and (b) the structured cathode C ($\varnothing_a = 30 \mu\text{m}$, $\Delta z = 25 \mu\text{m}$).

Guided by the $U(x, y)$ maps, local measurements of strong emitters were performed with the same anode up to their current limit. The local field E was calibrated by means of $U(z)$ plots [Lyse05]. Typical I-E curves and corresponding FN plots obtained for the four cathodes are shown in Fig. 6.6. At first sight, the shape of the curves of the measured spots appears similar despite different current and field levels. Small current fluctuations and hysteretic I-E curves (Fig. 6.6a, d) indicate stepwise (de-) activation of individual Cu-NCs, while strong current drops at the high field (Fig. 6.6b, c) hint at severe emitter destruction.

The field enhancement factor β of the emitters was determined from the stable low-field slope of each FN plot assuming a work function of 4.65 eV [Lide08]. At higher fields, current fluctuation and saturation effects were always observed which might be caused by successive processing of the Cu-NCs contributing to the emitter current.

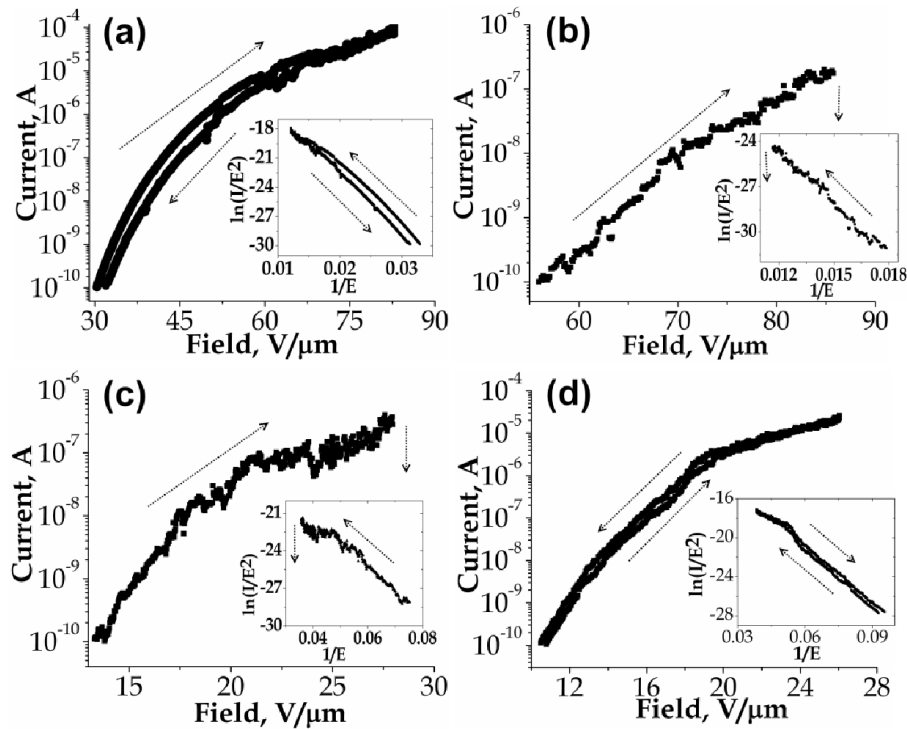


Fig. 6.6. Typical I - E curves and FN plots (inset) measured with the $\varnothing_a = 30 \mu\text{m}$ of cathodes A-D ((a)-(d), respectively). The arrows indicate up/down voltage cycles and strong current drops. Please note that cathodes A and D yield much higher currents ($>10 \mu\text{A}$) than cathodes B and C ($<1 \mu\text{A}$).

In figure 6.7a, E_{on} and β values of all locally measured emitters are displayed. At first, the overall hyperbolic correlation indicates the intrinsic FE behavior of the Cu-NC emitters with characteristic ranges caused by their aspect ratio and mutual shielding. The unstructured cathodes A and B with high density of Cu-NCs provide high mean E_{on} values of 52 (53) $\text{V}/\mu\text{m}$ and low mean β values of 84 (65), respectively. The structured cathode D with low density of Cu-NCs yields a mean $E_{\text{on}} = 26 \text{ V}/\mu\text{m}$ and $\beta = 153$, while C exhibits on average the lowest $E_{\text{on}} = 22 \text{ V}/\mu\text{m}$ and highest $\beta = 237$. The large scattering of these values for cathode C is attributed to the incomplete Cu-NC growth in the patches.

The actual status of the Cu-NC cathodes for potential vacuum nanoelectronic devices is shown in Fig. 6.7b, where the maximum stable currents ($\sim 10\%$ over some minutes from all measured spots of $30 \mu\text{m}$ in diameter) are plotted as a function of the applied field. For the unstructured cathodes with large number density (10^7 cm^{-2}), rather high current levels up to $280 \mu\text{A}$ are achieved from the slowly-grown cones (A) but only moderate ones ($0.1\text{-}20 \mu\text{A}$) from the fast-grown cones (B). This confirms the importance of a solid contact of the Cu-NC to the substrate for high current limits. In comparison, the structured cathodes with much less number density ($<10^6 \text{ cm}^{-2}$) provide rather low current levels of $20\text{-}700 \text{ nA}$ from sharp tips (C) and fairly good ones ($10\text{-}100 \mu\text{A}$) from broad tips (D). The operating field levels, however, are much lower for the structured cathodes ($\sim 20\text{-}60 \text{ V}/\mu\text{m}$) than for the unstructured

ones ($\sim 80\text{-}140\text{ V}/\mu\text{m}$). A clear average trade-off between low onset fields and high current limits is indicated by the wide spread of points in Fig. 6.7b.

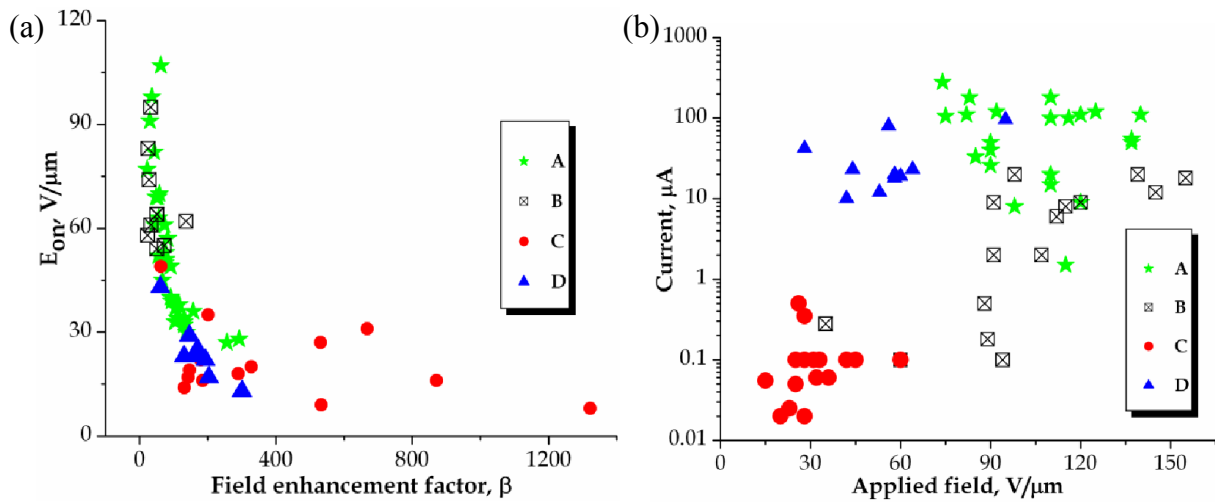


Fig. 6.7. (a) $E_{on}(1\text{ nA})$ vs. β values derived from the FN plots for all locally measured emitters of the four cathodes (A-D). (b) Maximum stable current plots values vs. applied electric field for all measured spots on the four Cu-NC cathodes (A-D).

The improved mechanical stability and solid contact interface of the copper nanocones result in much higher current values as compared to all previously tested metallic cylindrical nanowires. Systematic variation of the number density emitters might lead to lower operating fields and to higher current values.

6.3. Performance of Au-coated Cu-NCs of reduced number density

In order to improve the FE properties of structured Cu-NCs cathodes, new series of Cu-NC cathodes with reduced number density of emitters were fabricated. Moreover, to stabilize and get higher FE current, these cathodes were magnetron-sputtered with thin gold films. For a systematic study, one cathode was coated with a 10 nm Au layer, while the other one with 60 nm. The main parameters of the fabricated patch-structured bare and Au-coated Cu-NC cathodes are summarized in table 6.2. The FE properties of the Cu-NC cathodes before and after coating were compared.

Table. 6.2. Overview of parameters of the bare and Au-coated Cu-NC cathodes.

Parameters Sample	Type	Etching time (min)	Deposition voltage (mV)	N_{e_c} (cones/ cm^2)	\varnothing_{tip} , (nm)	Aspect ratio
65.2 (^{238}U ions)	bare	15	50	$4.4\text{-}8.7 \times 10^5$	197	286
	10 nm Au film				207 ± 43	270
52.3 (^{136}Xe ions)	bare	20	40	$1.4\text{-}4.7 \times 10^5$	186	301
	60 nm Au film				246 ± 64	227

Detailed SEM (Philips XL 30 S) investigations of fabricated Cu-NC patches show that not all Cu-NCs in the patch were grown completely. Investigations of 22 and 12 randomly chosen Cu-NC patches showed that the percentage of completely grown Cu-NCs per patch is about $78\pm 8\%$ and $65\pm 11\%$ for the 65.2 and 52.3 cathodes, respectively (Figs. 6.8, 6.9). The fabrication difficulties can be explained, firstly, by non-simultaneous pore filling at high deposition voltages. A similar explanation was proposed in [Schu00, Toim01a]. Secondly, as was explained by Hama et. al. [Hama98] the reduction of Cu^{+2} ions takes place in two steps, i.e. $\text{Cu}^{+2} + \text{e}^- \rightarrow \text{Cu}^{+1}$ and $\text{Cu}^{+1} + \text{e}^- \rightarrow \text{Cu}$. Oxidization of the Cu^{+1} ions during electrochemical deposition of copper into the pores by the air bubbles in the electrolyte again can produce Cu^{+2} ions. This process consumes current, but does not lead to any deposit [Bark01, Toim01a]. Finally, it can also be explained by the fact that not all the pores were completely opened after the chemical etching of PC membrane [Jord12b].

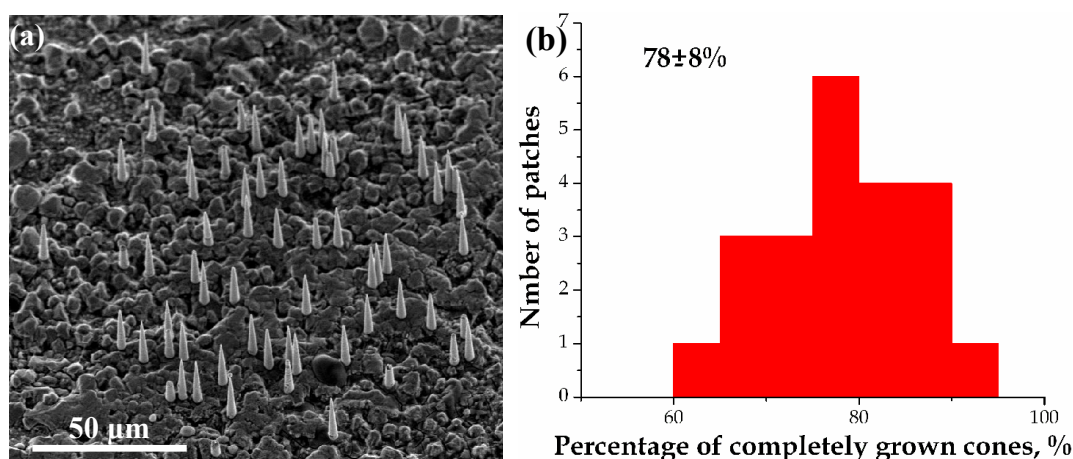


Fig. 6.8. Typical SEM image of a single 10 nm Au-coated patch shows 64 Cu-NC emitters, but only ~51 of them (or 79%) were grown completely (a). A percent histogram between the numbers of the fully grown nanocones and the total number of emitters per patch (b). The resulting mean value of completely grown NCs of 22 patches is about $78\pm 8\%$.

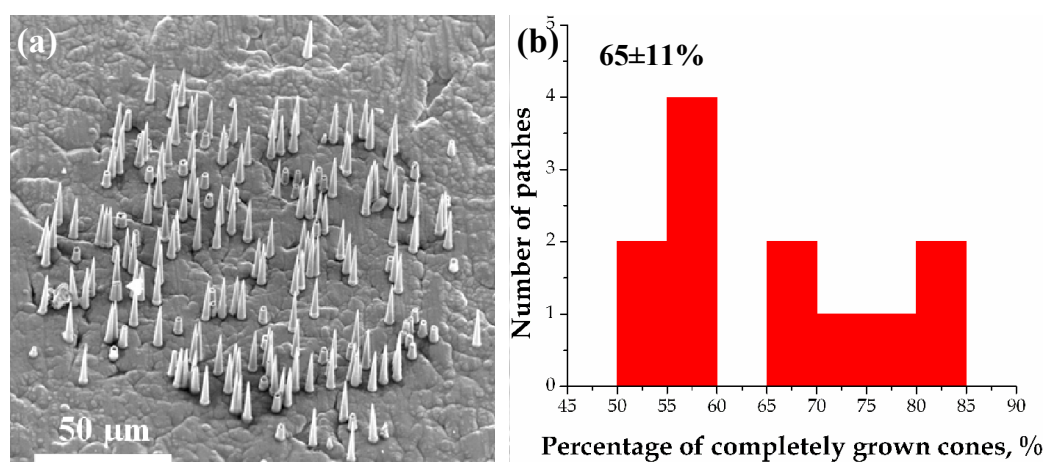


Fig. 6.9. Typical SEM image of a single 60 nm Au-coated Cu-NC patch shows about 71% of successfully grown emitters (a). A percent histogram between the numbers of the fully grown nanocones and the total number of emitters per patch (b). The resulting mean value of completely grown NCs of 12 patches is about $65\pm 11\%$.

Based on the fact that the deposited material replicates the shape of the pores, which increases almost linearly with the etching time [Flei75, Toim01b], the variation of the tip diameters for both types of cathodes (Fig. 6.10, 6.11) is due to different size and structure of ion tracks, that depends on the mass and energy of the impinging ions [Apel98, Trau95, Trau96] and on the position of the polycarbonate foil in the stack as mentioned above [Jord12a, Apel01b].

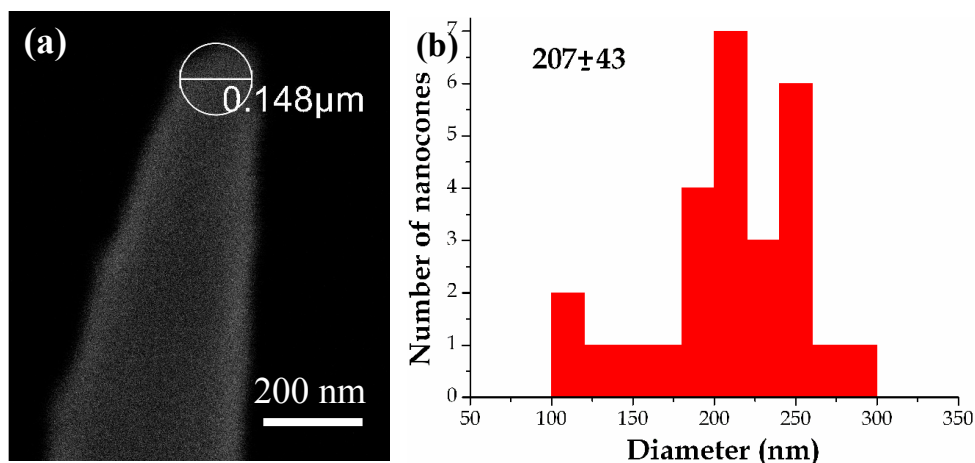


Fig. 6.10. SEM image of a 10 nm Au-coated Cu-NC tip at high magnification (a). Tip diameter distribution of 27 measured Au-coated NCs (b). The resulting mean value of tip diameter is 207 ± 43 nm.

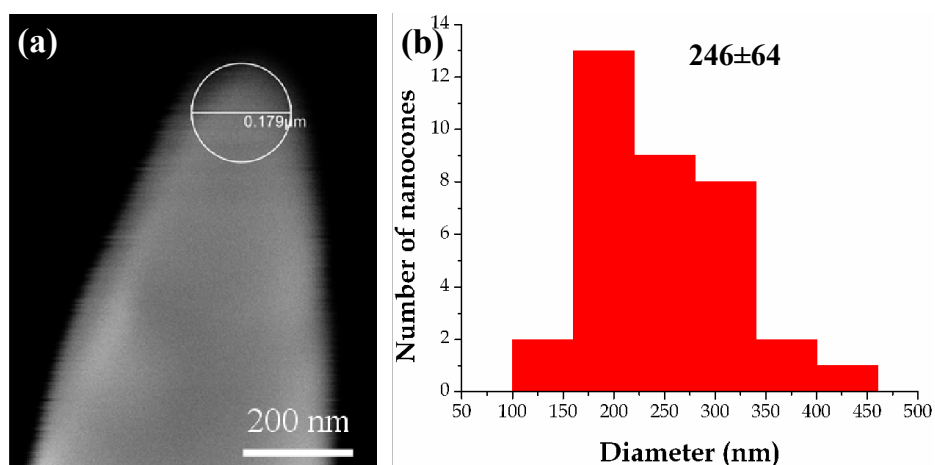


Fig. 6.11. SEM image of a 60 nm Au-coated Cu-NC tip at high magnification (a). Tip diameter distribution of 35 measured Au-coated NCs (b). The resulting mean value of tip diameter is 246 ± 64 nm.

The HRSEM analysis, presented above, is very important for better interpretation of the FE results from the Cu-NC cathodes. The variation of number of the fully-grown nanocones and their diameter per patch will lead to the variation of the current carrying capability under certain voltage due to the shielding effect. Therefore, a fabrication procedure of such emitters has to be improved.

EDX (attached to the HRSEM) analysis has been performed on the bare and Au-coated Cu-NC cathodes to characterize the elemental distribution from the surface. From the spectral

EDX images we see two and three (Fig. 6.12a, b) basic spectral lines that correspond to the presence of Cu and both Au and Cu elements for the bare and the Au-coated cathode, respectively. Some other peaks in the spectra correspond to the elements of the setup (beryllium) and chemical agents (sulphur, chlorine).

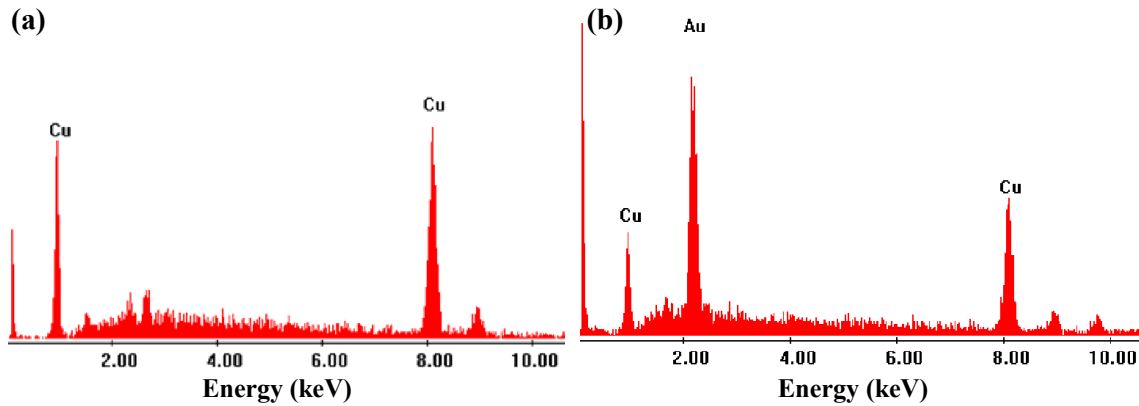


Fig. 6.12. EDX spectra of the bare (a) and Au-coated (b) Cu-NCs.

6.3.1. Properties of bare and 10 nm Au-coated Cu-NC cathode 65.2

In order to investigate the homogeneity and distribution of emitters PID regulated raster voltage scans $U(x,y)$ at a constant FE current of 1 nA at a fixed Δz were performed. In measurements tungsten anodes of truncated-cone shape and diameter \varnothing_a were used in order to obtain low and high resolution voltage maps.

Medium resolution voltage scan shows fairly homogeneous and well-aligned FE of all Cu-NC patches (Fig. 6.13a). The varying values of the E_{on} (1nA) are partially caused by the slightly tilted cathode or substrate unflatness and by different aspect ratio of emitters. High resolution voltage map prove the presence of at least 3 dominant emitters per patch (or $1.7 \times 10^{-4} \text{ cm}^{-2}$) which start to emit at field below than $10 \text{ V}/\mu\text{m}$ (Fig. 6.13b). Multiple emitters can play an important role in improvement of the stability of FE due to the replacement of destructed emitters with emitters which were shielded.

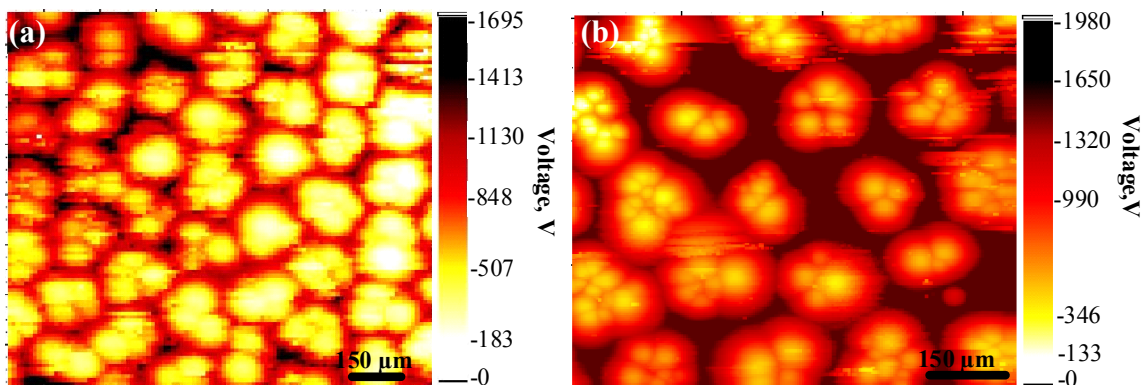


Fig. 6.13. Medium ($\varnothing_a = 60 \mu\text{m}$, $\Delta z = 30 \mu\text{m}$) and high ($\varnothing_a = 12 \mu\text{m}$, $\Delta z = 38 \mu\text{m}$) resolution voltage maps for the bare (a) and 10 nm Au-coated (b) Cu-NC cathodes.

Local measurements of whole patches were performed with 150 μm anode, in order to determine the FE characteristics of Cu-NC emitters more precisely. For each local measurement the field was calibrated by means of $U(z)$ -plots [Lyse05]. Typical I-F curves and corresponding FN-plots (inset) for the bare and 10 nm Au-coated Cu-NC cathodes are in Fig. 6.14. Current jumps at μA , 70 μA and ca. 260 μA levels for the bare cathode can be explained by the stepwise destruction of the dominant emitters (fig. 6.14left). In contrast, stable FE current up to 200 μA have been achieved for the 10 nm Au-coated emitters (fig. 6.14right).

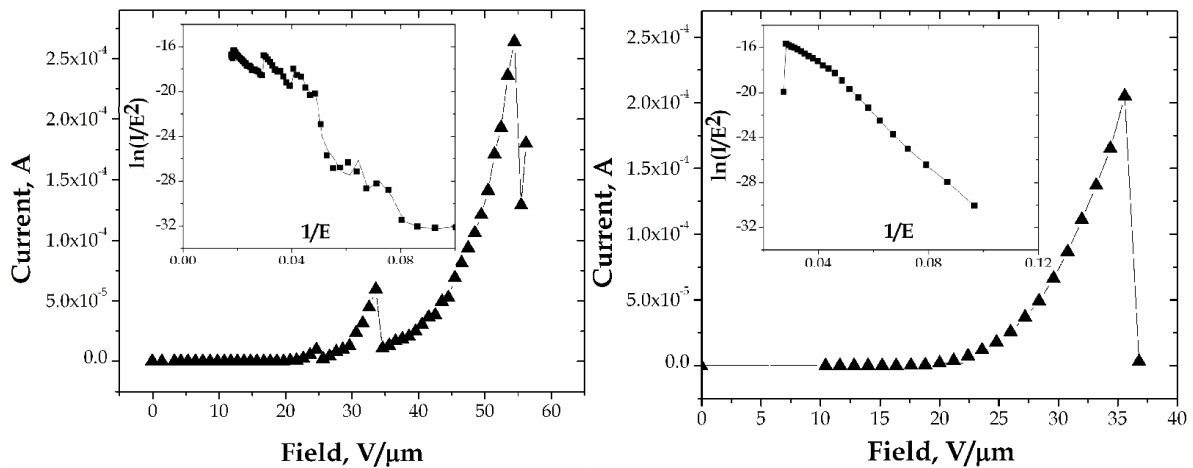


Fig. 6.14. Typical I-V curves and corresponding FN-plot (inset) for the bare (left) and 10 nm Au-coated (right) cathodes.

The maximum achieved currents per Cu-NC patches are presented as function of beta values (Fig. 6.15a.) and an applied electric field (Fig. 6.15b). Variation of current values (from 1 μA to 350 μA and from a few μA to 260 μA for the bare and Au coated emitters, respectively) and beta values might be explained by strong variation of emitters per patch and different tip diameters as mentioned above (see figs. 6.8-6.11).

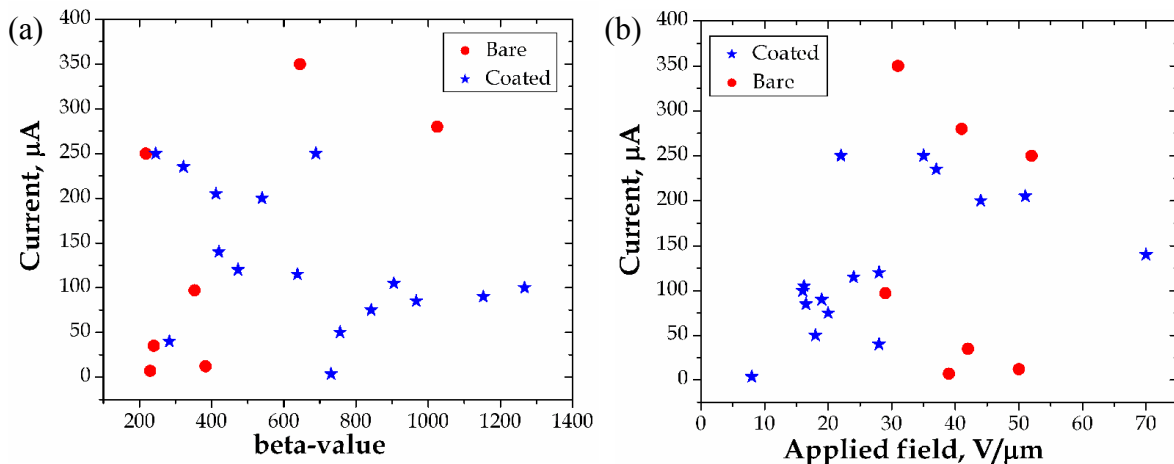


Fig. 6.15. Maximum achieved FE currents vs. β values (a) and applied field (b). On average the bare Cu-NCs yielded about 147 μA per patch ($\varnothing_a = 150 \mu\text{m}$) in comparison to 128 μA for 10 nm Au-coated ones.

The field enhancement factor was extracted from the FN plots of all measured patches. The distribution of these factors is presented in semilogarithmic histogram in Fig. 6.16a. As it can be seen from the histograms the mean beta values are 333 and 595 for the bare and 10 nm Au-coated cathode, respectively. Higher beta value for the 10 nm Au-coated cathode can be explained by presence of a few-nm sized gold clusters (islands) on the tip surface [Kaun09, Sieg11]. Similar explanation was suggested in ref. [Giva95], wherein the authors discussed in detail the FE from protrusions (nano-points) sitting on the tip surface of the silicon emitters (see also chapter 2.1). This also explains some of the differences among E_{on} of bare and Au-coated cathodes, because of the higher beta factor leads to the lower E_{on} (Fig.6.16b).

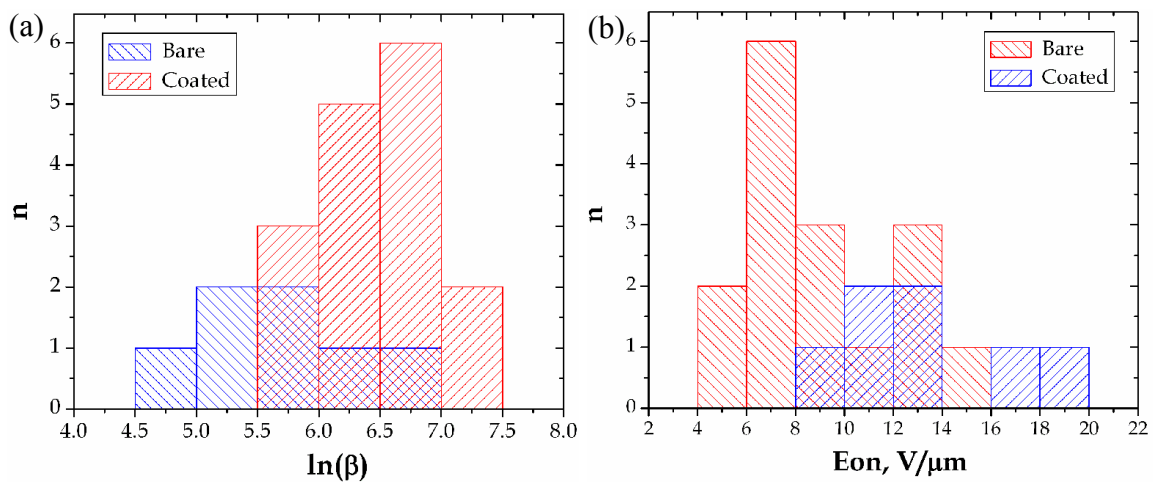


Fig. 6.16. Histograms of mean field amplification factor $\langle\beta\rangle \ln(5.81 (6.39)) = 333 (595)$ (a) and mean value of $\langle E_{on}\rangle = 12.85 (8.87) V/\mu m$ (b) for the bare (10 nm Au coated) cathode.

A current stability test for a single bare and 10 nm Au-coated patch measured with $\varnothing_a = 150 \mu m$ over a time period of 1 hour was performed. The result yielded fluctuations in the range of 17-25 μA ($\sim 22.2\%$) and 98-124 μA ($\sim 18.2\%$), respectively (Fig. 6.17). Fluctuations in the emission current might be interpreted as the result of morphological changes of emitters and/or due to the adsorbates (see chapter 2.1).

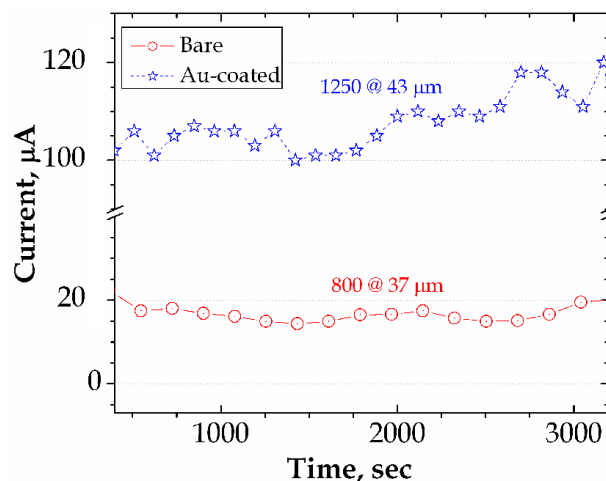


Fig. 6.17. Current stability of a single bare and 10 nm Au-coated patch.

SEM images of tested 10 nm Au-coated Cu-NC patches showed that after the current processing (~ 1 hour) at least 6 NCs were partially melted by the FE current. From SEM images, it is also possible to estimate an average current from a single nanocone. Relative stable current of about $100 \mu\text{A}$ have been achieved from 36 emitters (see fig. 6.17 and corresponding SEM image in Fig. 6.18), that corresponds to the average current value of about $2.7 \mu\text{A}$ per nanocone. Achieved value is nearly close to the current threshold of an individual single-walled carbon nanotube [Dean01]. Probably, such high current value is attributed to the screening effect: more closely spaced emitters showed less degree of damage than the well-separated ones, and hence not all NC were involved in FE process. The reasons of spheroidization and partial destruction of emitters after the current processing will be discussed in chapter 6.3.2.

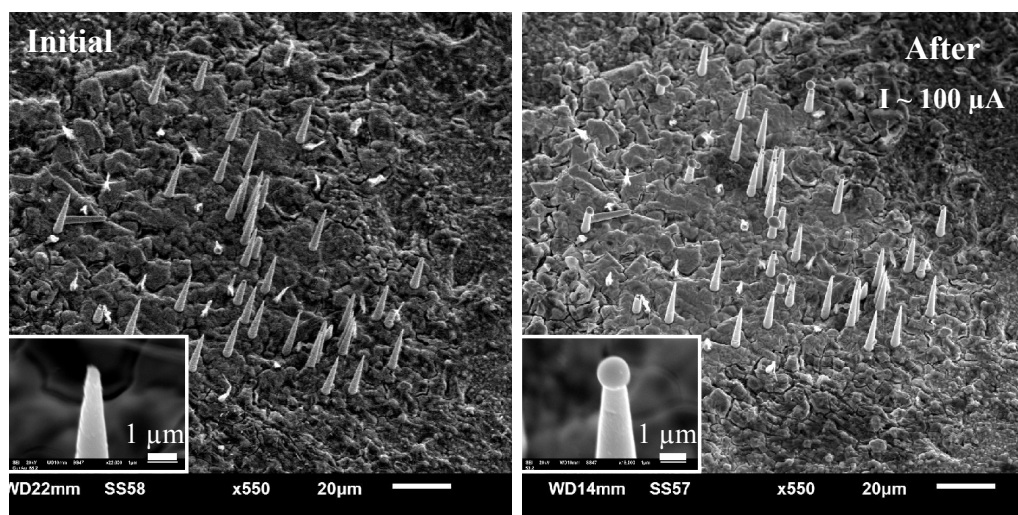


Fig. 6.18. SEM images of 10 nm Au-coated Cu-NC patch before and after the current processing (see fig. 6.18). Insets are Au-coated Cu-NCs at higher magnification. Spheroidization and partial destruction of emitters after the current processing were observed.

6.3.2. Properties of bare and 60 nm Au-coated cathode 52.3

The results of voltage scans $U(x,y)$ over the cathodes at a constant FE current ($I = 1 \text{ nA}$) show fairly distributed FE of the bare and 60 nm Au-coated Cu-NC cathodes at onset field E_{on} (for 1 nA) = $8\text{-}23 \text{ V}/\mu\text{m}$ and $E_{\text{on}} = 7\text{-}33 \text{ V}/\mu\text{m}$, respectively (Fig. 6.19). The variations of the E_{on} can be explained by mutual shielding of randomly distributed Cu-NCs per patch (see fig. 6.8, 6.9) and by different diameter of Cu-NCs (see fig. 6.10, 6.11). Concentrating only on the strongest emitters, that start to emit at E_{on} below $10 \text{ V}/\mu\text{m}$, one has to mention, that bare cathode yields a minimum of 4 dominant emitters per patch or $2.3 \times 10^4 \text{ cm}^{-2}$, while Au coating shows at least 12 emitters or $6.7 \times 10^4 \text{ cm}^{-2}$. These values are nearly close to the total number density of emitters mentioned above (see Tab.6.2). The results hint that the gold-

coated Cu-NCs leads to the activation of the emitters probably due to less oxide, as well as, one can say that the optimal number density of such NCs is about $2\text{-}7 \times 10^5 \text{ NC/cm}^2$ [Dang07].

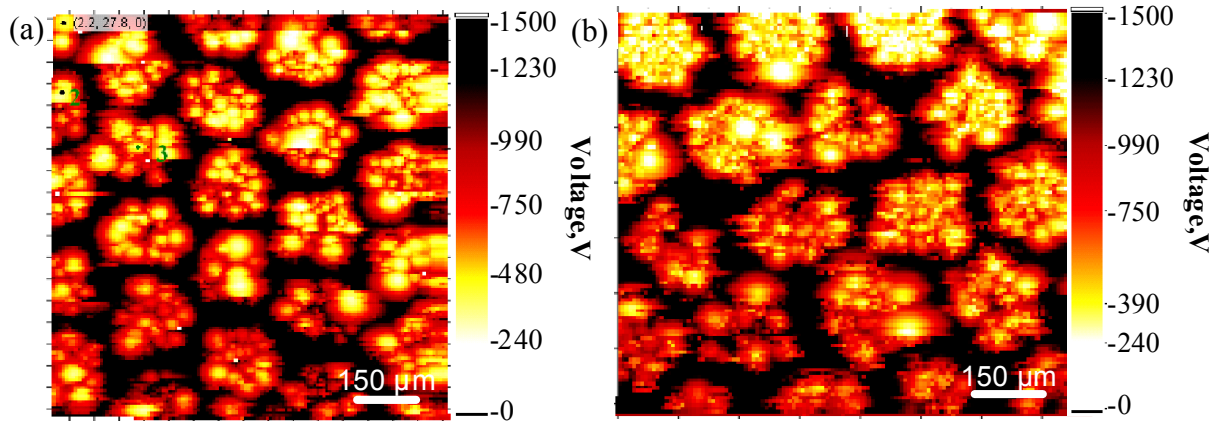


Fig. 6.19. High resolution onset field maps (area $< 1 \text{ mm}^2$, for 1 nA FE current, $\varnothing_{\text{anode}} = 12 \text{ }\mu\text{m}$, $\Delta z = 30 \text{ }\mu\text{m}$) of pure (a) and Au-coated (b) copper nanocones cathodes showing at least $N_e \sim 2.2 \times 10^4 \text{ cm}^{-2}$ and $\sim 6.7 \times 10^4 \text{ cm}^{-2}$ respectively.

In order to investigate FE characteristics of both cathodes, local measurements of whole Cu-NC patches were performed with $\varnothing_{\text{anode}} = 150 \text{ }\mu\text{m}$. The field was calibrated by means of $U(z)$ plot. Typical I-V curves obtained from the bare and Au-coated Cu-NC patches are shown in Fig. 6.20. Both type of cathodes showed fairly stable FN behavior, however, with strong irreversible changes in the I-V curves that might be explained by changing of the tip geometry of dominant emitters or their partial destruction.

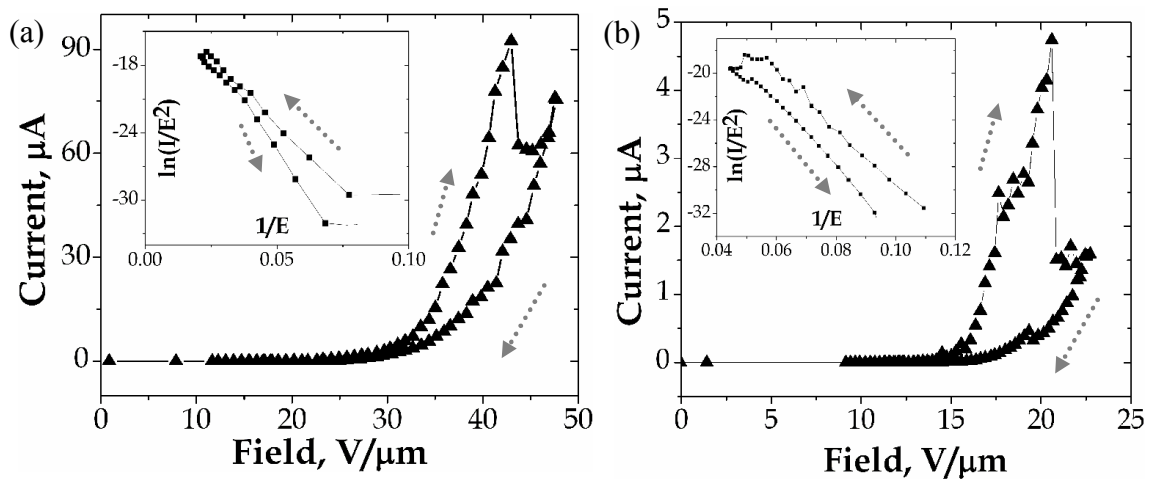


Fig. 6.20. Typical I-V curves and corresponding FN plots (insets) from a single bare (a) and 60 nm Au-coated (b) Cu-NC patch measured with $\varnothing_a = 150 \text{ }\mu\text{m}$, showing a partial destruction of emitters at about $5 \text{ }\mu\text{A}$ and $90 \text{ }\mu\text{A}$ respectively. The arrows indicate up/down voltage cycles.

The field enhancement factors were extracted from the FN plots at low currents of all measured patches assuming the nominal values of work function for copper and gold of $\varphi_{\text{Cu}} = 4.65 \text{ eV}$ and $\varphi_{\text{Au}} = 5.1 \text{ eV}$, respectively [Lide08]. The logarithms of these values are presented in Fig. 6.21. The resulting mean β values for the bare and for the 60 nm Au-coated cathodes

are 274 and 252 respectively. The result is nearly close to the aspect ratio estimated above. Decrease of the β value is associated with a higher ϕ_{Au} and larger tip diameter for the Au coated cathode.

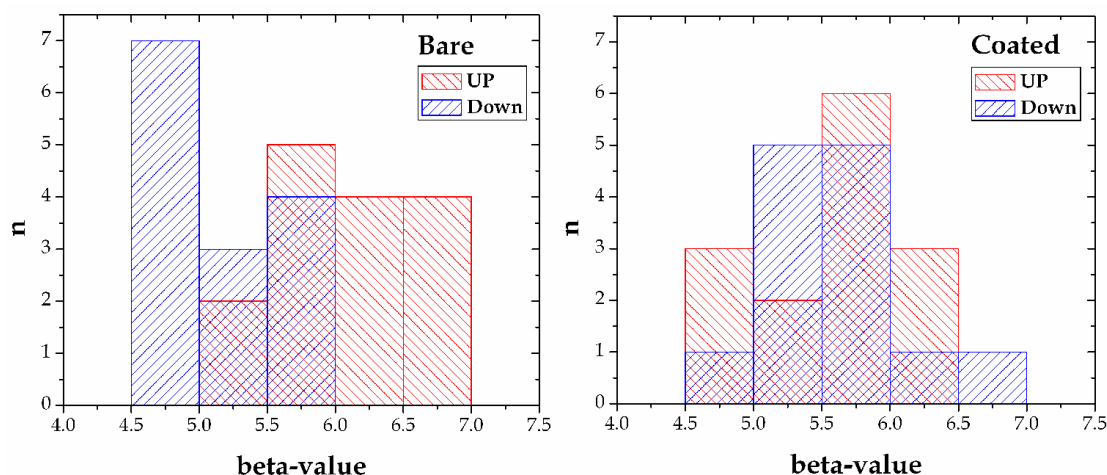


Fig. 6.21. Histograms of the natural logarithm of the beta values for the bare (left) and 60 nm Au-coated (right) cathodes for increasing (UP) and decreasing (Down) applied field. The resulting mean β -values are 274 and 252 for the bare and coated cathodes, respectively.

The large variation of β -values and E_{on} of measured bare and coated patches is presented in Fig. 6.22. It is visible, that the E_{on} (β) of the bare Cu-NCs after the current processing is getting higher (smaller). Such results indicate that the geometry of the emitters irreversibly changed irreversibly at high field (current). In contrast, measured 60 nm Au-coated Cu-NC patches seem to be more stable. Mean values of E_{on} are 13 V/ μ m and 17 V/ μ m for the bare and 60 nm Au-coated patches, respectively.

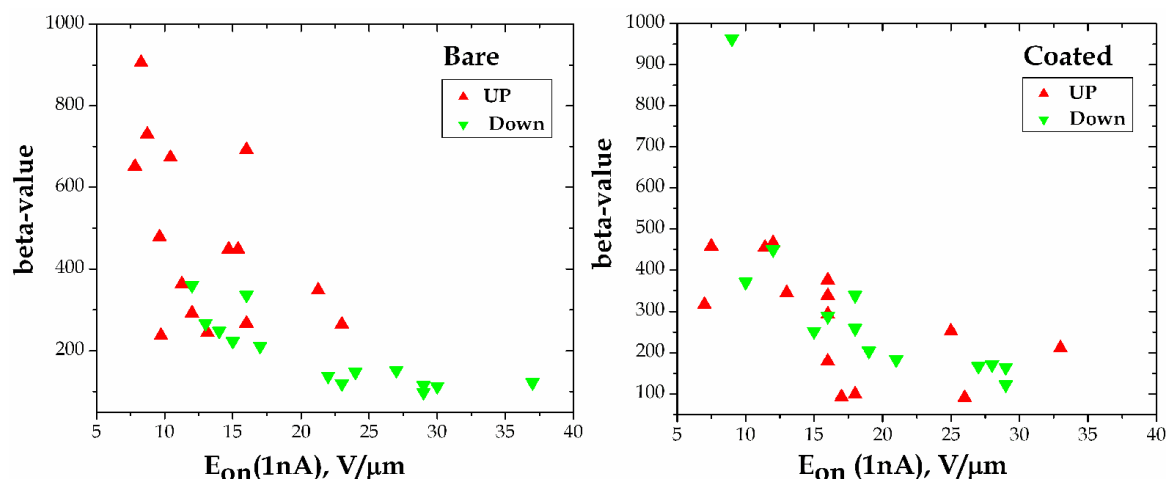


Fig. 6.22. Onset field E_{on} (1nA) vs. β -values for the bare (left) and 60 nm Au-coated (right) cathodes before (\blacktriangle UP) and after (\blacktriangledown Down) current processing.

The improved current capability of the gold-coated Cu-NC cathode in comparison to the bare cathode is also presented in fig. 6.23, where the maximum achieved stable currents

per patch are plotted as function of beta values (a) and an applied field (b). On average the bare Cu-NCs yielded about 30 μA at 32 $\text{V}/\mu\text{m}$ in comparison to 151 μA at 50 $\text{V}/\mu\text{m}$ for Au-coated ones.

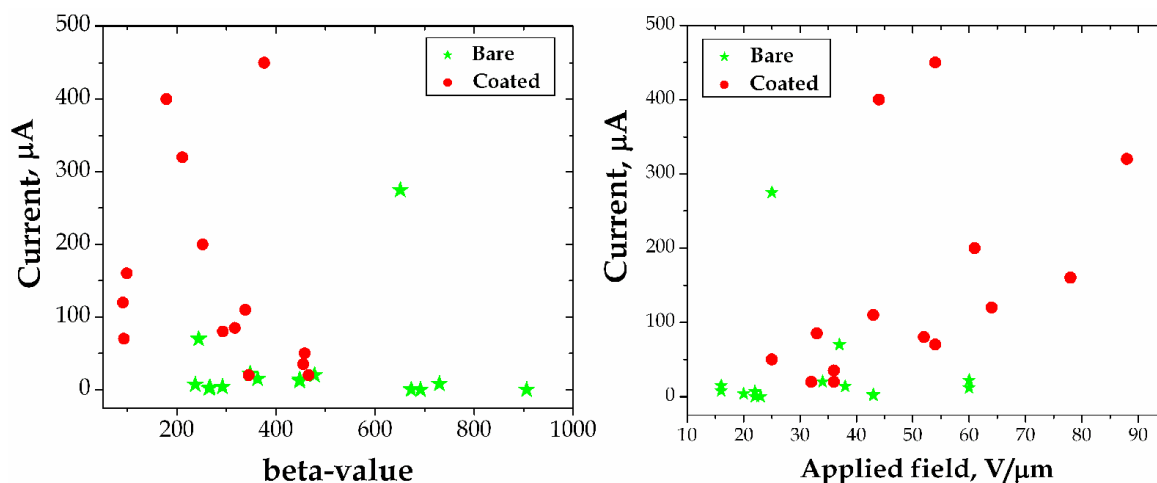


Fig. 6.23. Maximum achieved FE currents vs. beta values (a) and applied field (b) per patch for the bare and the 60 nm gold-coated Cu-NC cathodes.

Typical SEM images of the bare and 60 nm Au-coated patches before and after the current processing are presented in Fig. 6.24. SEM analysis of both types of cathodes showed that after the current processing (at current limits from 20 nA to 275 μA for bare and from 20 μA to 400 μA for Au-coated cathodes), on average 50-70% of all emitters in the patch were completely destroyed or melted, while the remaining bare and Au-coated emitters were partially modified. The observed spheroidization on the top of emitters is caused by melting of the metallic tips at the temperature lower than the melting point of the material (Rayleigh instability) [Reil79, Toim04, Kari06, Kari07]. The morphological/geometrical changes of Cu-NCs can be also explained by:

1. resistive (Joule) heating effect [Ho89];
2. electromigration effect (motion of metal ions under an applied field) [Ho89, Stah07].

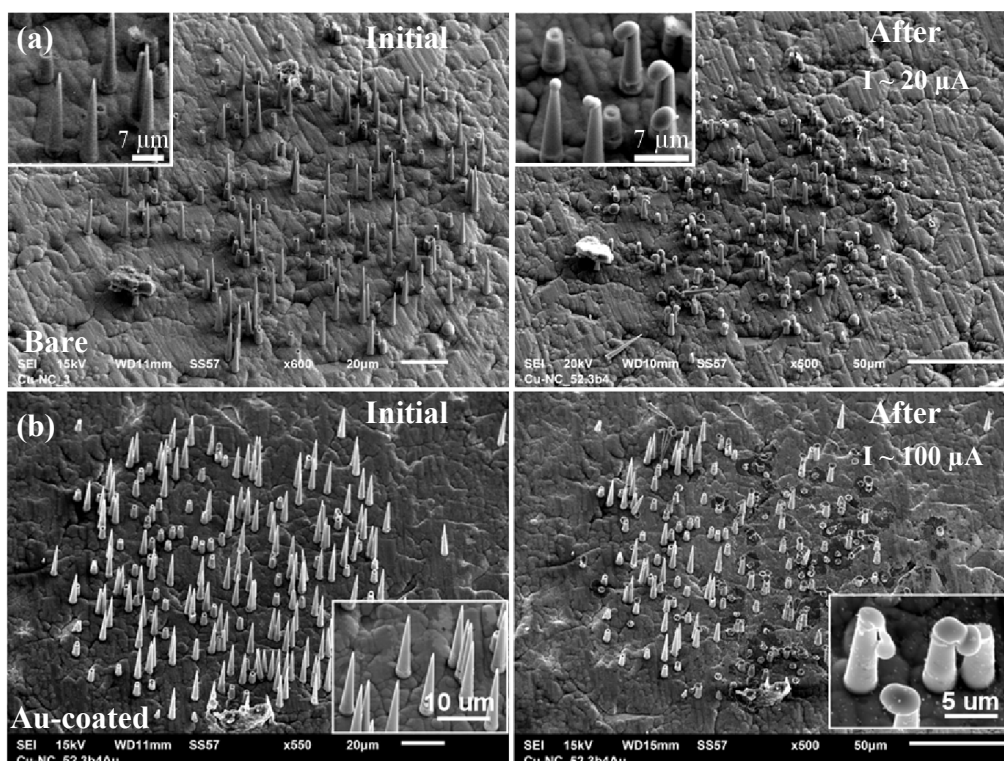


Fig. 6.24. SEM images of bare (a) and Au-coated Cu-NC patches before (on the left side) and after (on the right side) current processing at $\sim 20\mu\text{A}$ and $100\mu\text{A}$ for the bare and Au-coated cathodes, respectively. Spheroidization and partial destruction of emitters after the current processing were observed.

6.4. Current carrying capability of single bare copper nanocones

In order to investigate the FE properties of individual bare copper nanocones, cathode with low number density of emitters N_e in the patches was used (Fig. 6.25left). The main parameters of the cathode are summarized in Tab. 6.3.

Table. 6.3. Overview of parameters of the bare and Au-coated Cu-NC cathodes.

Parameters Sample	Type	Etching time (min)	Deposition voltage (mV)	N_e , (cones/cm ²)	\O_{tip} , (nm)	Aspect ratio
80.2 (²³⁸ U ions)	bare	12	40	$2.2\text{-}8.5 \times 10^4$	155 ± 40	363

At first, high-resolution voltage scan at constant FE current of 1 nA has been performed in order to determine the position of single emitters over the cathode. The result of the voltage scan over a certain area of the cathode shows a few well-defined single emitters and eight of them were tested (Fig. 6.25right). The maximum current carrying capability of the numbered emitters was measured. Onset electric field (for 1 nA FE current) as well as the field enhancement factors β assuming work function of 4.65 eV have been derived from corresponding I-E and FN plots. The results are summarized in Table 6.4.

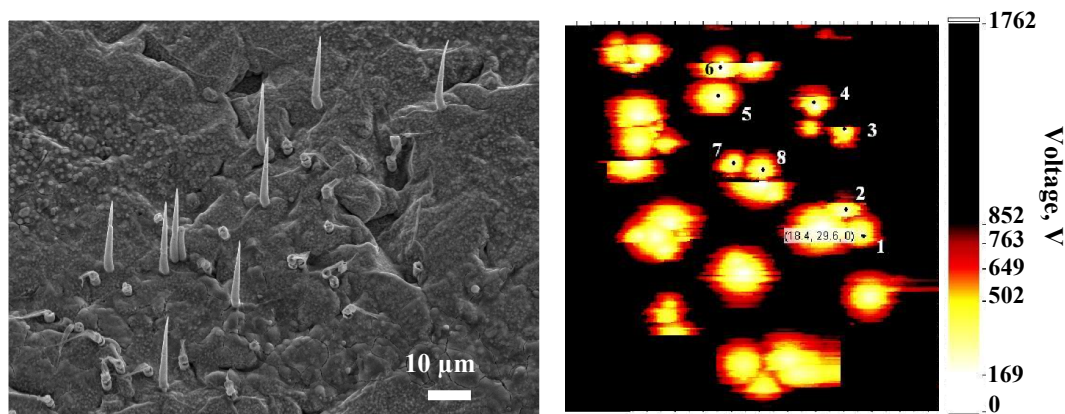


Fig. 6.25. Typical SEM image of a single patch on the left and voltage map on the right (at 1 nA , $\varnothing_a = 4\ \mu\text{m}$, $\Delta z \sim 20\ \mu\text{m}$, area $\sim 1\ \text{mm}^2$). Not all cones were grown due to some fabrication difficulties, as mentioned above. Typical N_e per patch varied from 2 to 10 cones. The numbered points are corresponds to the position and order of local measurements listed in Tab. 6.4.

Table. 6.4. FE measurement result for the eight single bare Cu-NCs.

Emitter num.	Δz , μm	$E_{\text{on}}(1\text{ nA})$, $\text{V}/\mu\text{m}$	I_{max} , nA	U_{max} , V	Beta ($\varphi = 4.65\text{ eV}$)
1	20	19	64	610	541
3	15	26	78	680	161
4	6	34	190	960	31
5	12	33	450	478	128
6	39	22	470	1250	214
7	49	22	11	1040	105
8	36	31	260	1480	121

The maximum FE current from a single Cu-NC varied between 11 nA and 470 nA. Scattering of current value might be explained by the different geometry of Cu-NCs, i.e. the sharper tip, the lower the maximum FE current value. Typical current-voltage curve and the corresponding F-N plot of a single Cu-NC is in Fig. 6.26.

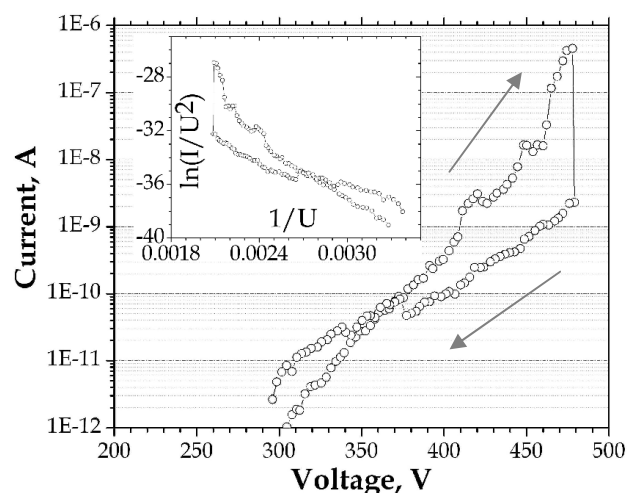


Fig. 6.26. Current-voltage curve and corresponding FN-plot (inset) of a single bare Cu-NC (emitter num.5 in the table 6.4). The anode-cathode distance Δz was $12.35\ \mu\text{m}$. The arrows indicate up/down voltage cycles.

Small current fluctuations at low field values, can be explained by the variation of the shape of the potential barrier and thus by the different tunnelling probability of electrons due to the adsorbate [Luon95] or/and by presence of a native copper oxide layer [Kiel07, Zhu05]. A. Zeitoun-Fakiris et. al. [Zeit88] reported that the various gases creates adsorption and desorption events on the tip surface that result in a redistribution of the electron emission sites. Moreover, this occurs without change of the emitter tip geometry. Irreversible current drop occurs at a high field value due to the partial destruction of the Cu-NC field emitter. The field enhancement factor beta (assuming a work function of $\phi = 4.65$ eV for copper [Lide08, Kohl97]) was extracted from the linear part of the FN plot. The resulting β values for both up and down voltage cycles are 128 and 216, respectively. Higher beta after the current processing can be explained by presence of gold particles on the top of the Cu-NC, as mentioned above [Giva95, Kaun09, Sieg11].

SEM analysis revealed some morphological changes of the processed emitters as shown in Fig. 6.27. Spheroidized ends of Cu-NCs can be observed that can be explained by Rayleigh instability - is the effect of the surface tension, above its thin metallic nanowires breaks into droplets at temperatures much lower than its melting point (i.e., at 400°C (600°C) for a Cu (Au) nanowire with a diameter of 100 nm (87 nm)) [Kara06, Kari07, Kohl97, Rayl78].

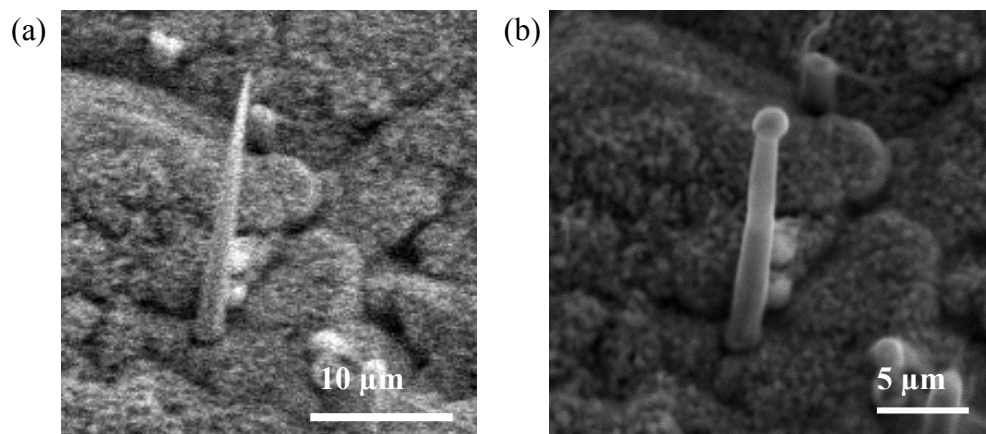


Fig. 6.27. SEM images at 30° tilted-view of a single bare Cu-NC before (a) and after (b) the current processing at ~450 nA.

6.5. Integral measurement results

To demonstrate the application of such Cu-NC cathodes (Fig. 6.28), integral measurement of 10 nm Au coated structured Cu-NC cathode (the same cathode 65.2 was also investigated in the FESM, see the results above) has been performed in the IMLS in dc mode.

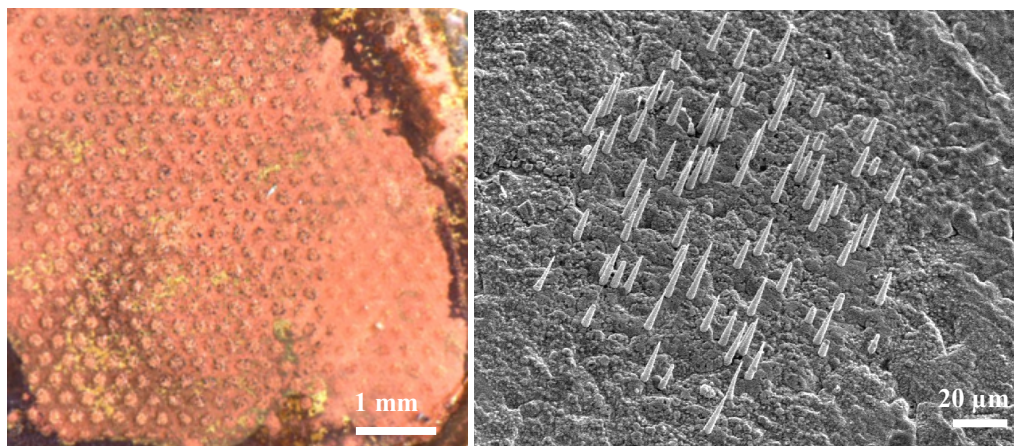


Fig. 6.28. Optical microscope image of the structured bare Cu-NC array (about 20×23 patches over $\sim 5 \times 5$ mm², 270 μ m pitch) and SEM image at 30° tilted-view of a single Cu-NC patch ($\varnothing \sim 150$ μ m). The right hand cone is slightly not in the focus due to the unflatness of the cathode. The variation of the cathode height is up to 125 μ m over 5 mm length.

In order to see how homogeneous FE on the luminescent screen, the investigation of the cathode in the IMLS was performed. After a few up and down voltage cycles, nearly stable FE current up to 16 μ A was achieved (Fig. 6.29). A nearly straight line of the current-voltage curve in the FN-coordinates suggests the presence of the FN tunnelling.

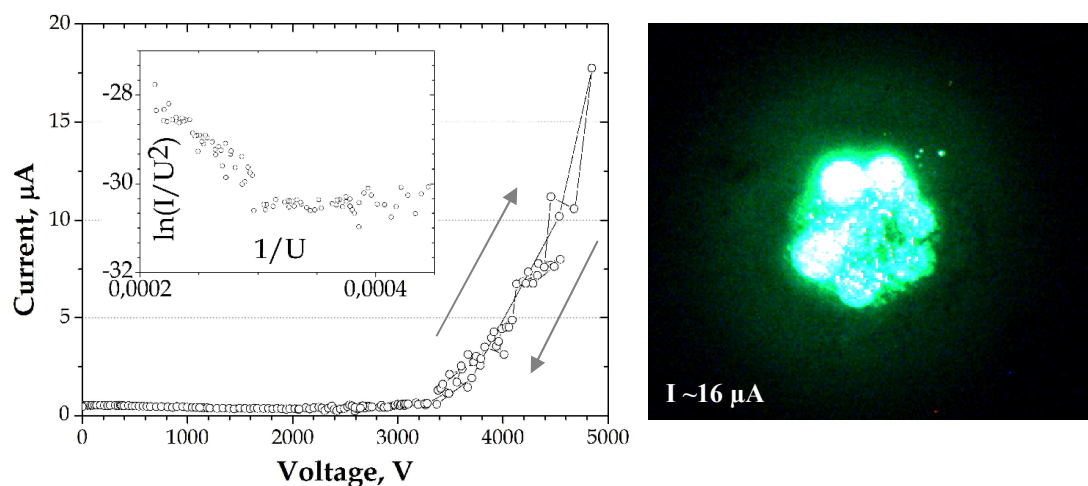


Fig. 6.29. Left: I - V curve and corresponding FN-plot (inset); Right: corresponding luminescent screen image of Cu-NC cathode measured in dc mode. The anode-cathode gap is about 150 μ m. Input power load to the screen is about 0.077 Watt. The size of the patch structured area is $\sim 5 \times 5$ mm².

From the luminescent screen, fairly homogeneous FE can be seen. Such result can be explained by the unflatness of the Cu-NC substrate (see fig. 6.29). Similar results were obtained during the FESM measurements (as presented in chapter 6.3.1). Actually, the fabrication of Cu-NC cathodes with a perfectly flat substrate is the difficult task and, unfortunately, still have not been solved. For instance, the surface of the actual Cu-NCs cathode (Fig. 6.29), investigated by an optical profilometer, yielded the height difference up to 125 μm over 5 mm length [Jord12b, Dzie12]. Therefore, the sample curvature results in the electric field difference over the whole cathode and explain the higher brightness at the edges of the patch structured area. A detailed study on the influence of the sample curvature on the FE characteristics is elsewhere [Lyse06]. In addition, ZnS based-phosphors have a minimum threshold for screen response of 100 nA at 500 V, hence, FE current below this value cannot be observed on the luminescent screen that resulting in a small black area. In this respect, FESM scans at a constant voltage would be more preferable.

The maximum current value from the cathode was investigated by using of a copper screen. As shown in fig. 6.30, a cathode current up to 2 mA (corresponding to a current density of 8 mA/cm²) was obtained at the anode voltage of 1270 V. The observed hysteresis is attributed to a partial or complete destruction of individual Cu-NC emitters or due to adsorbate effects [Lion95, Zeit88].

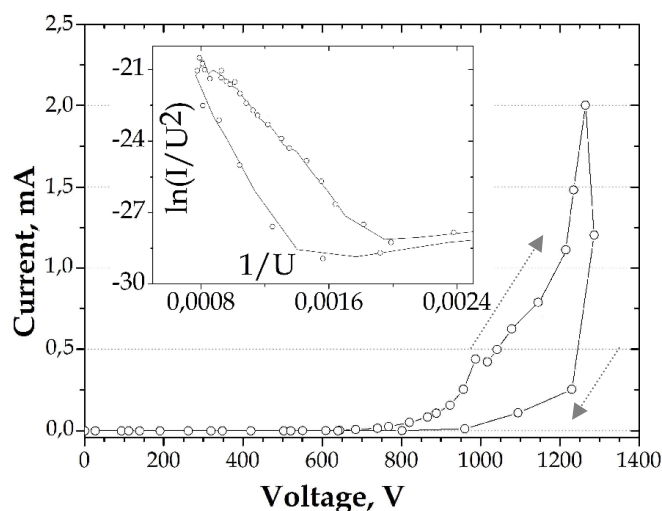


Fig. 6.30. I-V curve and corresponding FN-plot (inset) of Cu-NC cathode integrally measured in dc mode with metallic anode. The observed hysteresis is attributed to partial destruction of Cu-NC emitters and due to adsorbate effects. The gap is about 250 μm .

In the conclusion, the results of local measurements of the same cathode (see chapter 6.3.1) yielded on average about 128 μA per patch, while the IMLS measurement results yielded up to 2 mA from 20 \times 23 patches which corresponds to the average current of about 4.3 μA per patch. Such result indicates that there is still room for improvement in terms of the

flatness of the cathode substrate, uniformity and the number density of Cu-NCs. Different FE current values might be also explained by the different geometry of the anodes [Song13].

6.6. Conclusions and outlook

Sharp and mechanically stable metallic nanocones with solid contact interface were successfully fabricated by potentiostatic electrodeposition of copper in etched ion-track membranes. The sharp Cu-NCs can be grown using a polycarbonate foil irradiated with ^{136}Xe ions. By varying the number density of emitters, the optimal current value at suitable applied voltage can be achieved. The current carrying capability of bare Cu-NCs can be improved by a 60 nm Au coating providing current values up to 400 $\mu\text{A}/\text{patch}$, though at the expense of higher applied fields of $\sim 50 \text{ V}/\mu\text{m}$. SEM images of high-current processed patches revealed morphological or geometrical changes of both bare and Au-coated Cu-NC emitters due to the limited thermal conductance. Rayleigh instability, Joule heating and the electromigration effects are the main mechanisms responsible for the destruction of nanostructures at high current densities.

Ion-track etching and electrochemical filling conditions have been optimized to improve the uniformity of NCs and the flatness of the substrate. A possible option to get higher current densities is the coating of Cu-NC emitters by a carbonaceous layer [You10]. The second option is the fabrication of nanocones using other type of metal, for instance, gold. In terms of thermal stability, single-crystalline nanowires yield higher resistance to morphological changes than poly-crystalline metallic nanowires [Toim12, You10, Navi10c]. From the other side, poly-crystalline metallic emitters are easier and cheaper to fabricate. In spite of that, future work should focus on the fabrication of single-crystalline Au-nanocones. Moreover, electrothermal model calculations of nanocone-emitters are required for better understanding of the current limitations. Due to the randomly distributed arrays of NCs are not ideal for FE, fabrication of a regular array of individual uniform Au-NCs spaced apart by twice their height is required. With such further optimization, Au-NC field emitters might provide advantages over carbon-based ones.

7. Silicon tip arrays fabricated by anisotropic etching technology for FE device

The homogeneity of most actual field emission cathodes, including carbon and metallic nanostructures, and the emission stability of their individual emitters are still limited by fabrication difficulties leading to great variations in the field enhancement and current carrying capability [Dall13, Dean01, Navi09, Navi10a, Seme02, Serb12].

With respect to advanced cold cathode applications, the well-established silicon-based microelectronics technology still offers the best possibility for the reproducible fabrication of extended microstructure cathodes with highly controlled geometry and position [Wang04, Günt01, Günt03]. In addition, integration into micro- or nanoelectromechanical systems may lead to novel monolithic vacuum electronic devices [Schr11]. Furthermore, FE current out of p-doped silicon shows a current saturation region. This effect can be used for current stabilization and, due to the high photosensitivity, for fast optical modulation of the emission current too [Born12]. Si-based FE cathodes have been studied for many years. However, the previous fabrication methods did not allow overcoming the mentioned fabrication difficulties. Therefore, an improved microstructuring process applying modern silicon technology for the reliable fabrication of silicon-based cathodes with precisely shaped and aligned Si tips as field emitter arrays (FEAs) which might be applicable for miniaturized flat electron sources will be reported. Uniform arrays of p-doped, n-doped, and Au-coated Si tips with controlled heights and tip radii have been obtained. The FE properties and the current limits of these different cathodes are presented and discussed here with respect to some potential device applications, for instance, vacuum sensors.

The Si tip arrays were fabricated in the group of Prof. Dr. R. Schreiner in the Microsensors Laboratory at the Regensburg University of Applied Sciences, Germany.

7.1. Optimal tip shape considerations and silicon field emitter design

The electric field enhancement factor β plays the key role for the design of FE cathodes because it defines the extraction voltage required for cathode operation. The extraction voltage is inversely proportional to the β value. In a simple approximation, the geometrical field enhancement factor β is mainly given as the ratio of the emitter height h to the radius of the tip curvature. In a more precise approach, the factor β depends on the tip shape too and decreases with increasing tip apex angle [Utsu91, Forb03, Marc90] (Fig. 7.1a,b,c).

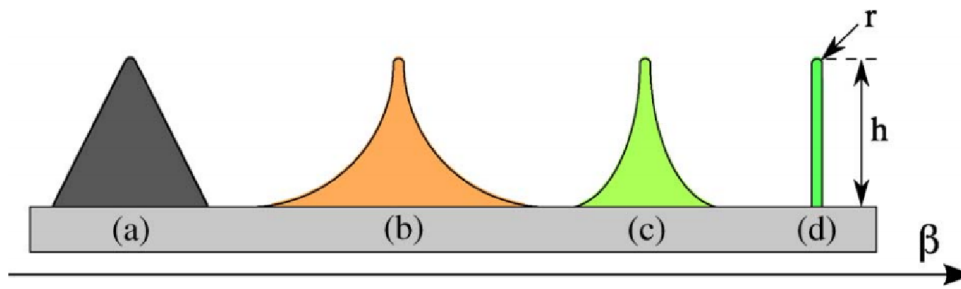


Fig. 7.1. Emitter shapes formed by (a) orientation-dependent etching, (b) isotropic etching, (c) anisotropic etching, and (d) an ideal whisker-like structure. The arrow indicates the increase of the field enhancement factor β of the emitters [Dams12].

The optimal shape of a field emitter for high β factor would be whisker-like with a tip radius r much smaller than the height h (Fig. 7.1d). However, in order to get mechanically more stable structures and higher FE current limits, conical shapes are more preferable. A compromise solution is a shape like the Eiffel Tower (Fig. 7.1c). In the literature, several ways are described to form a structure out of bulk silicon getting close to such a tapered shape [Shaw02].

The highest β factors are naturally found for extremely sharp tips (best in the atomic scale). However, a variation of the tip radii of some nanometers during fabrication is hardly to be avoided [Ding02]. In the case of atomically sharp tips, this has a strong influence on the variation of the field enhancement factor. Consequently, moderately sharpened tips (radii on the order of a few tens of nanometers) will lead to smaller relative deviations of the β factor, much more well working tips, and, therefore, a better uniformity of the FEAs. Furthermore, the larger allowable process windows during fabrication lead to a better reproducibility.

The influence of the tip geometry (height H , apex radius R , and aperture angle α) on the field enhancement factor was investigated by finite element simulations using COMSOL multiphysics software® (Fig. 7.2) [Lang12]. For a given α , an almost linear dependence of β on the aspect ratio H/R was found. As expected, the highest β -values result for an aperture angle of 0° . For apex radii in the order of a few tens of nanometers, this might lead to undesirable shape variations due to the fabrication process and hence to inhomogeneous emission properties of individual tips on one side and on the other side to unwanted limitations of the emission current and extreme joule heating due to the narrow cross section of the tips. For our applications β values in the order of 100 are sufficient; therefore, conically shaped tips with an $\alpha \approx 30^\circ$ and $H \approx 1\text{-}3 \mu\text{m}$ are preferable, because longer etching times will usually result in greater process deviations and thus to greater variations of the tip geometry.

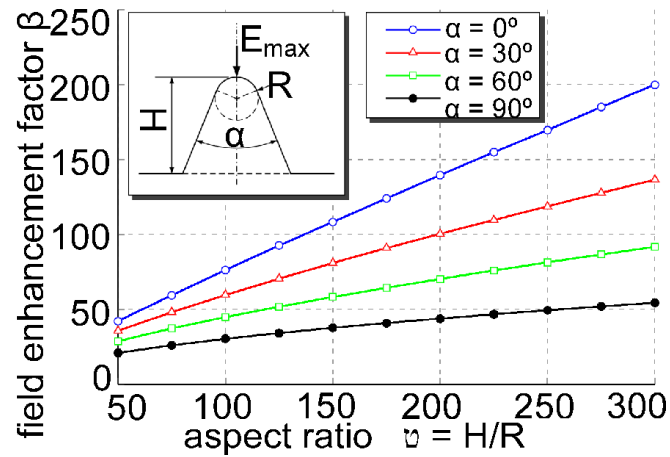


Fig. 7.2. Field enhancement factor of a single Si-tip as function of the aspect ratio v for different aperture angles α with an anode-cathode distance of $5H$ simulated by COMSOL multiphysics® [Lang12].

7.2. Fabrication

Common fabrication techniques for Si microstructures are orientation-dependent etching, isotropic wet or dry etching, and anisotropic dry etching [Shaw02]. In order to achieve reproducible cathodes with both high β factor and sufficient FE current limits, a combination of an anisotropic dry etching step followed by sharpening of the tips by wet thermal oxidation were chosen [Dams11, Dams12]. As base material, 4-in p-type or 2-in n-type silicon wafers (p-Si: (100) orientation, boron doped, and resistivity of 1-10 $\Omega\cdot\text{cm}$; n-Si: (111) orientation, phosphorus doped, and resistivity of 150-250 $\Omega\cdot\text{cm}$.) were used.

In the first step, a thermal oxide of 750 nm was grown on the whole wafer surface. The lateral position of the tips was defined by structuring the oxide layer. The layout consists of a triangular array of disks (diameter d and spacing a ; Fig.7.3).

Very uniform structures over large areas were achieved by means of high-resolution laser beam lithography using image reversal photoresist AZ5214E. The pattern was transferred into the SiO_2 film by reactive-ion etching (RIE) in an ‘‘Oxford Plasmalab 80 Plus’’ etching tool using CHF_3 and O_2 as process gases (Fig. 7.4a-c).

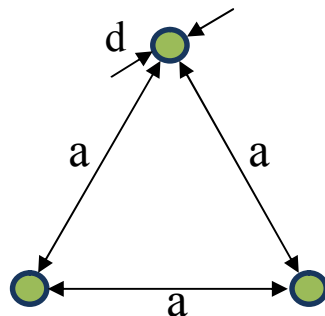


Fig. 7.3. Cell of a photomask to define lateral positions of the tips with grid size $a = 20\mu\text{m}$ and disk diameter $d = 2\mu\text{m}$ [Dams12].

The resulting disks have a diameter of 2 μm and are placed in a triangular array with 20 μm or 10 μm pitch. The change of the disk diameter will influence the final tip height. After removal of the photoresist, the vertical shape of the tips is defined by a subsequent dry RIE process with SF_6 and O_2 as process gases using the SiO_2 disks as etch mask (Fig. 7.3d). The anisotropy of the etching process can be widely controlled by adjusting the SF_6 and O_2 flows, chamber pressure, and RF power [Legt95].

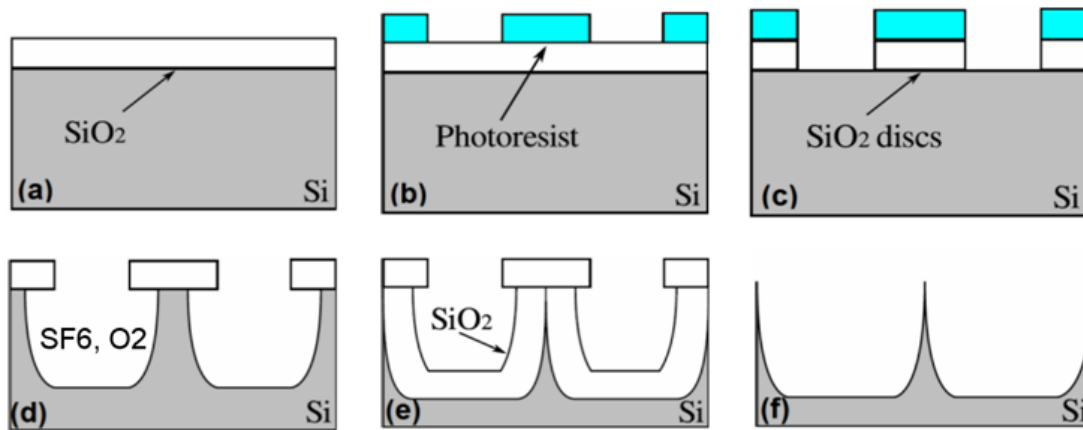


Fig. 7.4. Schematic of the structured cathode fabrication process: (a) Thermal growth of the SiO_2 layer. (b) Photolithography. (c) Transferring of the structures into SiO_2 . (d) Anisotropic dry RIE of the bulk Si. (e) Sharpening of the tips by wet thermal oxidation. (f) Wet chemical removal of SiO_2 [Dams12].

We observed that most homogeneous results were attained by low chamber pressures (50-100 mtorr) and an RF power of 120 W, which are in agreement with previously reported results [Wang04].

Thus, very uniform structures were achieved over the nearly complete etched surface. To prevent the disks from peeling off, the process parameters were adjusted to leave 1 μm of bulk silicon under the mask, i.e., to achieve around 0.5 μm mask undercut (Fig. 7.5). The vertical etch depth was chosen to be around four times the horizontal under etching, resulting in an anisotropy factor of 0.75 which is required to achieve the desired shape of the tips with $\alpha \sim 30^\circ$. The anisotropy factor needs to be adjusted by the RIE system-dependent process parameters depending on the substrate material, wafer size, mask geometry, and RIE chamber configuration. By adjusting the anisotropy of the RIE process, it is possible to vary the tip shape and, thereby, the opening angle of the tips.

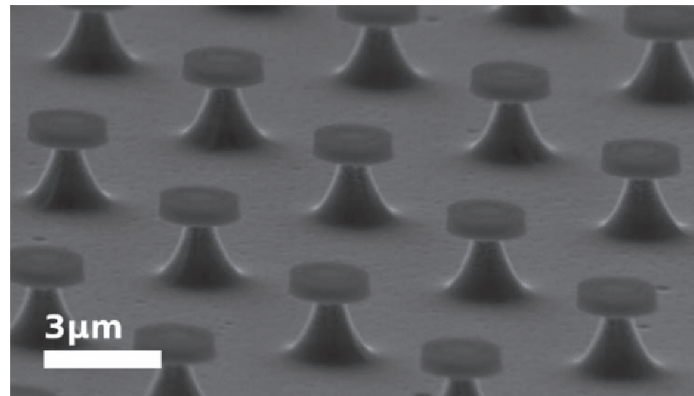


Fig. 7.5. SEM image of the silicon tips with SiO₂ mask disks after the anisotropic RIE of bulk Si [Dams12].

In the next step, the remaining silicon under the disks is wet oxidized at 940 °C in order to sharpen the tips (Fig. 7.4e). This relatively low temperature allows growing around 1 μm SiO₂ in a reasonable time and, on the other hand, keeping the oxidation rate as low as possible in order to make the process more controllable. The presence of the masking disks on the upper surface of the structures is most important at this step in order to decrease the vertical oxidation rate and, thus, to prevent blunting of the tips. The oxidation process needs to be stopped shortly after the merge of the oxidation fronts at the center of the tips. Too short oxidation times result in a circular plateau instead of a sharp tip, whereas longer oxidation times reduce the total height of the tips and, thus, the β factor. With an exact control of this step, it is possible to form sharp tips with upper curvature radius below 30 nm (Fig. 7.6). Finally, the silicon oxide layer ($\approx 1 \mu\text{m}$) is wet chemically removed by a HF-containing etchant (BOE 7:1).

The resulting silicon FE cathodes ($7 \times 7 \text{mm}^2$; top left of Fig. 7.6) contain about 3×10^5 Si tips/cm² in a triangular array with 20 μm spacing. Inspections of the tip geometries were done by a JEOL JSM-6510 SEM. About 20 tips per array at randomly chosen positions within the whole area were measured concerning their height and radius (down right of Fig. 7.6).

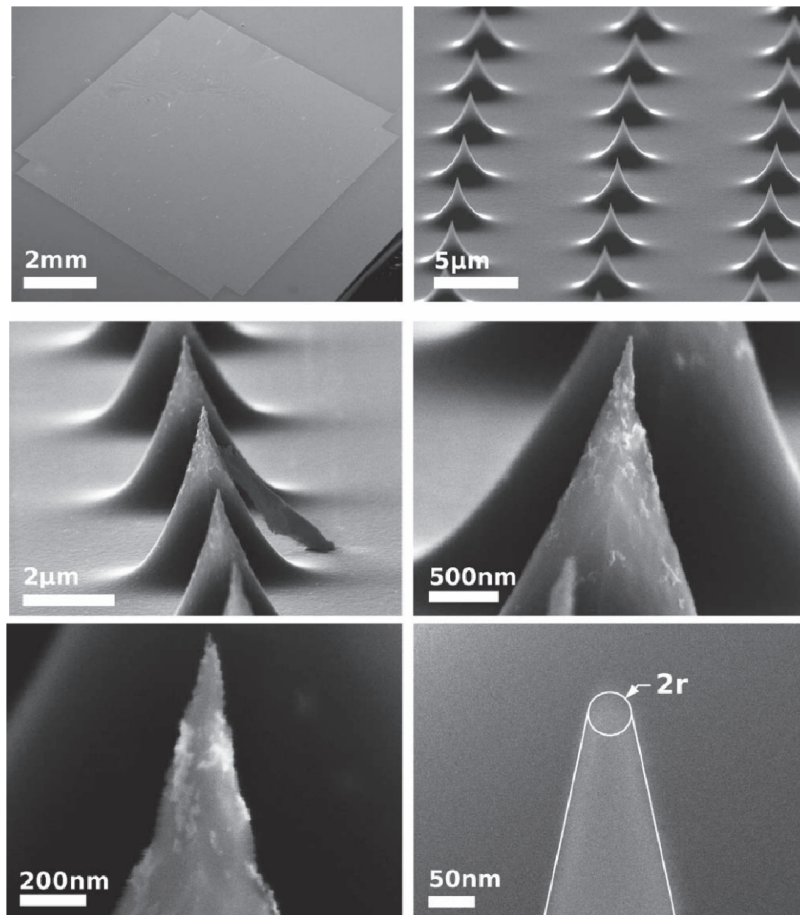


Fig. 7.6. SEM images of (7×7) mm² bare p-Si FEA and randomly chosen typical single tips [Dams12].

The tip heights were about 2.5 μm with a variation below 10%. The mean value of the tip radii over one array (p-type cathode) was 22 nm with a deviation of 15%; the deviation over a whole 4-in wafer was 25%. According to the aspect ratio h/r , the β factor is expected to be around 100 for this geometry.

In order to study the possibility to improve the lifetime, the stability, and the current carrying capability, some FEA cathodes were coated with a protecting bimetallic layer. It consists of 5 nm Cr buffer layer and 10 nm Au both deposited by means of electron beam evaporation. The Au layer is also supposed to protect Si during FE against chemical reactions with the residual gas.

Moreover, in order to systematically investigate and improve the field emission performance of p-type silicon tip arrays for pulsed sensor applications, two additional test chips which contain a series of hexagonal arrays of p-type Si-tips (wafers with a resistivity of 4 $\Omega \cdot \text{cm}$ were used) of different shape in triangular array (Fig.7.7) were fabricated by the same method as mentioned above [Dams12, Serb13]. The main parameters of these cathodes are summarized in Table 7.1.

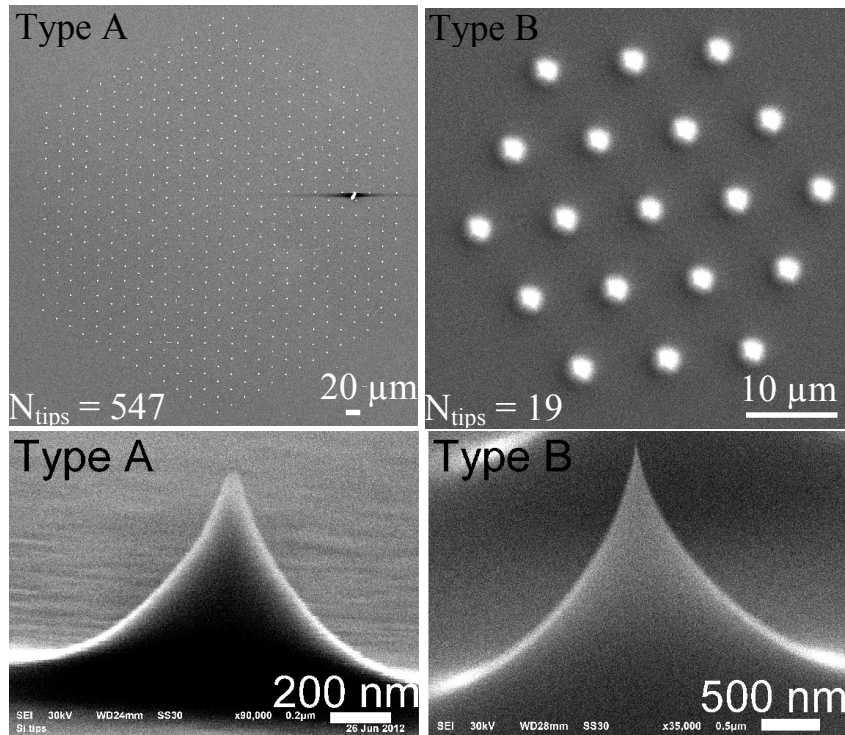


Fig. 7.7. Typical SEM images of fabricated *p*-Si arrays and single tips of types A and B.

Table 7.1. Overview of fabricated *p*-type Si-tip arrays.

Array types	Density [cm ⁻²]	Ø _{array} [μm]	Num. of tips	Tip height [μm]	Tip radius [nm]	Aspect ratio	Tip-to-tip distance [μm]	β-factor (measured)
A	3.5×10 ⁵	1	1	~ 1	< 20	> 50	20	85
		200	91					78
		520	547					127
B	1.2×10 ⁶	1	1	~ 2.5	< 20	> 120	10	158
		40	19					208
		360	1027					258
		750	4447					415

7.3 Field emission performance of highly uniform silicon emitters

Well-aligned and homogeneous emission from all types of Si tips (i.e., 100% efficiency) was reproducibly achieved at about 100 (250) V for *p* (*n*)-type bare Si tips and 350 V for metal-coated *n*-type Si tips as recorded by the regulated voltage scans at a fixed FE current of 1 nA using Ø_a = 3 μm tip anode at Δz of around 8 μm (Fig. 7.8) [Navi11a, Dams12]. The best result with amazingly homogeneous emission was achieved for bare *p*-type and metal-coated *n*-type FEAs. Previously reported FEAs with similar fabrication processes showed efficiencies less than 70% even for much smaller arrays [Günt01, Günt03, Marc90]. The increase of the onset voltage V_{on} (for 1-nA FE current) for the metal-coated

FEA can be explained by the higher work function of Au compared to that of Si and the rounding effects of the tips due to coating, resulting in a lower field enhancement factor β .

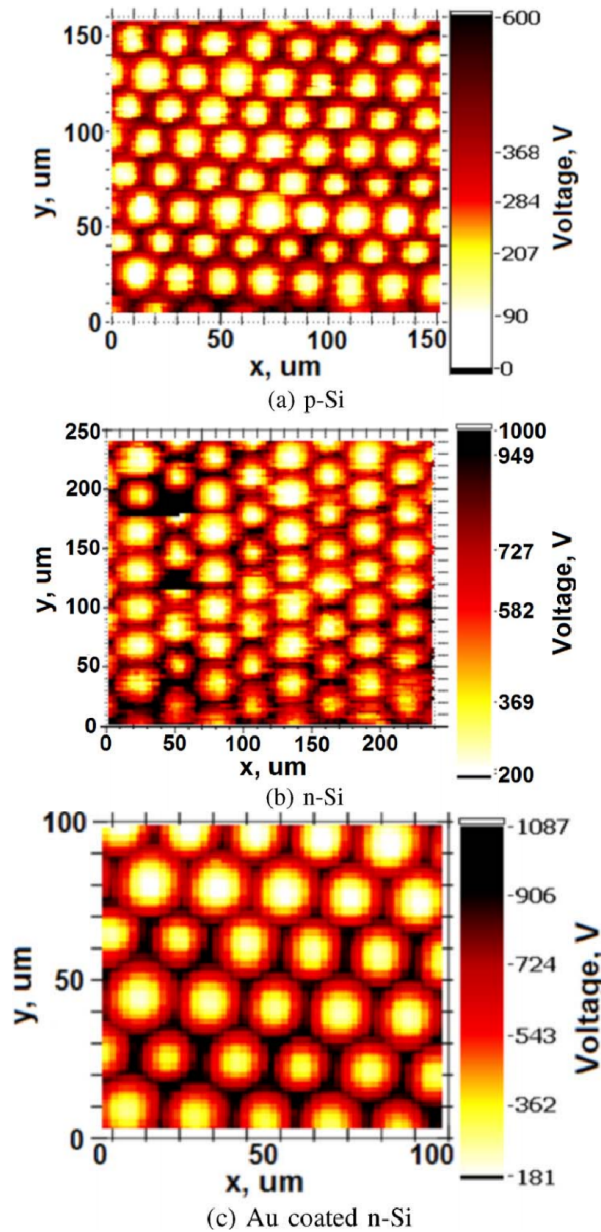


Fig. 7.8. Typical voltage maps of (a) bare p-type, (b) bare n-type, and (c) metal-coated n-type Si cathodes ($\Delta z \approx 8 \mu\text{m}$, 1-nA fixed FE current, and $\Phi_a = 3 \mu\text{m}$).

Local measurements of the p-doped Si cathodes exhibit the theoretically predicted current-voltage characteristics consisting of three sections (Fig.7.9):

- a linear FN-like part at low voltages;
- a current saturation regime starting at around 10 nA over a voltage range of about a factor of two with maximum stable currents of typically 100 nA; due to limited number of electrons or creating of a depletion area under the tip due to field penetration [Kane97];
- and, finally, a rapid current rise at high fields due to secondary charge effects (the black curve in Fig. 7.9) [Liu06b, Schr74, Navil1a].

The non-FN behavior in the current saturation region is due to a limitation of the emission current by the supply of electrons from a depletion layer created by a field penetration under the emitter tip [Kane97]. The boundaries and the location of the plateau region are determined by the size of the depletion region, which is influenced by the doping concentration [Teep05]. The use of uniformly doped substrates facilitates the uniformity of the depletion region and, finally, the FE homogeneity along the cathode arrays. Moreover, a high photosensitivity of the FE current in the saturation region was observed on the p-Si FEA that provides a unique possibility to modulate or switch the emission current by ultra short light pulses for applications in novel integrated microsystems [Schr11, Jens01, Liu06b]. Some initial study of this effect on the same cathodes is presented in [Born12].

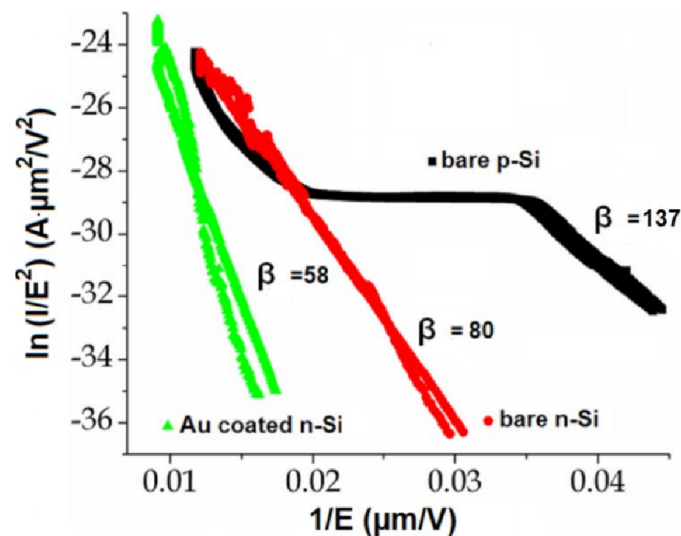


Fig. 7.9. Typical FN plots of bare p-type, bare n-type, and Au-coated n-type Si tips (integrally measured with $\varnothing_a = 100$ and $160 \mu\text{m}$ normalized to one tip, i.e., average of 30 and 75 tips, respectively).

In the case of bare and metal-coated n-type Si cathodes, the emission shows the usual FN behavior (the green and red curves in Fig. 7.9), and the current is limited only by severe tip destruction. Despite the remaining current fluctuations, maximum stable currents I_{max} of typically $0.1 \mu\text{A}$ for a single p-type Si tip and $0.6 \mu\text{A}$ for a single n-type Si tip were achieved. The current fluctuations can be explained by the native oxide, chemical reactions with residual gases, or changes in the tip geometry during operation.

Most stable and reproducible FE currents were achieved for the p-Si cathodes in the saturation region. Whereas the current fluctuations in the linear range of the FN plot were from 25% to 40% standard deviation, the fluctuations in the saturation range remained below 4% (Fig. 7.10a, b), i.e., the decrease of the noise level by one order of magnitude. This is in agreement with previously obtained results using similar p-Si FEAs [Teep05]. The FE current stability tests of the bare n-type FEA showed similar results as for the p-type ones in the

linear range with current fluctuations typically below 20% (Fig. 7.10c). The Au-coated Si tips exhibit an improved stability ($< 10\%$ standard deviation as compared to the average current; Fig. 7.10d) as well as for repeated I-V measurements.

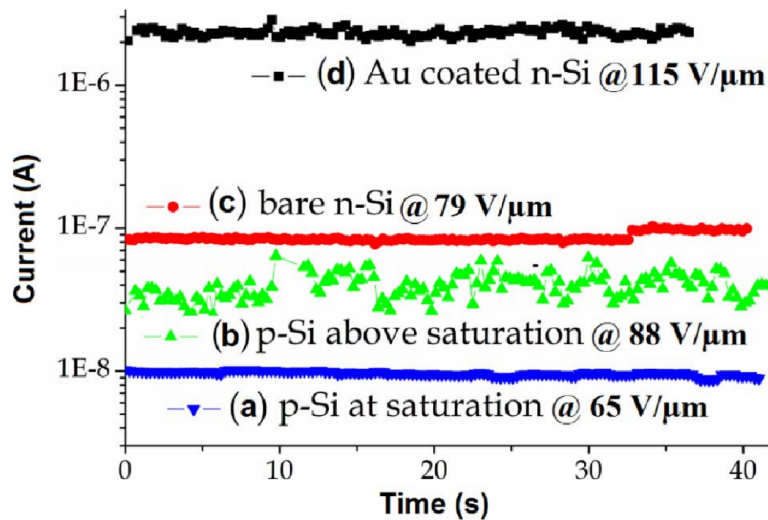


Fig. 7.10. Results of the current stability tests of single tips of the FEAs locally measured with $\varnothing_a = 3 \mu\text{m}$ at the given constant field (voltage).

Moreover, the additional metallic coating of the n-type FEA cathodes resulted in at least five times higher average maximum FE current ($\approx 3 \mu\text{A}$) compared to the bare ones (Fig. 7.11). The coating leads, however, to an increase of the onset voltage by about 30%. It was interesting to observe also the clear inverse correlation between the I_{max} and β factors of the three different types of FEAs (Fig. 7.11).

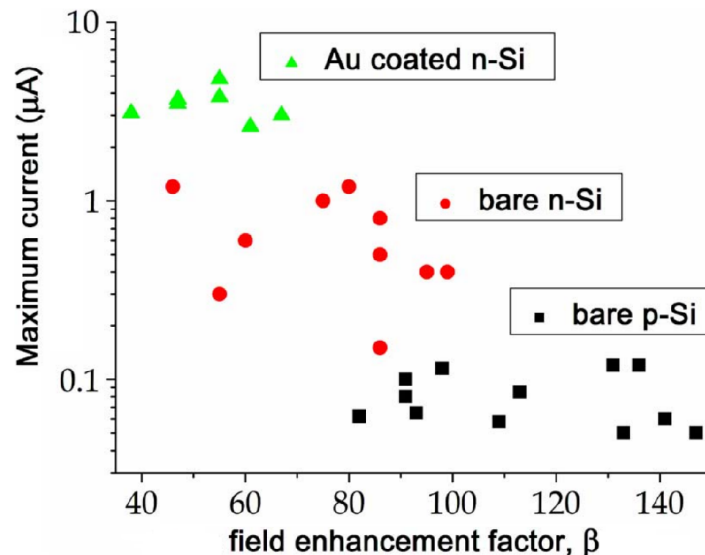


Fig. 7.11. Maximum current capability of single tips of the FEAs as a function of the β factor locally measured with $\varnothing_a = 3 \mu\text{m}$ without considering the field weakening due to the tip anode geometry.

It shows the possibility to find a compromise between a low onset voltage with sharp tips and high I_{max} of conical-shaped or metal-coated tips. The higher field enhancement factor

of the p-type tips compared to that of the n-type tips can be explained by the smaller substrate diameter of the n-type wafers (2 in instead of 4 in). The same process parameters were used for both substrates, which results in different anisotropy factors and, hence, different tip shapes. The average β factors and deviations ($58\% \pm 5\%$ for Au-coated Si, $80\% \pm 8\%$ for bare n-type Si, and $137\% \pm 15\%$ for p-type Si tips) derived from the FN plots (assuming work functions of 4.5 (4.8) eV for p- (n-) type Si and 5.1 eV for Au) are in good agreement with the ones expected from the tip geometry. The scatter of the β factor can be explained by the aforementioned remaining slight variation of the tip geometry over the full area of the cathode. It should be mentioned that the obtained values of the applied field (voltage) and β factor are more relevant for the actual measurement geometry than for real triode devices, where the shape of the gate and the gap has to be taken into account too [Zhir01, Zhon02].

7.2. Properties of single p-Si tips, optical current modulation and current scaling

In order to check the FE properties of the different types of B-doped Si tips (see Tab. 7.1), local FESM measurements were performed with a suitable tungsten anode (diameter $\varnothing_a = 3 \mu\text{m}$ for a gap $\Delta z = 10 \mu\text{m}$). At first, the dark current without light exposure was measured over the full voltage range. In Fig. 7.12, the measured current-voltage characteristics I-V and corresponding Fowler-Nordheim plots of the single p-type Si-tips are shown. For both types some unsteadiness effects were observed at low currents probably caused by the presence of adsorbates and native silicon oxide or a change of the tip shape.

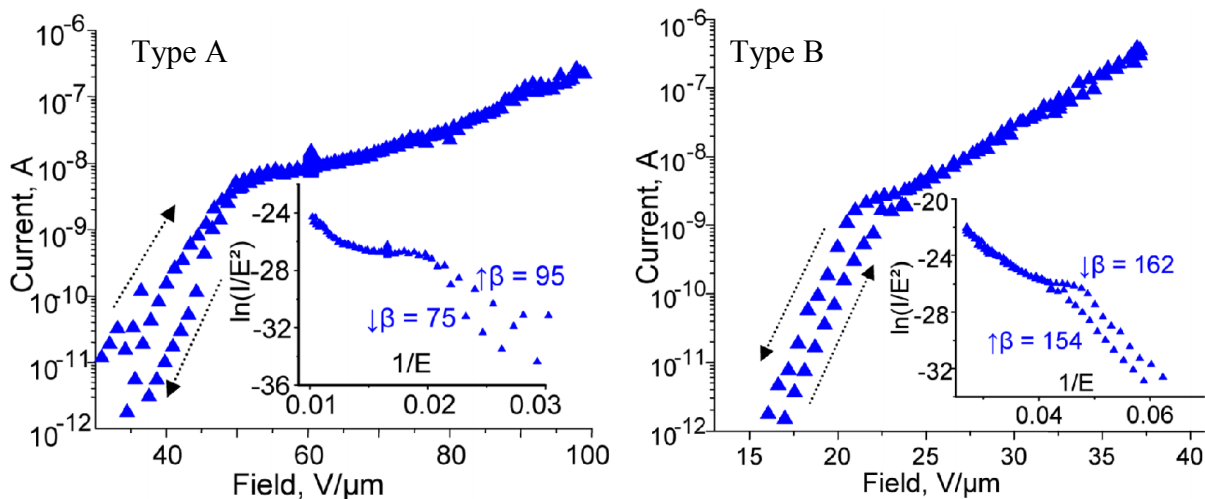


Fig. 7.12. I-V curves and corresponding FN-plots (insets) of single p-Si tip of different types.

The field enhancement factor β was derived from the resulting linear region of the FN plots assuming a work function of about 4.8 eV, which was determined by means of field emission spectroscopy [Born12]. As expected, lower average β values of 85 were obtained for

type A as compared to 158 for type B. Both values are in fair agreement with the calculated ones from Fig. 7.2. The current saturation which follows at field levels of about $50 \text{ V}/\mu\text{m}$ (type A), respectively, $20 \text{ V}/\mu\text{m}$ (type B) is caused by the occurrence of a charge depletion layer due to field penetration into emitter that is well known for p-type Si tips [Abou95, Liu06b, Qing97]. It is remarkable that the height and width of the current plateau depend on the tip geometry, too. The shorter tip A saturates at 10 nA until $65 \text{ V}/\mu\text{m}$, but the higher tip B at 3 nA until $25 \text{ V}/\mu\text{m}$. These different current values suggest that the depth to which the electric field penetrates into the silicon tip is larger for the higher tip. Accordingly, the following secondary charge generation [Schr74, Liu06b] is also more pronounced for the sharper tip. The maximum currents are limited by increasing current fluctuations for both types of tips at about 350 nA despite of the different field levels.

For sensor applications, the current plateau range of both Si tips is most attractive. As obvious in Fig. 7.12, it provides a much higher current stability ($< 5\%$) than the low ($> 50\%$) and high current regimes ($> 30\%$). The suppression of short-term current fluctuations due to carrier depletion is clearly demonstrated in Fig. 7.13.

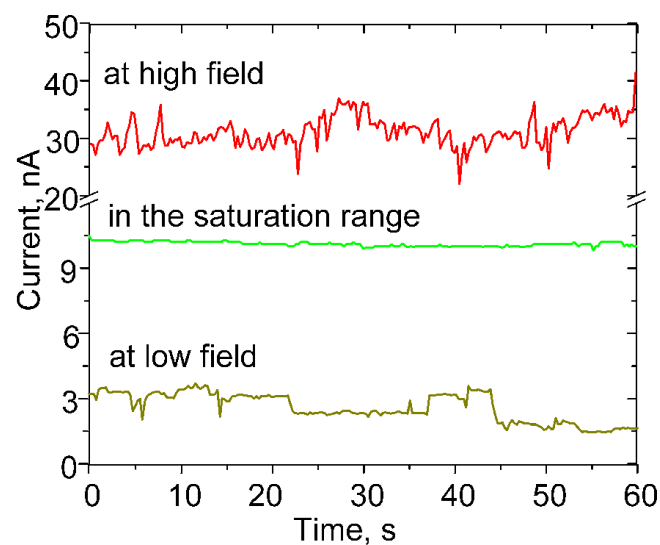


Fig. 7.13. Current stability of the single p-Si tip (type A) in three different current ranges.

The limited number of electrons in the conduction band, however, can be significantly enhanced by visible light illumination. The resulting photosensitivity of the FE current in the plateau range was investigated by means of a halogen lamp (KL 1500 LCD) which provides a spot light from the side of the Si tip as shown in Fig. 7.14.

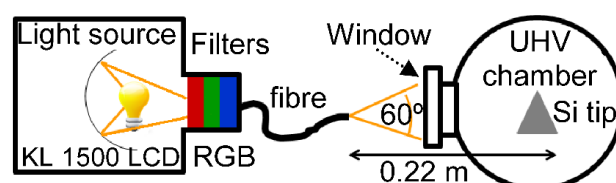


Fig. 7.14. Schematic of the experimental setup used for the illumination of the single tip.

Depending on the light intensity, a reproducible current switching from 5 up to 13 nA is obtained as shown in Fig. 7.15. The spectral dependence of this effect was further investigated with color filters in the halogen lamp and presented in Fig. 7.16. An optical current switching ratio of 2.28, 1.31, and 1.32 was reproducibly achieved for red, green, and blue filters, respectively. By taking the different intensities for each color into account (see inset of Fig. 7.16), the resulting intensity-normalized values of 2.3, 2.7, and 12 confirm qualitatively the expected dependence on the quantum energy.

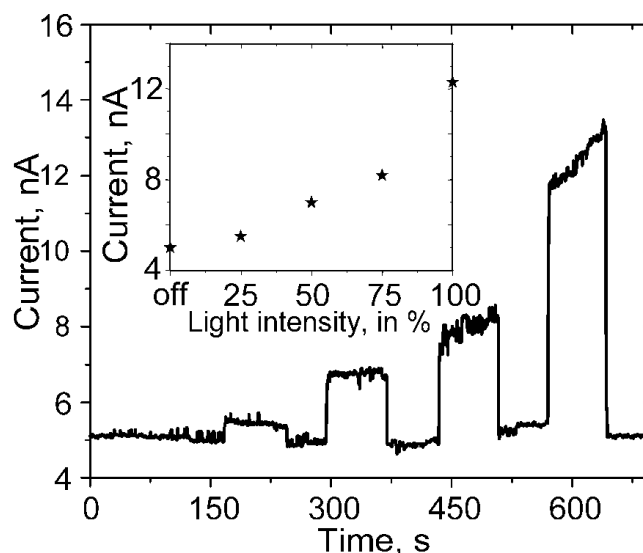


Fig. 7.15. FE current for different light intensities (inset) on the single p-type Si tip (type A).

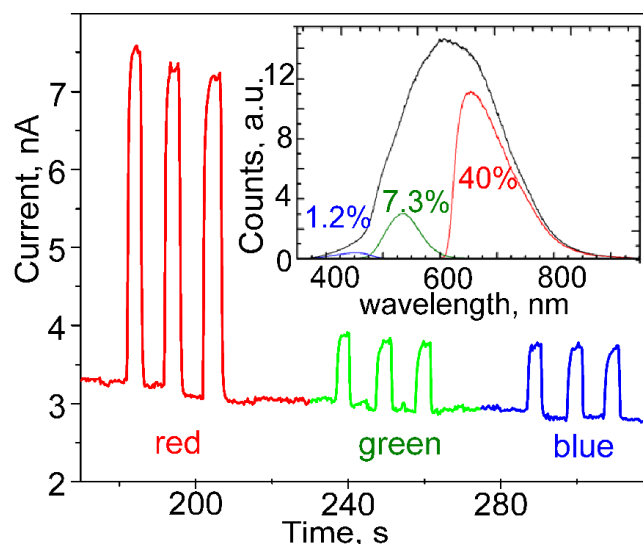


Fig. 7.16. FE current switching of the single p-Si tip (type B) under halogen-lamp illumination. Inset: spectrum of the halogen lamp (black line, $T_{color} = 2750^{\circ}\text{C}$) and spectra for red, green, and blue filters. The relative intensity for each filter is denoted.

The FE homogeneity and efficiency of the hexagonal Si tip arrays of both types were investigated by regulated voltage scans for a fixed current of 1 nA [Lyse06]. Typical voltage maps for arrays of 547 (type A) and 19 Si tips (type B) are shown in Fig. 7.17.

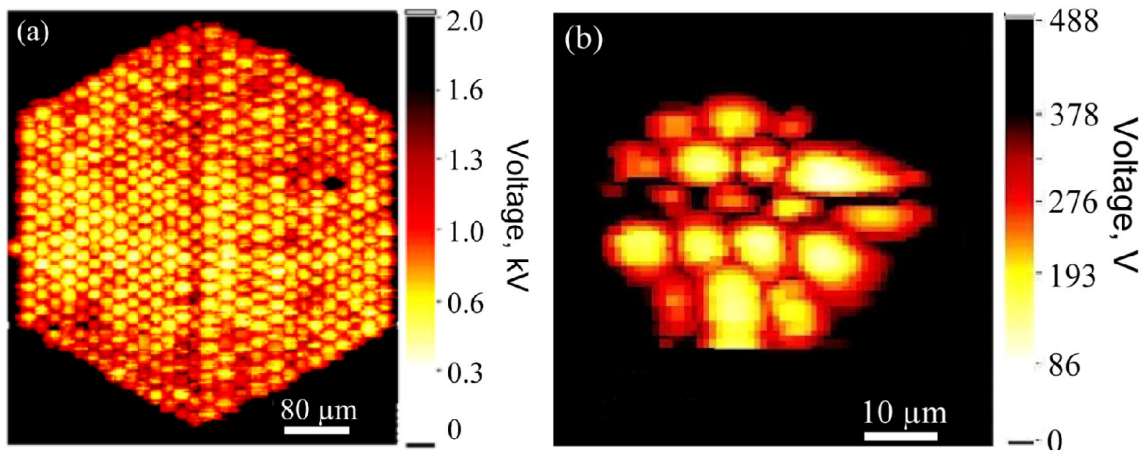


Fig. 7.17. Voltage maps ($\varnothing_a = 3 \mu\text{m}$, $\Delta z = 8 \mu\text{m}$) for 1 nA FE current of the arrays with (a) 547 Si tips of type A and (b) 19 Si tips of type B. The arrays are same as in fig. 7.7.

Almost all tips emit in the voltage range 400-700 V for the larger array and 80-220 V for the smaller array. Similar results were obtained for the other arrays, which yielded 80%-99% efficiency of the tips. The remaining spread of onset field, however, reflects a significant variation of the actual β factor (i.e., barrier width) and/or a varying influence of adsorbed gases and oxides on the tip surface (i.e., different barrier height).

The total FE current of the complete arrays was determined with truncated-cone shaped anodes of adjusted size. The results obtained for several Si tip arrays of both types are given in Fig. 7.18.

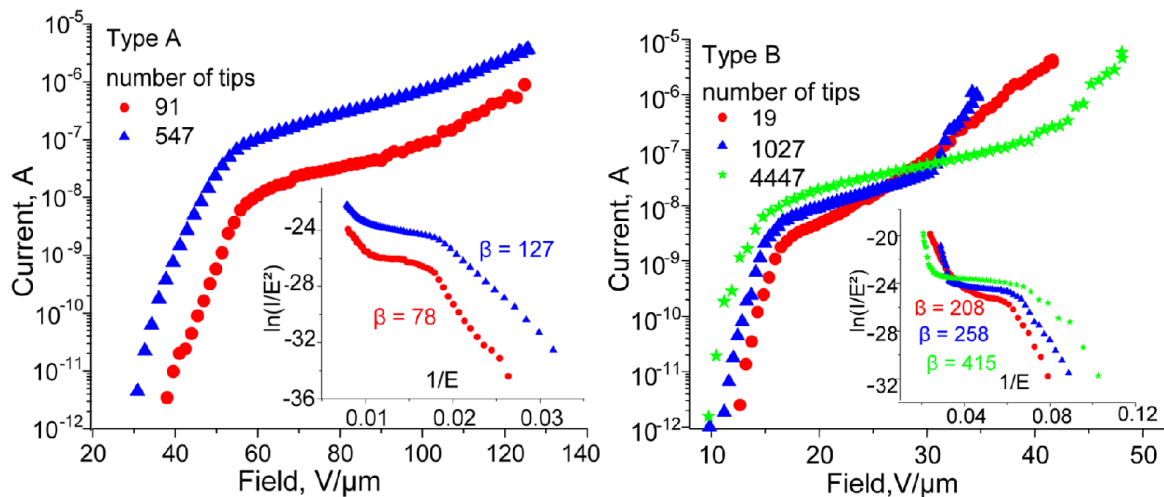


Fig. 7.18. I - V curves and corresponding FN-plots (inset) of integral current from various p -Si-tip arrays.

It is remarkable that the plateau range is still well defined despite of the varying onset field. The current plateau always starts at a field around 55 (16) $\text{V}/\mu\text{m}$ for the arrays with short (long) tips, but its width strongly increases with the number N of tips. Moreover, the β factor derived from the FN-slope at low fields also increases with N as can be seen from Table 7.1. The increase of the β factor as well as the shift of the center of the plateau range

can be explained by the dominant FE of the sharpest tip in each array. The total FE current of the arrays was most stable in the plateau range, e.g. the current fluctuations stayed within 1% over 1 h for the array with 547 tips. This improved stability in comparison to the single tips is expected from statistical considerations.

Finally, the increase of the height of the integral current plateau with the total number of tips N stays clearly below the predicted linear dependency due to the remaining inhomogeneities as can be seen from Fig. 7.19.

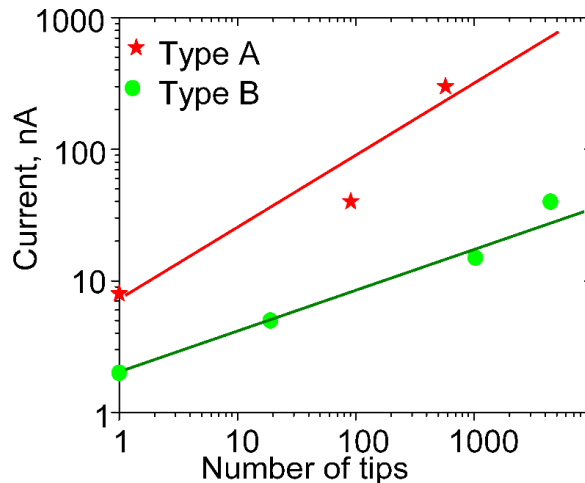


Fig. 7.19. Total FE current as function of the number of tips for all arrays.

Obviously higher total currents are achievable for the short Si tips (type A). Moreover, the resulting slope of the current scaling in the middle of the plateau region is 0.5 for the short tips (at 75 and 90 V/ μm for 91 and 547 tips, respectively) but only 0.35 for the long tips (at 20, 25, and 30 V/ μm for arrays with 19, 1027, and 4447 tips, respectively). Therefore, a trade-off between large integral currents and low operation field of the p-type Si-tip arrays must be considered for actual device applications.

7.3. Conclusions and outlook

Well-aligned and homogeneous FE from three types of Si-based FEAs has been reproducibly achieved. The optimized fabrication process based on the well-characterized silicon microstructuring technology described here opens the possibility to build advanced vacuum microelectronic devices as well.

Previously reported problems of Si FEAs like poor reproducibility, large relative deviation of tip geometry, and many nonworking tips [Wang04, Günt01, Günt03, Teep05, Ding02] could be partially solved by an improved tip geometry (moderately sharpened tips) and by the usage of the aforementioned optimized fabrication techniques.

Depending on the requirements of applications, it is possible to find a compromise between the low onset voltage of sharp whisker-like tips and the high maximum current capability of metal-coated or cone-shaped ones by tailoring the silicon tip geometry or by application of additional metal coating layers.

The systematic variation of the shape of B-doped Si tips and the size of hexagonal tip arrays and detailed measurements of single tips and tip arrays have revealed a deeper understanding of their FE properties. It was found that the operation field decreases with the height of the emitters, but the achievable integral current of the arrays in the most stable and highly photosensitive plateau region is higher for the smaller tips. The observed dependency of the photosensitivity on the wavelength of the illuminated light is very promising effect which may lead to further applications. An extended experimental setup including a widely tunable laser and an electron spectrometer is now under preparation.

Further investigation and improvement of the tip uniformity and FE homogeneity is required for the optimization of the Si-tip arrays for specific sensor applications. Moreover, the fabrication process should be extended to the integration of gate and focusing electrodes as well as of additional semiconductor components.

8. Thesis summary and outlook

The aim of this research was the fabrication of various types of nanostructures and their application-oriented investigation for using in vacuum electronics as field emission cathodes. Various techniques including scanning electron microscopy with energy-dispersive X-ray analysis, field emission scanning microscopy and integral measurement system with luminescent screen were used to study emission properties of nanomaterials and to reveal mechanisms accompanying this phenomenon.

In this study, for the first time, high-purity single-walled CNT networks were grown on n-type Si substrates by using recently developed CVD process based on the designed reactor with high and low temperature zones. This CVD process separates the catalytic pyrolysis of hydrocarbons at typically $\sim 700\text{-}800^\circ\text{C}$ from the growth of CNTs on the substrates at $\sim 100\text{-}150^\circ\text{C}$. The method allows the growth of horizontally aligned networks of highly entangled CNTs. Above the rather dense and some μm thick CNT floor, a thin layer of sparsely distributed single wall CNTs is present which should results in much reduced mutual shielding and very high field enhancement. In order to optimize the fabrication parameters of the CNTs and to evaluate their suitability for cold cathode devices, a series of cathodes with varying thickness has been grown on n-Si substrates. The results show well-homogeneous FE with $\sim 10^4$ emitters/ cm^2 at an electric onset field of ~ 4 V/ μm . The current carrying capability of the CNT networks was locally measured with a $\text{Ø}150$ μm anode which reproducibly yielded around 100-220 μA stable and up to 400-500 μA maximum current. The field enhancement factors derived from the non-saturated region of the FN-plot assuming a work function value of about 4.9 eV for carbon were more than 550. The integral measurements of the cathodes confirmed the emission homogeneity of the whole cathode area and revealed a maximum achievable current of at least 10 mA/ cm^2 . Samples with sparsely distributed hills of entangled CNT demonstrated lower onset and operation field as well as more stable FE current compared to the more dense ones. Effective FE cathodes for various vacuum devices which require a low onset field, high number density, and high current capability but not well-defined positioning of the emitters can be designed out of this material, e.g. flat cathode luminescent lamps.

In order to get high FE current by increasing the number of CNTs and to improve the contact interface, arrays of entangled CNT bundles of 1×2 μm^2 size and up to 2 μm height and 100, 10 or 5 μm pitch were grown onto highly-doped n-Si wafers with patterned trimetallic Mo/Al/Ni catalyst layers by chemical vapour deposition based on the pyrolysis of decane or ethanol at $680\text{-}700^\circ\text{C}$ under atmospheric pressure. Arrays with large pitch showed

high efficiency and good alignment of strong emitters at an onset field of about $15 \text{ V}/\mu\text{m}$. For small pitch, however, randomly but well-distributed emitters ($> 2500/\text{mm}^2$) could be resolved at similar field levels. During local measurements with an anode of $\text{Ø } 150 \mu\text{m}$, stable currents up to $\sim 50 \mu\text{A}$, $\sim 250 \mu\text{A}$ and $\sim 500 \mu\text{A}$ at 400 V were achieved for cathodes with a pitch of $100 \mu\text{m}$, $10 \mu\text{m}$ and $5 \mu\text{m}$, respectively. Integral pulsed measurements of the whole selected cathode with $p = 5 \mu\text{m}$ showed fairly homogeneous FE at $100 \text{ mA}/\text{cm}^2$ on the luminescent screen and maximum current densities up to $4.4 \text{ A}/\text{cm}^2$ with a Cu anode. Future work should be focused on the achievement of FE homogeneity and current stability from these cathodes, which might be improved by vertically-aligned CNTs grown using a plasma enhanced CVD method.

Rounded CNT columns of about $20 \mu\text{m}$ diameter and $5 \mu\text{m}$ height in an asymmetric triangular array of 256 and $270 \mu\text{m}$ pitch were grown on p-Si substrates with bimetallic (aluminum and patterned iron) catalyst by chemical vapor deposition based on the pyrolysis of ethylene. The voltage maps yielded 100% efficiency and good alignment of the CNT emitters at $E_{\text{on}} (1\text{nA}) \sim 11\text{-}18 \text{ V}/\mu\text{m}$. Local FE investigations of single columns revealed the current saturation above $1\text{-}2 \mu\text{A}$ at $\sim 20 \text{ V}/\mu\text{m}$. Above $40\text{-}60 \text{ V}/\mu\text{m}$, however, irreversible current jumps up to $10\text{-}40 \mu\text{A}$ occurred reproducibly for all measured emitters. Finally, stable FN-like current-voltage curves up to the maximum current of $\sim 40 \mu\text{A}$ were obtained. By using the energy band diagram, the observed current saturation and current jumps were explained not by the limited supply of electrons from the p-type substrate, but by the presence of a thin oxide layer between Si and Al/Ni/CNT interface and its electrical breakdown at high fields.

Vertically aligned CNT-columns of $250\text{-}\mu\text{m}$ -diameter and different height of $70 \mu\text{m}$ and $350 \mu\text{m}$, which forms quadratic arrays with a pitch of $650 \mu\text{m}$ were grown on highly-doped n-type silicon substrates by means of hot-filament chemical vapor deposition. Fairly-aligned FE from both types of CNT arrays was obtained at $E_{\text{on}} (1\text{nA}) = 2 \text{ V}/\mu\text{m}$. Local measurements on a single CNT column yielded maximum current values up to $600 \mu\text{A}$, which were achieved independent of the column height. Assuming a work function of 4.9 eV , the resulting β values are 1112 (831) for the CNT-columns of 70 (350) μm height. Thus, the experiment revealed that the FE current does not depend on the CNT height, but is determined by the CNTs outgrowth. As a step towards application, investigation of single CNT columns of 1.5 mm diameter and $250 \mu\text{m}$ height, was performed. Based on the electron trajectory simulation results, a triode construction (planar copper gate with a conical hole of $2.5/3.5 \text{ mm}$ in diameter, thickness $500 \mu\text{m}$) at a fixed anode-gate distance of 6.5 mm was realized. By

varying the cathode-gate distance from 500 to 800 μm and the anode voltage from 1 kV to 2.5 kV, the highest cathode-to-anode current ratio of $\sim 97\%$ at ~ 240 gate and 2.5 kV anode voltage and the cathode-gate distance of 500 μm was achieved.

Highly-dense CNW films ($35\text{-}300 \mu\text{m}^{-2}$) were grown on silicon and stainless steel substrates using inductively/capacitively coupled plasma-enhanced chemical vapor deposition. In order to decrease the shielding effect, structuring of the CNW films was successfully performed with a pulsed power laser. After the laser treatment CNW-patches with a nominal size of about $20 \times 20 \mu\text{m}^2$ demonstrated the variation of the geometry. Medium resolution V-maps showed that nearly all CNW-patches of both cathodes emit fairly aligned at fields of 10 - 20 $\text{V}/\mu\text{m}$, however, the homogeneity is rather limited due to the varying shape of the CNW-patches. The number of emitting sites of about 9×10^3 emitters/ cm^2 and 20×10^3 emitters/ cm^2 at 10-20 $\text{V}/\mu\text{m}$ have been estimated for CNWs on Si and stainless steel, respectively. Stable current values per individual emission patch varied between 1 μA and 100 μA for both types of cathodes.

Sharp and mechanically stable metallic nanocones with high aspect ratio, good conductivity and solid contact interface were successfully fabricated by potentiostatic electrodeposition of copper in asymmetrically etched ion-track membranes. Depending on the fabrication parameters, randomly distributed and freestanding copper nanocones of $\sim 28 \mu\text{m}$ length, $\sim 2.2\text{-}3 \mu\text{m}$ base, with different $\sim 60\text{-}300 \text{ nm}$ tip radius and number density were fabricated. It was shown that depending on the conditions of the ion-track etching, electrochemical filling and position of the foils in the stack, the stability and uniformity of these Cu-NCs can be controlled. For instance, the electrodeposition voltage of 40 mV is favourable due to a slow growth rate, resulting in uniform and mechanically stable Cu-NCs with completely filled contact interface, while fast growth at 90 mV started preferentially at the ring-like base structures and led to a rough cone surface. It has also been shown that the size of the conical pores in the membranes and hence of the Cu-NCs depends not only on the etching time but also on the stack position. Sharper Cu-NCs for the foil in the first stack position can be obtained rather than for the third one, as well as the sharpest Cu-NCs might be grown using a polycarbonate foil irradiated with ^{136}Xe ions rather than ^{238}U ones.

FE measurements of the unstructured cathodes with slowly-grown Cu-NCs of high number density (10^7 cm^{-2}) and excellent mechanical stability yield stable currents between 1-280 μA from an emission spot of 30 μm , while the other unstructured cathode with the same number density and applied fields, but with fast-grown Cu-NCs yield stable current between 0.1 and 20 μA . This confirms the importance of a solid contact of the Cu-NC to the substrate

for high current limits. In comparison, the structured cathodes with slowly-grown Cu-NCs of less number density ($<10^6 \text{ cm}^{-2}$) provide rather low current levels of 10-100 μA , however, the operating field levels are also much lower (3-4 times) than for the cathode with 10^7 cm^{-2} . In addition, a series of structured Cu-NC-based cathodes with reduced number density of about 10^5 cm^{-2} , demonstrated the average current of 30 μA per patch at 32 V/ μm . The FE performance of that cathode was greatly improved by a thin Au coating resulting in the average current of 151 μA .

Current carrying capability of single Cu-NC emitters was investigated. The maximum FE currents from a single bare Cu-NC varied between 11 nA and 470 nA. SEM analysis revealed some morphological changes of the Cu-NC tip ends, which are explained by Rayleigh instability. Integral FE measurements on 10 nm Au-coated Cu-NC cathode of 25 mm^2 showed fairly homogeneous FE at 64 $\mu\text{A}/\text{cm}^2$ on the luminescent screen and maximum current densities up to 8 mA/cm^2 with a Cu anode.

Silicon-based cathodes with precisely aligned field emitter arrays applicable for miniaturized electron sources were successfully fabricated. Rather homogeneous and well-aligned field emission from all tips (i.e. 100% efficiency) and maximum stable currents of typically 0.1 μA for p- and 0.6 μA for n-type Si were reproducibly achieved. Current-voltage characteristics of single p-type Si tips exhibit the expected saturation at around 10 nA due to the limited supply of electrons from the conduction band, while the n-type Si tips show the usual FN behaviour. Additional coating of the Si tips with Au layer resulted in at least 5 times higher average FE current levels but lead, however, to a 30% increase of the onset voltage.

In order to improve the field emission homogeneity and stability of p-type silicon tip arrays for pulsed sensor applications, the influence of the fabrication parameters on the tip shape and on the specific operating conditions was investigated. Based on detailed design calculations of the field enhancement, two series of hexagonal arrays of B-doped Si-tips of different height (1 and 2.5 μm) and number density (3.5×10^5 and $1.2 \times 10^6 \text{ cm}^{-2}$) were fabricated. Local measurement results on single emitters showed that the current saturation value and onset field depend on the tip geometry: the onset field is lower; however, the saturation region is lower and narrower for higher tips. In the saturation region, due to the limited number of carriers in the depletion region, single tips provide the highest current stability ($<5\%$) and optical current switching ratio (~ 2.5). The results of integral measurements on arrays with different number of p-Si emitters showed that the emission current is not linearly scaled and the width of plateau strongly increases with the number of

tips. From these results, a trade-off between large integral currents and low operation field of p-type Si arrays must be considered for device applications.

To sum up, the results presented here are important from both theoretical and practical points of view. New materials were fabricated and investigated, most of them showed better results than previously reported [Günt01, Günt03, Lyse06, Dang07, Navi10]. It was shown that CNT-based cathodes are suitable for high current applications, e.g. compact X-ray source, while particularly metal and semiconductor nanostructures require additional research and improvements, in order to become suitable for practical applications.

References

A

- [Abou95] A. Aboubacar, A. Chbini, M. Dupont, J. Gardes, M. Laguna, and M. Querrou, "Silicon cathodes with array of tips used as pulsed photoemitters", *J. Vac. Sci. Technol. B* 13, 616 (1995).
- [Afra13] B. Afra, M.D. Rodriguez, C. Trautmann, O.H. Pakarinen, F. Djurabekova, K. Nordlund, T. Bierschenk, R. Giulian, M. C. Ridgway, G. Rizza, M. Toulemonde, and P. Kluth, "Small angle X-ray scattering investigations of the morphology of swift heavy ion tracks in α -quartz", *J. Phys.: Condens. Matter* 25, 045006 (2013).
- [Aika12] S. Aikawa, E. Einarsson, T. Thurakitserree, S. Chiashi, E. Nishikawa, and S. Maruyama, "Derormable transparent all-carbon-nanotube transistirs", *Appl. Phys. Lett.* 100, 063502 (2012).
- [Alak13] M. Alakhras, R. Bourne, M. Rickard, K. Ng, M. Pietrzyk, and P. Brennan, "Digital tomosynthesis: A new future for breast imaging?", *Clinical Radiology* 68, e225 (2013).
- [Albe11] I. Alber, J. Krieg, C. Mueller, M. E. Toimil-Molares, C. Trautmann, P. Serbun, F. Jordan, A. Navitski, and G. Mueller, "Freestanding copper nanocones for field emission by ion-track technology and electrodeposition", *Technical Digest, 24th Int. Vacuum Nanoelectronics Conference, Wuppertal, IEEE Cat. No. CFP11VAC-PRT*, p. 106 (2011).
- [Alex07] S. Alexandrov, A. Arkhipov, M. Mishin, and G. Sominski, "Carbon-film field emission cathodes in a compact orbitron-type ionization vaccum sensor", *Surf. Interface Anal.* 39, 146 (2007).
- [Alfe67] M. Alferieff and C. Duke, "Field ionization near nonuniform metal surfaces", *J. Chem. Phys.* 46, 938 (1967).
- [Apel98] P. Apel, A. Schulz, R. Spohr, C. Trautmann, and V. Vutsadakis, "Track size and track structure in polymer irradiated by heavy ions", *Nucl. Instr. Methods in Phys. Res. B* 146, 468 (1998).
- [Apel01a] P. Apel, Y. Korchev, Z. Siwy, R. Spohr, and M. Yoshida, "Diode-like single-ion trtack membrane prepared by electrostopping", *Nucl. Instr. Methods in Phys. Res. B* 184, 337 (2001).
- [Apel01b] P. Apel, "Track etching technique in membrane technology", *Radiation Measurements* 34, 55 (2001).
- [Arth65] J. Arthur, "Photosensitive field emission from p-type germanium", *J. Appl. Phys.* 36, 3221 (1965).
- [Artu05] E. Artukovic, M. Kaempgen, D. Hecht, S. Roth, and G. Grüner, "Transparent and flexible carbon nanotube transistors", *Nano Lett.* 5, 4 (2005).
- [Azam10] S. Azam and Q. Wahab, "The present and Future trends in high power microwave and millimeter wave tachnologies, advanced microwave and millimeter wave technologies semiconductor devices circuits and systems", Moumita Mukherjee (Ed.), ISBN: 978-953-307-031-5, In Tech (2010).

B

- [Band13] D. Bandurin, V. Kleshch, E. Smolnikova, I. Obronov, A. Nasibulin, E. Kauppinen, and N. Obraztsov, "Scanning anode field emission microscopy of nanocarbons", *J. Nanoelectronics and Optoelectronics* 8, 114 (2013).
- [Bark05] R. Barker, J. Booske, N. Luhmann, and G. Nusinovich, "Modern microwave and millimeter-wave power electronics", Wiley-IEEE Press (2005).
- [Bari11] M. Bari, "Fabrication, characterization and modeling of self-assembled silicon nanostructure vacuum field emission devices", PhD thesis, Bangladesh University of Engineering and Technology (2011).
- [Bask71] L. Baskin, O. Lvov, and G. Fursey, "General features of field emission from semiconductors", *Solid State Phys.* 47, 49 (1971).
- [Barb53] J. Barbour, W. Dolan, J. Trolan, E. Martin, and W. Dyke, "Space-charge effects in field emission", *Phys. Rev.* 92, 45 (1953).
- [Bark01] D. Barkley and H. Dong. Oral presentation at the 2001 International Meeting in San Francisco (Electrochemistry Society and International Society of Electrochemistry). Abstract. (2001).
- [Born12] B. Bornmann, S. Mingels, F. Dams, C. Prommesberger, R. Schreiner, D. Lutzenkirchen-Hecht, and G. Muller, "Electron spectrometer in adjustable triode configuration for photo-induced field emission measurements", *Rev. Sci. Instrum.* 83, 013302 (2012).
- [Borz66] P. Borzuyak, A. Yatsenko, and L. Miroshnichenko, "Photo-field-emission from high-resistance silicon and germanium", *Phys. Status. Solidi* 14, 403 (1966).
- [Bona98] J. Bonard, J. Salvétat, T. Stöckli, W. Heer, "Field emission from single-wall carbon nanotube films", *Appl. Phys. Lett.* 73, 918 (1998).
- [Bona01a] J. Bonard, H. Kind, T. Stöckli, and L. Nilsson, "Field emission from carbon nanotubes: the first five years", *Solid-State Electronics* 45, 893 (2001).
- [Bona01b] J. Bonard, N. Weiss, H. Kind, T. Stockli, L. Forro, K. Kern, and A. Chatelain, "Tuning the field emission properties of patterned carbon nanotube films", *Adv. Mat.* 13, 184 (2001).
- [Bona03] J. Bonard, C. Klinke, K. Dean, and B. Coll, "Degradation and failure of carbon nanotube field emitters", *Phys. Rev. B* 67, 115406 (2003).
- [Boos08] J. Booske, "Plasma physics and related challenges of millimeter-wave-to terahertz and high power microwave generation", *Phys. Plasmas* 15, 055502 (2008).
- [Boos11] J. Booske, R. Dobbs, C. Joye, C. Kory, G. Neil, G. Park, J. Park, and R. Temkin, "Vacuum electronic high power terahertz sources", *IEEE Trans. Terahertz Science and Technology* 1, 54 (2011).
- [Brau98] C. Brau, "High-brightness electron beams small free-electron lasers", *Nucl. Instrum. Methods Phys. Res. A* 407, 1 (1998).
- [Brit] <http://www.britannica.com>
- [Brod89] I. Brodie, "Physical consideration in vacuum microelectronics devices", *IEEE Trans. Electron Devices* 36, 2641 (1989).

-
- [Brod94] I. Brodie and P. Schwoebel, "Vacuum Microelectronic devices", Proceedings of the IEEE, 82, 1006 (1994).
- [Buld03] A. Buldum and J. Lu, "Electron field emission properties of closed carbon nanotubes", Phys. Rev. Lett. 91, 236801 (2003).
- [Burg53] R. Burgess, H. Kroemer, J. Houston, "Corrected values of Fowler-Nordheim field emission function $v(y)$ and $s(y)$ ", Phys. Rev. 90, 515 (1953).
- [Bust92] H. Busta, "Vacuum microelectronics", Journal of Micromechanics and Microengineering 2, 43 (1992).

C

- [Coll97] P. Collins and A. Zettl, "Unique characteristics of cold cathode carbon-nanotube-matrix field emitters", Phys. Rev. B 55, 9391 (1997).
- [Coll00] P. Collins, K. Bradley, M. Ishigami, and A. Zettl, "Extreme oxygen sensitivity of electronic properties of carbon nanotubes", Science 287, 1801 (2000).
- [Cool13] W. Coolidge, "A powerful Röntgen ray tube with a pure electron discharge", Phys. Rev. 2, 409 (1913).
- [Chen03] C. Chen and M. Lee, "Ab initio calculations of dimensional and adsorbate effects on the workfunction of single-walled carbon nanotube", Diamond and Related Materials 12, 565 (2003).
- [Chen09] P. Chen, T. Cheng, J. Tsai, and Y. Shao, "Space charge effects in field emission nanodevices", Nanotechnology 20, 405202 (2009).
- [Chen11] J. Chen, J. Li, J. Yang, X. Yan, B.-K. Tay, and Q. Xue, "The hysteresis phenomenon of the field emission from the graphene film", App. Phys. Lett. 99, 173104 (2011).
- [Chen12] C. Cheng, M. Nakaschima, and K. Teii, "Low threshold field emission from nanocrystalline diamond/carbon nanowall composite films", Diamond Relat. Mater. 27, 40 (2012).
- [Chia09] C. Chiang, D. Yankelevich, and J. Heritage, "Picosecond photoassisted electron emission from gated p-silicon high density field emitter array", J. Appl. Phys. 106, 084505 (2009).
- [Cran12] W. Cranton, J. Chen, M. Fihn, "Handbook of visual display technology", Springer Heidelberg Dordrecht London New York (2012).

D

- [DARPA] Defense Advanced Research Projects Agency (DARPA)
http://www.darpa.mil/Our_Work/MTO/Programs/THz_Electronics.aspx
- [Dams11] F. Dams, C. Prommesberger, and R. Schreiner, "Fabrication process of silicon-tip-arrays for field emission applications", in Proc. 24th IVNC, Jul. 18–22, 2011, pp. 49-50 (2011.)
- [Dams12] F. Dams, A. Navitski, C. Prommesberger, P. Serbun, C. Langer, G. Müller, and R. Schreiner, "Homogeneous field emission cathodes with precisely adjustable

-
- geometry fabricated by silicon technology", *IEEE Trans. Electron Devices* 59, 2832 (2012).
- [Dall13] F. Dall Agnol and D. Engelsen, "Field emission from non-uniform carbon nanotube arrays", *Nanoscale Reseach Letters* 8, 319 (2013).
- [Dang07] A. Dangwal, "Enhanced field emission from metallic surfaces and nanowires", PhD thesis, University of Wuppertal (2007).
- [Dang07] A. Dangwal, G. Müller, F. Maurer, J. Brötz, and H. Fuess, "Field emission properties of bare and gold-coated nickel nanowires grown in polymer ion-track membranes", *J. Vac. Sci. Technol. B* 25, 586 (2007).
- [Dang08] A. Dangwal, C. Pandey, G. Müller, S. Karim, T. Cornelius, and C. Trautmann, "Field emission properties of electrochemically deposited gold nanowires", *Appl. Phys. Lett.* 92, 063115 (2008).
- [Day96] L. Day, "Biographical dictionary of the history of technology", London (1996).
- [Dean00] K. Dean and B. Chalamala, "Current saturation mechanisms in carbon nanotube field emitters", *Appl. Phys. Lett.* 76, 375 (2000).
- [Dean01] K. Dean, T. Burgin, B. Chalamala, "Evaporation of carbon nanotubes during electron field emission", *Appl. Phys. Lett.* 79, 1873 (2001).
- [Delz01] L. Delzeit, B. Chen, A. Cassell, R. Stevens, C. Nguyen, M. Meyyappan, "Multilayered metal catalysts for controlling the density of single-walled carbon nanotube growth", *Chem. Phys. Lett.* 348, 368 (2001).
- [Delz02] L. Delzeit, C. Nguyen, B. Chen, R. Stevens, A. Cassell, J. Han, and M. Meyyappan, "Multiwalled carbon nanotubes by CVD using multilayered metal catalysts", *J. Phys. Chem. B* 106, 5629 (2002).
- [DMRC] Davis MM-Wave Research Center
<http://www.ece.ucdavis.edu/dmrc/research/uwve.html>
- [Drag04] D. Dragoman and M. Dragoman, "Terahertz fields and applications", *Prog. Quantum Electron.* 28, 1 (2004).
- [Drag11] D. Dragoman, M. Dragoman and H. Hartnagel, "Terahertz generation using a resonant-tunneling-like configuration in graphene", *J. Appl. Phys.* 109, 124307 (2011).
- [Ding02] M. Ding, G. Sha, and A. Akinwande, "Silicon field emission arrays with atomically sharp tips: turn-on voltage and the effect of tip radius distribution", *IEEE Trans. Electron Devices* 49, 2333 (2002).
- [Ding99] M. Ding, H. Kim, and A. Akinwande, "Observation of valence band electron emission from n-type silicon field emitter arrays", *Appl. Phys. Lett.* 75, 823 (1999).
- [Ding06] F. Ding, K. Bolton, and A. Rosen, "Molecular dynamics study of bamboo-like carbon nanotube nucleation", *J. Electron. Mater.* 35, 207 (2006).
- [Dobr01] D. Dobrev, J. Vetter, R. Neumann, and N. Angert, "Conical etching and electrochemical metall replication of heavy-ion tracks in polymer foils", *J. Vac. Sci. Technol., B* 19 (4), 1385 (2001).
- [Dong03] C. Dong and M. Gupta, "Influences of the surface reactions on the field emission from multiwall carbon nanotubes", *Appl. Phys. Lett.* 83, 159 (2003).

-
- [Duan08] J. Duan, J. Liu, T. Cornelius, O. Picht, M. Rauber, C. Trautmann, and R. Neumann, "Apex angle controlled fabrication of Cu nanocones", GSI Scientific Report, PNI-MR. 23, 355 (2008).
- [Duke67] C. Duke and M. Alferieff, "Field emission through atoms adsorbed on a metal surface", *J. Chem. Phys.* 46, 923 (1967).
- [Dush23] S. Dushman, "Electron emission from metals as a function of temperature", *Physical Review*, 21, 623 (1923).
- [Dyke56] W. Dyke and W. Dolan, "Field emission", *Adv. Electron. Electron. Phys.* 8, 89 (1956).
- [Dyla06] H. Dylla, "Introduction to vacuum science and technology", CERN Accelerator school, Platja D'aro, Spain, May 16-24, (2006).
- [Dzie12] P. Dziennik and J. Niklas von Rath, "Untersuchung der Feldemissionseigenschaften kalter Kathoden", Projekt-praktikum, University of Wuppertal (2012).

E

- [Eda08] G. Eda, H. Unalan, N. Rupesinghe, G. Amaratunga, and M. Chhowalla, "Field emission from graphene based composite thin films", *Appl. Phys. Lett.* 93, 233502 (2008).
- [Edgc01] C. Edgcombe and U. Valdre, "The enhancement factor and the characterization of amorphous carbon field emitters", *Solid-state electronics* 45, 857 (2001).
- [Ehrl61] G. Ehrlich and F. Hudda, "Low temperature chemisorption. Studies in the field emission microscope", *J. Chem. Phys.* 35, 1421 (1961).
- [Eich08] J. Eichmeier and M. Thumm (Eds.), "Vacuum electronics: components and devices" Springer (2008).
- [Eng85] G. Eng, "A new correction to Schottky barrier lowering in cathodes", *J. Appl. Phys.* 58, 4365 (1985).
- [Eres04] G. Eres, A. Puretzky, D. Geohegan, and H. Cui, "In situ control of the catalyst efficiency in chemical vapor deposition of vertically aligned carbon nanotubes on predeposited metal catalyst films", *Appl. Phys. Lett.* 84, 1759 (2004).

F

- [Fan42] H. Fan, "Contacts between metals and between a metal and a semiconductor", *Phys. Rev.* 62, 388 (1942).
- [Fede10] J. Federici and L. Moeller, "Review of terahertz and subterahertz wireless communications", *J. Appl. Phys.* 107, 111101 (2010).
- [Flei75] R. Fleischer, P. Price, R. Walker (Eds.), "Nuclear Tracks in Solids: Principles and Applications", University of California Press, Berkeley (1975).
- [Fili13] V. Filip, L. Filip, and F. Okuyama, "Miniature X-ray tubes: current state and future prospects", *Journal of Instrumentation* 8, T03005 (2013).
- [Fink04] D. Fink, "Fundamentals of ion-irradiated polymers", Springer Series in Material Science, 63 (2004).

-
- [Fish88] L. Fisher, "A come back for the vacuum tube", *The New York Times*, May (1988).
- [Fitz98] J. Fitz-Gerald, T. Trottier, R. Singh, and P. Holloway, "Significant reduction of cathodoluminescent degradation in sulfide-based phosphors", *Appl. Phys. Lett.* 72, 1838 (1998).
- [Forb03] R. Forbes, C. Edgcombe, and U. Valdre, "Some comments on models for field enhancement", *Ultramicroscopy*, 95, 57 (2003).
- [Forb06] R. Forbes, "Simple good approximations for the special elliptic functions in standard Fowler-Nordheim tunneling theory for a Schottky-Nordheim barrier", *Appl. Phys. Lett.* 89, 113122 (2006).
- [Forb12b] R. Forbes, "Recent progress in reshaping the theory of orthodox field electron emission", *IVNC2012, Jeju, IEEE Cat. No. CFP12VAC-PRT*, p.167 (2012).
- [Forb13a] R. Forbes, "Progress with developing theory for Fowler-Nordheim plot interpretation", *IVNC2013, Roanoke, IEEE Cat. No. CFP13VAC-PRT*, p.1 (2013).
- [Forb12a] R. Forbes, "Extraction of emission parameters for large-area field emitters, using a technically complete Fowler-Nordheim-type equation", *Nanotechnology* 23, 095706 (2012).
- [Forb13] R. Forbes, "Improved approach to Fowler-Nordheim plot analysis", *J. Vac. Sci. Technol. B* 31, 02B103 (2013).
- [Fowl28] R. Fowler and L. Nordheim, "Electron emission in intense electric fields", *Proc. Roy. Soc. London A* 119, 173 (1928).
- [Frad10] J. Fraden, Ed. "Handbook of modern sensors: physics, designs, and applications", Springer (2010).
- [Furs05] G. Fursey, "Field emission in vacuum microelectronics", Kluwer Academic, Plenum Publishers, New York, ISBN: 0-306-47450-6 (2005).

G

- [Gadz95] J. Gadzuk, "Resonance-assisted, hot-electron-induced desorption", *Surface science* 342, 345 (1995).
- [Giva95] E. Givargizov, V. Zhirnov, A. Stepanova, E. Rakova, A. Kiselev, and P. Plekhanov, "Microstructure and field emission of diamond particles on silicon tips", *Appl. Surf. Sci.* 87, 24 (1995).
- [Gome93] R. Gomer, "Field emission and field ionization", American Institute of Physics, New York (1993).
- [Grön00] O. Gröning, O. Kuettel, Ch. Emmenegger, P. Gröning, and L. Schlapbach, "Field emission properties of carbon nanotubes", *J. Vac. Sci. Technol. B* 90, 5308 (2000).
- [Grön01] O. Gröning, L.-O. Nilson, P. Gröning, and L. Schlapbach, "Properties and characterization of chemical vapor deposition diamond field emitters", *Solid State Electronics* 45, 929 (2001).
- [Grön03] P. Gröning, P. Ruffieux, L. Schlapbach, and O. Grönig, "Carbon nanotubes for cold electron sources", *Advanced Engineering Materials* 5, 8 (2003).

[Günt01] B. Günther, A. Gohl, G. Müller, E. Givargizov, L. Zadorozhnaya, A. Stepanova, B. Spitsyn, A. N. Blaut-Bachev, B. Seleznev, and N. Suetin, "Microscopic field emission investigation of nanodiamond and AlN coated Si tips," *J. Vac. Sci. Technol. B* 19, 942 (2001).

[Günt03] B. Günther, F. Kaldasch, G. Müller, S. Schmitt, T. Henning, R. Huber, and M. Lacher, "Uniformity and stability of field emission from bare and metal coated Si tip arrays", *J. Vac. Sci. Technol. B* 21,427 (2003).

H

[Ha13] J. Ha, H. Kim, H. Raza and S. Cho, "Highly stable carbon nanotube field emitters on small metal tips against electrical arcing", *Nanoscale Research Lett.* 8, 355 (2013).

[Habe98] T. Habermann, "Rastermikroskopische untersuchung der Feldemission von Metall- und Diamandkathoden", PhD thesis, University of Wuppertal (1998).

[Han11] K. Han, Y. Lee, D. Jun, S. Lee, K. Jung, S. Yang, "Field emission ion source using a carbon nanotube array for micro time-of-flight mass spectrometer", *Jpn. J. Appl. Phys.* 50, 06GM04 (2011).

[Han12] J. Han, J. Oh, and M. Meyyappan, "Vacuum nanoelectronics: Back to the future? Gate insulated nanoscale vacuum channel transistor", *Appl. Phys. Lett.* 100, 213505 (2012).

[Hama98] C. Hamann and W. Vielstich, "Elektrochemie", Weinheim, 3. Edition (1998).

[Heo12] S. Heo, H. Kim, J. Ha, and S. Cho, "A vacuum-sealed miniature X-ray tube based on carbon nanotube field emitters", *Nanoscale Research Lett.* 7, 258 (2012).

[Ho89] P. Ho and T. Kwok, "Electromigration in metals", *Rep. Prog. Phys.* 52 301 (1989).

[Hofm03a] S. Hofmann, C. Ducati, and J. Robertson, "Low-temperature growth of carbon nanotubes by plasma-enhanced chemical vapour deposition", *Appl. Phys. Lett.* 83, 135 (2003).

[Hofm03b] S. Hofmann, C. Ducati, and J. Robertson, "Direct growth of aligned carbon nanotube field emitter arrays onto plastic substrates", *Appl. Phys. Lett.* 83, 4661 (2003).

[Hong09a] N. Hong, K. Koh, S. Lee, P. Minh, N. Tam, and P. Khoi, "Comparison of field-electron emission from different carbon nanotube array structures", *J. Vac. Sci. Technol. B.* 27, 749 (2009).

[Hong09b] N. Hong, K. Koh, N. Tam, P. Minh, P. Khoi, S. Lee, "Combined model for growing mechanism of carbon nanotubes using HFCVD: effect of temperature and molecule gas diffusion", *Thin Solid Films* 517, 3562 (2009).

[Hira08] A. Hiraki and H. Hirak, "Unique carbon nanostructure for high quality electron emitter to be employed in a variety of applications", *Rev. Mex. Fis.* S 54, 44 (2008).

[Hu09] Q. Hu, "Terahertz quantum cascade lasers and real-time T-rays imaging at video rate", *Terahertz Sci. and Technol.* 2, 120 (2009).

[Hu10] L. Hu, D. Hecht, and G. Gruner, "Carbon nanotube thin films: fabrication, properties, and applications", *Chem. Rev.* 110, 5790 (2010).

[Huan97] Q. Huang, M. Qin, and B. Zhang, "Field emission from surface states of silicon", *J. Appl. Phys.* 81, 7589 (1997).

[Huan97b] Q. Huang, M. Qin, B. Zhang, J. Sin, and M. Poon, "A field-enhanced generation model for field emission from p-type silicon", *IEEE Electron Device Lett.* 18, 616 (1997).

I

[Iiji91] S. Iijima, "Helical microtubes of graphitic carbon", *Nature* 354, 56 (1991).

[Ives04] R. Ives, "Microfabrication of high-frequency vacuum electron devices", *IEEE Trans. Plasma Sci.* 32, 1277 (2004).

J

[Jain11] H. Jain, H. Karacuban, D. Krix, H. Becker, H. Nienhaus, and V. Buck, "Carbon nanowalls deposited by inductively coupled plasma enhanced chemical vapor deposition using aluminum acetylacetonate as precursor", *Carbon* 43, 4987 (2011).

[Jain12] H. Jain, "Synthesis and characterization of carbon nanowalls by ICp-CVD using Aluminium-acetylacetonate precursor", PhD thesis, Ruhr-University Bochum, 2012.

[Jens01] K. Jensen, Y. Lau, and D. McGregor, "Photon assisted field emission from a silicon emitter", *Solid-State Electronics* 45, 831 (2001).

[Jens10] K. Jensen, "Space charge effects in field emission: Three dimensional theory", *J. Appl. Phys.* 107, 014905 (2010).

[Jeon11] H. Jeong, H. Jeong, H. Kim, J. Kim, S. Jeong, J. Han, d. Bang, and G. Lee, "All-carbon nanotube-based flexible field emission devices: from cathode to anode", *Adv. Funct. Mater.* 21, 1526 (2011).

[Jeon13a] J. Jeong, J. Kang, S. Choi, J. Kim, S. Ahn, and Y. Song, "A digital miniature X-ray tube with a high-density triode nanotube field emitter" 102, 023504 (2013).

[Jeon13b] J. Jeon, J. Kim, J. Kang, S. Choi, S. Ahn, and Y. Song, "A vacuum-sealed compact X-ray tube based on focused carbon nanotube field-emission electrons", *Nanotechnology* 24, 085201 (2013).

[Jong03] N. Jonge, "Brightness of carbon nanotube electron sources", *J. Appl. Phys.* 95, 673 (2004).

[Josh11] R. Joshi, J. Engstler, A. Navitski, V. Sakharuk, G. Müller, and J. Schreider, "Gas phase synthesis and field emission properties of 3D aligned double walled carbon nanotube/anatase hybrid architectures", *Nanoscale* 3, 3258-3264 (2011).

[Jord12a] F. Jordan, P. Serbun, A. Navitski, D. Lützenkirchen-Hecht, G. Müller, I. Alber, M. E. Toimil-Molares, and C. Trautmann, "Optimization of ion-track etching and electrochemical Cu nanocone deposition for field emission cathodes", *Thechn. Digest of the 25th Int. Vacuum Nanoelectronics Conf., Jeju, IEEE Cat. No. CFP12VAC-PRT*, 58 (2012).

[Jord12b] F. Jordan, "Elektrochemische Herstellung von konischen Metall-Nanostrukturen und systematische Untersuchung ihrer Feldemissionseigenschaften", Master Thesis, University of Wuppertal, 2012.

K

- [Kade04] V. Kadetov, "Diagnostics and modeling of an inductively coupled radio frequency discharge in hydrogen", PhD thesis, Faculty of Physics and Astronomy, Ruhr-University Bochum, 2004
- [Kale05] W. Kalender, "Computed tomography", Publicis Corporate Publishing (2005).
- [Kane97] S. Kanemaru, T. Hirano, H. Tanoue, and J. Itoh, "Control of emission currents from silicon emitter arrays using a built-in MOSFET", *Appl. Surf. Sci.*, vol. 111, pp. 218–223, Feb. 1997.
- [Kara01] A. Karabutov, V. Frolov, and V. Konov, "Diamond/sp²-bonded acarbon structures: quantum well field electron emission", *Diamond and Related Materials* 10, 840 (2001).
- [Kara06] T. Karabacak, J. DeLuca, and P. Wang, "Low temperature melting copper nanorod arrays", *J. Appl. Phys.* 99, 064304 (2006).
- [Kari06] S. Karim, M.E. Toimil-Molares, A. Balogh, W. Ensinger, T. Cornelius, E. Khan, and R. Neumann, "Morphological evolution of Au nanowires controlled by Rayleigh instability", *Nanotechnology* 17, 5954 (2006).
- [Kari07] S. Karim, M. E. Toimil-Molares, W. Ensinger, A. Balogh, T. Cornelius, E. Khan, and R. Neumann, "Influence of crystallinity on the Rayleigh instability of gold nanowires", *J. Phys. D: Appl. Phys.* 40, 3767 (2007).
- [Kart04] M. Kartikeyan, E. Borie, M. Thumm (Ed.), "Gyrotrons – High power microwave and millimeter wave technology", Springer-Verlag: Berlin, Germany (2004).
- [Kaun09] G. Kaune, M. Ruderer, E. Metwalli, W. Wang, S. Couet, K. Schage, R. Roehlsberger, S. Roth, and P. Mueller-Buschbaum, "In situ GISAXS study of gold film growth on conducting polymer films", *ACS Appl. Mater. Interfaces*, 1, 353 (2009).
- [Kend97] R. Kendall, "Cold cathode gauges for ultrahigh vacuum measurements", *J. Vac. Sci. Technol. A* 15, 740 (1997).
- [Kend99] R. Kendall, "Ionization gauge errors at low pressures", *J. Vac. Sci. Technol. A* 17, 2041 (1999).
- [Kemp06] M. Kemp, "Millimetre wave and Terahertz technology for the detection of concealed threats – a review", *Proc. of SPIE* 6402, 6402D-1 (2006).
- [Koop12] H. Koops, S. Daffaia, H. Hartnagel, and A. Rudzinski, „Development of a miniaturized dynatron THz-socillator with a FEBIP system“, *Tech. Digest 25th Int. Vacuum Nanoelectronics Conf. Jeju, IEEE Cat. No. CFP12VAC-PRT (IEEE, NJ)* p.1-4 (2012).
- [Kohl97] W. Kohl, "Handbook of Materials and Techniques for Vacuum Devices", American Inst. of Physics (1997).
- [Keil07] P. Keil, D. Lützenkirchen-Hecht, and R. Frahm, "Investigation of room temperature oxidation of Cu in air by Yoneda-XAFS", *AIP Conference Proceedings*, 882, 490 (2007).
- [Kimb] www.kimballphysics.com

L

- [Labu12] V. Labunov, B. Shulitski, A. Tymoshchuk, Y. Tamashevich, and P. Serbun, "Method of low-temperature formation of horizontally aligned CNT networks on various substrates", IVNC2012, IEEE Cat. No. CFP12VAC-PRT, p.182 (2012).
- [Laff98] J. Lafferty (Ed.), "Foundations of Vacuum Science and Technology", John Wiley and Sons, New York (1998).
- [Lang12] C. Langer, C. Prommesberger, F. Dams, and R. Schreiner, "Theoretical investigations into the field enhancement factor of silicon structures", Technical Digest, 25th International Vacuum Nanoelectronics Conference, Jeju, IEEE Cat. No. CFP12VAC-PRT (IEEE, NJ), pp. 148–149 (2012).
- [Lath95] R. Latham, "High voltage insulation", Academic Press, London, ISBN:0-12-437175-2 (1995).
- [Lee91] H. Lee and R. Huang, "A novel field emission pressure sensor", IEEE Trans. Electron Devices ED 39, 313 (1991).
- [Lee92] H. Lee and R. Huang, "A theoretical study on field emission array for microsensors", IEEE Electron Devices 39, 313 (1992).
- [Legt95] R. Legtenberg, H. Jansen, M. de Boer, and M. Elwenspoek, "Anisotropic reactive ion etching of silicon using SF₆/O₂/CHF₃ gas mixtures", J. Electrochem. Soc. 142, 2020 (1995).
- [Lide08] D. Lide, CRC Handbook on Chemistry and Physics, 89th Ed. (Taylor & Francis, London, UK, (2008).
- [Lin05] M. Lin, K. Huang, P. Lu, P. Lin, and R. Jao, "Field-emission based vacuum device for the generation of terahertz waves", J. Vac. Sci. B 23, 849 (2005).
- [Lin07] M. Lin and P. Lu, "Millimeter wave generator based on field emission cathode", J. Vac. Sci. B 25, 636 (2007).
- [Lin08] M. Lin and P. Lu, "Injection-locked millimeter wave oscillator based on field-emission cathodes", J. Vac. Sci. Tech. B 26, 694 (2008).
- [Liu01] C. Liu, C. Cutshaw, and Y. Tzeng, "Hysteresis of electron field emission from single-walled carbon nanotubes brazed on iron substrates", Proceedings of the Sixth Applied Diamond Conference/Second Frontier Carbon Technology Joint Conference(ADC/FCT 2001), Auburn, Alabama, NASA/CP-2001-210948, 1, p.742 (2001).
- [Liu06c] Z. Liu, G. Yang, Y. Lee, D. Bordelon, J. Lu, and O. Zhou, "Carbon nanotube based microfocus field emission X-ray source for microcomputed tomography", Appl. Phys. Lett. 89, 103111 (2006).
- [Liu06] J. Liu, J. Duan, M. E. Toimil-Molares, S. Karim, T. W. Cornelius, D. Dobrev, H. Yao, Y. Sun, M. Hou, Z. Wang, and R. Neumann, "Electrochemical fabrication of single-crystalline and polycrystalline Au nanowires: the influence of deposition parameters", Nanotechnology 17, 1922 (2006).
- [Liu06b] K. Liu, C. J. Chiang, and J. Heritage, "Photoresponse of gated p-silicon field emitter array and correlation with theoretical models", J. Appl. Phys. 99, 034502 (2006).
- [Lugi96] J. Luginsland, A. Valfells, and Y. Lau, "Effect of a series resistor on electron emission from a field emitter", Appl. Phys. Lett. 69, 2770 (1996).

-
- [Luon95] M. Luong, B. Bonin, H. Long, and H. Safa, "Role of adsorbates on current fluctuations in dc field emission", proceedings of the 1995 Workshop on RF superconductivity, Gif-sur-Yvette, France, SRF95C27, 509 (1995).
- [Lyth07] S. Lyth, R. Hatton, and R. Silva, "Efficient field emission from Li-salt functionalized multiwall carbon nanotubes on flexible substrates", *App. Phys. Lett.* 90, 013120 (2007).
- [Lyse05] D. Lysenkov and G. Müller, "Field emission measurement technique for the optimisation of carbon nanotube cathodes", *Int. J. Nanotechnology* 2, 239 (2005).
- [Lyse06] D. Lysenkov, "Optimization of nanostructures for field emission", PhD thesis, University of Wuppertal, WUB-DIS 2006-2 (2006).

M

- [Made84] T. Madey and W. Brown (Eds.) "History of vacuum science and thechnology", American Institute of Physics, New York (1984).
- [Mahn95] E. Mahner, "Untersuchung der erhöhten Feldemission von Niob mit einem UHV-Rastermikroskop", PhD thesis, University of Wuppertal (1995).
- [Marc90] R. Marcus, K. Chin, Y. Yuan, H. Wang, and W. Carr, "Silicon field emission", *IEEE Trans. Electron Devices* 37, 1545 (1990).
- [Marg47] N. Margulis, (in russian) *J. Phys. USSR* 11, 451 (1947).
- [Mano05] H. Manohara, M. Bronikowski, M. Hoenk, B. Hunt, and P. Siegel, "High-current-density field emitters based on arrays of carbon nanotube bundles", *J. Vac. Sci. Technol. B.* 23(1), Jan/Feb (2005).
- [Mano08] H. Manohara, M. Bronikowski, and R. Toda, "Carbon-nanotude cathodes for miniature analytical instruments", *SPIE Newsroom* (2008).
- [Maur06] F. Maurer, A. Dangwal, D. Lysenkov, G. Müller, M. E. Toimil-Molares, C. Trautmann, J. Brötz, and H. Fuess, "Field emission of copper nanowires grown in polymer ion-track membranes", *Nucl. Instr. Methods Phys. Res. B* 245, 337 (2006).
- [Mele05] A. V. Melechko, V. I. Merkulov, T. E. McKnight, M. A. Guillorn, K. L. Klein et al.: "Vertically aligned carbon nanofibers and related structures: Controlled synthesis and directed assembly", *J. Appl. Phys.* 97, 041301 (2005).
- [Miln04] W. Milne, K. Teo, G. Amaratunga, P. Legagneux, L. Gangloff, J. Schnell, V. Semet, V. Thien Binh, and O. Groening, "Carbon nanotubes as field emission sources", *J. Mater. Chem.* 14, 933 (2004).
- [Miln06] W. Milne, K. Teo, M. Mann, I. Bu, G. Amaratunga, N. Jonge, M. Allieux, J. Oostveen, P. Legegneux, E. Minoux, L. Gangloff, L. Hudanski, J. Schnell, L. Dieumegard, F. Peauger, T. Wells, and M. El-Gomati, "Carbon nanotubes as electron sources", *Phys. Stat. Sol.* 203, 1058 (2006).
- [Miln06a] W. Milne, K. Teo, E. Minoux, O. Groening, L. Gangloff, L. Hudanski, J. Schnell, L. Dieumegard, F. Peauger, I. Bu, M. Bell, P. Legegneux, G. Hasko, and G. Amaratunda, "Aligned carbon nanotubes/fibers for applications in vacuum microwave amplifiers", *J. Vac. Sci. Technol. B.* 24, 345 (2006).
- [Modi74] A. Modinos, "Field emission from surface states in semiconductors", *Surface Science* 42, 205 (1974).

-
- [Modi84] A. Modinos, "Field, thermionic, and secondary electron emission spectroscopy", Springer (1984).
- [Mura00] L. Muray, J. Spallas, C. Stebler, K. Lee, M. Mankos, Y. Hsu, M. Gmur, and T. Chang, "Advances in arrayed microcolumn lithography", *J. Vac. Sci. Technol.*, B 18, 3099 (2000).
- [Murr13] P. Murray, T. Back, M. Cahay, S. Fairchild, B. Maruyama, N. Lockwood, and M. Pasquali, "Avoidance for adsorbate-enhanced field emission from carbon nanotube fibres", *Appl. Phys. Lett.* 103, 053113 (2013).

N

- [Nam07] J. Nam, P. Alegaonkar, J. Park, J. Yoo, D. Choe, J. Kim, and W. Kim, "Field emission properties of plasma treated multiwalled carbon nanotube cathode layers", *J. Vac. Sci. Technol. B* 25, 2 (2007).
- [Navi09] A. Navitski, G. Müller, V. Sakharuk, T. Cornelius, C. Trautmann, and S. Karim, "Efficient field emission from structured gold nanowire cathodes", *Eur. Phys. J. Appl. Phys.* 48, 30502 (2009).
- [Navi10] A. Navitski, "Scanning field emission investigations of structured CNT and MNW cathodes, niobium surfaces and photocathodes", PhD thesis, University of Wuppertal (2010).
- [Navi10a] A. Navitski, G. Müller, V. Sakharuk, A.L. Prudnikava, B.G. Shulitski and V.A. Labunov: "Efficient high-current field emission from arrays of CNT columns", *J. Vac. Sci. Technol. B* 28, C2B14-19 (2010).
- [Navi10c] A. Navitski, P. Serbun, G. Müller, I. Alber, M. E. Toimil-Molares, and C. Trautmann, "Correlation between field emission current limits and morphology changes of poly- and single-crystalline gold nanowire patches", GSI scientific report, PNI-MR-36, 404 (2010).
- [Navi10d] A. Navitski, P. Serbun, G. Müller, I. Alber, M. E. Toimil-Molares, and C. Trautmann, "Correlation between field emission current limits and morphology changes of gold nanowire patches", *Tech. Digest. of the 23rd Int. Vacuum Nanoelectronics Conf.*, Palo Alto, IEEE Cat. No. CFP10VAC-PRT, 163 (2010).
- [Navi11a] A. Navitski, P. Serbun, G. Müller, R. Schreiner, and F. Dams, "Efficient and reliable field emission from silicon tip arrays for miniaturized electron sources", *Techn. Digest of the 24th Int. Vacuum Nanoelectronics Conf.*, Wuppertal, Germany IEEE Cat. No. CFP11VAC-PRT, 98 (2011).
- [Navi11] A. Navitski, P. Serbun, G. Müller, R. Joshi, J. Engstler, and J. Schneider, "Homogeneity, activation effects and current limits of structured CNT column cathodes on Si substrates", *Techn. Digest of the 24th Int. Vacuum Nanoelectronics Conf.*, Wuppertal, Germany, IEEE Cat. No. CFP11VAC-PRT, 35 (2011).
- [Navi12] A. Navitski, P. Serbun, G. Müller, R.K. Joshi, J. Engstler, and J.J. Schneider: "Role of height and contact interface of CNT microstructures on Si for high current field emission cathodes", *Eur. Phys. J. Appl. Phys.* 59, 11302/1-6 (2012).
- [Nati99] J. Nation, L. Schächter, F. Mako, L. Len, W. Peter, C. Tang, and T. Srinivasan-Rao, "Advanced in cold cathode physics and technology", *Proceedings of the IEEE* 87, 865 (1999).

-
- [Neub11] M. Neubert and V. Buck, "From Titanium Carbide to Carbon Nanowalls, the influence of process parameters on metalorganic plasma enhanced chemical vapor deposition", Proceedings of 1st joined Workshop on Surface Techniques, Ilmenau, Germany, 15.-16. September 2011, Isle Press, ISBN 978-3-938843-68-0 (2012).
- [Nied86] Ph. Niedermann, "Experiments on enhanced field emission", PhD thesis, University of Geneva, 2197 (1986).
- [Nils00] L. Nilsson, O. Gröning, C. Emmenegger, O. Kuettel, E. Schaller, and L. Schlapbach, H. Kind, J. Bonard, and K. Kern, "Scanning field emission from patterned carbon nanotube films", Appl. Phys. Lett. 76, 2071 (2000).
- [Nils01] L. Nilsson, O. Gröning, P. Gröning, and L. Schlapbach, "Collective emission degradation behavior of carbon nanotube thin-film electron emitters", App. Phys. Lett. 79, 1036 (2001).
- [Ning78] T. Ning, "Hot electron emission from silicon into silicon dioxide", Solid-State Electronics, 21, 273 (1978).
- [Nord28] L. Nordheim, "The effect of the image force on the emission and reflection of electrons by metals", Proceedings of the Royal Society of London, Series A, Containing papers of mathematical and physical character, 121, 626 (1928).

O

- [Obra00] A. Obraztsov, I. Pavlovsky, A. Volkov, E. Obraztsova, A. Chuvilin, and V. Kuznetsov, "Aligned carbon nanotube films for cold cathode applications", J. Vac. Sci. Technol. B, 18, 2 (2000).
- [Obra03] A. Obraztsov, Al. Zakhidov, A. Volkov, and D. Lyashenko, "Nano-carbon materials for cold cathode applications", Microelectronics Engineering 69, 405 (2003).
- [Obra03] A. Obraztsov, A. Zakhidov, A. Volkov, and D. Lyashenko, "Non-classical electron field emission from carbon materials", Diamond Relat. Mater. 12, 446 (2003).
- [Obra13] A. Obraztsov, V. Kleshch, and E. Smolnikova, "A nano-graphite cold cathode for an energy-efficient cathodoluminescent light source", Beilstein J. Nanotechnol. 4, 493 (2013).
- [Ohan98] J. O'Hanlon, "A user's guide to vacuum technology", 3rd Ed., John Wiley and Sons, New York (1998).

P

- [Patt10] B. Patterson, R. Abela, H. Braun, U. Flechsig, R. Ganter, Y. Kim, E. Kirk, A. Oppelt, M. Pedrozzi, S. Reiche, L. Rivkin, Th. Schmidt, B. Schmidt, V. Strocov, S. Tsujino, and A. Wrulich, "Coherent science at the SwissFEL X-ray laser", New J. Phys. 12, 35012 (2010).
- [Peac91] R. Peacock, N. Preacock, and D. Hauschulz, "Comparison of hot cathode and cold cathode ionization gauges", J. Vac. Sci. Technol A 9, 1977 (1991).
- [Pier50] J. Pierce, "Traveling-wave tubes", New York D. Van Nostrand Company, Inc. (1950).
- [Prox] www.proxivision.de

-
- [Purc02] S. Purcell, P. Vincent, C. Journet, and V. Binh, "Hot nanotubes: stable heating of individual multiwall carbon nanotubes to 2000K induced by the field-emission current", *Phys. Rev. Lett.*, 88, 105502 (2002).
- [Pupe96] N. Pupeter, "Untersuchung der überhöhten Elektronenfeldemission an chemisch und mechanisch polierten Nb-, Nb₃Sn-, Cu- und Al-Oberflächen in Verbindung mit Heizbehandlungen", PhD thesis WUB-DIS 96-16, University of Wuppertal (1996).

Q

- [Qian09] X. Qian, R. Rajaram, X. Calderon-Colon, G. Yang, T. Phan, D. Lalush, J. Lu, and O. Zhou, "Design and characterization of a spatially distributed multibeam field emission X-ray source for stationary digital breast tomosynthesis", *Med. Phys.*, 36, 1624 (2009).
- [Qian12] X. Qian, A. Tucker, E. Gidcumb, J. Shan and G. Yang, X. Calderon-Colon and S. Sultana, J. Lu, O. Zhou, D. Spronk, F. Sprenger, Y. Zhang, D. Kennedy, T. Farbizio, and Z. Jing, "High resolution stationary digital breast tomosynthesis using distributed carbon nanotube X-ray source array", *Med. Phys.*, 39, 2090 (2012).
- [Qing97] A. Qing, Q. Ming, Z. Bin, J. Sin, and M. Poon, "A field-enhanced generation model for field emission from p-type silicon", *IEEE Electron Device Lett.* 18, 616 (1997).
- [Qiu09] J. Qiu, B. Levush, J. Pasour, A. Katz, C. Armstrong, D. Whalay, J. Tucek, K. Kreischer, and D. Gallagher, "Vacuum tube amplifiers", *IEEE Microw. Mag.* 10, 38 (2009).

R

- [Rayl78] L. Rayleigh, On the instability of jets. *Proc. Lond. Math. Soc.* S1-10 (1), 4-13 (1878).
- [Raga09] T. Ragab and C. Basaran, "Joule heating in single-walled carbon nanotubes", *J. Appl. Phys.*, 106,063705 (2009).
- [Rash00] C. Rash, "Helmet-mounted displays: design issues for rotary-wing aircraft", SPIE press (2000).
- [Redh68] P. Redhead, J. Hopson, and E. Kornelsen, "The Physical Basis of Ultrahigh Vacuum", Chapman and Hall, Ltd. London (reprinted by the AVS) (1968).
- [Reil79] L. Rayleigh, "On the instability of jets", *Proc. London Math. Soc.* 10, 4 (1879).
- [Rowe06] M. Rowell, M. Topinka, M. McGehee, H. Prall, G. Dennler, N. Sariciftci, L. Hu, and G. Gruner, "Organic solar cells with carbon nanotube network electrodes", *Appl. Phys. Lett.* 88, 233506 (2006).
- [Reim98] L. Reimer, "Scanning electron microscopy: physics of image formation and microanalysis", 2nd Edition Springer-Verlag Berlin Heidelberg New York (1998).
- [Ren13] Z. Ren, "Aligned Carbon Nanotubes: physics, concepts, fabrication and devices", Springer-Verlag Berlin Heidelberg (2013).
- [Robe78] M. Roberts and J. Thomas, "Chemical physics of solids and their surfaces: volume 7", Royal Society of Chemistry (1978).
- [Roth76] A. Roth, "Vacuum technology", North-Holland, Amsterdam (1976).

[Rutk12] S. Rutkowski, "Messungen und Simulation von kalten Kathoden in Triodenanordnung", Diplomarbeit (2012).

S

- [Sait10] Y. Saito, "Carbon nanotubes and related field emitters", Wiley-VCH (2010).
- [Schr11] R. Schreiner, F. Dams, C. Prommesberger, B. Bornmann, P. Serbun, A. Navitski, and G. Müller, "Silicon-based Integrated Field Emission Electron Sources for Sensor Applications", Technical Digest. 24th Inter. Vacuum Nanoelectronics Conf., Wuppertal, IEEE Cat. No. CFP11VAC-PRT, (IEEE, NJ) p.22-23 (2011).
- [Scho23] W. Schottky, "Über kalte und warme Elektronenentladungen", Z. Phys. 14, 63 (1923).
- [Schi68] L. Schiff, "Quantum mechanics", 3rd edn. McGraw Hill, New York (1968).
- [Schr74] D. Schroder, R. Thomas, J. Vine, and H. Nathanson, "The semiconductor field-emission photocathode", IEEE Trans. Electron Devices 21, 785 (1974).
- [Schu00] I. Schuchert, "Electrochemische untersuchungen zur Abscheidung und zum Korrosionsverhalten von Kupfermikrostrukturen", PhD thesis (2000).
- [Seme02] V. Semet, V. T. Binh, P. Vincent, D. Guillot, K. B. K. Teo, M. Chhowalla, G. A. J. Amaratunga, W. I. Milne, P. Legagneux, and D. Pribat, "Field electron emission from individual carbon nanotubes of a vertically aligned array", Appl. Phys. Lett. 81,343 (2002).
- [Send04] S. Senda, Y. Sakai, Y. Mizuta, S. Kita, and F. Okuyama, "Super-miniature X-ray tube", Appl. Phys. Lett. 85, 5679 (2004).
- [Serb11] P. Serbun, S. Rutkowski, A. Navitski, G. Müller, N. Hong, and S. Lee, "Field emission from carbon nanotube arrays and triode test of single CNT columns", Tech. Digest of the 24th Int. Vacuum Nanoelectronics Conf. Wuppertal, IEEE Cat. No. CFP11VAC-PRT, 38 (2011).
- [Serb12a] P. Serbun, F. Jordan, A. Navitski, G. Müller, I. Alber, M.E. Toimil-Molares, and C. Trautmann, "Copper nanocones grown in polymer ion-track membranes as field emitters", Eur. Phys. J. Appl. Phys. 58, 10402 (2012).
- [Serb12b] P. Serbun, F. Jordan, G. Müller, I. Alber, M.E. Toimil-Molares, and C. Trautmann, "Optimization of copper nanocones for field emission cathodes", GSI Scientific Report 2012, PNI-INHOUSE-EXP-51, p.420, (2013).
- [Serb13] P. Serbun, B. Bornmann, A. Navitski, C. Prommesberger, C. Langer, F. Dams, G. Müller, and R. Scheiner, "Stable field emission of single B-doped Si tips and linear current scaling of uniform tip arrays for integrated vacuum microelectronic devices", J. Vac. Sci. Technol. B 31, 02B101 (2013).
- [Serb13a] P. Serbun, G. Müller, A. Tymoshchyk, I. Kashko, B. Shulitski, V. Labunov, "High field emission current density from structured CNT bundle cathodes", Proc. of the 26th Int. Vacuum Nanoelectronics Conference, Roanoke, USA (2013).
- [Shaw02] J. Shaw and J. Itoh, "Silicon field emitter arrays in Vacuum microelectronics", W. Zhu, Ed. New York: Wiley (2002).
- [Sieg11] J. Siegel, O. Lzutakov, V. Rybka, Z. Kolska, and V. Svorcik, "Properties of gold nanostructures sputtered on glass", Nanoscale Research Letters 6, 96 (2011).

-
- [Smit98] R. Smith, "Electronics developments for field emission displays", *Information display*, 14, 2-12 (1998).
- [Song02] Y. Song, C. Hwang, Y. Cho, B. Kim, S. Ahn, C. Chung, D. Kim, H. Uhm, J. Lee, and K. Cho, "Active-matrix field emission display with amorphous silicon thin-film transistors and Mo-tip field emitter arrays", *ETRI Journal* 24, 290 (2002).
- [Song13] Y. Song, D. Shin, S. Jeon, J. Kim, and C. Lee, "Field emission properties of carbon nanotube emitters dependent on electrode geometry", *J. Vac. Sci. Technol. B* 31, 052203 (2013).
- [Spin76] C. Spindt, I. Brodie, L. Humphrey, and E. Westerberg, "Physical properties of thin-film emission cathodes with molybdenum cones", *J. Appl. Phys.* 47, 5248 (1976).
- [Spin86] C. Spindt, C. Holland, P. Schoebel, I. Brodie, "Field emitter array development for microwave applications", *J. Vac. Sci. Technol. B* 14, 1996 (1986).
- [Spin88] C. Spindt, T. Fahlen, J. Macaulay, C. Curtin, and R. Duboc, "ThinCRT flat-panel-display construction and operating characteristics", *Tech. Digest of Society for Information Display Symposium*, pp. 99-102 (1988).
- [Stah07] B. Stahlmecke and G. Dumpich, "Resistance behaviour and morphological changes during electromigration in gold wires", *J. Phys. Condens. Matter* 19, 046210 (2007).
- [Stra55] R. Stratton, "Field emission from semiconductors", *Proc. Phys. Soc. B* 68, 746 (1955).
- [Sugi01] H. Sugie, M. Tanemura, V. Filip. K. Iwata, K. Takahashi, and F. Okuyama, "Carbon nanotubes as electron source in an X-ray tube", *Appl. Phys. Lett.* 78, 2578 (2001).
- [Sun11] D. Sun, M. Timmermans, Y. Tian, A. Nasibulin, E. Kauppinen, S. Kishimoto, and Y. Ohno, "Flexible high-performance carbon nanotube integrated circuits", *Nature nanotechnology* 6, 156 (2011).
- [Sze07] S. Sze and K. Hg, "Physics of semiconductor devices", 3rd ed., Wiley-Interscience, Hoboken (2007).

T

- [Teep05] T. Teepen, A. van Veen, H. vant Spijker, S. Steenbrink, A. van Zuuk, C. Heerkens, M. Wieland, N. van Druten, and P. Kruit, "Fabrication and characterization of p-type silicon field-emitter arrays for lithography", *J. Vac. Sci. Technol. B* 23, 359 (2005).
- [Teo02] K. Teo, M. Chhowalla, G. Amaratunga, W. Milne, G. Pirio, P. Legagneux, F. Wyczisk, D. Pribat, and D. Hasko, "Field emission from dense, sparse, and patterned arrays of carbon nanofibers", *App. Phys. Lett.* 80, 2011 (2002).
- [Teo03a] K. B. K. Teo, C. Singh, M. Chhowalla, W. I. Milne: in *Encyclopedia of Nanoscience and Nanotechnology*, ed. H. S. Nalwa, American Scientific Publishers, California, 1, 665 (2004).
- [Teo03b] K. B. K. Teo et al., "Plasma enhanced chemical vapour deposition carbon nanotubes/nanofibres - how uniform do they grow?", *Nanotechnology* 14, 204 (2003).
- [Toim01] M. E. Toimil-Molares, J. Brötz, V. Buchmann, D. Dobrev, R. Neumann, R. Scholz, I. Schuchert, C. Trautmann, and J. Vetter, "Etched heavy ion tracks in polycarbonate

as template for copper nanowires", Nucl. Instr. Methods Phys. Res. B 185, 192 (2001).

- [Toim01a] M. E. Toimil-Molares, "Fabrication and characterization of copper nanowires electrochemically deposited in etched ion-track membranes", PhD thesis (2001).
- [Toim01b] M. E. Toimil-Molares, J. Brötz, V. Buschmann, D. Dobrev, R. Neumann, R. Scholz, I.U. Schuchert, C. Trautmann, and J. Vetter., "Etched heavy ion tracks in polycarbonate as template for copper nanowires", Nucl. Inst. and Meth. in Phys. Res. B 185, 192 (2001).
- [Toim04] M.E. Toimil-Molares, A. Balogh, T. Cornelius, R. Neumann, and C. Trautmann, "Fragmentation of nanowires driven by Rayleigh instability", Appl. Phys. Lett. 85, 5337 (2004).
- [Toim12] M. E. Toimil-Molares, "Characterization and properties of micro- and nanowires of controlled size, composition, and geometry fabricated by electrodeposition and ion-track technology", Beilstein J. Nanotechnol. 3, 860 (2012).
- [Toya96] T. Toyama, K. Hiratsuka, H. Okamoto, Y. Hamakawa, "Hot-electron induced electroluminescence and avalanche multiplication in hydrogenated amorphous silicon", J. Non-Cryst. Solids 198, 198 (1996).
- [Tsai09] T. Tsai, C. Lee, N. Tai, and W. Tuan, "Transfer of patterned vertically aligned carbon nanotubes onto plastic substrates for flexible electronics and field emission devices", Appl. Phys. Lett. 95, 013107 (2009).
- [Tson79] T. Tsong, "Field penetration and band bending for semiconductor of simple geometries in high electric fields", Surface Science 85, 1 (1979).
- [Trau95] C. Trautmann, "Observation and chemical treatment of heavy-ion tracks in polymers", Nucl. Instr. and Meth. in Phys. Res. B 105, 81 (1995).
- [Trau96] C. Trautmann, S. Bouffard, and R. Spohr, "Etching threshold for ion tracks in polyimide", Nucl. Instr. and Meth. in Phys. Res. B 116, 429 (1996).

U

- [Utsu91] T. Utsumi, "Vacuum microelectronics: What's new and exciting", IEEE Trans. Electron Devices 38, 2276 (1991).

V

- [Vila04] L. Vila, P. Vincent, L. de Pra, G. Pirio, E. Minoux, L. Gangloff, S. Demoustier-Champagne, N. Sarazin, E. Ferain, and R. Lagras, "Growth and field-emission properties of vertically aligned cobalt nanowire arrays", Nano Lett. 4, 521 (2004).
- [Vinc02] P. Vincent, S. Purcell, C. Journet, and V. Binh, "Modelization of resistive heating of carbon nanotubes during field emission", Phys. Rev. B 66, 075406 (2002).

W

- [Wang04] L. Wang, R. Stevens, E. Huq, I. Loader, B. Kent, K. Aplin, and J. She, "Optimization of silicon field-emission arrays fabrication for space applications", J. Vac. Sci. Technol. B, Microelectron. Nanometer Struct. 22, 1407 (2004).

-
- [Wang07] C. Wang, T. Chen, and S. Chang, "Flexible field emitter made of carbon nanotubes microwave welded onto polymer substrates", *App. Phys. Lett.* 90, 103111 (2007).
- [Wei01] Y. Wei, C. Xie, K. Dean, and B. Coll, "Stability of carbon nanotubes under electric field studied by scanning electron microscopy", *Appl. Phys. Lett.* 79, 4527 (2001).
- [Wen07] W. Wen, L. Wang, J. Gao, and D. Sun, "Studies on MEMS vacuum sensor based on field emission of silicon tips array", *Proceedings of the 2nd IEEE International Conference on Nano/Micro Engineered and Molecular Systems*, January 16-19, Bangkok, Thailand (2007).
- [Whal00] D. Whaley, B. Gannon, C. Smith, C. Armstrong, and C. Spindt, "Application of field emitter arrays to microwave power amplifiers", *IEEE Trans. Plasma Sci.* 28, 727 (2000).
- [Whal09] D. Whaley, R. Duggal, C. Armstrong, C. Bellew, C. Holland, and C. Spindt, "100 W Operation of a cold cathode TWT", *IEEE Trans. Electr. Devices* 56, 896 (2009).
- [Will06] G. Williams, "Filling the THz gap – high power sources and applications", *Rep. Prog. Phys.* 69, 301 (2006).
- [Will07] B. Williams, "Terahertz quantum-cascade lasers", *Nature photonics* 1, 517 (2007).
- [Wilf12] S. Wilfert and C. Edelmann, "Field emitter-based vacuum sensors", *Vacuum* 86, 556 (2012).
- [Wood97] R. Wood, "A new form of cathode discharge and the production of X-rays, together with some notes on diffraction", *Phys. Rev.* 5, 1 (1897).
- [Wu09] J. Wu, M. Wyse, D. McClain, N. Thomas, and J. Jiao, "Fabrication and field emission properties of triode-type carbon nanotube emitter arrays", *Nano Lett.* 9, 595 (2009).

X

- [Xin] <http://www.xinraysystems.com>
- [Xue06] X. Xue, L. Li, C. Yu, Y. Chen, Y. Wang, and T. Wang, "Extremely stable field emission from AlZnO nanowire arrays", *App. Phys. Lett.* 89, 043118 (2006).

Y

- [Yats70] A. Yatsenko, "On a model of photo-field emission from p-type semiconductors", *Solid State Phys.* 1, 333 (1970).
- [Yell11] S. Yellampalli, "Carbon nanotubes – synthesis, characterization, applications", *Intech* (2010).
- [Yosh07] N. Yoshimura, "Vacuum Technology: practice for scientific instruments", *Springer-Verlag Berlin Heidelberg* (2007).
- [You09] J. You, X. Zhang, P. Cai, J. Dong, Y. Gao, Z. Yin, N. Chen, R. Wang, and H. Yan, "Enhancement of field emission of the ZnO film by the reduced work function and the increased conductivity via hydrogen plasma treatment", *Appl. Phys. Lett.* 94, 262105 (2009).
- [You10] G. You, H. Gong and J. Thong, "Improving the morphological stability of a polycrystalline tungsten nanowire with a carbon shell", *Nanotechnology* 21, 195701 (2010).

-
- [Yue02] G. Yue, Q. Que, B. Gao, Y. Cheng, J. Zhang, H. Shimoda, S. Chang, J. Lu, and O. Zhou, "Generation of continuous and pulsed diagnostic imaging X-ray radiation using a carbon-nanotube-based field-emission cathode", *Appl. Phys. Lett.* 81, 355 (2002).

Z

- [Zeit88] A. Zeitoun-Fakiris and B. Jüttner, "The effect of gases on the emission currents from metallic micropoints in ultra-high vacuum", *J. Phys. D. Appl. Phys.* 21, 960 (1988).
- [Zeit91] A. Zeitoun-Fakiris and B. Jüttner, "On the dose of bombarding residual gas ions for influencing pre-breakdown field emission in a vacuum", *J. Phys. D. Appl. Phys.* 24, 750 (1991).
- [Zhan05] J. Zhang, Yang, Y. Cheng, B. Gao, Q. Qiu, J. Lu, and O. Zhou, "Stationary scanning X-ray source based on carbon nanotube field emitters", *Appl. Phys. Lett.* 86, 184104 (2005).
- [Zhan06] J. Zhang, G. Yang, Y. Lee, Y. Cheng, B. Gao, Q. Qiu, J. Lu, O. Zhou, "A multi-beam X-ray imaging system based on carbon nanotube field emitters", *Proceedings of SPIE, Medical Imaging*, 6142, 614204 (2006).
- [Zhan10] D. Zhang, K. Ryu, X. Liu, E. Polikarpov, J. Ly, M. Tompson, and C. Zhou, "Transparent, conductive, and flexible carbon nanotube films and their application in organic light-emitting diodes", *Nano Lett.* 6, 9 (2006).
- [Zhang05] M. Zhang, S. Fang, A. Zakhidov, S. Lee, A. Aliev, C. Williams, K. Atkinson, R. Baughman, "Strong, transparent, multifunctional, carbon nanotube sheets", *Science* 309, 1215 (2005).
- [Zhon02] D. Zhong, G. Zhang, S. Liu, T. Sakurai, E. Wang, "Universal field-emission model for carbon nanotubes on a metal tip", *Appl. Phys. Lett.* 80, 506 (2002).
- [Zhir01] V. Zhirnov, C. Lizzul-Rinne, G. Wojak, R. Sanwald, and J. Hren, "Standardization of field emission measurements", *J. Vac. Sci. Technol. B* 19, 87 (2001).
- [Zhu01] W. Zhu (Ed.), "Vacuum micro-electronics", Wiley, New York (2001).
- [Zhu05] Y. Zhu, T. Yu, F. Cheong, X. Xu, C. Lim, V. Tan, J. Thong, and C. Sow, "Sarge-scale synthesis and field emission properties of vertically oriented CuO nanowire films", *Nanotechnology* 16, 88 (2005).

Acknowledgements

First, I would like to thank my supervisor, **Prof. Dr. Günter Müller** for his inspiring guidance, constant availability, encouragement, patience, and professional support that he provided over the past several years. He continually stimulated my scientific growth and greatly assisted me with scientific writing.

I would like to give very special thank to **Prof. Dr. Ronald Frahm** for his kind agreement to review this work.

I thank my colleagues from the FE laboratory over the years: **Dr. Aliaksandr Navitski, Felix Jordan, Simon Rutkowski, Benjamin Bornmann, Stefan Lagotzky, Stefan Mingels, Jahan Pouryamout, Dr. Dirk Lützenkirchen-Hecht and Dr. Ralf Heiderhoff** for great help with measurements and for constructive discussions about field emission results and measurement techniques.

I would also like to thank: **Denis Bandurin, Alina Herzog, Andrey Khoroshilov, Nikita Shpilevoy, Anna Krechetnykova, Roman Kuzmenko, Eugeny Muha, Polina Kaminskaya, Andrey Stepanov, Alexey Serbun, Alex Gubarevich and my school friends.**

I would like to thank all of our cooperation partners:

Andrey Tymoshchyk, Y. Tamashevich, I. Kashko, B. Shulitski, Prof. Dr. Vladimir Labunov, Dr. A. Prudnikava and Prof. Dr. Alexander Smirnov (scientific adviser) at the Belarusian State University of Informatics and Radioelectronics, (Minsk, Belarus) for providing CNT samples and for close cooperation.

Prof. Dr. Christina Trautmann, Dr. M.-E. Toimil Molaes and Dr. Ina Alber at GSI (Darmstadt, Germany) for providing metallic samples.

Prof. Dr. Rupert Schreiner, F. Dams, C. Prommesberger and C. Langer at the Regensburg University of Applied Sciences (Regensburg, Germany) for providing Si samples.

Prof. Dr. Jörg, J. Schneider, Dr. Jörg Engstler, and Dr. Ravi K. Joshi at TUD, (Darmstadt, Germany) for providing CNT samples.

Prof. Dr. Volk Buck, Dr. Markus Neubert, Dr. H.G. Jain, N. Hartmann, D. Behrenberg at the University of Duisburg-Essen and CeNIDE, Germany.

Dr. Nguyen Tuan Hong and Prof. Dr. Soonil Lee at Ajou University (Suwon, South Korea) for providing CNT samples fabricated by HF-CVD.

This work was financially supported by the following projects: (1) GSI R&D project W-MUELL1012 “*Optimierung der Feldemission metallischer Nanodrähte für kalte Elektronenquellen*“ (2010-2012); (2) FP 7-INCO.2011-6.2 EU project Nr. 295043 BELERA “*Reinforcing carbon nanotubes and photonics research cooperation between the Belarusian State University of Informatics and Radioelectronics and the European Rearch Area*” (2012-2013).

List of publications

Some aspects of the work described herein have been published in reviewed journals:

- P. Serbun, B. Bornmann, A. Navitski, G. Müller, C. Prommesberger, C. Langer, F. Dams, R. Schreiner, “*Stable field emission of single B-doped Si tips and linear current scaling of uniform tip arrays for integrated vacuum microelectronic devices*”, J. Vac. Sci. Technol. B **31**, 02B1011-6 (2013).
- P. Serbun, F. Jordan, A. Navitski, G. Müller, I. Alber, M.E. Toimil-Molares, and C. Trautmann, “*Copper nanocones grown in polymer ion-track membranes as field emitters*“, Eur. Phys. J. Appl. Phys. **58**, 10402 (2012).
- F. Dams, A. Navitski, C. Prommesberger, P. Serbun, C. Langer, G. Müller, and R. Schreiner, “*Homogeneous field emission cathodes with precisely adjustable geometry fabricated by silicon technology*”, IEEE Trans. Electron Devices **59**, 2832 (2012).
- A. Navitski, P. Serbun, G. Müller, R.K. Joshi, J. Engstler, and J.J. Schneider: “*Role of height and contact interface of CNT microstructures on Si for high current field emission cathodes*”, Eur. Phys. J. Appl. Phys. **59**, 11302/1-6 (2012).